JAEA-Conf 2016-004
INDC(JPN)-202
DOI:10.11484/jaea-conf-2016-004

Proceedings of the 2015 Symposium on Nuclear Data
November 19-20, 2015,
Ibaraki Quantum Beam Research Center,
Tokai-mura, Ibaraki, Japan

(Eds.) Osamu IWAMOTO, Toshiya SANAMI, Satoshi KUNIEDA, Hiroyuki KOURA
and Shoji NAKAMURA

Nuclear Science and Engineering Center
Sector of Nuclear Science Research

JAEA-Conf

September 2016
Japan Atomic Energy Agency
日本原子力研究開発機構

国立研究開発法人日本原子力研究開発機構　研究連携成果展開部　研究成果管理課
〒319-1195 茨城県那珂郡東海村大字白方２番地4
電話 029-282-6387, Fax 029-282-5920, E-mail:ird-support@jaea.go.jp

Institutional Repository Section,
Intellectual Resources Management and R&D Collaboration Department,
Japan Atomic Energy Agency.
2-4 Shirakata, Tokai-mura, Naka-gun, Ibaraki-ken 319-1195 Japan
Tel +81-29-282-6387, Fax +81-29-282-5920, E-mail:ird-support@jaea.go.jp

JAEA-Conf 2016-004
INDC(JPN)-202

Proceedings of the 2015 Symposium on Nuclear Data
November 19-20, 2015,
Ibaraki Quantum Beam Research Center,
Tokai-mura, Ibaraki, Japan

(Eds.) Osamu IWAMOTO, Toshiya SANAMI*, Satoshi KUNIEDA,
Hiroyuki KOURA† and Shoji NAKAMURA

Nuclear Science and Engineering Center, Sector of Nuclear Science Research,
Japan Atomic Energy Agency
Tokai-mura, Naka-gun, Ibaraki-ken

(Received June 13 , 2016)

The 2015 Symposium on Nuclear Data was held at Ibaraki Quantum Beam Research Center, on November 19 and 20, 2015. The symposium was organized by the Nuclear Data Division of the Atomic Energy Society of Japan in cooperation with Nuclear Science and Engineering Center of Japan Atomic Energy Agency and North Kanto Branch of Atomic Energy Society of Japan. In the symposium, there were two tutorials, “ Theory of Few-Body Systems and Recent Topics ” and “ Use of Covariance Data 2015 ” and four oral sessions, “Recent Research Topics”, “Progress of AIMAC Project”, “Present Status of JENDL Evaluated Files ” , and “ Nuclear Data Applications ” . In addition, recent research progress on experiments, evaluation, benchmark and application was presented in a poster session. Among 99 participants, all presentations and following discussions were very active and fruitful. This report consists of total 46 papers including 13 oral and 33 poster presentations.

Keywords: Nuclear Data Symposium 2015, Experiments, Nuclear Theory, Nuclear Data Evaluation, Benchmark Test, Nuclear Data Applications

---

† Advanced Science Research Center

* High Energy Accelerator Research Organization

Organizers: O. Iwamoto (JAEA, Chair), T. Sanami (KEK, Vice-Chair), M. Aikawa (Hokkaido U.), N. Yamano (Fukui U.), K. Katoh (Hokkaido U.), T. Yoshii (TEPSYS), J. Hori (Kyoto U.), I. Murata (Osaka U.), K. Nakajima (Kyoto U.), T. Hazama (JAEA), S. Kunieda (JAEA), H. Koura (JAEA), S. Chiba (Tokyo Tech.), S. Nakamura (JAEA), K. Kino (Hokkaido U.)

JAEA-Conf 2016-004
INDC(JPN)-202

2015年度核データ研究会報告集
2015年11月19日~ 20日、
いばらき量子ビーム研究センター、茨城県東海村

日本原子力研究開発機構　原子力科学研究部門　原子力基礎工学研究センター
(編) 岩本　修、佐波　俊哉*、國枝　賢、小浦　寛之†、中村　詔司

(2016年6月13日受理)

2015年度核データ研究会は、2015年11月19日~ 20日に、茨城県東海村のいばらき量子ビーム研究センターにて開催された。本研究会は、日本原子力学会核データ部会が主催、日本原子力研究開発機構原子力基礎工学研究センターと日本原子力学会北関東支部が共催した。今回、チュートリアルとして「少数多体系理論の最近の話題」、「核データ共分散の利用法2015」の2件を、講演・議論のセッションとして「最近の話題」、「AIMACプロジェクトの進捗」、「JENDL評価ファイルの現状」、「核データの応用」の4件を企画・実施した。さらに、ポスターセッションでは、実験、評価、ベンチマーク、応用など、幅広い研究内容について発表が行われた。参加者総数は99名で、それぞれの口頭発表及びポスター発表では活発な質疑応答が行われた。本報告書は、本研究会における口頭発表13件、ポスター33件の論文をまとめている。

原子力科学研究所：〒319-1195 茨城県那珂郡東海村大字白方2-4
† 先端基礎研究センター
* 高エネルギー加速器研究機構

2015年核データ研究会実行委員会：岩本修（委員長、原子力機構）、佐波俊哉（副委員長、KEK）、合川正幸（北大）、山野直樹（福井大）、加藤幾芳 (北大)、吉井貴（テプコシステムズ）、堀順一（京大）、村田勲（阪大）、中島健（京大）、羽様平（原子力機構）、國枝賢（原子力機構）、小浦寛之（原子力機構）、千葉敏（東工大）、中村詔司（原子力機構）、木野幸一（北大）

Contents

Papers presented at Oral sessions

Papers presented at a Poster session

目 次

口頭発表論文

ポスター発表論文

This is a blank page.

1 Program of 2015 Symposium on Nuclear Data

Date : November 19(Thu)13:00 – 20(Fri) 17:00, 2015
Venue : Ibaraki Quantum Beam Research Center, 2F Multipurpose Hall
Host : Nuclear Data Division, Atomic Energy Society of Japan
Co-host : North Kanto Branch of Atomic Energy Society of Japan,
Nuclear Science and Engineering Center of JAEA

November 19 (Thu), at Multipurpose Hall

13:00 – 13:15 **Opening Address** O. Iwamoto(JAEA)

13:15 - 14:45
Session 1 : Recent Research Topics 【Chair: S. Chiba (Tokyo Tech.)】
1-1 Measurement of the first ionization potential of lawrencium, element 103 [30] T. Sato (JAEA)
1-2 Present status on fission study and perspectives [30] K. Nishio (JAEA)
1-3 Photoneutron cross section measurements for IAEA-CRP[30] H. Utsunomiya（Konan U.）

14:45 - 15:10 Photo, and Coffee Break [25]

15:10 - 16:40 **Poster Session** [90] （Venue: IQBRC 2F Coffee Lounge）

18:00 - 20:00 Convivial Gathering（Venue: Tokai Kaikan）

November 20 (Fri), at Multipurpose Hall

9:30 – 11:10
Session 2 : **Progress of AIMAC Project** 【Chair: T. Sanami (KEK)】
2-1 Precise isotopic analysis of samples mainly by thermal ionization mass spectrometry [20]
Y. Shibahara（Kyoto U.）
2-2 Accurate Measurements of Gamma-ray Emission Probabilities [20] K. Terada（JAEA）
2-3 Nuclear data measurements extending to fast neutron energy region [20] T. Katabuchi (Tokyo Tech.)
2-4 Re-analysis of MA reaction rate ratio measurement at the KUCA [20] T. Sano (Kyoto U.)
2-5 Development of evaluation method for improvement of nuclear data precision
in MA isotopes [20] K. Mizuyama（JAEA）

11:10 – 11:20 Coffee Break [10]

11:20 – 12:20 【Chair: H. Koura (JAEA)】
Tutorial-I: Theory of Few-Body Systems and Recent Topics [60] S. Oryu (TUS)

12:20 – 13:20 Lunch Time [60]

13:20 – 14:20 【Chair: T. Yoshii (TEPSYS)】

Tutorial-II: Use of Covariance Data 2015 [60] M. Ishikawa (JAEA)

14:20 - 14:30 Coffee Break [10]

14:30 – 15:30

Session 3 : **Present Status of JENDL Evaluated Files** 【Chair: M. Aikawa (Hokkaido U.】

3-1 Overview of JENDL-4.0/HE and benchmark calculations [20] S. Kunieda (JAEA)
3-2 Activation Cross-section File for Decommissioning of LWRs [20] K. Shibata (JAEA)
3-3 Photonuclear Data File [20] N. Iwamoto (JAEA)

15:30 – 15:40 Coffee Break [10]

15:40 – 16:40

Session 4 : **Nuclear Data Applications** 【Chair: I. Murata (Osaka U.)】

4-1 Neutron Nuclear Data for Medical Radioisotope Production [20] Y. Nagai (JAEA)
4-2 Overview of the PHITS code and application to nuclear data
–Radiation damage calculation for materials- [20] Y. Iwamoto (JAEA)
4-3 Neutronic Study of Transmutation Experimental Facility at J-PARC [20] H. Iwamoto (JAEA)

16:40 – 16:55 **Poster Award** Nuclear Data Division, AESJ

16:55 – 17:00 **Closing Address** T. Sanami (KEK)

Poster Presentation

Date : November 19 (Thu), 15:10 - 16:40

1. Interaction cross sections using thick-target transmission method
   M. Aikawa(Hokkaido U.)
2. Current status in development of new EXFOR editor
   S. Aiganym (Hokkaido U.)
3. Intranuclear Cascade model for alpha induced reactions at incident energies 50-150MeV
   M. J. Kobra (Kyushu U.)
4. Microscopic nuclear structure calculation for nuclear data evaluation of various nuclei produced via nuclear transmutation of long-lived fission products
   N. Furutachi (JAEA)
5. Isotopic-distribution of ^{235}U + n --> ^{236}U at low E* using 4D-Langevin calculation
   C. Ishizuka (Tokyo Tech.)
6. A way for synthesis of doubly magic super heavy nuclei, located in the center of Island of Stability
   Y. Aritomo (Kindai U.)
7. Comparison of several state-of-the-art deexcitation models coupled with an intranuclear-cascade model for proton-induced reactions at intermediate energies
   M. Hagiwara (KEK)
8. Nuclear Data Adjustment with Integral Data Sensitive to Fast Neutron Energy Range
   G. Chiba (Hokkaido U.)
9. Preliminary Calculation with JENDL-4.0 for Evaluation of Dose Rate Distribution in the Primary Containment Vessel of the Fukushima Daiichi Nuclear Power Station
   K. Okumura (JAEA)
10. Uncertainty Quantification of Decay Heat Regarding Thorium Fuel
    T. Kajihara (Hokkaido U.)
11. A function formation of source neutron production by the ^{9}Be + p reaction at 7 MeV at RANS
    Y. Wakabayashi (RIKEN)
12. Evaluation of neutron cross sections of Nb-93 in the energy range between 10-5 and 20 MeV
    A. Ichihara (JAEA)
13. Evaluation of neutron nuclear data on copper isotopes by an consistent method
    S. Nakayama (JAEA)
14. 3T Photo-nuclear Data Evaluation and Preliminary Study of Reduction of 3T Density in Waste Water by Photon Irradiation
    T. Murata(JAEA OB)
15. Measurement of double differential (d,xn) cross sections for carbon at an incident energy of 100 MeV
    S. Araki (Kyushu U.)
16. Theoretical model analysis of (d,xn) reactions on beryllium
    H. Kouno (Kyushu U.)
17. Measurements of neutron production double-differential cross-section and thick target neutron yields on carbon bombarded with 430MeV/nucleon carbon ions
    Y. Itashiki (Kyushu U.)
18. Evaluation of neutron spectrum in KURRI-LINAC for nuclear data measurement
    N. Takayama (Kyoto U.)
19. Measurement of gamma-ray spectra from proton-Lithium nuclear reactions for development of a BNCT neutron source
    T. Saito (Tokyo Tech.)
20. Measurement of the keV-Neutron Capture Cross Sections and Capture Gamma-ray Spectra of Cs-133 and I-127
    S. Umezawa (Tokyo Tech.)
21. Measurement of the Cl-35(n,γ) reaction cross section in ANNRI at J-PARC
    Kaoru Y. Hara (Hokkaido U.)
22. Neutron and X-ray imaging measurements by using a composite source system at Hokkaido University
    Kaoru Y. Hara (Hokkaido U.)
23. Optimization of experimental system design for benchmarking of large angle scattering reaction cross section at 14 MeV using a shadow bar
    N. Hayashi (Osaka U.)

24. Contribution from Gd capture gamma-rays in GAGG based SPECT for boron neutron capture therapy N. Saraue (Osaka U.)
25. Development of An Epi-thermal Neutron Field for Fundamental Researches of BNCT with A DT Neutron Source Y. Osawa (Osaka U.)
26. Development plan of real-time gamma-ray spectrum / dose measurement system for medical staff M. Kobayashi (Osaka U.)
27. Investigation for Copper Nuclear Data based on New Integral Experiment on Copper with DT Neutron Source at JAEA/FNS S. Kwon (JAEA)
28. New Benchmark Experiment on Lead with DT Neutron Source at JAEA/FNS S. Kwon (JAEA)
29. Some comments on KERMA factors and DPA cross-section data in ACE and MATXS files of JENDL-4.0 C. Konno (JAEA)
30. A simple method for modification of capture reaction and elastic scattering nuclear data in analyses of nuclear data benchmark experiments C. Konno (JAEA)
31. Validation of IRDFF in Neutron Field in Li_2O Assembly with DT Neutrons at JAEA/FNS S. Sato (JAEA)
32. New Integral Experiment on Tungsten and Vanadium-alloy with DT Neutrons at JAEA/FNS S. Sato (JAEA)
33. Analysis of Benchmark Experiment on Molybdenum at JAEA/FNS M. Ohta (JAEA)

2 Experimental Fission Research Activity at the JAEA Advanced Science Research Center

K. Nishio
Advanced Science Research Center, Japan Atomic Energy Agency
Tokai, Ibaraki 319-1195, Japan
e-mail : nishio.katsuhisa@jaea.go.jp

Among several experimental fission research programs going on at the ASRC (Advanced Science Research Center) of JAEA, recent development to measure fission of excited compound nuclei populated by multi-nucleon transfer reactions will be introduced. This approach has an advantage that we can study fission of neutron-rich nuclei which cannot be accessed by particle or charged-particle capture reactions. Unique feature in our setup is that we can produce fission data for many nuclei depending on different transfer channels. Also wide excitation energy range can be populated, allowing us to measure the excitation energy dependence of the fission properties.

1. Introduction

Nuclear fission was found by irradiating uranium by neutrons. Fission can be also triggered by charged particles such as proton, α particle and heavy-ions. Gamma-ray and muon sources are also used for the fission study. Mass asymmetric fission was found already in the very beginning of the fission study. The phenomenon was not explained by the liquid-drop model of a nucleus, and it is essential to include the shell effects in nuclei. By exploring another region of the chart of nuclei, new phenomena in fission have been found. In the fission of heavy actinide nuclei, sharp transition from asymmetric to symmetric fission was found, suggesting the appearance of two ^{132}Sn-like clusters in the nucleus [1]. Existence of two fission modes was clearly observed in a systematic study of fission for actinide and pre-actinide nuclei using electro-magnetic induced fission [2]. Recently, mass asymmetric fission was observed in the low energy fission of proton-rich nucleus ^{180}Hg [3], which is populated as a daughter by the β^+/EC-decay of ^{180}Tl.

At Japan Atomic Energy Agency, we started a campaign to study fission of actinide nuclei including those whose fission data do not exist. Multi-nucleon transfer reactions are used to populate these nuclei (see Fig. 1). Advantage of this reaction is that we can produce many nuclei in one reaction depending on different transfer channels including neutron-rich nuclei which cannot be accessed by fusion reaction. Another unique feature is that the excitation energy of the fission system distributes widely, so that the excitation energy dependence of the fission properties can be obtained.

In this report, we describe the experimental setup. Preliminary data for the fission fragment mass distributions obtained in the ^{18}O + ^{238}U reaction is discussed.

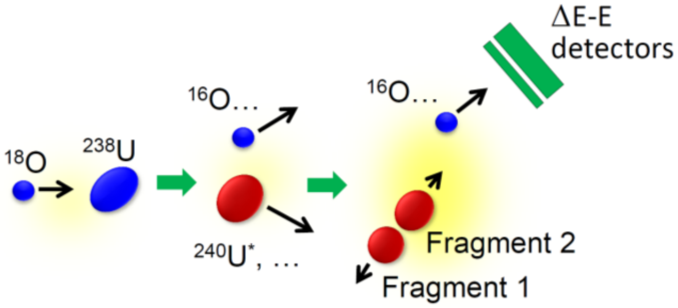

Fig.1 Multi-nucleon transfer induced fission

2. Experimental Setup

Experiment was carried out at the JAEA tandem facility, Tokai, Japan. A thin ^{238}U target was irradiated by ^{18}O beams at energy of 157.5 MeV. The ^{238}U target was prepared by electrodeposition of natural $^{238}UO_2$ on a Ni backing of 90 μg/cm^2-thickness. Transfer channel was identified by detecting the projectile-like nucleus using a silicon ΔE-E detector array which was mounted to the forward direction of the target. Thickness of the ΔE detector was 75 μm. Twelve pieces of the ΔE detectors were used to form a ring shape around the beam axis to make an efficient collection of the projectile-like nuclei. The particles passing through the ΔE detector were detected by a silicon strip E detector (SSD) with thickness of 300 μm, and their energies (E_{res}) were determined. The E detector has an annular shape, and the detector covers the scattering angle from 17.2^o to 30.9^o relative to the beam direction. The SSD has 16 annular strips within the active area, and each strip define the scattering angle θ of the particle with respect to the beam.

Figure 2 shows an example of the projectile-like nuclei plotted on the ($\Delta E+E_{res}$, ΔE) plane. Oxygen isotopes are clearly separated as well as those of lighter-element isotopes. By choosing a specific channel, we can assign the transfer channel and the corresponding compound nucleus. Excitation energy of the system is identified even-by-event.

Fission fragments were detected using four multi-wire proportional counters (MWPCs). Each MWPC has an active area of 200×200 mm^2. The MWPC consists of the central cathode which is sandwiched by two wire planes. The wire planes were designed to detect the incident position of fission fragment. The MWPCs were operated with an isobutene gas of about 1.5 Torr. The operation gas was shielded by an aluminum-coated Mylar window of 2.0 μm thickness. Induced charge in the cathode was used to separate fission fragments from scattered particles and/or lighter ions. Time difference signal, ΔT, from the two facing MWPCs was recorded. Fission fragment masses were determined kinematically using ΔT value and fission fragment directions.

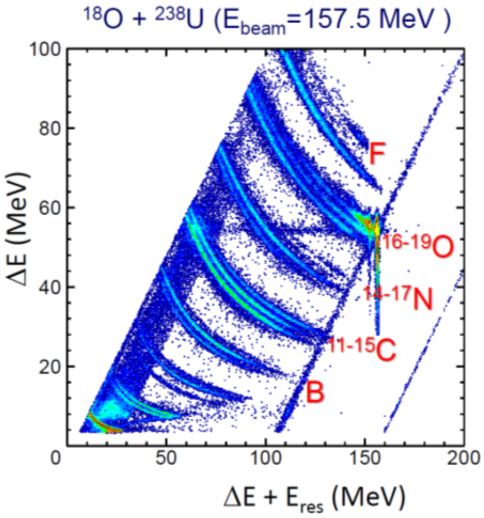

Fig.2 Plot of the projectile nuclei on the ($\Delta E+E_{res}$, ΔE) plane obtained in the ^{18}O + ^{238}U reaction

3. Experimental Results and Discussions

Results of the fission fragment mass distributions of the compound nucleus $^{239}U^*$ are shown in Fig. 3. The nucleus is populated by the $^{18}O + ^{238}U \rightarrow ^{17}O + ^{239}U^*$ reaction. Fission events are plotted on the fragment mass and excitation energy of the compound nucleus. It is found that excitation energy (E^*) reaches to more than 50 MeV. It is evident that fission fragment yield is asymmetric at the low excitation energies, whereas symmetric fission dominates toward higher excitation energies.

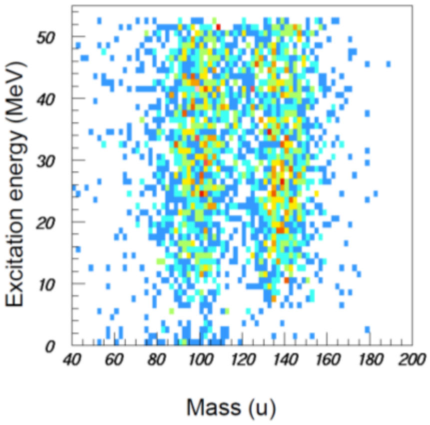

Fig.3 Fission fragment mass distribution of $^{239}U^*$

Similar analysis was carried out for the different transfer channels. Figure 4 shows the fission fragment mass distribution for uranium isotopes $^{237,238,239,240}U^*$ and their excitation energy dependence, obtained by neutron-transfer channels. Mass yield data for the fission of $^{240}U^*$ was obtained for the first time. Looking at the peak to valley ratio (P/V) of the distribution, it is evident that heavier isotopes have larger P/V values at excitation energy region of E^* >30 MeV when the spectra are compared at the same excitation energy. A possible explanation is that neutron-rich fissioning nucleus generates more neutron-rich heavy fragments, which is closer to the doubly-magic nucleus ^{132}Sn, thus the fission is more likely connected to the structure of ^{132}Sn. Such a system keeps shell structure even at high excitation energies.

Excitation energy dependence of the fission yield would have information on the damping of the shell. Recent model calculation uses an unexpectedly large shell damping energy E_D [4] to reproduce the measured fission fragment charge distribution than those obtained from the neutron resonance spacing [5]. Present experimental data covering wide excitation energy range would be useful to discuss the E_D value.

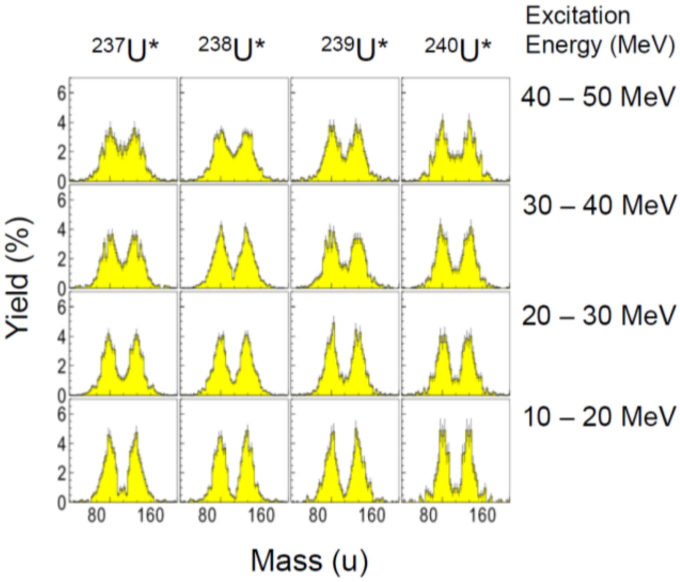

Fig.4 Fission fragment mass distribution of $^{237,238,239,240}U^*$. Excitation energy range is shown.

In this experiment, we could also obtain the fission data for heavier actinides than target nucleus. Our preliminary analysis shows that fission data for more than 15 nuclei can be generated in this reaction. Another interesting and important feature in this experimental method is that the reaction plane, defined by the directions of scatted projectile-like nucleus and recoiled nucleus, can be fixed. This allows us to obtain angular distribution of fission fragments, which is a function of spin J and its projection K on the symmetric axis of the fissioning system. Correlation between these variables and fission properties are under analysis.

Acknowledgements

The authors thank the crew of the JAEA-tandem facility for the beam operation. This work is supported by the program 'Comprehensive study of delayed-neutron yields for accurate evaluation of kinetics of high-burn up reactors' by the Ministry of Education, Sports, Science and Technology of Japan (MEXT).

Reference

[1] Vandenbosch, R. and Huizenga, J.R. "*Nuclear Fission*", Academic Press (1973).

[2] Schmidt, K.-H. *et al.*, Nucl. Phys. A, **665** (2000) p.221.

[3] Andreyev, A., Phys. Rev. Lett., **105** (2010) p.252502.

[4] J. Randrup, J. *et al.*, Phys. Rev. C, **88** (2013) p.064604.

[5] Reisdorf, W., Z. Phys. A, **300** (1981) p.227.

3 Photonuclear Data for the IAEA-CRP F41032

Hiroaki UTSUNOMIYA
Department of Physics, Konan University
Okamoto 8-9-1, Higashinada, Kobe 658-8501 Japan
e-mail: hiro@konan-u.ac.jp

I coordinate international research activities in collaboration with the Lomonosov Moscow State University, the Extreme Light Infrastructure-Nuclear Physics (ELI-NP), the University of Oslo, the University of Hyogo, the Kyoto University, and the Japan Atomic Energy Agency to provide : 1) new data of total and partial (γ,xn) cross sections with x=1-3 for 11 nuclei from ^{209}Bi to ^{9}Be and 2) new data of (γ,n) cross sections for 18 nuclei from ^{205}Tl to ^{58}Ni for the CRP (Coordinated Research Project) of the IAEA (International Atomic Energy Agency) with the code number F41032**.** The experiments are performed at the NewSUBARU facility using laser-Compton scattering γ-ray beams.

1. Introduction

The preceding experiments on photonuclear reactions were led by the Lawrence Livermore National Laboratory (LLNL) in USA and the Saclay in France during 1950s – 1980s with the use of quasi-monochromatic gamma-ray beams produced by the positron annihilation in flight. The experimental data have been compiled in the Atlas [1] and the IAEA-TECDOC-1178 [2]. The recent re-evaluation by the Lomonosov Moscow State University [3] has revealed large discrepancies between the Livermore and Saclay data compiled in the photonuclear data library that cannot be resolved in any systematic manner. The discrepancy has remained significant especially for partial photoneutron cross sections, σ(γ,xn) (x=1-3). This fact led to a new Coordinated Research Project (CRP) of the International Atomic Energy Agency (IAEA) “Updating the Photonuclear Data Library and Generating a Reference Database for Photon Strength Functions” with the code F41032. The two compilations are important not only in the basic science of nuclear physics and astrophysics but also in the field of applications, radiation detection and measurement, radiation shielding, radiotherapy, non-destructive inspection technologies, atomic energy and possibly nuclear transmutation.

We have made technical and methodological contributions to the CRP F41032. The previous gamma-ray beam suffered from a large amount of background gamma-rays arising from the positron bremsstrahlung. We have measured (γ,n) cross sections for many nuclei for more than decade by using low-background quasi-monochromatic gamma-ray beams produced in the Compton backscattering of laser photons from relativisitic electrons. We have developed a new methodology called “the γ-ray strength function method” [4] of indirectly determining (n,γ) cross sections for unstable nuclei in the content of the s-process nucleosynthesis and nuclear engineering. The methodology is a product of the JSPS-FNRS bilateral program between the Konana University in experiment and the Université Libre de Bruxelles in theory. The past research covered 17 elements (Se, Ge, Mo, Zr, Pd, Sn, La, Pr, Nd, Sm, Dy, Ta, W, Re, Os, Au, Pb) and 51 isotopes in experiments perfomed at the National Institute of Advanced Industrial Science and Technology and the NewSUBARU facility in Japan. The research output partly contributes to generating a reference database for photon strength functions of the CRP F41032.

The (γ,n) cross sections provide absolute normalization to photon strength functions deduced from particle-gamma coincidence data with the Oslo method [5]. Thus, we can experimentally construct photon strength functions by combining the proposed data and the Oslo data. The photon strength functions constructed are tested with the γ-ray strength function method. Namely, the strength functions are to be justified by reproducing inverse (n,γ) cross sections, whenever experimental capture data are available. Figure 1 shows an example of the photon strength function for ^{117}Sn which is the product of the collaboration between the Konan University and the University of Oslo.

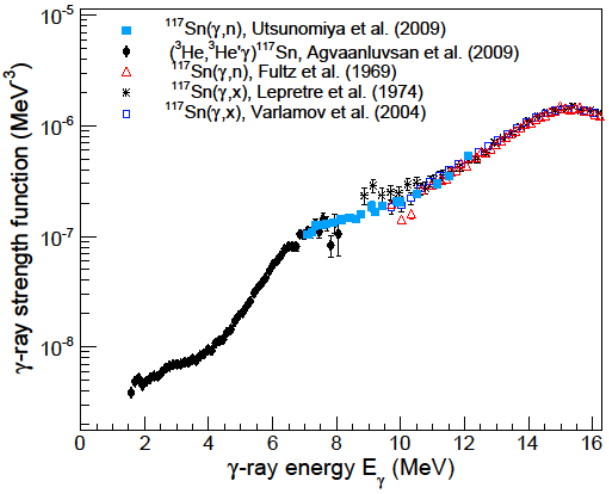

FIG. 1. Photon strength function for ^{117}Sn constructed by combining the (γ,n) data of Konan University and the data taken with the Oslo method

The Skobeltsyn Institute of Nuclear Physics of the Moscow State University (MSU) has proposed to measure the neutron yield cross section, σ(γ,Sn) = σ(γ,n) + 2σ(γ,2n) + 3σ(γ,3n) + … by photoactivation using bremsstrahlung produced by the race-track microtron, where the breakdown of the yield cross section into individual (γ,xn) cross sections is performed with the help of model calculations. In contrast, we propose to determine (γ,xn) cross sections by direct neutron-multiplicity sorting. The previous measurement of (γ,xn) cross sections at LLNL suffered from a technical defect in direct neutron multiplicity sorting. We have to overcome this technical defect.

2. Konan Phoenix Project

I propose an international research project named Konan PHOENIX (PHOto Excitation and Neutron emIssion cross (X) sections) Project for the IAEA-CRP F41032 that is carried out by using laser-Compton scattering γ–ray beams at the NewSUBARU facility. The purpose of the project is to provide the IAEA with (γ,n) cross sections for 18 nuclei for generating a reference database for photon strength functions in collaboration with the University of Oslo (Oslo) and (γ,xn) cross sections with x=1-3 for 11 nuclei for updating the photonuclear data library in collaboration with the Moscow State University (MSU) and ELI-NP. The 18 nuclei for (γ,n) data and 11 nuclei for (γ,xn) data are listed below. The Konan, MSU, ELI-NP, and Oslo teams are assigned their own (γ,xn) and (γ,n) data.

1. (γ,n) data for 18 nuclei for generating a reference database for photon strength functions
   The Konan team: ^{160}Gd, ^{158}Gd, ^{157}Gd, ^{156}Gd, ^{64}Ni, ^{60}Ni, ^{58}Ni
   The Oslo team: ^{205}Tl, ^{203}Tl, ^{192}Os, ^{185}Re, ^{184}W, ^{183}W, ^{182}W, ^{89}Y, ^{68}Zn, ^{66}Zn, ^{64}Zn
2. (γ,xn) data with x=1-3 for 11 nuclei for updating the photonuclear data library
   The Konan team: ^{197}Au, ^{181}Ta, ^{139}La, ^{9}Be
   The ELI-NP team: ^{209}Bi, ^{169}Tm, ^{165}Ho, ^{159}Tb
   The MSU team: ^{103}Rh, ^{89}Y, ^{59}Co

Figure 2 shows a schematic diagram of the research teams involved in this project.

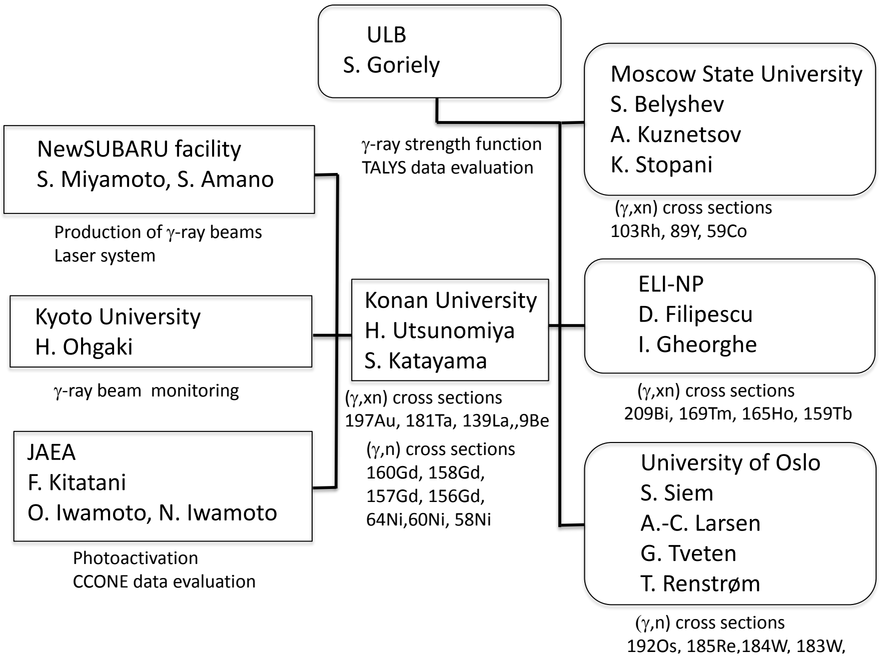

FIG. 2. Research teams of the project Phoenix and their roles

3. Facility and Equipment

Figure 3 shows the γ-ray production beamline of the NewSUBARU. In this project, we produce γ-ray beams for (γ,n) and (γ,xn) cross section measurements with the INAZUMA (Nd:YVO$_4$) 1064nm laser and a newly-introduced 532nm-1kHz laser, respectively. A 1 GeV electron beam is injected into the NewSUBARU storage ring from the linear accelerator. The injected beam is either decelerated down to 0.5 GeV or accelerated up to 1.5 GeV. The electron beam energy is calibrated with the accuracy on the order of 10^{-5} [6]. Quasi-monochromatic γ-ray beams are produced in "head-on" collisions of laser photons with relativistic electrons which is called inverse Compton scattering. The energy of the γ-ray beam is tuned in the energy range from 6 MeV to 50 MeV by changing the electron beam energy. We can produce γ-ray beams with energy spreads 1-2% by using a 2mm-diameter collimator (C2) at a typical intensity 10^5 cps in the fundamental (1064nm) operation mode of the INAZUMA laser. Figure 4 shows examples of the energy distribution of the γ-ray beam that were determined by the GEANT4 simulation of response functions of a 3.5” x 4.0” $LaBr_3(Ce)$ detector.

The NewSUBARU is a synchrotron radiation facility which is operated during day-time at a fixed electron beam energy (1.0 or 1.5 GeV) for users of the synchrotron radiation. We run experiments at the experimental hutch, GACKO (GAmma Collaboration hutch of KOnan University), during night-time to change the electron beam energy.

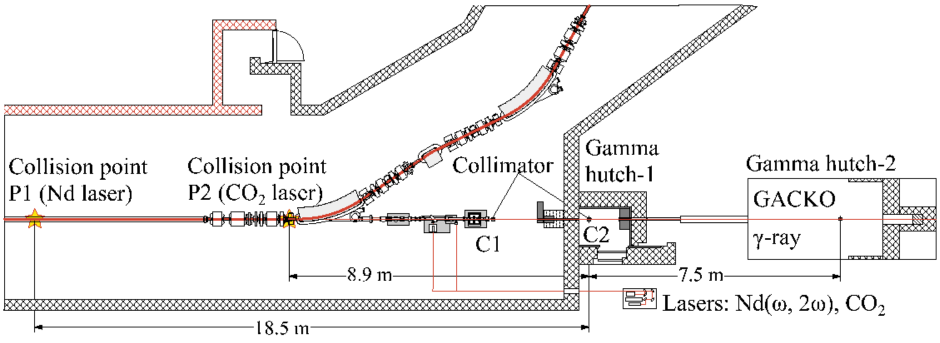

FIG. 3. The γ-ray production beam line at the NewSUBARU synchrotron radiation facility

FIG. 4. Typical spectra of the γ-ray beams recorded with the $LaBr_3(Ce)$ detector (solid lines) and the simulations of the response function (dotted lines) and of the incident γ-ray beam (gray lines). A double collimation with a C1 collimator of 6-mm aperture and a C2 collimator of 2-mm aperture was employed.

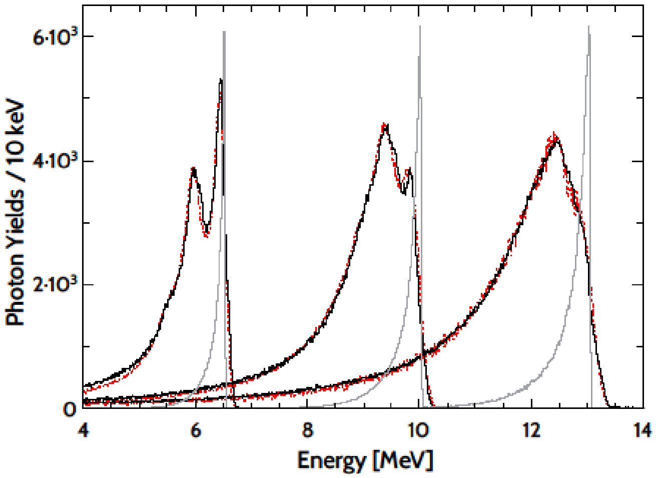

We have long measured (γ,n) cross sections for many nuclei with a high-efficiency 4π neutron detector consisting of twenty ^3He counters embedded in a polyethylene moderator in three concentric rings (Ring-1, Ring-2, Ring-3) of 4, 8, 8 ^3He counters placed at 3.8, 7.0, and 10.0cm from the γ-ray beam axis. The detector is characterized by a strong energy dependence of the detection efficiency which is 60-70% for neutrons with energies less than 1 MeV as shown in Fig. 5. The mean neutron energy is determined with the ring-ratio technique [7]. We continue to use the high-efficiency detector in (γ,n) cross section measurements for the CRP.

FIG. 5. The detection efficiencies of the Ring-1, Ring-2, Ring-3 and the total efficiency for s-wave (solid lines) and p-wave (dotted lines) neurons obtained by the GEANT4 simulation. The efficiencies measured with a calibrated ^{252}Cf source are shown by the solid triangles and those simulated with the MCNP Monte Carlo code are shown by the open circles.

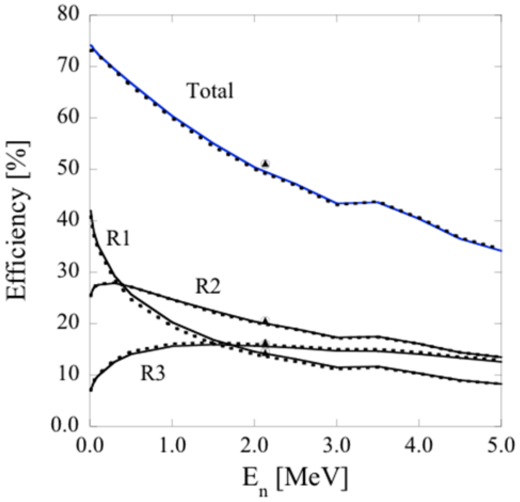

We employ an innovative method of direct neutron-multiplicity sorting by overcoming the defect which the Livermore experiments were supposed to face in the past. The defect originated from the strong neutron-energy dependence of the total detection efficiency and a lack of the capability of determining the mean neutron kinetic energies separately in the (γ,n), (γ,2n), and (γ,3n) channels. It is obvious that the only way to overcome the defect is to develop a flat-efficiency 4π neutron detector. We have successfully developed a flat-efficiency detector by a number of the GEANT4 simulations with the numbers of ^{3}He counters and the distances of triple rings as free parameters. The triple-ring configuration which assures flatness in the total detection efficiency is shown in Fig. 6(a). Ring-1 of four, Ring-2 of nine, and Ring-3 of eighteen ^{3}He counters are placed at 5.5, 13.0, and 16.0cm from the beam axis, respectively. The detection efficiencies of the three rings along with the total efficiency are shown in Fig. 6(b). The decreasing efficiency of Ring-1 with increasing

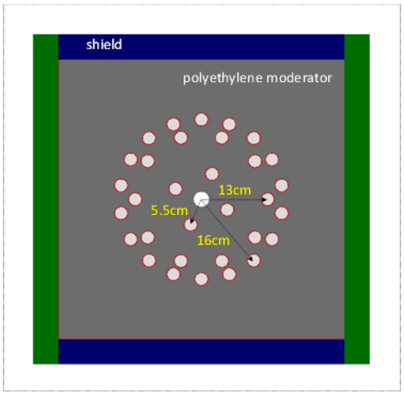

FIG. 6(a) Triple-ring configuration for the flat-efficiency neutron detector

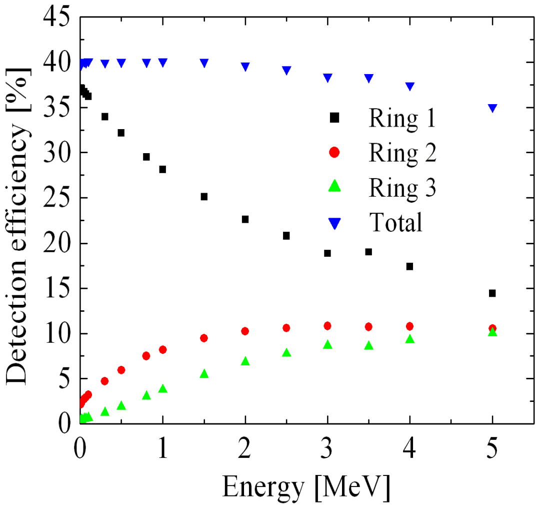

FIG. 6(b) Detection efficiencies of the three rings and the total efficiency of the flat-efficiency neutron detector neutron energy is compensated by the increasing efficiencies of Ring-2 and Ring-3, making the total efficiency constant around 40% independent of neutron energies within 5% in the range of 0 – 4 MeV [6]. The 40% efficiency for single neutron detection is sufficiently high to make neutron coincidence measurements feasible up to 3 neutrons with 6.4% efficiency. The development of the present flat 4π neutron detector marks a milestone in the history of fast-neutron detection techniques.

4. Outlook

We performed the first neutron-multiplicity sorting measurement for ^{209}Bi in July 2015 in collaboration with the ELI-NP and Moscow State University and the second measurement for ^{9}Be in November 2015 along with (γ,n) cross section measurements for ^{205}Tl, ^{203}Tl, and ^{89}Y in collaboration with the University of Oslo and the ELI-NP. We used a flat-efficiency neutron detector shown in Fig. 7 for the (γ,xn) cross section measurements. The detection efficiency was calibrated to be 38.5% with a ^{252}Cf source whose absolute emission rate was determined to be 1.59 x 10^{4} cps with 2.2% uncertainty at the National Metrology Institute of Japan.

FIG. 7. Flat-efficiency neutron detector developed and used for the ^{209}Bi and ^{9}Be experiments in 2015.

We have made a good start of the Phoenix project for the IAEA-CRP. In the first three years (2016-2018) of the CRP which will officially start in 2016, we will obtain the planned (γ,n) and (γ,xn) data. The Konan, MSU, ELI-NP, and Oslo teams follow the timeline of the data acquisition (though not shown here) and share the responsibility for analyses of their own (γ,xn) and (γ,n) data, publications in peer-reviewed journals, and presentations in international conferences followed by preparation of the final technical report of the CRP of updating the photonuclear data library and generating a reference database for photon strength functions in 2019, the final year of the project.

References

[1] S.S. Dietrich and B.L. Berman, Atomic Data and Nuclear Data Tables **38**, 199 (1988).
[2] IAEA-TEDOC-1178,"Handbook on Photonuclear Data for Applications Cross-sections and Spectra Final Report of a Co-ordinated Research Project 1996-1999", published October 2000: https://www-nds.iaea.org/publications/tecdocs/iaea-tecdoc-1178/
[3] V.V. Varlamov *et al.*, INDC(CCP)-440, IAEA NDS, 37 (2004).
[4] H. Utsunomiya *et al.*, Phys. Rev. C **80**, 055806 (2009).
[5] A. Schiller *et al.*, Nucl. Instrum. Meth. Phys. Res. A **447**, 498 (2000).
[6] H. Utsunomiya *et al.*, IEEE Transactions on Nuclear Science **61**, 1252 (2014).
[7] B. L. Berman and S. C. Fultz, Rev. Mod. Phys. **47**, 713 (1975).

4 Isotopic analysis of americium by thermal ionization mass spectrometry

Yuji SHIBAHARA(1), Koichi TAKAMIYA(1), Toshiyuki FUJII(1), Satoshi FUKUTANI(1),
Tadafumi SANO(1), Jun-ichi HORI(1), Hideo HARADA(2)

1) Research Reactor Institute, Kyoto University,
2-1010 Asashiro Nishi, Kumatori-cho, Sennan-gun, Osaka, Japan, 590-0494
2) Japan Atomic Energy Agency,
2-4 Shirakata, Tokai-mura, Naka-gun, Ibaraki Japan, 319-1195

The isotopic compositions of two Am samples (^{241}Am sample and ^{243}Am sample) used for nuclear cross-section measurements in AIMAC project were analyzed by thermal ionization mass spectrometry and α-spectrometry. In the thermal ionization mass spectrometry of Am, it was confirmed that (1) only the peak of ^{241}Am was observed in the analysis of ^{241}Am sample, and (2) the peaks of ^{243}Am, ^{241}Am and ^{242m}Am were observed in that of ^{243}Am sample. These results were agreed with that with α-spectrometry. The both method also showed that these two samples have the impurities such as ^{239}Pu, ^{240}Pu, ^{242}Cm and ^{244}Cm.

INTRODUCTION

For the improvement accuracy of neutron nuclear data for minor actinides and long-lived fission products, a nuclear data project entitled as “Research and development for Accuracy Improvement of neutron nuclear data on Minor ACtinides (AIMAC)” has been started at 2013 [1]. This project consists of four research field groups such as differential nuclear data measurement, integral nuclear data measurement, nuclear chemistry, and nuclear data evaluation. The objective of our group is to obtain the high quality isotopic composition data of samples contributing to the analysis of nuclear cross-section measurement data by mass spectrometry etc. In this study, it was analyzed the isotopic composition of two Am samples (main component was ^{241}Am and ^{243}Am, respectively) used for the nuclear cross-section measurements by the thermal ionization mass spectrometry (TIMS) and α-spectrometry.

EXPERIMENT

Two Am samples of ^{241}Am sample and ^{243}Am sample were purchased from JSC Khlopin Radium Institute Russia and were used without further purification. The certified values of these samples

Table 1 Certified value of ^{241}Am sample and ^{243}Am sample

	^{241}Am sample	^{243}Am sample
Concentration of radioactivity	132. 78 kBq/mL	9.98 kBq/mL
Activity measurement error	3%	3%
Radioactivity impurities/ Radionuclide components by α-spectrometry (for ^{243}Am)	No more than 0.3%	^{241}Am: 16.99% ^{243}Am: 38.32% ^{244}Cm: 43.99% ^{242}Cm: 0.7%
Isotopic composition	^{241}Am: 99.9%	^{243}Am: 97.3% ^{241}Am: 2.7%
Chemical composition	Am: 99.9% Pu: 0.09% Np: 0.01%	Am: 99.58% Fe, Ca, Na: 0.07% B: 0.09% Gd: 0.03% etc

such as the isotopic composition and the chemical composition were summarized in Table 1.

Analysis by TIMS

In the analysis by TIMS, a thermal ionization mass spectrometer (TRITON-T1^{TM}, Thermo Fisher Scientific) with a rhenium double filament system was used. About 1 μL of Am sample solution was loaded on a rhenium evaporation filament: the loading amount was estimated as 1.5 ng. Because of the total amount of Am loaded on the filament, the mass spectrometry of Am was conducted with a secondary electron multiplier detector and the peak jump method.

A rhenium ionization filament was heated until the intensity of ^{187}Re beam became 50 mV without the rapid increasing of the vacuum: the vacuum during the preparation of the analytical procedure was kept less than 2.0×10^{-7} mbar in the ion source. After the optimization of the ion lens with the ion beam of ^{187}Re, the intensity of ^{187}Re beam was adjusted as 50 mV. The current of a rhenium evaporation filament was raised gradually until the Am ion beam showed the enough intensity. After the optimization of the ion lens with the ion beam of Am (^{241}Am for ^{241}Am sample, and ^{243}Am for ^{243}Am sample) and the confirmation of the stability of the ion beam of Am, the isotopic compositions of Am samples were analyzed: the measurement procedure was based on our previous study on U and Pu [2, 3], and the vacuum the during data acquisitions were better than 1.0×10^{-7} mbar in the ion source.

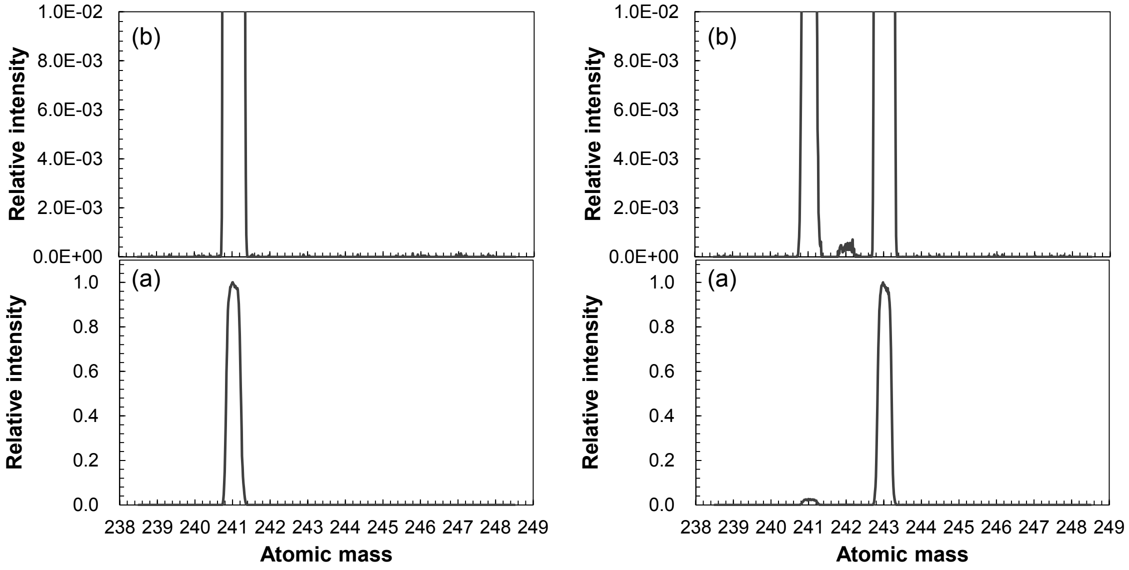

Fig. 1 Mass spectra of ^{241}Am sample (left) and ^{243}Am sample (right).

(a) Overviews of mass spectra. (b) Magnified views of mass spectra.

Analysis by α-spectrometry

The Am sample solution was dropped on the petri dish of 2.0 cm in diameter, and the α-ray source of 1 kBq of Am was prepared. The α-ray measurement system having 200 mm of the distance between the α-ray source and the detector was designed to improve the energy resolution and to decrease the geometric effect. For the enough counting statistics, the data acquisition was conducted with the sufficient time.

RESULTS AND DISCUSSION

Analysis by TIMS

The mass spectra of ^{241}Am sample and ^{243}Am sample were shown in Fig. 1. The ^{241}Am sample showed the only peak of ^{241}Am. Because of the S/N ratio of ^{241}Am peak (*ca.* 2×10^5, this value was

Table 2 Results of analyses of ^{241}Am sample and ^{243}Am sample by TIMS

	^{241}Am sample		^{243}Am sample	
	^{241}Am	other	^{243}Am	^{241}Am
Run-1	100.0000(5)%	< 0.0005%	97.71(3)%	2.29(3)%
Run-2	100.0001(3)%	< 0.0003%	97.72(3)%	2.28(3)%
Run-3	100.0000(3)%	< 0.0003%	97.71(5)%	2.29(5)%

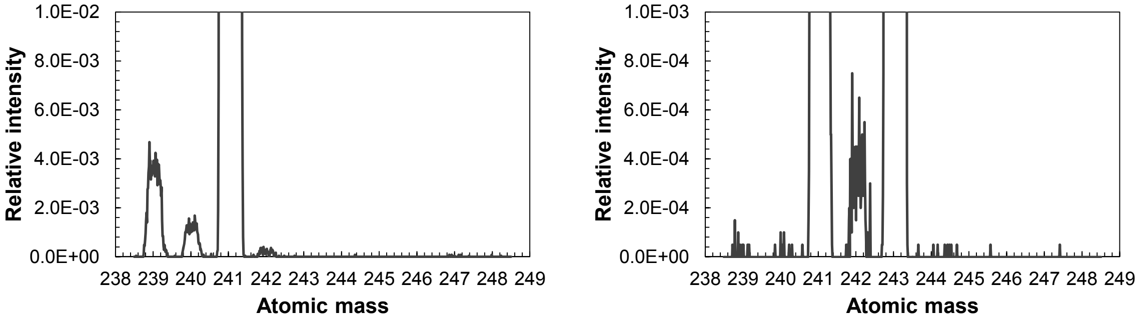

Fig. 2 Peaks of impurities observed in heat up process. ^{241}Am sample (left) and ^{243}Am sample (right).

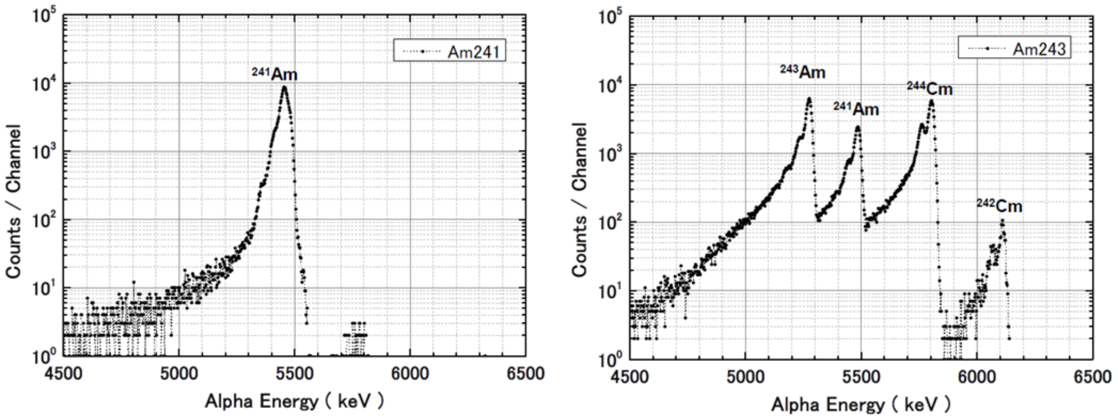

Fig. 3 α-spectra of ^{241}Am sample (left) and ^{243}Am sample (right).

obtained by the isotopic ratio data of ^{243}Am/^{241}Am), the isotopic abundance of ^{241}Am in the ^{241}Am sample would be expected as *ca*. 100%. The result of three times measurement of the isotopic composition of ^{241}Am sample was summarized in Table 2. By comparison Table 2 with Table 1, it could be concluded that the isotopic composition of ^{241}Am sample was improved in double digits by TIMS.

In the analysis of ^{243}Am sample, the peaks of ^{243}Am and ^{241}Am were observed (Fig. 1). By the three times measurement of ^{243}Am sample, the abundances of ^{243}Am and ^{241}Am were obtained as *ca*. 97.7% and 2.3% as shown in Table 2. It was found that the isotopic composition of ^{243}Am and ^{241}Am of Table 2 by TIMS showed 0.4% of different from them of Table 1. Addition to this, there was 0.04% of ^{242m}Am in ^{243}Am sample as shown in Fig. 1: the isotopic abundance of ^{242m}Am was not reported as the certified value.

During the heating up of the evaporation filament, the ion beams of ^{239}Pu, ^{240}Pu, ^{242}Cm, and ^{244}Cm were detected as shown in Fig. 2. For our objective, the quantitative evaluation of Pu would be important. The certified value of ^{241}Am sample in Table 1 shows the existence of Pu, while that of ^{243}Am sample does not show the existence of Pu. Because of the difference in the ionization efficiency between Am and the impurities such as Pu, the quantitative evaluation of the impurities would be hard from these mass spectra. The quantitative analysis of them (especially, the evaluation of Pu) has been under consideration and would be further study.

Analysis by α-spectrometry

The α-spectra of ^{241}Am sample and ^{243}Am sample were shown in Fig. 3. The α-spectrum of ^{241}Am sample shows the peaks corresponding only to ^{241}Am, although the presence of Pu is noted in the certification as shown in Table 1 and is observed by TIMS. By considering about the chemical abundance of Pu as the certified value and the half-lives of Pu and Am, it might be hard to detect Pu.

The α-spectrum of ^{243}Am sample showed the peaks corresponding to ^{243}Am, ^{241}Am, ^{244}Cm and ^{242}Cm. The isotopic compositions of ^{243}Am and ^{241}Am were estimated as 97.71±0.01% and 2.29±0.01%, showing the good agreement with the results by TIMS. The chemical compositions of ^{244}Cm and ^{242}Cm were also estimated as 0.00009±0.00002% and 0.240±0.001% respectively. These values were also agreement with the certified values in Table 1: other impurities such as ^{242m}Am and Pu isotopes were not observed in this study.

CONCLUSIONS

The isotopic compositions of two Am samples (^{241}Am sample and ^{243}Am sample) used for nuclear cross-section measurements in AIMAC project were analyzed by TIMS and α-spectrometry. In the TIMS, the isotopic composition of ^{241}Am sample was improved in double digits and the impurities of Pu isotopes were observed. The analysis of the isotopic composition of ^{243}Am sample showed that the isotopic compositions of ^{243}Am and ^{241}Am were different in 0.4% compared with the certified value, and this result was supported by the result by α-spectrometry. In the analysis of ^{243}Am sample by both methods, the impurities such as ^{242}Cm and ^{244}Cm were also observed. In the analysis by TIMS for ^{243}Am sample, the unreported impurities such as ^{242m}Am, ^{239}Pu and ^{240}Pu were also observed. It was confirmed that the combination of TIMS and α-spectrometry would provide the more detail information contributing to the analysis of nuclear cross-section measurement data.

ACKNOWLEDGEMENTS

Present study includes the result of “Research and Development for accuracy improvement of neutron nuclear data on minor actinides” entrusted to the Japan Atomic Energy Agency by the Ministry of Education, Culture, Sports, Science and Technology of Japan (MEXT).

REFERENCES

[1] Harada H., Iwamoto O., Iwamoto N., Kumura A., Terada K., Nakao T., Nakamura S., Mizuyama K., Igashira M., Katabuchi T., Sano T., Takahashi Y., Takamiya K., Pyeon C.H., Fukutani S., Fujii T., Hori J., Yagi T., Yashima H. Accuracy improvement of neutron nuclear data on minor actinides. EPJ Web of Conferences. 2015, 93, 06001.

[2] Shibahara Y., Kubota T., Fujii T., Fukutani S., Ohta T., Takamiya K., Okumura R., Mizuno S., Yamana H. ^{235}U/^{238}U isotopic ratio in plant samples from Fukushima Prefecture. J. Radioanal. Nucl. Chem. 2014 Sep; 303: 1421-1424.

[3] Shibahara Y., Kubota T., Fujii T., Fukutani S., Takamiya K., Konno M., Mizuno S., Yamana H. Determination of isotopic ratios of plutonium and uranium in soil samples by thermal ionization mass spectrometry. J. Radioanal. Nucl. Chem. 2015 Oct; DOI 10.1007/s10967-015-4551-1

5 Accurate measurements of gamma-ray emission probabilities

K. Terada[1], S. Nakamura[1], A. Kimura[1], T. Nakao[1], H. Harada[1],
T. Katabuchi[2], M. Igashira[2], J. Hori[3]

[1] *Nuclear Data Center, Japan Atomic Energy Agency,*
2-4 shirane, Tokai-mura, Naka-gun, Ibaraki 319-1195, Japan

[2] *Research Laboratory for Nuclear Reactors, Tokyo Institute of Technology,*
2-12-1 Ookayama, Meguro-ku, Tokyo 152-8550

[3] *Research Reactor Institute, Kyoto University,*
2, Asashiro-nishi, Kumatori-cho, Sennan-gun, Osaka 590-0494, Japan

E-mail: terada.kazushi@jaea.go.jp

Abstract

Precise measurements of the gamma-ray emission probabilities of ^{241,243}Am, ^{237,239}Np and ^{233}Pa have been performed. Standard radioactive solutions were used to prepare samples. Activities of the prepared samples were standardized by alpha-ray spectroscopic methods with a Si detector. Gamma-ray measurements of the samples were made with a planar type High-Purity Germanium (HPGe) detector. An efficiency curve of the HPGe detector was obtained with uncertainties from 0.7% to 2.5% by combining measured data and Monte Carlo simulation. The gamma-ray emission probabilities of these nuclides were determined with uncertainties less than 1.2%.

1 Introduction

Measurements of neutron capture cross sections of Minor Actinides (MA) have been performed with the Accurate Neutron Nucleus Reaction Measurement Instrument (ANNRI) of the Materials and Life science experimental Facility (MLF) in the Japan Proton Accelerator Research Complex (J-PARC). Although recent studies have given capture cross sections of MA with good energy dependence, uncertainty corresponding to the normalization still remains[1–3)]. The research project entitled "Research and development for Accuracy Improvement of neutron nuclear data on Minor ACtinides (AIMAC)" has been proceeded to improve the reliability of the neutron cross section date for the R&D of innovative nuclear systems and environmental load reduction from the disposal of nuclear wastes. In order to obtain accurate cross section data, it is indispensable to determine the mass of MA sample accurately and non-destructively. Since, mass of the sample has a more direct influence on the absolute value of cross section data. However, the uncertainty concerning the sample mass is not assured in some cases. In order to determine the mass of MA in the sample with high precision, accurate data on relevant gamma-ray emission probabilities are required.

From the viewpoint described above, we measured the gamma-ray emission probabilities of ^{241,243}Am, ^{237,239}Np and ^{233}Pa. The activities of the samples were obtained using a Si semiconductor detector by counting alpha-particles from the samples, and decay gamma-rays were measured with a planar type High-Purity Germanium (HPGe) detector. Efficiencies at various energies were experimentally measured, and then the Monte Carlo code PHITS[4)] was used to interpolate these values.

2 Experiment

2.1 Sample preparation and activity determination

The gamma-ray emission probabilities of ^{241,243}Am, ^{237,239}Np and ^{233}Pa were measured accurately. The details of measurements for ^{241,243}Am and ^{239}Np are were summarized$^{5)}$, it is briefly described. A ^{237}Np standard solution of $Np(NO_3)_4$ supplied by Japan Radioisotope Association. Its specific radioactivity was 16.3 ± 0.5 kBq/g. 10 μl of the solution was dropped on a high purity quartz plate, and dried by an infrared lamp. Four measuring samples were prepared in the same way. Their diameters and radioactivities were approximate 5~10 mm and 1 kBq. The thicknesses of the samples were sufficiently thin, thus preventing self-absorption of alpha-rays in the samples. The activities of the samples were determined by counting alpha particles with a Si detector (BU-016-300-100) of 300 mm^2 active area manufactured by ORTEC. The distance between the sample and the front of surface of the detector was43 mm. **Figure 1.** indicate the alpha-ray spectrum of the sample. We used an ^{241}Am standard source (AM241EASD20) supplied from AREVA in order to determine the solid angle between the sample and the detector.

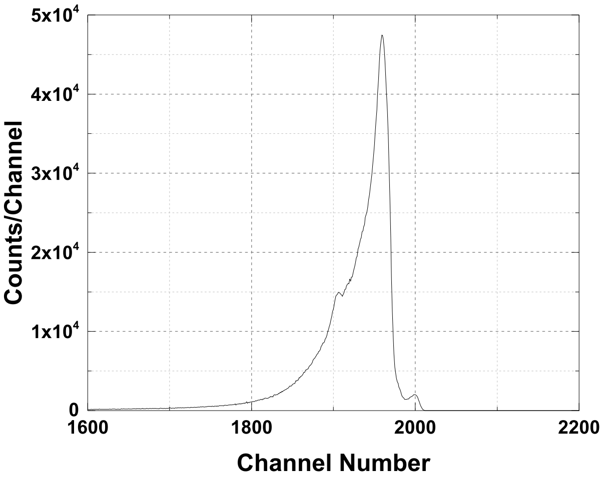

Figure 1. Alpha-ray spectra from the decay of ^{237}Np

2.2 Gamma-ray spectrometry

Gamma-ray measurements of the samples and standard gamma-ray sources (^{60}Co, ^{137}Cs, ^{133}Ba) were made by using a planar type low energy photon HPGe detector (GLP-36360/13P4) manufactured by ORTEC. The Ge crystal with diameter of 36 mm and a thickness of 13 mm was installed in Al housing and a Be window with a thickness of 0.254 mm, where the cap-to-crystal distance was 7 mm. The X-COOLER Ⅲ made by ORTEC was utilized for cooling of the HPGe detector. Signals from the HPGe detector were fed to a Lynx digital signal analyzer made by CANBERRA and spectral data was recorded on a PC. The full width at half maximum (FWHM) at 122 keV (^{57}Co gamma-ray) was 0.6 keV. All measurements were carried out with a source-detector distance of 20.0 cm. **Figure 2.** shows the gamma-ray spectrum from the sample. The peak around 1600 ch. is caused by ^{233}Pa 312 keV decay gamma-rays. The statistical uncertainties were 0.3%.

In order to interpolate the measured efficiencies accurately, Monte Carlo calculations by using the PHITS code were performed. In the PHITS calculations, experimental geometry and materials were taken into account. Then, parameters of the HPGe detector (radius, length and dead layer thickness) were adjusted to reproduce the measured efficiencies. The calculations were carried out until the statistical uncertainty of the full-energy-peak efficiency was less than 0.1%. The length of the HPGe detector was mainly determined so as to reproduce the measured efficiencies with the ^{60}Co source. We determined the dead layer thickness of 1.58 μm with K X-rays from ^{133}Ba at 35.00 keV and ^{137}Cs at 32.04 keV and 36.51 keV. The detector radius was determined considering with the entire consistency from 32 to 1332 keV. The PHITS calculations were in good agreement with the measured efficiencies with a reduced

χ^2 of 1.76. The uncertainties of the efficiency curve were obtained from 0.7% to 2.5% ranging from 25 to 1332 keV.

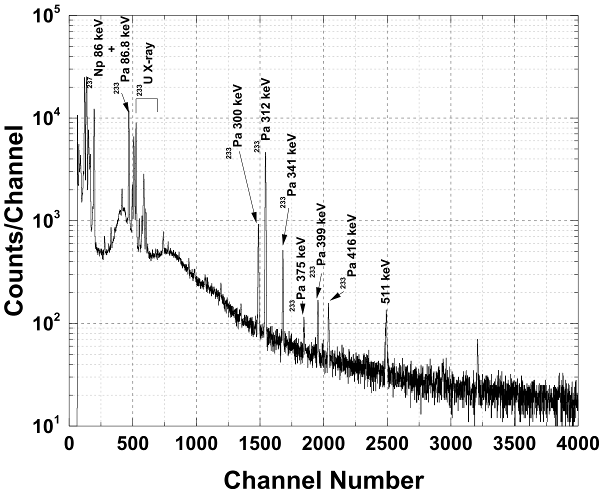

Figure 2. Gamma-ray spectra of the Np sample

3 Results

The gamma-ray emission probability of ^{241,243}Am, ^{237,239}Np and ^{233}Pa were determined by dividing the peak areas for each peak by the activities of the samples and the calculated efficiencies. The obtained gamma-ray emission probabilities of ^{241,243}Am, ^{239}Np with a standard deviation of 1σ are given in **Table 1**, **2** and **3**. The gamma-ray emission probability of 312 keV from the decay of ^{233}Pa was determined with an uncertainty of 1.2%. **Figure 3.** shows the obtained gamma-ray emission probability of 312 keV from the decay of ^{233}Pa and the previous measurement data$^{6\text{–}10)}$.

Table 1. Gamma-ray emission probabilities of ^{241}Am

E_γ [keV]	I_γ [%]
26.34	2.3 ± 0.1
59.54	35.64 ± 0.46

Table 2. Gamma-ray emission probabilities of ^{243}Am

E_γ [keV]	I_γ [%]
43.53	5.87 ± 0.09
74.66	67.72 ± 0.65

Table 3. Gamma-ray emission probabilities of ^{239}Np

E_γ [keV]	I_γ [%]
106.12 +106.47	26.01 ± 0.26
209.75	3.31 ± 0.04
228.18	11.18 ± 0.12
277.60	14.34 ± 0.16
285.46	0.76 ± 0.02
315.88	1.60 ± 0.03
334.31	2.05 ± 0.04

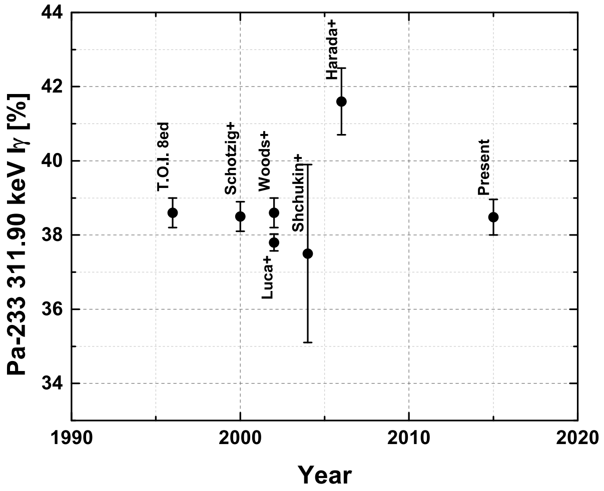

Figure 3. Gamma-ray emission probability of 312 keV of ^{233}Pa$^{6-10)}$

4 Summary

The gamma-ray emission probabilities of ^{241,243}Am, ^{237,239}Np and ^{233}Pa were measured with gamma- and alpha-ray spectroscopic methods. The activities of the samples were determined by measuring alpha-particles emitted from the samples by using the Si detector. The efficiencies of the HPGe detector were derived with precisions ranged from 0.7% to 2.5%. The gamma-ray emission probabilities of these nuclides were determined with uncertainties less than 1.2%.

Acknowledgments

Present study includes the result of “Research and Development for accuracy improvement of neutron nuclear data on minor actinides” entrusted to the Japan Atomic Energy Agency by the Ministry of Education, Culture, Sports, Science and Technology of Japan (MEXT).

References

1) H. Harada *et al*, Measurements of ^{241}Am(n,γ) at J-PARC/MLF/ANNRI. Nuclear Data Sheets **119**, 61-64 (2014).

2) A. Kimura *et al*, Neutron-Capture Cross-Sections of ^{244}Cm and ^{246}Cm Measured with an Array of Large Germanium Detectors in the ANNRI at J-PARC/MLF, Journal of Nuclear Science and Technology, **49**, 708-724 (2011).

3) K. Hirose *et al*, Cross-Section Measurement of ^{237}Np(n,γ) from 10 meV to 1 keV at Japan Proton Accelerator Research Complex, Journal of Nuclear Science and Technology, **50**, 188-200 (2013).

4) T. Sato *et al*, Particle and Heavy Ion Transport Code System PHITS Version 2.52. J. Nucl. Sci. Technol. **50**, 913-923 (2013).

5) K. Terada *et al*, Measurements of gamma-ray emission probabilities of ^{241,243}Am and ^{239}Np. J. Nucl. Sci. Technol. Published online: 26 Apr 2016, DOI: 10.1080/00223131.2016.1174167.

6) R. B. Firestone *et al*, Table of Isotopes, Eighth Edition, John Wiley and Sons, Inc., New York, (1999).

7) H. Harada *et al*, Emission Probabilities of Gamma Rays from the Decay of ^{233}Pa and ^{238}Np, and the Thermal Neutron Capture Cross Section of ^{237}Np, Journal of Nuclear Science and Technology, **43**, 1289-1297 (2006).

8) A. Luca *et al*, Emission probabilities of the KX-rays following the decay of ^{237}Np in equilibrium with ^{233}Pa, Applied Radiation and Isotopes, **56**, 173-180 (2002).

9) S. A. Woods *et al*, Standardization and decay data of ^{237}Np, Applied Radiation and Isotopes, **56**, (2002).

10) G. Shchukin *et al*, Analysis of the ^{237}Np- ^{233}Pa photon spectrum using the full response function method, Applied Radiation and Isotopes, **60**, (2004).

6 Nuclear Data Measurements Extending to Fast Neutron Energy Region

Tatsuya KATABUCHI1)*, Hideo HARADA2), Jun-ich HORI3), Masayuki IGASHIRA1),
Atsushi KIMURA2), Shoji NAKAMURA2), Taro NAKAO2), Kazushi TERADA2)
1) Research Laboratory for Nuclear Reactors, Tokyo Institute of Technology,
2-12-1 Ookayama, Meguro-ku, Tokyo 152-8550, Japan
2) Nuclear Science and Engineering Center, Japan Atomic Energy Agency
2-4 Shirakata Shirane, Tokai, Ibaraki 319-1195, Japan
3) Research Reactor Institute, Kyoto University
2-1010, Asashiro Nishi, Kumatori-cho, Sennan-gun, Osaka 590-0494, Japan
*e-mail: buchi@nr.titech.ac.jp

To extend the high energy limit of nuclear data measurement with the Accurate Neutron Nucleus Reaction Measurement Instrument at the Japan Proton Accelerator Research Complex, technical development is ongoing. Recent progress and development are presented.

1. Introduction

The Accurate Neutron Nucleus Reaction Measurement Instrument (ANNRI) [1-4] has been built to conduct neutron nuclear data measurement utilizing an intense pulsed neutron beam from a spallation neutron source of the Japan Proton Accelerator Research Complex (J-PARC). In 2014, we began a new project, "*Research and Development for accuracy improvement of neutron nuclear data on minor actinides*", also called AIMAC, which is aimed to improve nuclear data uncertainties on minor actinides and long-lived fission products. As a part of the AIMAC project, an effort to extend the high energy limit of measurement at ANNRI has been taken. ANNRI has NaI(Tl) detectors for neutron capture cross section measurement in high energy region. The current high-energy limit of measurement with the NaI(Tl) detectors is around 100 keV. To extend the limit, we improved the NaI(Tl) detector system by (1) developing a fast data acquisition system and (2) adding a neutron shield to reduce scattering neutron background. In this report, we present our progress to upgrade the NaI(Tl) detector system for high energy measurement.

2. ANNRI NaI(Tl) detectors

The ANNRI NaI(Tl) detectors are located at a flight path length of 27.9 m from the neutron source. The detectors consist of two NaI(Tl) detectors placed at angles of 90° and 125° with respect to the neutron beam axis, as shown in Fig. 1. The 90° detector was designed to provide a large detection efficiency because of closer geometry to the sample position with a larger detector volume than the 125° detector. The 125° detector is for measurement at the special angle of 125°, where the angular dependent term of the dominant *E1* and *M1* γ-ray transitions vanishes. Both the 90° and 125° detectors reside in annular plastic scintillation detectors to suppress cosmic-ray background by anti-coincidence detection. Shielding of the detectors were made with several shielding materials: lead, cadmium, borated polyethylene, borated rubber and isotopically enriched Lithium-6 hydride.

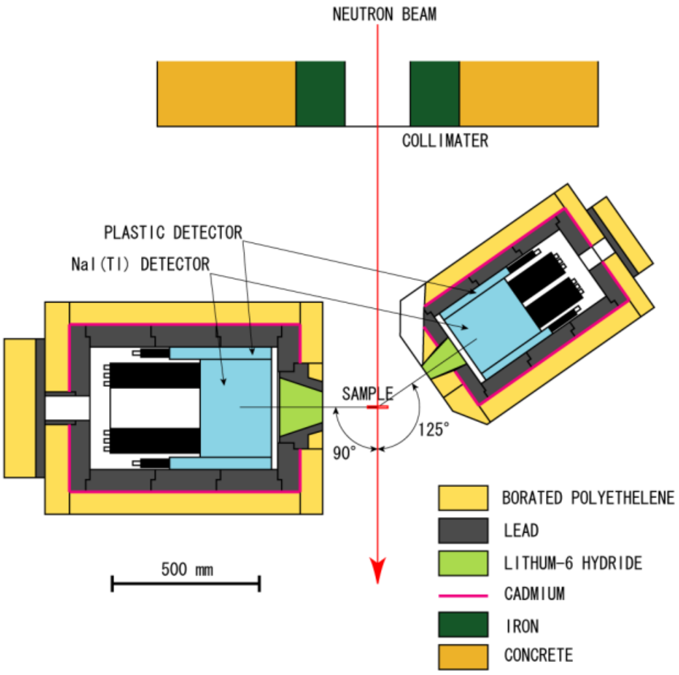

Fig. 1 NaI(Tl) detectors of ANNRI

2.1 Fast data acquisition

A fast data acquisition method to analyze the pulse height of a signal with a small processing dead time was developed [5]. Pulse-height analysis is required for pulse-height weighting technique to derive neutron capture cross sections. However, a strong γ-ray burst, so-called gamma-flash, emitted from the J-PARC neutron source at the beginning of each TOF cycle introduced a considerably large input in the detectors and saturated a conventional analog pulse-height analysis system. Distortion of the signal caused by the gamma-flash was observed in a certain duration of time (10 μs - 1 ms). This hampered measurement in fast TOF region (high energy region). In the new data acquisition method, the pulse width of the detector signal is measured instead of analyzing the pulse height of the signal. The pulse-width is converted to the corresponding pulse-height afterwards, according to a width-height relation determined from calibration experiments. Pulse-width measurement is made with a fast time digitizer that can detect threshold-crossing times of a signal. We chose a time digitizer FAST ComTec MPA4T for this application. The old data acquisition system consisting of analog modules and peak-holding analog-to-digital converters was replaced with the new time digitizer system. A pulse-height spectrum was successfully reconstructed from pulse-width spectrum in the high energy region. Detail of the data acquisition method and test experiments was described in Ref. [5].

2.2 Scattering neutron background shieling

In high energy measurements, neutron background becomes severe due to its high penetrability. High-energy neutrons easily penetrate shields that have enough thickness for low energy neutrons, and cause background signals in a detector. One possible source is scattering neutrons from a sample. To reduce the scattering neutron background from the sample, we designed and built an additional neutron shield.

We designed the neutron shield such that a cylindrical neutron shield covered the sample section of the neutron beam duct. Enriched ^{6}Li in chemical form of $LiCO_3$ was chosen as a neutron shielding material. Lithium-6 absorbs neutrons via the $^{6}Li(n,t)^{4}He$ reaction with a large reaction cross section. $LiCO_3$ powder was formed into doughnut-shaped rings. The $LiCO_3$ rings were stacked and sealed in a hollow cylindrical container with an inner hole matching to the carbon-fiber beam duct. The total mass of $LiCO_3$ was 4.5 kg. The dimensions were 155 mm OD × 95 mm ID × 300 mm thickness. Figure 2 shows the neutron shield attached to the beam duct.

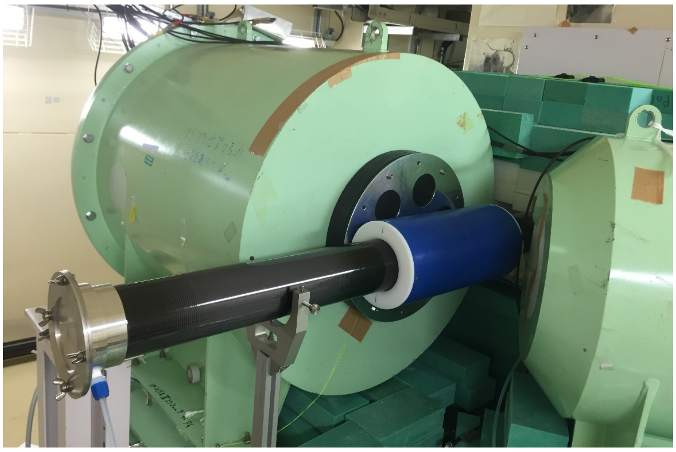

Fig. 2 Neutron shield attached to the beam duct. The blue cylinder contains neutron shielding material $^{6}LiCO_3$. The black pipe is the neutron beam duct.

Shielding test experiments were performed. An enriched ^{208}Pb sample was placed at the sample position and scattering neutron background from the sample was evaluated. The neutron capture cross section of ^{208}Pb is very small. Events with the ^{208}Pb sample can be interpreted as ones caused by sample scattering neutrons. Comparisons with and without the neutron shield in different energy ranges are shown in Figs. 3, 4 and 5. Blank background was already subtracted in the TOF spectra. As seen in Fig. 3, events in the thermal energy region decreased drastically. The scattering neutron background was reduced by 60%. In higher energy region, the background also decreased, for example, by 30% at 400 eV (100 μs) and 17% at 250 keV (4 μs).

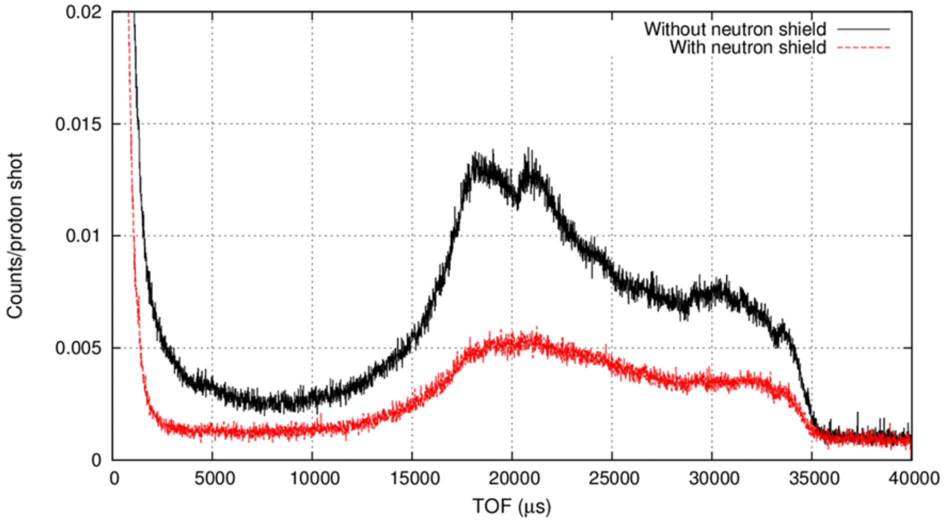

Fig. 3　Comparison of TOF spectra with (red) and without (black) the new neutron shield in thermal energy region.

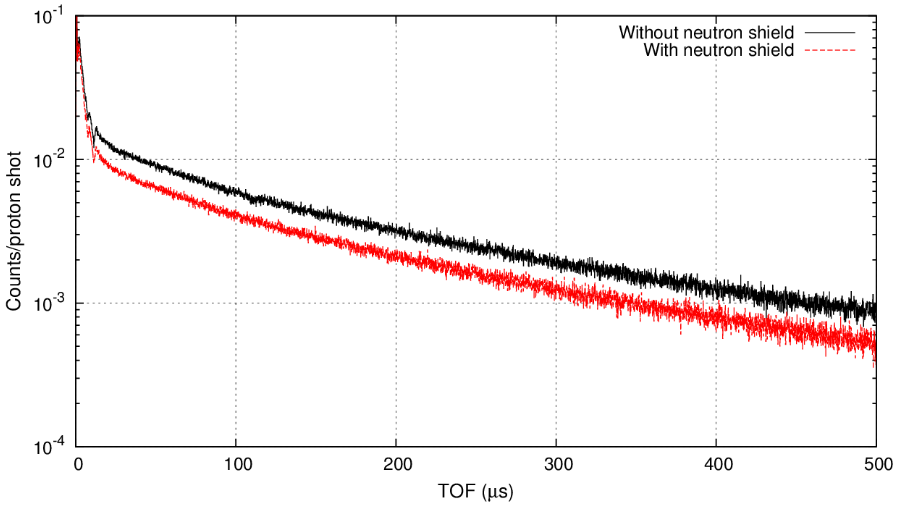

Fig. 4　Comparison of TOF spectra with (red) and without (black) the new neutron shield in high energy region. 100 μs in TOF corresponds to 400 eV in neutron energy.

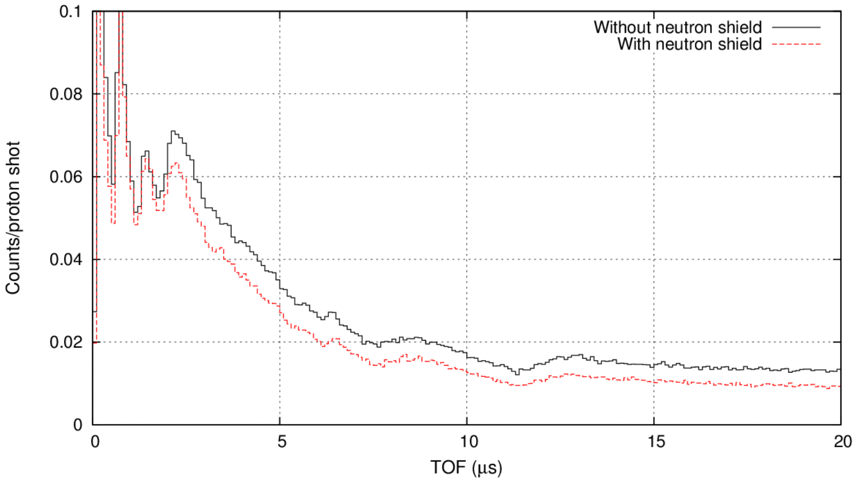

Fig. 5 Comparison of TOF spectra with (red) and without (black) the new neutron shield in high energy region. 4 μs in TOF corresponds to 250 keV in neutron energy.

3. Summary

In this report, recent progress and development to extend the high energy limit of measurement using the ANNRI NaI(Tl) detectors were reported. A fast data acquisition method based on pulse width analysis with a fast time digitizer was developed. Using the new data acquisition method, signal distortion caused by gamma flash, which had been observed with previous analog module system, was successfully eliminated, thus allowing us to carry out experiments in the fast neutron energy region. To reduce scattering neutron background, a new neutron shield was designed and built. The neutron shield was tested counting scattering neutron events from a ^{208}Pb sample. TOF spectra was compared with and without the new neutron shield. It is confirmed that the neutron shield successfully reduced scattering neutron background from thermal to fast neutron energy region.

Actual measurements using the upgraded ANNRI NaI(Tl) detector system are now ongoing. Experiments to measure the neutron capture cross section of ^{99}Tc have been made and data analysis is underway. We are planning to start measurement for ^{241}Am in the next year.

Acknowledgements

Present study includes the result of “Research and Development for accuracy improvement of neutron nuclear data on minor actinides” entrusted to the Japan Atomic Energy Agency by the Ministry of Education, Culture, Sports, Science and Technology of Japan (MEXT).

References

[1] M. Igashira *et al.*, Nuclear Data Study at J-PARC BL04, Nuclear Instruments and Methods in Physics Research A 600, 332-334 (2009).

[2] Y. Kiyanagi *et al.*, The ‘Study on Nuclear Data by Using a High Intensity Pulsed Neutron Source for Advanced Nuclear System’ Nuclear Data Project and the Characteristics of the Neutron Beam Line for the Capture Cross Section Experiments at J-PARC, Journal of Korean Physical Society, 59, 1781-1784 (2011).

[3] K. Kino *et al.*, Measurement of Energy Spectra and Spatial Distributions of Neutron Beams Provided by the ANNRI Beamline for Capture Cross-Section Measurements at the J-PARC/MLF, Nuclear Instruments and Methods in Physics Research A 626-627, 58-66 (2011).

[4] K. Kino *et al.*, Energy resolution of pulsed neutron beam provided by the ANNRI beamline at the J-PARC/MLF, Nuclear Instruments and Methods in Physics Research A 736, 66-74 (2014).

[5] T. Katabuchi *et al.*, Pulse-width analysis for neutron capture cross-section measurement using an NaI(Tl) detector, Nuclear Instruments and Methods in Physics Research Section A, 764, 369-377 (2014).

7 Re-analysis of MAs reaction rate ratio measurement in the KUCA

Tadafumi SANO[a], Jun-ichi HORI[a], Yoshiyuki TAKAHASHI[a], Yuji SHIBAHARA[a],
Hiroshi YASHIMA[a], Koichi TAKAMIYA[a], Cheol Ho PYEON[a], Hideo HARADA[b]
[a]Kyoto University Research Reactor Institute, [b]Japan Atomic Energy Agency

In order to improve accuracy of minor actinides (MAs) and long life fission products (LLFPs), the project entitled as "Research and development for Accuracy Improvement of neutron nuclear data on Minor Actinides (AIMAC)" has been started as one of the "Innovative Nuclear Research and Development Program" in Japan at October 2013. In this project, differential experiments of MAs and LLFPs nuclear data with pulsed neutron source are carried out. In addition, measurements of reaction rate ratio as integral validation are performed using Kyoto University Critical Assembly (KUCA) to be cross-checked with differential data. The target nuclides are Np237, Am241 and so on.

In 1998 to 2000, the Np237 and Am241 fission rate ratios relative to U235 and the neutron capture rate ratio of Np237/Au197 have been measured in the six cores [1]. The weighted average of C/E values of Np237/U235 fission rate ratio in the B18P60EUEU core (H/U235 : 52) was 0.975±2.6% [1] when the cross sections of the JENDL-3.2 [2] were used.

In this work, the experiments were re-analyzed by the MVP2.0 [3] and the JENDL-4.0 [4]. As the results, the C/E values with B18P60EUEU core was slightly decreased as 0.961±2.8% . Errors of the C/E value had the experimental error, the statistical error by Monte-Carlo calculation and the uncertainties caused by the JENDL-4.0 error. However, impurities in the Np237 sample were neglected in the both numerical calculations with the JENDL-3.2 and the JENDL-4.0. Numerical calculation was newly carried out using the information of the impurities of Pu239 (1.1ppm) and Pu238 (0.3ppm) in ref. [1]. As the results, the C/E values became 0.992±2.8%. This result indicates that identification and quantification of impurities included in a sample is important when we carry out analysis of integral experiment for nuclear data.

Present study includes the result of "Research and Development for accuracy improvement of neutron nuclear data on minor actinides" entrusted to the Japan Atomic Energy Agency by the Ministry of Education, Culture, Sports, Science and Technology of Japan (MEXT).

[1] Unesaki H, Doctor Thesis, Nov. 2001 (2001).
[2] Nakagawa T, *et. al.*, J. Nucl. Sci. Technol. 32, 1259 (1995).
[3] Nagaya Y, *et. al.*, JAERI 1348, 2005.
[4] Shibata K, *et. al.*, J Nucl Sci Technol. 2011; 48(1):1-30.

This is a blank page.

8 Development of evaluation method for improvement of nuclear data accuracy in MA isotopes

Kazuhito Mizuyama, Nobuyuki Iwamoto, and Osamu Iwamoto
Nuclear Science and Engineering Center, Japan Atomic Energy Agency
Tokai-mura, Naka-gun, Ibaraki-ken 319-1195, Japan
e-mail: mizuyama.kazuhito@jaea.go.jp

There is large difference among the reported data of the thermal neutron capture cross sections of minor actinides (MAs) measured by the activation technique. This is attributed to the presence of resonances with energies lower than the cadmium cut-off energy within the Westcott convection. We developed the correction method to improve the existing difference and obtained the successful improvement of the discrepancy by applying the method to the measured data. Next, we developed an external code to search for the proper parameters of resolution function on the pulsed neutron beam, together with the resonance parameters in the time-of-flight experiments. It is confirmed that the code can reproduce the resonance shape with adjusting the parameters of resolved resonance and resolution function alternately.

1 Introduction

Accuracy improvement of the nuclear data for minor actinides (MAs) is required for developing transmutation systems. In general, precise measurements and accurate evaluation are necessary to obtain the accurate nuclear data. For the accurate evaluation, it is necessary to find out the reason of the discrepancy among reported data based on the precise investigation of measurements.

The thermal neutron capture cross section σ_0 is usually determined in the activation technique. It is used to fix the absolute value of energy-dependent neutron capture cross section $\sigma(E)$ derived by the time-of-flight (TOF) technique, where E is the neutron energy. In activation measurement, σ_0 can be determined by the Westcott convention [1] using measured reaction rates. It has been well known that there is large discrepancy among reported σ_0 of MAs. The current status of σ_0 for ^{241}Am is shown in the left panel of Fig. 1, for example. This dispersion is due to the low-lying resonances below the cadmium (Cd) cut-off energy E_{Cd}, below which the component of neutron spectrum is removed by the Cd-filter. The filter has been adopted for the determination of the Cd-ratio R/R', where R and R' are non-covered and Cd-covered reaction rates, respectively. It is used for the estimation of the resonance contribution in the reaction rates of the Westcott convention. If there are resonances near or below E_{Cd}, the Cd-ratio cannot provide the proper resonance contribution because the Cd-filter cannot get rid of all the resonances. In the case of MAs, it is found that some of the resonances have lower energies than E_{Cd} (e.g., 0.308 and 0.573 eV in ^{241}Am, 0.419 eV in ^{243}Am, 0.490 eV in ^{237}Np). Hence, attention should be paid to applying the Westcott convention for the MAs. Recently, we developed the correction method in order to take into account those contribution in the Westcott convention [2, 3].

We are going to derive resonance parameters from the $\sigma(E)$ of MAs, using the least-squares multilevel R-matrix code REFIT [4]. The data used for this analysis were measured by the ANNRI in the J-PARC/MLF. In the TOF measurement at this facility, there are mainly two difficulties, the double-bunch structure and the resolution function of the pulsed neutron beam which affect the shape of resonance. In order to overcome those difficulties, we used the revised REFIT [5] which includes the function of describing the double bunch structure and the resolution function for J-PARC/MLF. The parameters of resolution function based on the formulation of Ikeda-Carpenter [6] were derived at a certain operation conditions of J-PARC/MLF [7]. However, the operation condition can be changed. Moreover, the REFIT cannot adjust the parameters of resolution function within its own formulation. Therefore, we developed an external code to obtain the proper parameters of the resolution function in an arbitrary operation condition.

In Sec. 2, we explain the correction method for the measured σ_0 of MAs and show the corrected results for ^{241}Am. In Sec. 3, we describe the external code to search for the proper resolution parameters. The applicability to two cases are presented.

2 Correction of measured thermal capture cross section

The correction method of σ_0 measured by the activation technique and derived by the Westcott convention is briefly explained in this section. The Westcott convention for the non-covered and Cd-covered reactionrates R and R' represents

$$R/\sigma_0 = g\phi_1 + s_0^C \phi_2, \tag{1}$$

$$R'/\sigma_0 = g\phi_1' + s_0^C \phi_2', \tag{2}$$

where g is the g-factor. $\phi_1^{(')}$ and $\phi_2^{(')}$ are the non-covered(Cd-covered) conventional neutron flux which is measured by the neutron flux monitor of e.g., ^{59}Co and ^{197}Au. The s-factor s_0^C is defined by

$$s_0^C = \frac{2}{\sigma_0\sqrt{\pi}} \int_{E_{Cd}}^{\infty} \frac{dE}{E} \left(\sigma(E) - g\sigma_0 \sqrt{\frac{E_0}{E}} \right). \tag{3}$$

Inserting the measured R and $R^{'}$ into Eqs. (1) and (2), σ_0 and s_0^C are obtained. However, according to the exact definition of the reaction rate, Eq. (1) is represented by

$$R/\sigma_0 = g\phi_1 + s_0^C \phi_2 + \delta s_0 \phi_2, \tag{4}$$

where δs_0 is defined by

$$\delta s_0 = \frac{2}{\sigma_0\sqrt{\pi}} \int_{\mu kT}^{E_{Cd}} \frac{dE}{E} \left(\sigma(E) - g\sigma_0 \sqrt{\frac{E_0}{E}} \right). \tag{5}$$

If there is no resonance in the energy region $\mu kT \leq E \leq E_{Cd}$, the δs_0 is negligibly small by definition. It has been ignored in most of the analysis in activation measurements. It cannot, however, be ignored in the case of MAs. Estimating its contribution by the use of JENDL-4.0 [8], we corrected the activation data in [2,3].

We show the corrected results of σ_0 for ^{241}Am in the right panel of Fig. 1. Experimental data were taken from [9–14]. Maidana *et al.* measured the ground-state production cross section. Their data were multiplied by a factor of 1.11, considering the contribution of meta-state production to the total ^{242}Am production to be 10%. The difference in the experimental data before the correction was about 25% as illustrated in the left panel of Fig. 1. After the correction was made, almost all σ_0 were distributed within 10% of the JENDL-4.0. Obviously, the discrepancy among the activation data is improved.

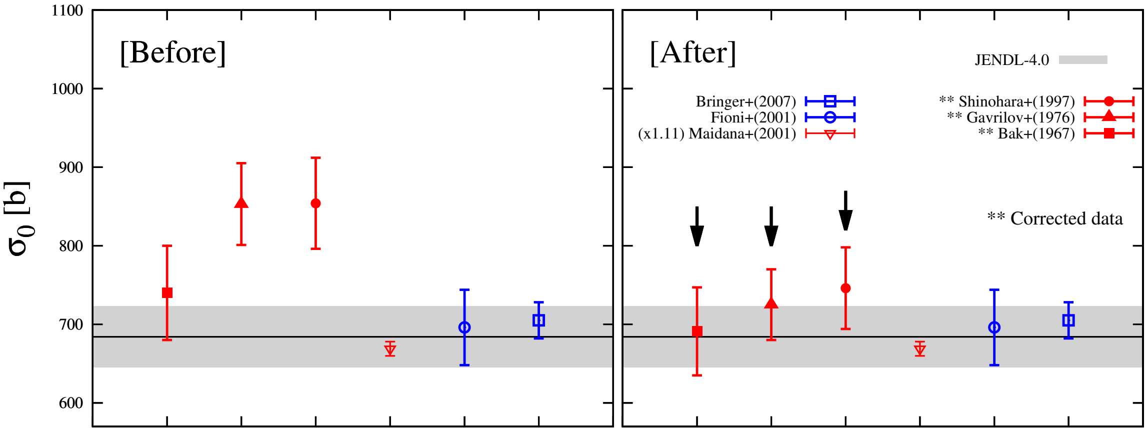

Figure 1: Comparisons of the thermal neutron capture cross sections of ^{241}Am by the activation measurements before correction (left panel) and after one (right panel). The averaged cross sections were presented by the open symbols. The cross sections derived by the Westcott convention were shown by the filled symbols.

3 Evaluation of resolution function in the TOF measurements

The REFIT calculates the cross section from the resonance parameters (the resonance energy E_r, the neutron width Γ_n and the radiation width Γ_γ) together with resolution function, and modifies the resonance parameters to reproduce experimental data. Adjustment of the parameters for resolved resonance and resolution function is important to fit the experimental data. However, the REFIT cannot search for the latter parameters. Hence, the external code was developed in order to adjust the parameters of resolution function (t_0, α, β and R which were introduced by the formulation of Ikeda-Carpenter [6, 7]). The adjustment of both parameters was performed by the external code and the REFIT alternately as shown in Fig. 2. It is expected that both of the parameters are fixed when the difference between the calculated and experimental data becomes small.

First of all, we checked the external code using simulated cross section data. The simulated data were made by the REFIT with ^{118}Sn data of the JENDL-4.0 and with the resolution function parameters of the 1 MW operation condition. The initial values of the parameters for the resolved resonance and resolution function were taken from those given in the second column of Table 1 and in the 17.5 kW operation condition. We adjusted the initial resonance and resolution parameters to reproduce the simulated data by the REFIT and external code. We confirmed that the use of both codes could reproduce the JENDL-4.0 and the 1 MW resolution parameters as shown in the fourth column of Table 1. On the other hand, if the resolution parameters were not adjusted, the agreement between the fitted results and the original parameters of JENDL-4.0 was not obtained (see the third column of Table 1).

Secondly, we applied the external code to the data of ^{118}Sn measured by the ANNRI. Figure 3 shows the result obtained by adjusting both resonance and resolution parameters (solid curve), together with the result fitted by the REFIT with the fixed resolution parameter of 1 MW condition (dotted curve). Obviously, the agreement of the solid curve with the experimental data is better than the dotted curve especially at the lower energy side of the resonance, which is also seen from the difference between the fitted and experimental data in the bottom panel of Fig. 3.

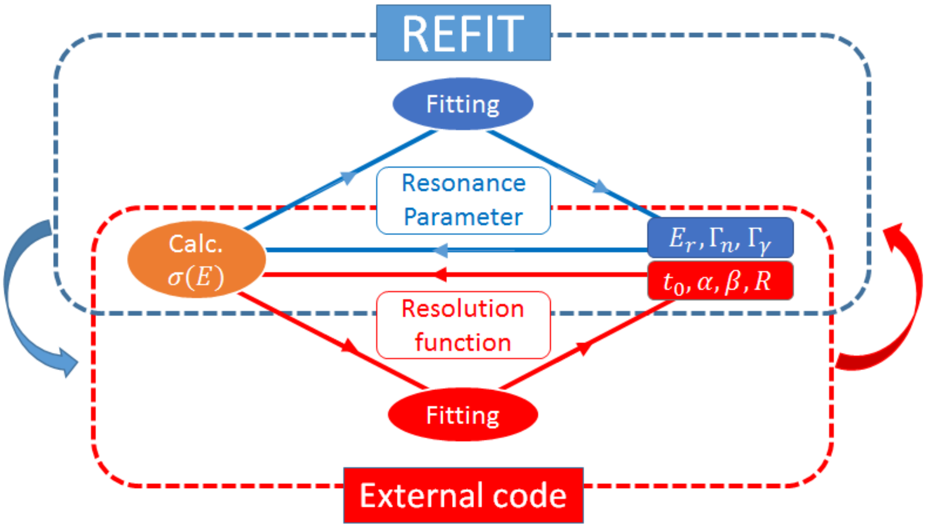

Figure 2: Schematic picture of iterative searches for resonance parameters by the REFIT and resolution function parameters by the external code.

Table 1: Fitted results (in unit of eV) to the simulated data.

	Initial	only REFIT	All fit	JENDL-4.0
E_r	354	359	359	359
Γ_n	0.715	1.09	0.315	0.315
Γ_γ	0.0250	0.0280	0.0851	0.0850

4 Summary

We developed the correction method for the thermal neutron capture cross section for MAs. In our method the contribution of the resonances with energies lower than the Cd cut-off energy was taken into account in the Westcott convention. The discrepancy among the measured data by the activation technique was successfully improved as shown in the case of e.g., ^{241}Am.

Next, we developed the external code for fitting to the experimental data by using the REFIT. The external code estimates the parameters of the resolution function for the purpose of the precise derivation of the resonance parameters from the TOF measurements by the ANNRI in the J-PARC/MLF. For the check of the external code, the simulated data were made from JENDL-4.0 and the resolution parameters of the 1 MW operation condition. Those parameters were successfully reproduced by adjusting the parameters in the use of the REFIT and the external code alternately. In the application of our code to the experimental data of ^{118}Sn measured by ANNRI, it was found that the resonance shape at the lower energy side was especially improved.

Acknowledgement

The authors are grateful for the financial support of “Research and development for Accuracy Improvement of neutron nuclear data on Minor ACtinides (AIMAC)” project entrusted to Japan Atomic Energy Agency by Ministry of Education, Culture, Sport, Science and Technology of Japan (MEXT).

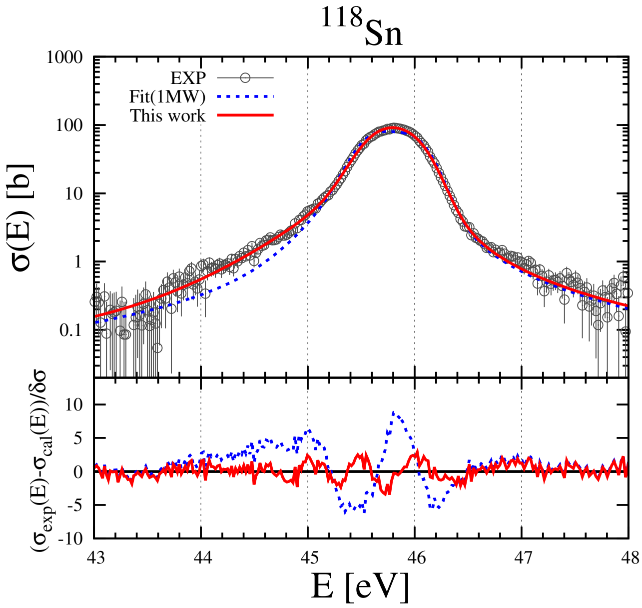

Figure 3: Fitted results to the experimental capture cross section of ^{118}Sn measured by ANNRI. The solid curve was obtained by adjusting both resonance and resolution parameters. The dotted curve shows the result obtained by REFIT with the resolution parameters corresponding to the 1 MW condition.

References

[1] C. H. Westcott, W. H. Walker, T. K. Alexander, Proc. 2 nd Int. Conf. Peaceful Use of Atomic Energy.

[2] K. Mizuyama et al., submitted to J. Nucl. Sci. Technol.

[3] K. Mizuyama et al., Proceedings of Int. Topical Meeting on Reactor Physics (PHYSOR 2016).

[4] M. C. Moxon, T. C. Ware, C. J. Dean, UKNSF(2010)P243 (2010).

[5] H. Hasemi, et al., Nucl. Instrum. Meth. Phys. Res. A773, 137-149 (2015).

[6] S. Ikeda, J. M. Carpenter, Nucl. Instrum. Methods, A239, 536 (1985).

[7] K. Kino et al., Nucl. Instrum. Meth. Phys. Res. A736, 66 (1985).

[8] K. Shibata et al., J. Nucl. Sci. Technol., 48(1), 1-30 (2011).

[9] N. L. Maidana, M. S. Dias, M. F. Koskinas, Radiochim. Acta 89, 419 (2001).

[10] N. Shinohara, Y. Hatsukawa, K. Hata, N. Kondo, J. Nucl. Sci. Technol. 34 (1997), pp. 613-621.

[11] V. D. Gavrilov, V. A. Goncharov, V. V. Ivanenko, V. P. Smirnov, V. N. Kustov, At. Energ. 41, 808 (1976).

[12] M. A. Bak , A. S. Krivohatskiy, K. A. Petrzhak, E. A. Ronanov, Ju. F. Shljamin, At. Energ. **23**, 316 (1967).

[13] O. Bringer et al., Int. Conf. on Nuclear Data for Science and Technology - ND2007, Nice (EDP Science, Les Ulis, 2007), pp. 619-622.

[14] G. Fioni, M. Cribier, F. Marie *et al.*, Nucl. Phys. A**693**, 546 (2001).

9 Overview of JENDL-4.0/HE and Benchmark Calculations

S. Kunieda[1], O. Iwamoto[1], N. Iwamoto[1], F. Minato[1], T. Okamoto[1], T. Sato[1], H. Nakashima[1], Y. Iwamoto[1], H. Iwamoto[1], F. Kitatani[1], T. Fukahori[1], Y. Watanabe[2], N. Shigyo[2], S. Chiba[3], N. Yamano[4], M. Hagiwara[5], K. Niita[6], K. Kosako[7], S. Hirayama[8] and T. Murata[9]

1 Japan Atomic Energy Agency
2 Kyushu University
3 Tokyo Institute of Technology
4 Fukui University
5 High Energy Accelerator Research Organization
6 Research Organization for Information Science and Technology
7 Shimizu Corporation
8 Hitachi, Ltd.
9 Non-affiliated

Abstract : We overview our new high-energy cross-section library JENDL-4.0/HE which is based on the recent progress on the nuclear models, codes, evaluation methods and inheritance of existing libraries. Through the benchmark calculation, it is found that present library shows reasonable performance.

1. Introduction

The cross-section data are required in a wide energy range, beyond several tens of MeV, for the design of a number of accelerator applications. A recent progress in Intra-Nuclear Cascade (INC) model (e.g., INCL [1]) is a bright news as it gives reasonable estimation of the cross-sections up to GeV-energy region. However, there still exists its applicable limit below several hundreds of MeV where the typical pre-equilibrium and compound reaction processes are dominant.

Present work is devoted to having an advanced high-energy cross-section library, JENDL-4.0/HE, to supplement the limitation of the INC calculation. The new library includes evaluated cross-sections for incident neutrons and protons up to 200 MeV for 130 and 133 nuclei, respectively, relevant to accelerator applications. Substantial features of this new library are, (1) systematic evaluation using the CCONE code [2] with recent progress in the optical model and pre-equilibrium model calculations [3,4], (2) challenges on the evaluations of light nuclei such for the p+^{6,7}Li and p+^{9}Be reactions, and (3) inheritance of JENDL-4.0 [5] and JENDL/HE-2007 [6].

In this paper, we shortly describe our evaluation methods, comparing the estimated cross-sections with experimental data and the evaluated values from the other libraries [7,8]. We also present the typical results of benchmark calculation to show the performance/advantage of the present library.

2. Evaluation Approaches

(1) Systematic evaluation for medium-mass nuclei with the CCONE code

Experimental cross-sections are scarce in the high-energy region even for major nuclei. Therefore, we decided to perform a systematic model-based evaluation for medium-mass nuclei such as ^{28,29,30}Si, ^{31}P, $^{40,42-44,46,48}$Ca, ^{46,47,48,49,50}Ti, ^{50,51}V, ^{50,52,53,54}Cr, ^{55}Mn, ^{54,56,57,58}Fe, ^{59}Co, ^{58,60,61,62,64}Ni, ^{63,65}Cu, ^{64,66,67,70}Zn, ^{69,71}Ga, ^{70,72,73,74,76}Ge, ^{75}As, ^{74,76,78,80,82}Se, ^{90,91,92,94,96}Zr, ^{93}Nb, ^{92,94,98,100}Mo, ^{113,115}In, $^{112,114-120,122,124}$Sn, ^{127}I, ^{133}Cs, ^{181}Ta, $^{180,182-184,186}$W, ^{197}Au, $^{196,198-202,205}$Hg, $^{204,206-208}$Pb and ^{209}Bi. We adopted the CCONE code for the model calculation as it has been improved to accommodate the estimation of cross-section up to several hundreds of MeV [9]. Let us emphasize that such an evaluation was made based not only on the code but also on the model parameters systematically optimized. For instance, we adopted the optical model potential of Kunieda et al. [3] for neutrons and protons as it covers a medium-to-heavy nuclei up to 200 MeV. Furthermore, a clustering pre-equilibrium model [4] was applied to the present evaluation, which gives a reasonable prediction of the composite-particle emission spectra.

(2) Interpolation/extrapolation of measured data for the p+^{6,7}Li and p+^{9}Be cross-sections

It is not easy to perform theoretical estimation of cross-section for the light-nuclei because of the limitation of the nuclear models. Therefore, we evaluated cross-sections for the p+^{6,7}Li and p+ ^{9}Be reactions through the interpolation/extrapolation of measured values.

For the p+^{7}Li reactions, such an approach was carried out with the R-matrix fit in the resonance energy range up to 10 MeV, where we included measured (p,p_0), (p,p_1), (p,n_0), (p,n_1) and (p,α) cross-sections as much as possible. Above this energy, the direct (p,n) reaction cross-sections were taken from the phenomenological analysis by Matsumoto et al. [10], while the other parts, such as (p,n) continuum spectra were calculated with CCONE where the absolute values were normalized to the spectra measured by Nakao et al. [11] and Nakamura et al. [12].

For the p+^{9}Be reaction, several resonant cross-sections were evaluated with Breit-Wigner formula, while the CCONE code was applied to interpolation/extrapolation of experimental (p,xn) double-differential spectra of Y.Iwamoto et al. at 10 MeV [13] and Meier et al. at 113 MeV [14]. In this case, the (p,n) direct reaction cross-sections were calculated with the coupled-channel optical model of the OPTMAN-10 code [15].

(3) Inheritance of the existing libraries

The main purpose of this study is to extend the upper energy limit of the current general-purpose neutron data library. Therefore, all the present neutron-induced data thoroughly inherit those of JENDL-4.0 [5] below 20 MeV except for the covariance data which are not included in JENDL-4.0/HE. We decided to adopt the updated version, JENDL-4.0u [16], because minor errors have been fixed since its first release.

The present library also inherits the previous high-energy evaluations in JENDL/HE-2007 [6], for light-mass nuclei: ^{1}H, ^{12,13}C, ^{14}N, ^{16}O, ^{17}F, ^{23}Na, ^{24,25,26}Mg, ^{27}Al, ^{35,37}Cl, ^{36,38,40}Ar, ^{31,41}K, and for all the actinides: ^{235,238}U, ^{237}Np, $^{238\text{-}242}$Pu, ^{241,242,242m}Am. It is because the in-depth evaluation had been performed exclusively for those nuclei.

3. Results

(1) Evaluated cross-sections

Figure 1-a) shows double-differential cross-sections of the Fe(p,xn) reaction at 113 MeV where the present evaluation is compared with the experimental data of Meier et al. [14] and also the data from the other libraries [7,8]. Over a wide scale of the emitted-neutron energy, the present values reproduce measured data as well as the other libraries except JENDL/HE-2007 which overestimates experimental data below 10 MeV.

The evaluated double-differential cross-sections are also plotted in Fig. 1-b) for the ^{58}Ni(p,xα) reaction at 175 MeV together with the experimental values of Ignatowicz et al. [17]. The present evaluation reproduces the experimental data reasonably well while the other libraries show different shapes of the spectra due to the limitation of the semi-empirical pre-equilibrium model.

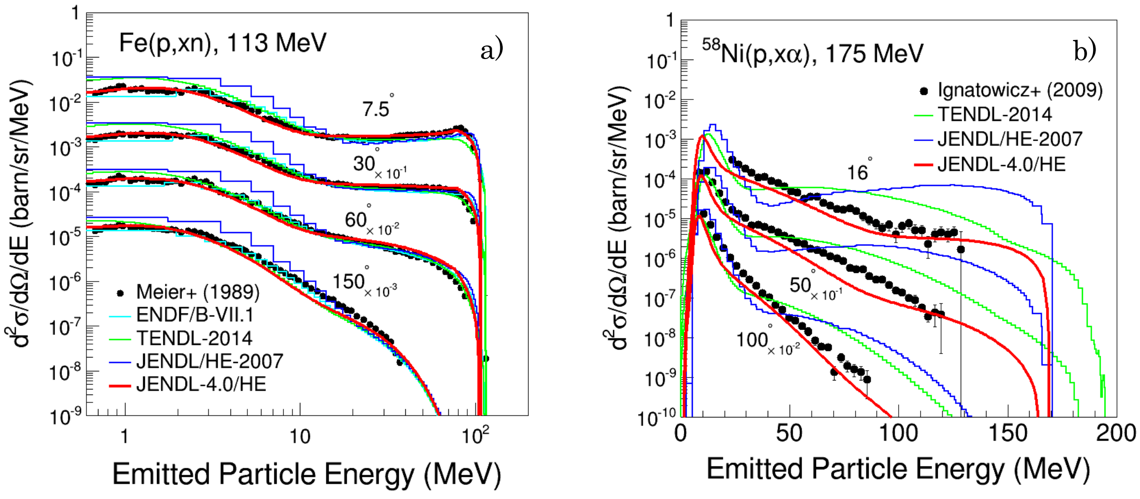

Figure 1 Double-differential cross-sections of the Fe(p,xn) and ^{58}Ni(p,xα) reactions

Figure 2 illustrates the results of the production cross-sections of ^{88}Y and ^{83}Rb from the p+^{nat}Zr reaction together with the available experimental data taken from EXFOR [17]. It is found that, as seen in this example, our calculation shows a better agreement with the measurements than those from the other evaluations both for the heavier and lighter products.

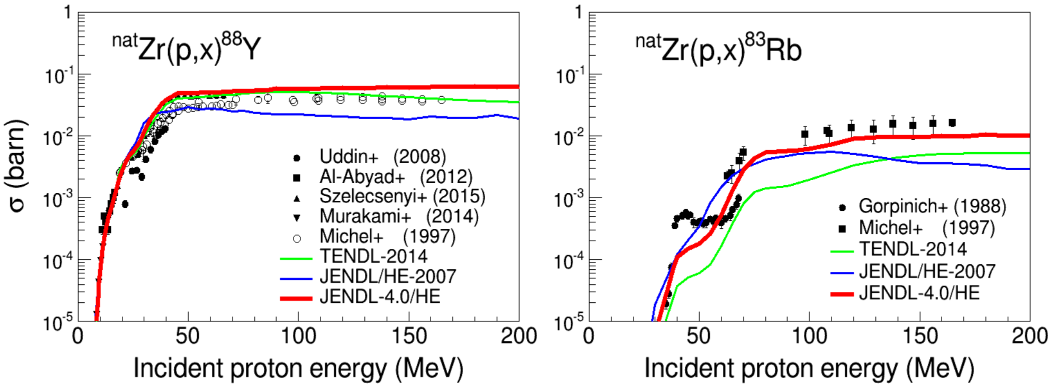

Figure 2 Example results of isotope production cross-sections for the p+^{nat}Zr reaction

As a typical example of the evaluation on the light-mass nuclei, let us show the neutron spectra from the ^{7}Li(p,xn) reaction at the emission angle of 0 degree in Fig. 3 where the present results are compared with experimental data of Nakao et al. [11] and the evaluated data from TENDL-2014 [8]. The present evaluation reproduces measured spectra which are characterized by a strong peak from the direct reaction and the continuous spectrum from the pre-equilibrium process. This is an advantageous feature of the present evaluation as the direct reaction is missing in the other library.

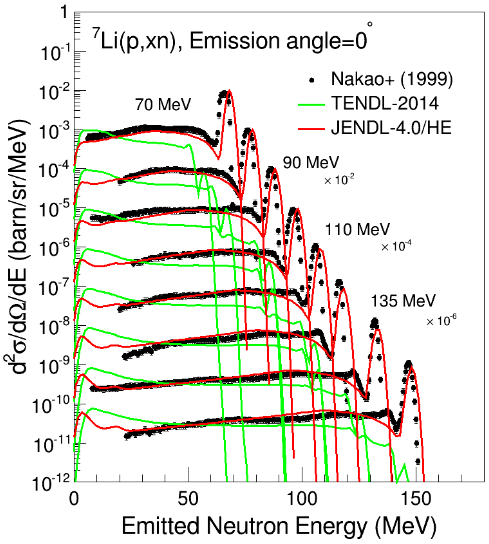

Figure 3 Neutron spectra from the ^{7}Li(p,xn) reaction at emission angle of 0 degree where the evaluated spectra are broadened with experimental resolution.

(2) Validation with benchmark analysis

Figure 4 illustrates neutron yields from the 0.5 cm-thick natural iron bombarded with 50-MeV protons, which were calculated by the PHITS code [18]. With the intra-nuclear cascade model (INCL) [1], calculated values strongly deviate from the measurements at forward and backward angles in this energy range. This kind of problem will be resolved if the present library is adopted. It is found that JENDL/HE-2007, which is based on the individual evaluation of isotope, also gives a reasonable estimation. However, let us stress that the present library achieved such a nice result based on the systematic calculation of the cross-sections.

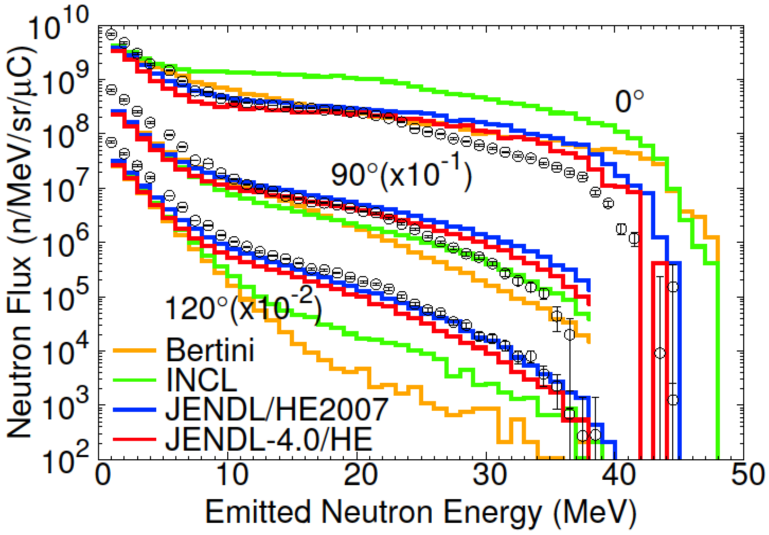

Figure 4 Neutron yields from 0.5 cm-thick natural iron by 50-MeV protons where the experimental data are taken from Itoga *et al.* [19].

4. Summary

The present high-energy nuclear data library JENDL-4.0/HE includes evaluated cross-sections of incident neutrons and protons up to 200 MeV for 130 and 133 nuclei, respectively, relevant with accelerator applications. The systematic evaluation was performed with the CCONE code for a number of the medium-mass nuclei, while the measured cross-sections were interpolated/extrapolated with combination of the several nuclear models (e.g., R-matrix, DWBA) for the p+^{6,7}Li and p+^{9}Be reactions. The library also inherits JENDL-4.0u for all the neutron data and JENDL/HE-2007 for a number of the light-nuclei and all the actinides. Through the benchmark calculation with this new library, it was found that the present library shows quite nice performance, better than pure-model calculation such as from INC model.

References

1. A. Boudard, J. Cugnon, J.C. David, *et al*., Phys. Rev., **C87**, 014606 (2013).
2. O. Iwamoto, N. Iwamoto, S. Kunieda, F. Minato, K. Shibata, Nuclear Data Sheets **131**, p.259 (2016).
3. S. Kunieda, S. Chiba, K. Shibata, *et al*., J. Nucl. Sci. and Technol., **44**, p.838 (2007).
4. S. Kunieda, R. C. Haight, T. Kawano, *et al*., Phys. Rev., **C85**, 054602 (2012).
5. K. Shibata, O. Iwamoto, T. Nakagawa, *et al*., J. Nucl. Sci. and Technol., **48**, p.1 (2011).
6. Y. Watanabe, K. Kosako, S. Kunieda, *et al*., in Proceedings, International Conference on Nuclear Data for Science and Technology, Jeju Island, Korea, April 26-30, 2010 (2011); J. Kor. Phys. Soc., **59**, p.1040 (2011).
7. M. B. Chadwick, M. Herman, P. Oblozinsky, *et al*., Nuclear Data Sheets **112**, p.2887 (2011).
8. A. Koning, D. Rochman, Nuclear Data Sheets **113**, p.2841 (2012).
9. O. Iwamoto, J. Nucl. Sci. and Technol., **50**, p.409 (2013).
10. Y. Matsumoto, Y. Watanabe, S. Kunieda, O. Iwamoto, in Proceedings of the 2014 Symposium on Nuclear Data Nov. 27-28, JAEA-Conf 2015-003, pp.191-196.
11. N. Nakao,Y. Uwamino, T. Nakamura, *et al*., Nucl. Instrum. Methods in Physics Res., Sect. A, Vol. **420**, p.218 (1999).
12. T. Nakamura, M. Takada, N. Nakao, *et al*., Conf. on Nucl. Data for Sci. and Technol., Trieste 1997 Vol. **2**, p.1508 (1997).
13. Y. Iwamoto, Y. Sakamoto, N. Matsuda, *et al*., Nucl. Instrum. Methods in Physics Res., Sect. A, Vol. **598**, Issue.3, p.687 (2009).
14. M. M. Meier, D. A. Clark, C. A. Goulding, *et al*., Nucl. Sci. and Eng. Vol.**102**, p.310 (1989).
15. E. Sh. Soukhovitski, S. Chiba, R. Capote, *et al*., Supplement to OPTMAN Code, Manual version 10 (2008), JAEA-Data/Code 2008-025 (2008).
16. JAEA Nuclear Data Center HP (Nov.-20, 2015) : http://wwwndc.jaea.go.jp/jendl/j40/J40_J.html
17. Taken from EXFOR : N. Otuka, E. Dupont,V. Semkova, *et al*., Nucl. Data Sheets **120**, p.272 (2014).
18. T. Sato, K. Niita, N. Matsuda, *et al*., J. Nucl. Sci. Technol. **50**:9, pp.913-923 (2013).
19. T. Itoga, M. Hagiwara, N. Kawata, *et al*., AIP Conf. Proc. Vol.**769** part 2 (2005).

10 Activation Cross-section File for Decommissioning of LWRs

Keiichi SHIBATA, Nobuyuki IWAMOTO, Satoshi KUNIEDA,
Futoshi MINATO and Osamu IWAMOTO

Nuclear Data Center, Japan Atomic Energy Agency
Tokai-mura, Ibaraki-ken 319-1195, Japan
Email: shibata.keiichi@jaea.go.jp

A neutron-induced activation cross-section file for 302 nuclides has been produced for the decommissioning of light-water reactors (LWRs) in the framework of the joint research with the Japan Atomic Power Company (JAPC). The cross sections were mainly taken from the JENDL-4.0, JENDL/A-96 and post-JENDL-4.0 evaluations. Further modifications were done by taking account of experimental data.

1. Introduction

Estimation of radio-activities is important for the decommissioning of nuclear facilities from the viewpoints of safety evaluation, exposure dose and waste disposal. The Japan Atomic Energy Agency undertook a program of preparing a standard database to be used for the decommissioning of LWRs in the framework of the joint research with the Japan Atomic Power Company in the period of FY2011-2014. The program includes the development of a material-composition database for structural materials and activation cross-section data, and the calculation of neutron flux distributions and activities induced by neutron irradiation as well as the production of a group-wise cross-section library. We were responsible for the activation cross-section data, while other JAEA research groups were involved in the rest of the program mentioned above.

This paper presents how the activation cross-section data were prepared. Section 2 deals with a brief explanation of available neutron activation files. In Section 3, we describe the file-making procedure for the activation file. Comparisons of the present work with other activation files are made in Section 4. Finally, Section 5 summarizes the conclusion.

2. Status of Available Activation Files

As a special-purpose file, JENDL/A-96 [1] was produced in 1996. In its evaluation, emphasis was placed on the targets and products having half-lives ($T_{1/2}$) larger than 1 day, and so the data for 233 nuclides and 1,246 reactions were produced. The JEFF-3.1/A file [2] was released in 2006 as a member of the JEFF-3.1 family, and it contains the data for 774 nuclides and 12,617 reactions. The EAF-2010 file [3], which was released in 2010, contains the data for 816 nuclides and 66,256 reactions. It covers the neutron energy range of 10^{-5} eV to 60 MeV, whereas the other two files are applied to 10^{-5} eV to 20 MeV. The EAF-2010 file has proton- and deuteron-induced reaction data in addition to neutron data. All of these files were developed essentially for fusion applications. Therefore, their low-energy performances, which are regarded as important in the present work, are very uncertain.

3. File-making Procedures

3.1 Selection of Target Nuclei

First of all, we have to select the target nuclei for which activation data are produced. For the decommissioning of LWRs, the 227 nuclides having $T_{1/2} \geq 30$ days, which are listed in **Table 1**, are regarded as important. In this work, we also consider 12 extremely long-lived nuclides given in **Table 2**. The nuclides are all reaction products. Thus, target nuclei were selected by considering possible reaction paths. For example, ^{3}H can be produced by the binary reactions $^{2}H(n,\gamma)^{3}H$, $^{3}He(n,p)^{3}H$, $^{6}Li(n,\alpha)^{3}H$, $^{7}Li(n,n'\alpha)^{3}H$, and $^{10}B(n,2\alpha)^{3}H$. On the other hand, ^{48}Ca can be formed by the 2-step reactions $^{46}Ca(n,\gamma)^{47}Ca(n,\gamma)^{48}Ca$ and $^{50}Ti(n,\gamma)^{51}Ti(n,\alpha)^{48}Ca$. In this work, such 2-step reactions were also considered. Even considering 2-step reactions, it is unlikely to produce 35 nuclides,

Table 1 227 nuclides with $T_{1/2} \geq 30$ days

H-3, Be-7,10, C-14, Na-22, Al-26, Si-32, S-35, Cl-36, Ar-37,39,42, K-40, Ca-41,45, Sc-46, Ti-44, V-49,50, Mn-53,54, Fe-55,59,60, Co-56,57,58,60, Ni-59,63, Zn-65, Ge-68, As-73, Se-75,79, Kr-81,85, Rb-83,84,87, Sr-85,89,90, Y-88,91, Zr-88,93,95, Nb-91,91m,92,93m,94,95, Mo-93, Tc-95m,97,97m,98,99, Ru-103,106, Rh-101,102,102m, Pd-107, Ag-105,108m,110m, Cd-109,113,113m,115m, In-114m,115, Sn-113,119m, 121m,123,126, Sb-124,125, Te-121m,123,123m,125m,127m,129m, I-125,129, Xe-127, Cs-134,135,137, Ba-133, La-137,138, Ce-139,141,144, Nd-144, Pm-143,144,145,146,147,148m, Sm-145,146,147,148,151, Eu-148,149,150,152,154,155, Gd-146,148,150,151,152,153, Tb-157,158,160, Dy-154,159, Ho-163,166m, Tm-168,170,171, Yb-169, Lu-173,174,174m,176,177m, Hf-172,174,175,178m,181,182, Ta-179,180m,182, W-181,185,188, Re-183,184,184m,186m,187, Os-185,186,194, Ir-192,192n,194m, Pt-190,193, Au-195, Hg-194,203, Tl-204, Pb-202,205,210, Bi-207,208,210m, Po-208,209,210, Ra-226,228, Ac-227, Th-228,229, 230,232, Pa-231, U-232,233,234,235,236,238, Np-235,236,237, Pu-236,237,238,239,240,241,242,244, Am-241,242m,243, Cm-241,242,243,244,245,246,247,248,250, Bk-247,249, Cf-248,249,250,251,252,254, Es-254,255, Fm-257, Md-258 for example ^{7}Be, ^{56}Co, ^{257}Fm and ^{258}Md. Although the former 2 nuclides can be produced by the (p,n) reactions on ^{7}Li and ^{56}Fe, we do not intend to include proton-induced reactions in this work. It is almost impossible to produce the latter 2 nuclides in LWRs. As a result, we should deal with the production of 204 radioactive nuclides.

Table 2 Additional 12 nuclides

Ca-48 (1.9×10^{19}y), Cr-50 (>1.3×10^{18}y), Mn-53 (3.74×10^{6}y),
Se-82 (8.3×10^{19}y), Kr-78 (≧1.5×10^{21}y), Zr-96 (2.0×10^{19}y),
Nb-92 (3.47×10^{7}y), Mo-100 (7.3×10^{18}y), Cd-116 (3.3×10^{19}y),
Te-128 (2.3×10^{24}y), Te-130 (8.0×10^{20}y), Xe-136 (> 3.6×10^{20}y)

3.2 File Structure

The activation file should contain MF1, 2, 3, 8, 9, and 10 blocks in the ENDF-6 format [4]. The MF1 block gives comment data which describe how the evaluation was performed. Resonance parameters are given in MF2 if they are available. It should be noted that the activation files mentioned in Section 2 do not have any resonance parameters. The resonance parameters were stored in the present data files only for self-shielding calculations. The cross section, which is the sum of partial activation cross sections, exactly speaking, is given in MF3. The MF8 block is just a dummy block which indicates the decay data exist in a separate file. The MF9 and 10 blocks contain partial activation cross sections. The MF10 data are absolute cross sections, while MF9 is a ratio of MF10 to MF3. The MF9 data are usually used for resonant cross sections, namely, capture cross sections, since the amount of data can be reduced by adopting theoretically-determined smooth ratios. If there is no meta-stable state in the residual nucleus of a certain reaction, the corresponding MF9 and 10 blocks never exist.

3.3 Data Sources

This joint research had to be completed practically less than 3 years. Therefore, it was impossible to newly evaluate all the nuclides. Alternatively, the data were taken from JENDL-4.0 [5] and JENDL/A-96 to some extent. Since JENDL-4.0 does not contain partial activation cross sections except for ^{209}Bi, ^{237}Np and ^{241}Am, only MF3 data were used. However, the partial activation cross sections were actually evaluated for JENDL-4.0, although they were not compiled into the data files. In this work, these evaluated partial cross-sections could be utilized. Some excitation functions were supplemented with JEFF-3.1/A. After the release of JENDL-4.0, we have carried out new evaluations especially for fission products, which were also useful to make the activation file. All the evaluated data were compared with experimental data, and data modification was performed if necessary.

3.4 Compiled Results

We produced the activation files at the temperatures of 0 K and 293.6 K. Most of the data (227 nuclides) were taken from the post-JENDL-4.0 new evaluations and from the partial activation cross sections which had been evaluated for JENDL-4.0 but were not compiled into JENDL-4.0. The data on 69 nuclides are based on JENDL-4.0, and those on 6 nuclides are based on JENDL/A-96. We managed to produce the data files for a total of 302 nuclides, as listed in **Table 3**.

Table 3 Target nuclei

H-2 He-3 Li-6 Li-7 Be-9 B-10 B-11 C-12 N-14 N-15 O-17 Si-30 Si-31 S-34 S-35 Cl-35 Ar-36 Ar-38 Ar-40
Ar-41 K-39 K-40 Ca-40 Ca-42 Ca-44 Ca-45 Ca-46 Ca-47 Sc-45 Ti-46 Ti-47 Ti-48 Ti-50 Ti-51 V-50 V-51 Cr-50
Fe-54 Fe-58 Fe-59 Co-57 Co-59 Ni-58 Ni-60 Ni-61 Ni-62 Ni-63 Cu-63 Zn-64 Se-74 Se-78 Br-79 Kr-80 Kr-84
Rb-85 Sr-84 Sr-88 Sr-89 Y-89 Y-90 Zr-92 Zr-93 Zr-94 Zr-95 Zr-96 Nb-91 Nb-93 Nb-94 Mo-92 Mo-93 Mo-94
Mo-95 Mo-96 Mo-98 Mo-99 Tc-95 Tc-97 Tc-98 Ru-96 Ru-98 Ru-99 Ru-100 Ru-102 Ru-103 Ru-104 Ru-105
Rh-101 Rh-102 Rh-103 Pd-102 Pd-103 Pd-106 Pd-108 Pd-109 Ag-105 Ag-107 Ag-109 Cd-106 Cd-108 Cd-109
Cd-110 Cd-111 Cd-112 Cd-113 Cd-114 Cd-116 In-111 In-113 In-115 Sn-112 Sn-114 Sn-115 Sn-116 Sn-118
Sn-119 Sn-120 Sn-122 Sn-124 Sn-125 Sb-121 Sb-123 Sb-124 Te-120 Te-122 Te-124 Te-125 Te-126 Te-128
Te-129M Te-130 I-127 I-128 I-130 Xe-124 Xe-126 Xe-128 Xe-129 Xe-130 Xe-131 Xe-132 Xe-133 Xe-134
Xe-135 Cs-132 Cs-133 Cs-134 Cs-135 Cs-136 Ba-130 Ba-132 Ba-134 Ba-135 Ba-136 Ba-137 Ba-138 Ba-139
La-137 La-138 La-139 La-140 Ce-136 Ce-138 Ce-140 Ce-142 Ce-143 Pr-138 Pr-140 Pr-141 Nd-142 Nd-144
Nd-146 Nd-147 Pm-148 Sm-144 Sm-145 Sm-147 Sm-148 Sm-149 Sm-150 Eu-150 Eu-151 Eu-153 Eu-154
Eu-156 Gd-151 Gd-152 Gd-153 Gd-154 Gd-155 Gd-156 Tb-155 Tb-157 Tb-158 Tb-159 Dy-155 Dy-156
Dy-158 Dy-159 Dy-160 Dy-161 Ho-161 Ho-163 Ho-165 Er-162 Er-164 Er-166 Er-167 Tm-169 Tm-170
Tm-172 Yb-168 Yb-170 Yb-171 Yb-172 Lu-173 Lu-174 Lu-175 Lu-176 Lu-177 Hf-174 Hf-176 Hf-177 Hf-178
Hf-180 Hf-181 Ta-179 Ta-180M Ta-181 W-180 W-181 W-182 W-183 W-184 W-185 W-186 W-187 Re-183
Re-185 Re-187 Re-188 Os-184 Os-186 Os-187 Os-188 Os-190 Os-191 Os-192 Os-193 Ir-190 Ir-191 Ir-193
Pt-189 Pt-190 Pt-192 Pt-193 Pt-194 Pt-195 Pt-196 Pt-197 Au-195 Au-197 Hg-195 Hg-196 Hg-202 Tl-203
Pb-204 Pb-206 Pb-208 Pb-209 Bi-209 Th-228 Th-232 Pa-231 U-234 U-235 U-236 U-238 Np-236 Np-237
Pu-236 Pu-238 Pu-239 Pu-240 Pu-241 Pu-242 Am-241 Am-243 Cm-242 Cm-244 Cm-245 Cm-246 Cm-247
Cm-248 Cm-249 Bk-249 Cf-249 Cf-250 Cf-251 Cf-253 Cf-254 Es-253 Es-254

4. Comparisons with Other Evaluations and Experimental Data

The present evaluation is compared with other evaluations and available experimental data. As for the ^{92}Mo(n,γ)^{93m}Mo reaction illustrated in **Figure 1**, the JEFF-3.1/A evaluation exhibits unphysical oscillation in the low-energy region, which is probably a compilation error. The JENDL/A-96 data become extremely small with decreasing incident energies. The present data, which were obtained from theoretical calculations, were renormalized to the experimental data in the whole energy region. The γ-ray transitions need to be reconsidered for the theoretical calculations in order to reproduce the measured production of ^{93m}Mo having a spin-parity value of 21/2+. The newly evaluated capture cross section of ^{126}Te [6] obviously reproduces the measurements

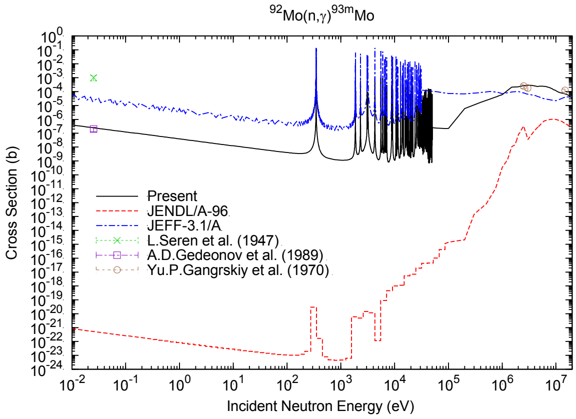

Fig. 1 ^{92}Mo(n,γ)^{93m}Mo cross section

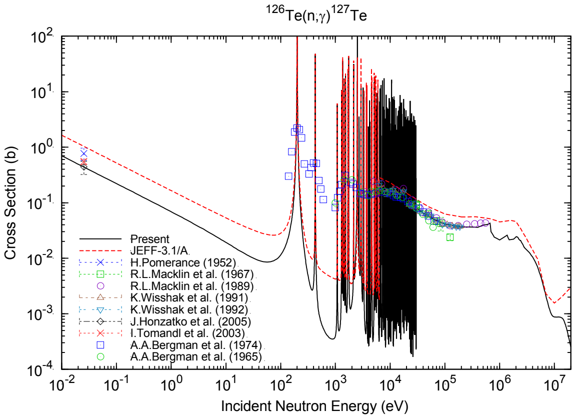

Fig. 2 ^{126}Te(n,γ)^{127}Te cross section

better than the JEFF-3.1/A evaluation, as seen in **Figure 2**.

Figure 3 shows the ^{181}Ta(n,γ)^{182m2}Ta cross section. The second meta-stable state of ^{182}Ta is a high spin state ($J = 10$). As in the case of ^{92}Mo, the JENDL/A-96 evaluation is

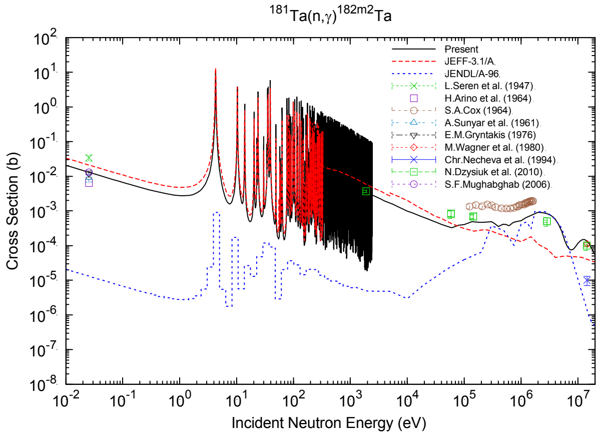

Fig. 3 ^{181}Ta(n,γ)^{182m2}Ta cross section

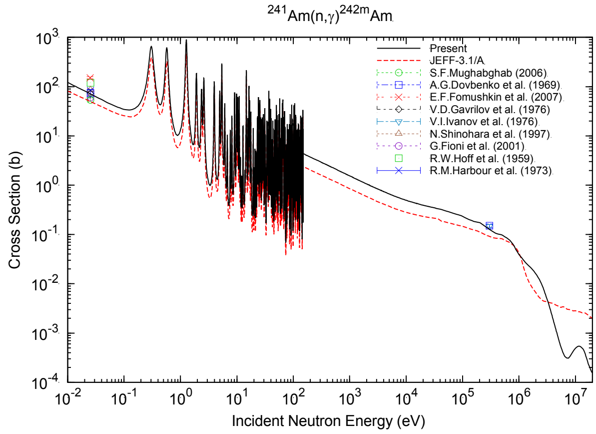

Fig. 4 ^{241}Am(n,γ)^{242m}Am cross section

very lower than the present and JEFF-3.1/A data. The present evaluation [7] was renormalized to the measurements below 60 keV. The ^{241}Am(n,γ)^{242m}Am reaction is one of the important reactions for nuclear enegineering. It is found from **Figure 4** that there is a difference between the present and JEFF-3.1/A data even in the thermal region. The present data, which were taken from JENDL-4.0, yields a thermal capture cross section of 71.17 b, while the JEFF-3.1/A evalution gives a value of 49.85 b.

5. Concluding Remarks

Neutron-induced activation data were produced for 302 nuclides in the framework of the joint research with the Japan Atomic Power Company. Most of the data were taken from new evaluations and from the theoretical calculations for JENDL-4.0. Partial activation cross sections were compiled into the MF9 and MF10 blocks of the ENDF-6 format. Special care was taken for the MF2 block, in which resonance parameters were stored for self-shielding calculation. The other activation files mentioned in Section 2 contain only scattering radii in the MF2 block.

It is found that a large difference exists between the present and other evaluations especially for the capture cross section leading to meta-stable states having large spin values.

The presently produced file will be released in FY2016 after achieving further improvements.

Acknowledgment

The authors would like to thank the Japan Atomic Power Company for supporting this work.

References

[1] Y. Nakajima: “JENDL Activation Cross Section File,” JAERI-M 91-032, p. 43-57 (1991).

[2] A. Koning, R. Forrest, M. Kellet, R. Mills, H. Henriksson, Y. Rugama (eds.): “The JEFF-3.1 Nuclear Data Library,” OECD/NEA, JEFF Report 21 (2006).

[3] J.-Ch. Sublet, L.W. Packer, J. Kopecky, R.A. Forrest, A.J. Koning, D.A. Rochman: “The European Activation File: EAF-2010 Neutron-induced Cross Section Library,” CCFE-R (10) 05 (2010).

[4] A. Trkov, M. Herman, D.A. Brown: “ENDF-6 Formats Manual, Data Formats and Procedures for the Evaluated Nuclear Data Files ENDF/B-VI and ENDF/B-VII,” BNL-90365-2009 Rev.2 (2012).

[5] K. Shibata, O. Iwamoto, T. Nakagawa, N. Iwamoto, A. Ichihara, S. Kunieda, S. Chiba, K. Furutaka, N. Otuka, T. Ohsawa, T. Murata, H. Matsunobu, A. Zukeran, S. Kamada, J. Katakura: “JENDL-4.0: A New Library for Nuclear Science and Engineering,” J. Nucl. Sci. Technol., **48**, 1 (2011).

[6] K. Shibata: “Evaluation of Neutron Nuclear Data on Tellurium Isotopes,” J. Nucl. Sci. Technol., **52**, 490 (2015).

[7] K. Shibata: “Evaluation of Neutron Nuclear Data on Tantalum Isotopes,” J. Nucl. Sci. Technol., 53, No.7, pp.957-967 (2016).

11 Photonuclear Data File

Nobuyuki Iwamoto[1], Kazuaki Kosako[2], Toru Murata[3]
[1]*Nuclear Data Center, Nuclear Science and Engineering Center, Japan Atomic Energy Agency, Tokai, Ibaraki 319-1195, Japan*
[2]*Shimizu Corporation, 3-4-17 Etchujima, Koto-ku, Tokyo 135-8530, Japan*
[3]*Former JENDL Committee, Japan Atomic Energy Agency, Tokai Ibaraki 319-1195, Japan*
e-mail: iwamoto.nobuyuki@jaea.go.jp

The JENDL photonuclear data library has been revised in order to meet the needs of extensive application fields. The evaluation of photon-induced reaction cross sections was performed with twofold: (i) resonance cross section analyses in the low energy region for light nuclides, and (ii) nuclear reaction model calculations in the higher energy region for light nuclides, and in the whole region for heavier nuclides. It is found that the obtained results are consistent with available experimental data. The benchmark test was also made for the nuclides of structural material by calculating the angular distributions of neutron dose rates and showed reasonable results in the case of higher electron energies. The new library is planned to include the nuclear data of 181 nuclides from ^{2}H to ^{237}Np, covering the incident photon energy range up to 140 MeV.

1 Introduction

The experimental researches were efficiently carried out to obtain photon-induced reaction cross sections, especially photoneutron ones in the incident photon energy range of about 8 to 30 MeV, since 1950s. The results were compiled in, e.g., Ref. [1]. The major activities of generating photonuclear data library were belatedly started at several institutes during the 1990s. Then, the first development of massive photonuclear data library (so-called IAEA photonuclear data library [2]) was organized by the IAEA. The library included 164 nuclides whose data were collected from the libraries (being developed) of institutes, e.g., JAERI (JENDL/PD-2004 [3], Japan), KAERI (KAERI photonuclear data library [4], Korea), LANL (LA150 [5], USA). It was finally made available in 1999. One of the up-to-date libraries is ENDF/B-VII.1 [6]. The included data and nuclides, however, are the same as those of ENDF/B-VII.0 [7]. Most of them were taken from the KAERI library released in 2000. Recent TALYS-based library TENDL-2014 also has photonuclear data. The included number of nuclides is extremely large and exceeds 2600 [8]. The brief summary of photonuclear data libraries is presented in **Table 1**, in which the released year and included number of nuclides were given.

Photonuclear data have been mainly required in four application fields: (i) radiation safety related to accelerator (e.g., shielding design of electron linac, and management of activation materials), (ii) technology of fission and fusion reactors (e.g., high energy runaway electrons which occasionally emerge in the plasma of Tokamak fusion reactor), (iii) medical therapy (e.g., high-energy radiation therapy, and estimation of absorbed dose), and (iv) nuclear security and non-proliferation (e.g., non-destructive assay for detecting fissile material).

The previous version of JENDL photonuclear data library JENDL/PD-2004 was distributed in 2004. It contains photon-induced reaction cross section data (absorption cross section, total fission cross section, production cross sections of residuals, production cross sections and energy-angle double differential ones of emitted particles and gamma-rays, and so on). The library includes 68 nuclides from ^{2}H to ^{237}Np. The photon energy range is from particle threshold energy to 140 MeV, except for ^{3}He, ^{40}Ca, ^{60}Ni, Gd, Hg, and Bi isotopes (150 MeV as the upper energy) and ^{181}Ta (160 MeV). In order to respond to the above extensive needs, the development of new photonuclear data library has been performed since 2004 [9, 10]. The new library is aimed

Table 1: Brief summary of photonuclear data library

Library	Released year	Number of nuclides
LA150	1999	12
IAEA Photonuclear data library	1999	164
KAERI Photonuclear data library	2000	143
JENDL/PD-2004	2004	68
ENDF/B-VII.0 (ENDF/B-VII.1)	2006 (2011)	163
TENDL-2014	2014	2629

at increasing the included number of nuclides which makes the application fields extended, and improving the nuclear data by adopting new experimental data as well as up-to-date reaction models and nuclear structural information. In addition, systematic evaluation was assumed, based on a same methodology for light nuclides of Li to Ca.

2 Evaluation method

Evaluation was newly performed from ^{6}Li to ^{237}Np. The nuclear data of ^{2}H and ^{3}He[†] were only carried over from JENDL/PD-2004. The evaluation methodology of the new library is twofold. Nuclear data of stable light nuclides from Li to Ca isotopes were evaluated with experimental cross sections and nuclear structure data in low energy region, in which resonance components are present and fitted by the following equation for photon absorption [11]:

$$\sigma_{abs} = \frac{2\pi}{k^2}\sum_i \frac{2J_i+1}{2I_0+1}B_{i0}\frac{(E\Gamma_i)^2}{(E_i^2-E^2)^2+(E\Gamma_i)^2}, \tag{1}$$

where E is the photon energy, k is the corresponding wave number, I_0 is the target spin, E_i, Γ_i, J_i and B_{i0} are the energy, width, spin and gamma-ray transition branching ratio to the ground-state for the i-th pseudo-resonance level, respectively.

For the light nuclides in a high energy region and for nuclides with atomic number $20 < Z < 30$, the photonuclear reaction cross sections were calculated by the nuclear reaction model code ALICE-F [12]. On the other hand, a more modern code CCONE was also used to evaluate the nuclear data of nuclides with $Z \geq 30$ [13]. The incident photon energy covers the range up to 140 MeV from the particle threshold energy or 1 MeV for the ALICE-F or CCONE-based evaluations, respectively. The photon absorption cross sections were described by giant dipole resonance (GDR) and quasideuteron disintegration processes [14]. The form of the GDR was represented by the multiple-standard and modified Lorentzian models [15] in the ALICE-F and CCONE, respectively. The emissions of neutron, proton, deuteron, triton, ^{3}He, and α-particles were assumed as the particle decay. The E1, M1 and E2 radiations were taken into account for gamma-ray emissions from excited nuclei. The both codes included preequilibrium process, for which the hybrid and two-component exciton models were adopted in the ALICE-F and CCONE, respectively. The discrete levels of each nucleus were only considered in the CCONE and their information was taken from RIPL-3 [16]. The nuclear level density above the discrete levels was represented by the composite formula of Fermi-gas and constant temperature models.

The new library is planned to include the nuclear data of 181 nuclides as the standard version. In addition, an extended version is considered to be released for potential use in unexpected subjects. In the latter version, systematic calculations by the ALICE-F were made for about 2500 nuclides other than those included in the standard file.

[†] For the data of ^{3}He the upper energy and used format were only revised.

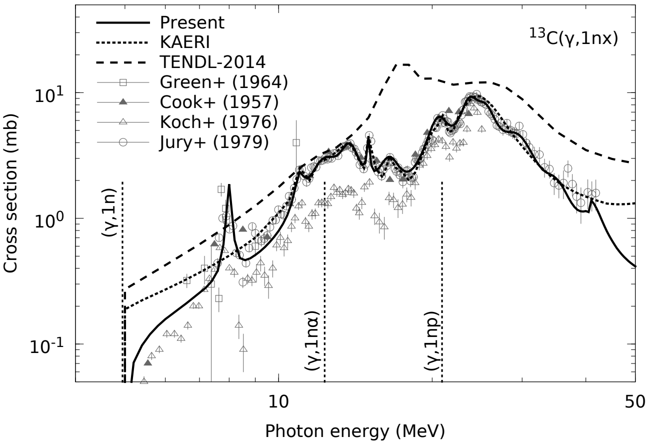

Figure 1: Comparison of the present single-neutron production cross section of ^{13}C with the experimental data and evaluated ones of KAERI and TENDL-2014. The threshold energies for $(\gamma, 1n)$, $(\gamma, 1np)$ and $(\gamma, 1n\alpha)$ reactions were shown by the vertical lines.

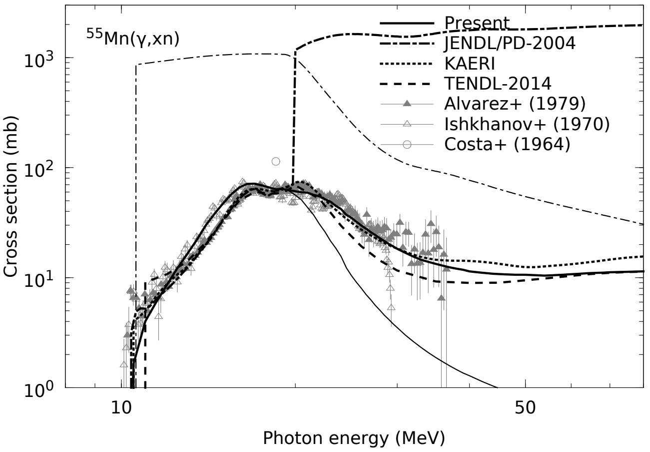

Figure 2: Comparison of the present neutron and ^{54}Mn production cross sections of ^{55}Mn with the experimental data and evaluated ones of JENDL/PD-2004, KAERI, and TENDL-2014. The thick and thin lines for the present results and JENDL/PD-2004 represent the neutron and ^{54}Mn production cross sections, respectively.

3 Evaluated results

The evaluated result of ^{13}C is shown in **Fig. 1** [10], in which the single-neutron production cross section is illustrated with experimental data and evaluated ones of KAERI and TENDL-2014. Since JENDL/PD-2004 does not include the data of ^{13}C which is an important nuclide to compose natural carbon even with very small abundance 1.07%, the new library took into account them. The present evaluation considered 12 pseudo-levels of ^{13}C, which make sharp peaks in the cross section. The most prominent one is located at around 8 MeV, which may correspond to 7.69 MeV-level and possible weaker 7.95 MeV-level [17]. The obtained result reproduces experimental data, especially neutron emission peaks, and shows the similar behavior to the cross section of KAERI at 10 to about 40 MeV photon energies. TENDL-2014 may be the result of a default calculation and are larger than the experimental data in this energy region shown in Fig. 1.

In **Fig. 2** the present neutron and ^{54}Mn production cross sections for the ^{55}Mn target are compared with experimental data and the evaluated ones of JENDL/PD-2004, KAERI, and TENDL-2014, and depicted by thick and thin lines, respectively. JENDL/PD-2004 gives con-

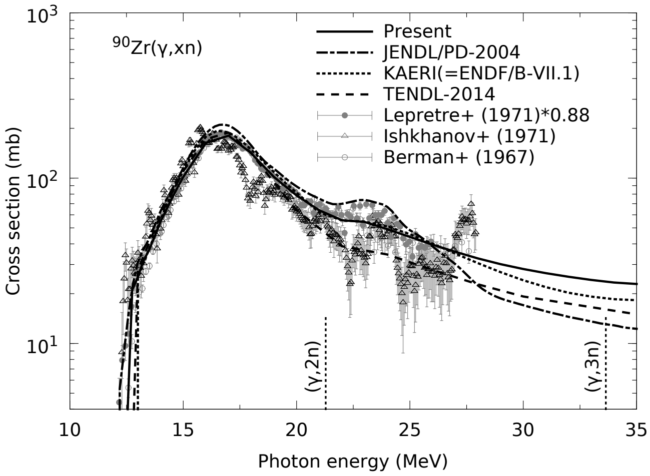

Figure 3: Comparison of the present neutron production cross section of ^{90}Zr with the experimental data and evaluated ones of JENDL/PD-2004, KAERI, and TENDL-2014. The data of Lepretre *et al.* were multiplied by a factor of 0.88. ENDF/B-VII.1 has the same data as KAERI. The threshold energies of $(\gamma, 2n)$ and $(\gamma, 3n)$ reactions were shown by the vertical lines.

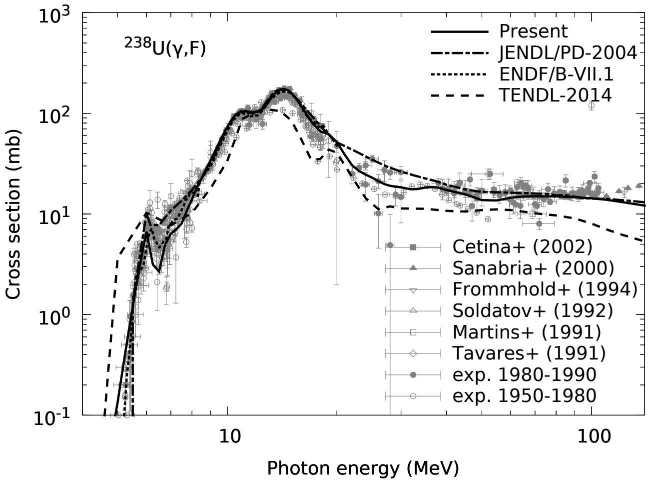

Figure 4: Comparison of the present total photofission cross section of ^{238}U with the experimental data and evaluated ones of JENDL/PD-2004, ENDF/B-VII.1 and TENDL-2014.

tradicting data between the two cross sections. The ^{54}Mn production cross section corresponds to the single-neutron one below 17.8 MeV. The cross sections for single-neutron emission is much larger than the experimental ones at the energy range. On the other hand, the cross section for neutron production is in agreement with the experimental data below 20 MeV. It is, however, suddenly changed into barn-level at 20 MeV, and remains large above the energy. In the present evaluation each result is compatible and is consistent with the experimental data in the energy range of 10 to 40 MeV.

Figure 3 shows the present neutron production cross section of ^{90}Zr, together with experimental data and evaluated ones of JENDL/PD-2004, KAERI, and TENDL-2014. The data of ENDF/B-VII.1 are the same as those of KAERI. The data measured by Lepretre *et al.* [18] were normalized by a factor of 0.88, whose value was derived from careful analyses based on the experiments of Berman *et al.* [19]. The present result explains those experimental data by considering a supplementary small resonance at 21 MeV as well as the GDR component. It almost coincides with those of KAERI and TENDL-2014 below 20 MeV. However, the cross section of

TENDL-2014 is smaller above $\sim$ 20 MeV, in comparison with the present one, and is consistent with the data of Ishkhanov *et al.* [20], whose data show complicated structure obtained by the bremsstrahlung experiment. Since JENDL/PD-2004 reproduced the original data of Lepretre *et al.*, it resulted in 14% larger cross section than the present one.

The evaluated result of total photofission cross section for ^{238}U is compared with experimental data and evaluated ones of JENDL/PD-2004, ENDF/B-VII.1 and TENDL-2014 in **Fig. 4**. The total photofission cross section is dominated by the successive fission of U isotopes in the relevant energy range. The present data well reproduce the experimental ones below 20 MeV where many experimental efforts have been done, as well as above 40 MeV where the quasideuteron disintegration process is important for photon absorption. The obtained result has almost similar characteristics to JENDL/PD-2004 and ENDF/B-VII.1. The latter library has the upper energy limit of 20 MeV for all U isotopes. TENDL-2014 slightly underestimates with respect to the experimental data.

The benchmark test on the new library was performed on the basis of the experiment which measured the angular distributions of photoneutrons [9]. The calculated angular distributions of ambient dose equivalent rates of neutrons, which came from the iron and copper bombarded by 18-38 MeV electrons, are compared with the measured data. The present results are consistent with the angle-dependent shapes and values measured by 28 and 38 MeV electrons, except for the case of 18 MeV electrons, in which the calculated data are relatively small.

4 Summary

The new JENDL photonuclear data library has been developed to respond to the extensive needs and applications. The evaluation of nuclear data for light nuclides from Li to Ca isotopes was performed by consistent methodology, which took into account the resonance cross sections in the low energy region. For the higher energy region where the resonance feature disappears and for the heavier nuclides the nuclear reaction model codes ALICE-F and CCONE were used to evaluate the photon-induced reaction cross sections in comparison with the experimental data available. Several evaluated results were illustrated together with the experimental data and existing evaluated ones of JENDL/PD-2004, KAERI, ENDF/B-VII.1 and TENDL-2014. They show a reasonable agreement with the experimental data. The validation check especially for the nuclides of structural material was done by the benchmark calculations on experimental results.

The new library includes the nuclear data of 181 nuclides from ^{2}H to ^{237}Np, covering the incident photon energy range from particle threshold energy (ALICE-F-based data) or 1 MeV (CCONE-based data) to the pion production threshold energy of 140 MeV. The ALICE-F-based extended version including the nuclear data of nuclides other than the above-mentioned ones is also considered to be distributed for making available for unforeseen applications.

Acknowledgments

The authors are grateful to Dr. T. Fukahori for his activity and encouragement of the development of new JENDL photonuclear data library. This work was partly supported by JSPS KAKENHI Grant Number 26420876.

References

[1] Dietrich SS, Berman BL. Atlas of photoneutron cross sections obtained with monoenergetic photons. Atomic Data Nucl. Data Tables, 38, 199-338 (1988).

[2] Chadwick MB, Blokhin AI, Fukahori T, Lee YO, Martins MN, Varlamov VV, Yu B. Handbook on photonuclear data for applications Cross-sections and spectra. IAEA-TECDOC-1178, IAEA (2000).

[3] Kishida N, Murata T, Asami T, Kosako K, Maki K, Harada H, Lee YO, Chang J, Chiba S, Fukahori T. JENDL Photonuclear Data File. Proc. of International Conference on Nuclear Data for Science and Technology, Santa Fe, New Mexico, USA, vol. 1, pp.199-202 (2004).

[4] Lee YO, Han Y. KAERI photonuclear data library. KAERI/TR-1512 (2000).

[5] Chadwick MB. Neutron, Proton, and Photonuclear Cross Sections for Radiation Therapy and Radiation Protection. Los Alamos National Laboratory; LA-UR-98-4139 (1998).

[6] Chadwick MB, Herman M, Obložinský P, Dunn ME, Danon Y, Kahler AC, Smith DL, Pritychenko B, Arbanas G, Arcilla R, *et al.* ENDF/B-VII.1 Nuclear Data for Science and Technology: Cross Sections, Covariances, Fission Product Yields and Decay Data. Nucl. Data Sheets. 112, 2887-2996 (2011).

[7] Chadwick MB, Obložinský P, Herman M, Greene NM, McKnight RD, Smith DL, Young PG, MacFarlane RE, Hale GM, Frankle SC, *et al.* ENDF/B-VII.0: Next Generation Evaluated Nuclear Data Library for Nuclear Science and Technology. Nucl. Data Sheets. 107, 2931-3060 (2006).

[8] Koning AJ, Rochman D. TENDL-2014: TALYS-based Evaluated Nuclear Data Library. 2014. Available from: ftp://ftp.nrg.eu/pub/www/talys/tendl2014/tendl2014.html.

[9] Kosako K, Murata T, Iwamoto N. Status of new JENDL photonuclear data file. Nuclear Physics and Gamma-Ray Sources for Nuclear Security and Nonproliferation. World Scientific. (eds.) Hayakawa T. *et al.* pp.261-268 (2014).

[10] Murata T, Kosako K, Fukahori T. Renewal of JENDL photonuclear data file 2004. JAEA-Conf 2011-002, pp.235-240 (2011).

[11] Fuller EG, Hayward E. The giant resonance of the nuclear photoeffect. NUCLEAR REACTIONS Vol.II. North-Holland P.C. (eds.) Endt PM, Smith PB. pp.113-194 (1962).

[12] Fukahori T. ALICE-F Calculation of Nuclear Data up to 1 GeV. Proc. of the Specialists' Meeting on High Energy Nuclear Data, Tokai, Japan, 1991, JAERI-M 92-039, pp.114-122 (1992).

[13] Iwamoto O, Iwamoto N, Kunieda S, Minato F, Shibata K, The CCONE code system and its application to nuclear data evaluation for fission and other reactions. Nucl. Data Sheets, 131, 259-288 (2016).

[14] Chadwick MB, Oblozinsky P, Hodgson PE, Reffo G. Pauli-blocking in the quasideuteron model of photoabsorption. Phys. Rev. C44, 814 (1991).

[15] Plujko VA, Ezhov SN, Kavatsyuk MO, Grebenyuk AA, Yermolenko RV. Testing and Improvements of Gamma-Ray Strength Functions for Nuclear Model Calculations. J. Nucl. Sci. Technol. Suppl. 2, 811 (2002).

[16] Capote R, Herman M, Obložinský P, Young PG, Goriely S, Belgya T, Ignatyuk AV, Koning AJ, Hilaire S, Plujko VA, *et al.* RIPL - Reference Input Parameter Library for Calculation of Nuclear Reactions and Nuclear Data Evaluations. Nucl. Data Sheets. 110, 3107-3214 (2009).

[17] Woodworth JG, McNeill KG, Jury JW, Georgopulos PD, Johnson RG. Photoneutron angular distributions from the reaction ^{13}C$(\gamma, n_0)^{12}$C. Nucl. Phys. A327, 53-63 (1979).

[18] Lepretre A, Beil H, Bergere R, Carlos P, Veyssiere A, Sugawara M. The giant dipole states in the $A = 90$ mass region. Nucl. Phys. A175, 609 (1971).

[19] Berman BL. Pywell RE, Dietrich SS, Thompson MN, McNeill KG, Jury JW. Absolute photoneutron cross sections for Zr, I, Pr, Au, and Pb. Phys. Rev. C36, 1286 (1987).

[20] Ishkhanov BS, Kapitonov IM, Piskarev IM, Shevchenko OP. The Photoneutron Cross Sections in Zr^{90}. Yadernaya Fizika. 14, 27 (1971); Soviet J. Nucl. Phys. 14, 16-17 (1972).

12 Production of Radioisotopes for Medical Use and Neutron Induced Nuclear Reaction Data

Yasuki NAGAI
Nuclear Engineering Research Collaboration Center, Japan Atomic Energy Agency,
Tokai-mura, Naka-gun, Ibaraki-ken 319-1195 Japan
e-mail: nagai.yasuki@qst.go.jp

A new production route of radioisotopes by using fast neutrons provided by an accelerator is described by mainly discussing the production of ^{99}Mo used for nuclear medicine diagnosis. Using ~14 MeV neutrons high-quality ^{99}Mo was produced with a minimum level of radioactive wastes without ^{235}U. Neutrons with most probable energy of 14 MeV with an intensity of 10^{14} n/s, necessary to produce a large amount of ^{99}Mo, can be produced by the ^{nat}C(*d,n*) reaction using 40 MeV 5 mA deuterons. A new system has been proposed for the generation of radioisotopes with accelerator neutrons by deuterons (GRAND).

1. Introduction

Many short-lived ($T_{1/2} \leq$ a few days) radioisotopes (RIs) have been used for diagnostic and therapeutic applications in nuclear medicine [1]. Neutron-rich RIs mostly produced in nuclear reactors emit β^--rays and/or γ-rays, radiopharmaceuticals containing these RIs are used to kill cancer cells and to diagnose the dynamics of a medicine in the living body. While, many proton-rich RIs produced using accelerators mostly emit β^+-rays or α-rays. Hence, radiopharmaceuticals containing β^+-rays and α-rays emitting radionuclides are used for diagnostic imaging studies and cancer therapy, respectively.

^{99m}Tc ($T_{1/2}$=6 h), the daughter nuclide of ^{99}Mo ($T_{1/2}$=66 h), is the most common RI used in diagnosis [2]. In Japan, about 0.7 million diagnostic procedures are performed using ^{99m}Tc. ^{99}Mo has been produced mostly by the fission of ^{235}U in foreign research reactors. However, recent ^{99}Mo shortage due to a number of incidents of the reactors stimulated widespread discussions to reliably supply ^{99}Mo worldwide [3]. In fact, a variety of production methods of ^{99}Mo in reactors by the ^{98}Mo$(n,\gamma)^{99}$Mo reaction or ^{99}Mo (and/or ^{99m}Tc) in accelerators by the ^{100}Mo$(p,pn)^{99}$Mo, ^{100}Mo$(d,p2n)^{99}$Mo, and ^{100}Mo$(p,2n)^{99m}$Tc reactions have been studied. In addition, ^{99}Mo productions by the ^{235}U$(n,\text{fission})^{99}$Mo or ^{98}Mo$(n,\gamma)^{99}$Mo reactions using spallation neutrons, and by the ^{238}U(γ,fission)^{99}Mo or ^{100}Mo(γ,n)^{99}Mo reactions have also been proposed. In 2009, we proposed a new route to produce ^{99}Mo by the ^{100}Mo(n,2n)^{99}Mo reaction using neutrons from an accelerator [4].

2. ^{99}Mo (^{99m}Tc) Production Method

Fast neutrons from an accelerator have been used to investigate the neutronics performance in the fusion blanket and components related. However, to the best of our knowledge, the neutrons have not yet been used for producing any radioisotopes, at least for medical use. In Ref. [4] we could show that the neutrons are very useful to produce a large quantity of high-quality ^{99}Mo with a minimum level of radioactive wastes without ^{235}U. In fact, the ^{100}Mo(n,2n)^{99}Mo reaction cross section is quite large ~1.5 barn at $10<E_n<18$ MeV, and the (n,α), (n,$n'p$), and (n,p) reaction the cross sections on ^{100}Mo producing impurity RIs are less than a few mb at E_n~14 MeV. Neutrons of ~14 MeV with an intensity of ~ 10^{11} n/cm^2/s can be produced by the ^{3}H(d,n)^{4}He reaction. A recent progress of accelerator technology can provide neutrons with an intensity of 10^{14} n/s within 20° in forward direction with most probable energy of 14 MeV [5]. They are produced by the ^{nat}C(d,n) reaction using 40 MeV 5 mA deuterons.

We estimated the production yield of ^{99}Mo using the evaluated cross section of ^{100}Mo(n,2n)^{99}Mo of JENDL-4.0 together with the above neutrons, in which we used the latest data on neutrons from ^{nat}C(d,n) at $E_d = 40$ MeV [6]. Note that since the cross section in JENDL-4.0 is up to 20 MeV, the cross section is extended up to neutron energy of 30 MeV with the same inputs as ones adopted in JENDL-4.0. A typical calculated ^{99}Mo yield was 2.7 TBq at the end of irradiation for two days for a metallic ^{100}Mo sample (251 g 100% enriched in ^{100}Mo). About 20-25 % of the ^{99}Mo demand in Japan can be obtained constantly with a single accelerator facility.

In discussing the alternative ^{99}Mo production method, a criterion on the potential for other isotopes co-production at the same time was introduced in the OECD report [7]. It is an important issue in the economic sustainability, demand risk mitigation and the ability to avoid creating other isotope shortage. The co-production of other isotopes is possible in reactors via the fission reaction of ^{235}U, but not in an RI production using charged particles in accelerators. On the contrary, co-production of other radioisotopes is possible using fast neutrons, because the neutron has no charge, the traveling range is much longer than that of a charged particle. It should be also noted that not only the (n,2n) reaction cross section of a neutron-rich nucleus but also the cross section of a charge exchange reaction, such as (n,p) and (n,α), of a sample nucleus with a medium-weight mass (<100) has a sizable cross section of from ~50 to ~500 mb at ~$10<E_n<18$ MeV. Therefore, many carrier-free RIs (without any other isotope of a sample nuclide) can be produced using neutrons from the ^{nat}C(d,n) reaction at $E_d = 40$ MeV. In fact, we have proposed new routes to produce carrier-free medical radioisotopes of ^{90}Y[8], ^{64}Cu, and ^{67}Cu[9] using fast neutrons from an accelerator. Note that a radiopharmaceutical agent (Zevarin®) containing a radionuclide ^{90}Y ($T_{1/2}$=64h) has been used for cancer therapy. ^{67}Cu ($T_{1/2}$=61.8h) is believed to be a promising radionuclide to treat small distant metastases. ^{64}Cu ($T_{1/2}$=12.7h) is a promising radionuclide suitable for labeling many radiopharmaceuticals for PET imaging. Currently, a carrier-free grade of ^{90}Y is imported into Japan. Because of the short half-life of ^{90}Y, the domestic production of ^{90}Y is highly required. In the present study, we estimated the production yield of ^{90}Y via the ^{90}Zr(n,p)^{90}Y reaction using neutrons from the ^{nat}C(d,n) reaction. As for the production of ^{67}Cu, the generally adopted route of ^{64}Cu production is ^{64}Ni(p,n)^{64}Cu. Since the natural abundance of ^{64}Ni is as low as 0.93%, the high price of ^{64}Ni is, however, a major drawback of the ^{64}Cu production route. The ^{68}Zn(p,2p)^{67}Cu reaction is currently used to produce ^{67}Cu. Note that the proton energy used in the ^{68}Zn(p,2p)^{67}Cu reaction is high, a large amount of impurity radionuclide of ^{64}Cu is produced by ^{68}Zn(p,αn)^{64}Cu. We proposed a new route to produce ^{67}Cu with very little radionuclide impurity via the ^{68}Zn(n,x)^{67}Cu reaction, and showed the ^{64}Zn(n,p)^{64}Cu reaction to be a promising route to produce ^{64}Cu, in which we emphasized that both ^{67}Cu and ^{64}Cu can be produced by using fast neutrons.

3. Summary

On the basis of the results mentioned above, a new prototype system for the generation of radioisotopes with accelerator neutrons by deuterons (GRAND) has been proposed [10]. The system consists of an azimuthally variable field (AVF) cyclotron with a carbon converter to produce intense accelerator neutrons with a most probable energy of 14 MeV. The system has unique features in the production of a wide variety of radioisotopes, including ^{99}Mo, useful for nuclear medicine diagnosis procedures. High-quality radioisotopes can be produced continuously using fast neutrons from an accelerator with a minimum level of radioactive waste, and without using uranium. The system has a potential for the co-production of other radioisotopes at the same time. The proposed system is compact in size, and easy to operate, and therefore could be used in many countries for medical radioisotopes production.

Acknowledgements

I thank N. Iwamoto, O. Iwamoto, F. Minato, S. Shibata for their useful discussions. This work was supported by a Grant-in-Aid for Specially Promoted Research from the Japan Ministry of Education, Culture, Sports, Science, and Technology (23000005) and in part by the Adaptable and Seamless Technology Transfer Program through Target-driven R&D (A-STEP) of the Japan Science and Technology Agency (JST).

References

[1]Report by Science Council of Japan (July 24, 2009) [in Japanese].

[2]F. F. Knapp, Jr. and S. Mirzadeh: Eur. J. Nucl. Med. 21 (1994) 1151.

[3]K. Bertsche: Proceedings of IPAC'10, Kyoto, Japan. (2010) 121.

[4]Y. Nagai and Y. Hatsukawa: J. Phys. Soc. Jpn. 78 (2009) 033201.

[5]O. Alyakrinskiya *et al*,: Nucl. Instr. Meth. A **578** (2007) 357.

[6]F. Minato and Y. Nagai: J. Phys. Soc. Jpn. 79 (2010) 093201.

[7]The supply of Medical Radioisotopes: Report by Nuclear Energy Agency June 2011.

[8]Y. Nagai *et al.*: J. Phys. Soc. Jpn. 78 (2009) 113201.

[9]T. Kin *et al.*: J. Phys. Soc. Jpn. 82 (2013) 034201.

[10] Y. Nagai *et al.*: J. Phys. Soc. Jpn. 82 (2013) 064201.

13 Overview of the PHITS code and application to nuclear data

- Radiation damage calculation for materials -

Yosuke IWAMOTO[1*], Tatsuhiko SATO[1], Koji NIITA[2], Shintaro HASHIMOTO[1],
Tatsuhiko OGAWA[1], Takuya FURUTA[1], Shinichiro ABE[1], Takeshi KAI[1], Norihiro MATSUDA[1],
Hiroshi IWASE[3], Hiroshi NAKASHIMA[1], Tokio FUKAHORI[1], Keisuke OKUMURA[1],
Tetsuya KAI[1], and Lembit SIHVER[4]

[1]*Japan Atomic Energy Agency, Shirakata 2-4, Tokai, Ibaraki, 319-1195, Japan;*
[2]*Research Organization for Information Science and Technology, Shirakata 2-4, Tokai, Ibaraki, 319-1106, Japan;*
[3]*High Energy Accelerator Research Organization, Oho 1-1, Tsukuba, Ibaraki, 305-0801, Japan;*
[4]*Atominstitut, TU Wien, Stadionallee 2, 1020 Vienna, Austria;*
[*]E-mail: iwamoto.yosuke@jaea.go.jp

A general purpose Monte Carlo Particle and Heavy Ion Transport code System, PHITS, is being developed through the collaboration of several institutes in Japan and Europe. PHITS can deal with the transport of nearly all particles, including neutrons, protons, heavy ions, photons, and electrons, over wide energy ranges using various nuclear reaction models and data libraries. All components of PHITS such as its source, executable and data-library files are assembled in one package. More than 2,000 researchers have been registered as PHITS users, and they apply the code to various research and development fields such as nuclear technology, accelerator design, medical physics, and space science.

This report briefly summarizes the physics models implemented in PHITS, and introduces the new event generator mode. We will also present the radiation damage data for materials such as the energy spectra for the Primary Knock-on Atoms (PKA) and the Kinetic Energy Released per unit MAss (KERMA) factors calculated by the new event generator mode under the IAEA-CRP activity titled “Primary radiation damage cross section (2013-2017).”

1. Introduction

Particle and Heavy Ion Transport code System, PHITS [1], is one of the most successful Monte Carlo particle transport simulation codes that are widely used in all over the world. It can deal with the transport of nearly all particles, including neutrons, protons, heavy ions, photons, and electrons, over wide energy ranges using various nuclear reaction models and data libraries. PHITS is written in Fortran language, and is originally derived from the NMTC/JAM code [2]. The source files of PHITS can be compiled using Intel Fortran (11.1 or later versions) or GFortran (4.7 or 4.8 version). The platforms on which PHITS can be executed are Windows, Mac and Linux. Distributed and shared memory parallelization techniques are available using MPI protocols and OpenMP directives, respectively. Hybrid parallelization using both MPI and OpenMP is also feasible [3]. Various quantities, such as heat deposition, track length, and production yields, can be deduced from the PHITS simulation using implemented "tally" estimator functions. Estimation of the time evolution of radioactivity has become feasible after the realization of version 2.52 owing to the incorporation of an activation calculation program DCHAIN-SP [4] into the PHITS package. This report briefly summarizes the physics models implemented in PHITS, and introduces the radiation damage calculations using the event generator mode.

2. Brief summary of physics models and the event generator mode

Figure 1 summarizes the physics models recommended for use in PHITS for simulating nuclear and atomic collisions. The intra-nuclear cascade models JAM [5] and INCL4.6 [6] and the quantum molecular dynamics model JQMD [7, 8] are generally employed for simulating the dynamic stage of nuclear reactions induced by hadrons and nucleus, respectively. On the other hand, the evaporation and fission model GEM [9] are adopted for simulating their static stage. The statistical multi-fragmentation model SMM [10] can be optionally activated before the simulation of GEM. The energy losses of charged particles, except for electrons, are calculated using the SPAR [11] or ATIMA [12] codes with the continuous slowing down approximation. The generation of knocked-out electrons, so-called δ-rays, around the trajectory of a charged particle can be explicitly considered. Nuclear and atomic data libraries are generally used for simulating low-energy neutron-induced nuclear reactions and photo- and electro-atomic interactions, respectively. Photons, electrons and positions are transported using the algorithm and database of the Electron Gamma Shower Version 5 (EGS5 [13]). Photo-nuclear reactions can be treated below 1 TeV.

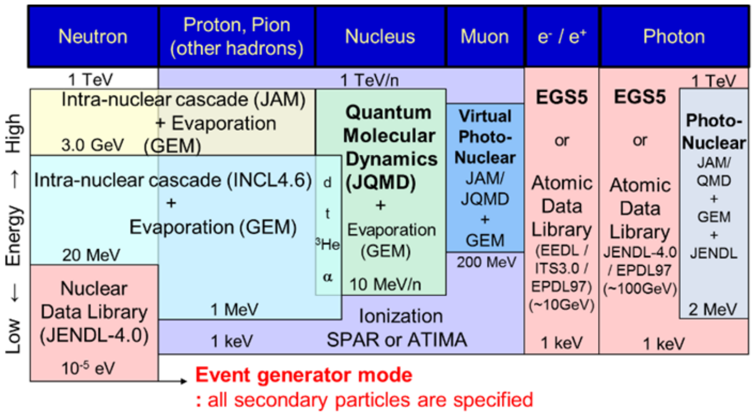

Figure 1 Physics models recommended for use in PHITS for simulating nuclear and atomic collisions

The highest energy of particles recommended to be simulated using PHITS is 1 TeV (per nucleon for ions). Note that PHITS can deal with the transport of particles above 1 TeV, but the accuracy of simulations for such high-energy particles has not been verified. On the other hand, the lowest particle energy that can be simulated using PHITS is 1 keV, except for neutrons, because the continuous slowing down approximation cannot be applied to the transport simulation of charged particles below this energy. For neutrons, PHITS can handle transport down to 10^{-5} eV using the neutron data library. PHITS implements some unique functions such as event generator mode [14,15], beam transport function, microdosimetric function [16] and DPA calculation function [17]. The important function for low-energy neutron interaction is an event generator mode. Most nuclear reaction models, such as the intra-nuclear cascade model, are “event generators,” but Monte Carlo simulations using nuclear data libraries are generally “non-event generators,” because only inclusive cross-section data are contained in the libraries. It is occasionally necessary to estimate the distribution around the mean value, such as for the response function of detectors and the soft-error rates of semiconductor devices. Based on these considerations, we implemented a unique “event generator mode” in PHITS for simulating low-energy neutron-induced reactions using nuclear data libraries. **Figure 2** shows an overview of an event generator mode for the new version (e-mode=2) [15].

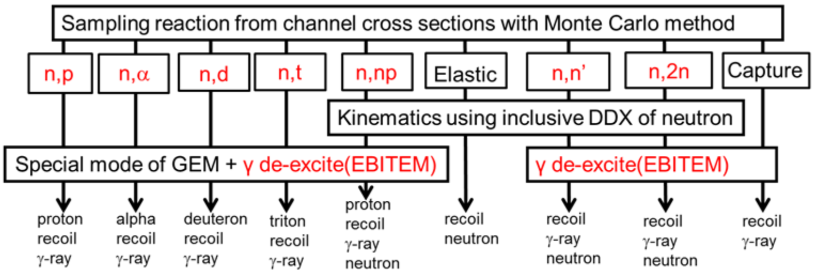

Figure 2 Overview of the event generator mode for the new version (e-mode=2).

Firstly, the neutron incident reaction with the specific energy is sampled by the Monte Carlo method with the channel cross sections in the evaluated nuclear data library. The new version of the event generator mode can treat not only elastic, capture and (n, Nn’) cross sections implemented in the old version (e-mode=1) but also the channel cross sections for the charged particle emissions such as (n,p), (n,α), (n,d), (n,np) cross sections. When neutron emission channels and elastic scatterings are selected, the double differential cross sections of outgoing neutrons are used to determine the energy, momentum and the scattering angle of emitted neutron and recoils. When the capture reaction and charged particle emissions are selected, the excitation energy and momentum of residual nucleus are determined uniquely from the incident energy of neutron and target nucleus. For the decay process of this excited nuclei, the special statistical decay plus gamma de-excitation model (EBITEM) [18] implemented in the new version is applied to emit particles except for neutrons. All information of ejectiles such as charged particles, photon and residual nucleus can be determined. By these processes, a low energy neutron collision is treated as an “event”, which means the energy and momentum are conserved in an event.

3. Radiation damage calculations under the IAEA-CRP activities 2013-2017

For the evaluation of the radiation damage evaluation, uncertainties are needed for the PKA spectra and the KERMA factors. The PKA spectra are the starting point for the consequent damage energy and displacement cross sections calculations. The KERMA factors are related with the integration of the total energy of the PKA. However, the PKA spectra and the KERMA factors derived from the main evaluated neutron cross section libraries are different. Although the NJOY code [19] is used as the standard method for calculations, the accuracy of the code has not been investigated [20]. Under the IAEA-CRP activities for the radiation damage evaluation [20], we investigated the PKA spectra and the KERMA factors calculated with different process steps (PHITS Event Generator mode (PHITS-EG) and NJOY-SPKA) and different ACE libraries (JENDL-4.0 and ENDF/B-VII.1) [21]. PHITS-EG can determine all ejectiles with keeping energy and momentum conservation described in section 2. On the other hand, the PKA spectra and the KERMA factors are available in the evaluated cross section files and could be derived or calculated by the NJOY code. The SPKA code [22] was used to read the NJOY output files for the further processing of PKA data.

Figure 3 shows the PKA spectra for interactions of neutrons with ^{56}Fe at the incident neutron energies of 5 and 14.5 MeV calculated using different data processing and libraries. Calculated results by SPKA-JENDL-4.0 (dashed red line) disagree with others due to lack of the PKA matrixes in JENDL-4.0. On the other hands, there are good agreements among the different process steps except for SPKA-JENDL-4.0.

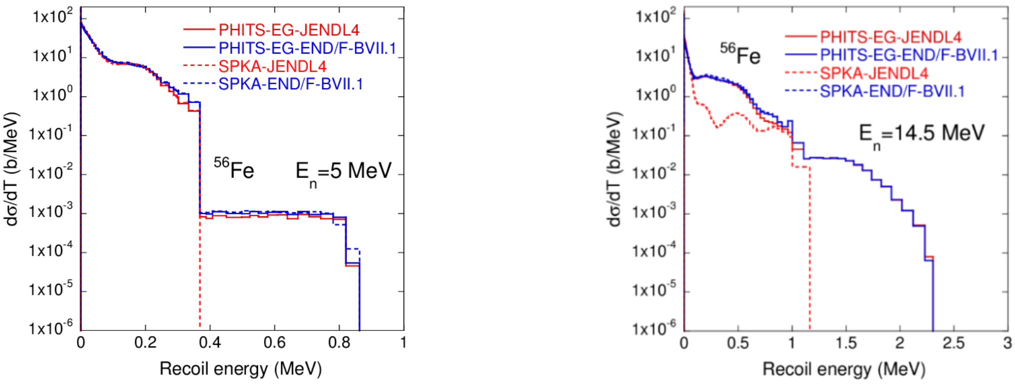

Figure 3 PKA spectra for interactions of 5 and 14.5 MeV neutrons with ^{56}Fe calculated using different data processing and libraries.

Figure 4 shows the heating numbers related with the KERMA factors for ^{40}Ca and ^{208}Pb with energy range between 10^{-10} and 20 MeV (solid red line for EG-JENDL-4 and solid blue line for EG-ENDF/B-VII.1). The heating numbers are also taken from the ACE files of JENDL-4.0 (dashed red line) and the ENDF/B-VII.1 (dashed blue line). The disagreement results from the difference of the (n, α) cross sections between JENDL-4 and ENDF/B-VII.1. The (n, α) cross section of ^{40}Ca in JENDL-4.0 is zero below 0.1 MeV, but that in ENDF/B-VII.1 increases with decreasing the neutron energy. The difference of the (n, α) cross sections for ^{208}Pb was also observed in libraries. Therefore, the evaluation of the (n,α) reactions should be re-evaluated to improve the KERMA factors for ^{40}Ca and ^{208}Pb.

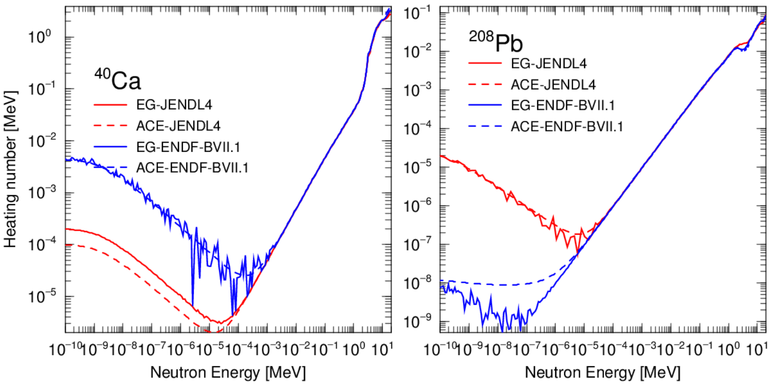

Figure 4 Heating numbers related with the KERMA factors for ^{40}Ca and ^{208}Pb.

4. Summary

The PHITS can analyze the motion of nearly all particles over wide energy ranges and implements sophisticated nuclear reaction models and data libraries, and some unique functions such as event generator mode, beam transport function, and microdosimetric function. Owing to these features, PHITS has been used by more than 2,000 users in various research fields. Recently, new functions such as the nuclear resonance fluorescence model, the tetrahedral mesh geometry (a type of polygon mesh geometry) and the point estimator have been implemented in the version 2.82. We are planning to implement the JENDL-4.0/HE data library evaluated for neutron and proton incident reactions with energies up to 200 MeV in the PHITS package and to improve user support functions using a Graphical User Interface (GUI).

Under the activities in the IAEA-CRP activity for the radiation damage evaluation, we investigated the PKA spectra and the KERMA factors calculated with different process steps (PHITS-EG and NJOY-SPKA) and different ACE libraries (JENDL-4.0 and ENDF/B-VII.1). We will continue the intercomparison of radiation damage data using the different processes and the different data libraries and contribute the IAEA publication of the numerical database for the displacement cross sections, the PKA spectra and the KERMA factors.

Acknowledgment

The development and distribution of PHITS have been greatly supported by the Center for Computational Science & e-Systems of JAEA. We thank our colleagues at Kyushu University, RIKEN, CEA/Saclay, and JAXA for their supports under the collaboration contracts between JAEA and each institute.

References

[1]Sato T, Niita K, Matsuda N, Hashimoto S, Iwamoto Y, Noda S, Ogawa T, Iwase H, Nakashima H, Fukahori T, Okumura K, Kai T, Chiba S, Furuta T, Sihver L. Particle and heavy ion transport code system PHITS, version 2.52. J Nucl Sci Technol. 2013;50:913-923.

[2] Niita K, Takada H, Meigo S, Ikeda Y, High-energy particle transport code NMTC/JAM. Nucl Instruments Methods B. 2001;184:406-420.

[3] Furuta T, Ishikawa K.L, Fukunishi N, Noda S, Takagi S, Maeyama T, Fukasaku K, Himeno R. Implementation of OpenMP and MPI hybrid parallelization to Monte Carlo dose simulation for particle therapy. IFMBE Proceedings, 2012;39:2099-2102.

[4] Kai T, Maekawa F, Kosako K, Kasugai Y, Takada H, Ikeda Y. DCHAIN-SP 2001: High energy particle induced radioactivity calculation code. JAERI-Data/Code 2001-016, 2001. [in Japanese]

[5] Nara Y, Otuka H, Ohnishi A, Niita K, Chiba S. Relativistic nuclear collisions at 10A GeV energies from p+Be to Au+Au with the hadronic cascade model. Phys Rev C. 2000;61:024901.

[6] Boudard A, Cugnon J, David J.C, Leray S, Mancusi D. New potentialities of the Liege intranuclear cascade model for reactions induced by nucleons and light charged particles. Phys Rev C. 2013;87:014606.

[7] Niita K, Chiba S, Maruyama T, Maruyama T, Takada H, Fukahori T, Nakahara Y, Iwamoto A. Analysis of the (N,Xn') reactions by quantum molecular-dynamics plus statistical decay model. Phys Rev C. 1995;52:2620-2635.

[8] Ogawa T, Sato T, Hashimoto S, Satoh D, Tsuda S. Energy-dependent fragmentation cross sections of relativistic ^{12}C. Phys Rev C. 2015;92:024614.

[9] Furihata S. Statistical analysis of light fragment production from medium energy proton-induced reactions. Nucl Instruments Methods B. 2000;171:251-258.

[10] Ogawa T, Sato T, Hashimoto S, Niita K. Analysis of multi-fragmentation reactions induced by relativistic heavy ions using the statistical multi-fragmentation model. Nucl Instruments Methods A. 2013;723:36-46.

[11] Armstrong T.W, Chandler K.C. SPAR, a FORTRAN program for computing stopping powers and ranges for muons, charged pions, protons and heavy ions. 1973; ORNL-4869.

[12] Geissel H, Scheidenberger C, Malzacher P, Kunzendorf J, Weick H. ATIMA. GSI. Aveiravle from: http://web-docs.gsi.de/~weick/atima/

[13] Hirayama H, Namito Y, Bielajew A.F, Wilderman S.J, Nelson W.R. The EGS5 code system. 2005; SLAC-R-730 and KEK Report 2005-8.

[14] Niita K, Iwamoto Y, Sato T, Matsuda N, Sakamoto Y, Nakashima H, Iwase H, Shiver L. Event generator models in the particle and heavy ion transport code system; PHITS. J. Korean. Phys. Soc. 2011;59:827-832.

[15] Ogawa T, Sato T, Hashimoto S, Niita K. Development of a reaction ejectile sampling algorithm to recover kinematic correlations from inclusive cross-section data in Monte-Carloparticletransportsimulations. Nucl Instruments Methods A. 2014;763:575-590.

[16] Sato T, Kase K, Watanabe R, Niita K, Sihver L. Biological dose estimation for charged-particle therapy using an improved PHITS code coupled with a microdosimetric kinetic model. Radiat. Res. 2009;171:107-117.

[17] Iwamoto Y, Niita K, Sawai T, Ronningen RM, Baumann T. Displacement damage calculations in PHITS for copper irradiated with charged particles and neutrons. Nucl Instruments Methods B. 2013;303:120–124.

[18] Ogawa T, Hashimoto S, Sato T, Niita K. Development of gamma de-excitation model for prediction of prompt gamma-rays and isomer production based on energy-dependent levelstructure treatment. Nucl Instruments Methods B. 2014;325:35-42.

[19] MacFarlane RE, Muir D. W, Boicourt RM, Kahler AC. The NJOY Nuclear Data Processing System,Version 2012. LA-UR-12-27079 Rev. Available from http://t2.lanl.gov/nis/codes/NJOY12/.

[20] Stoller RE, Greenwood L.R, Simakov SP. (Eds). Summary Report of the First Research Coordination Meeting on Primary Radiation Damage Cross Sections IAEA International Nuclear Data Committee, November 4 - 8, 2013, IAEA Headquarters, Vienna, Austria, INDC(NDS)-0648, 2013, 62p.

[21] Iwamoto Y. Calculations of PKA spectra and kerma factors using PHITS code and measurement of displacement cross section of copper irradiated with 125 MeV protons. Summary Report of the First Research Coordination Meeting on Primary Radiation Damage Cross Sections IAEA International Nuclear Data Committee, June 29 - July 2, 2015, IAEA Headquarters, Vienna, Austria, INDC(NDS)-0691, 2015, pp.22-27.

[22] Simakov SP. SPKA code, FZK, 2007. Available from https://www-nds.iaea.org/CRPdpa/.

14 Neutronics study of Transmutation Experimental Facility at J-PARC

Hiroki IWAMOTO
J-PARC Center, Japan Atomic Energy Agency
2-4, Shirakata, Tokai-mura, Naka-gun, Ibaraki 319-1195, Japan
e-mail: iwamoto.hiroki@jaea.go.jp

Abstract

To promote research, development, and demonstration of elemental technologies for accelerator-driven systems (ADSs), the Japan Atomic Energy Agency (JAEA) has a plan to construct Transmutation Experimental Facility (TEF) at J-PARC, where various experiments will be conducted. The TEF is divided into two facilities according to their own objectives; the Transmutation Physics Experimental Facility (TEF-P) and the ADS Target Test Facility (TEF-T). The objective of TEF-P is to conduct various reactor-physics experiments with minor-actinide (MA) fuel, and that of TEF-T is to perform irradiation tests using various candidate materials installed in a lead-bismuth eutectic (LBE) target by injecting a 400-MeV proton beam under the condition of LBE flow and thermal field. This report describes the preliminary results on TEF-P and TEF-T.

Keywords: *Transmutation Experimental Facility, J-PARC, accelerator-driven system, nuclear-data-induced uncertainty, cross-section adjustment method, irradiation field*

1 Introduction

To promote research, development, and demonstration of elemental technologies for accelerator-driven systems (ADSs), the Japan Atomic Energy Agency (JAEA) has a plan to construct Transmutation Experimental Facility (TEF) at J-PARC and to conduct various experiments on the transmutation technology. The TEF is divided into two facilities according to their own objectives; the Transmutation Physics Experimental Facility (TEF-P) and the ADS Target Test Facility (TEF-T). The objective of TEF-P is to conduct various reactor-physics experiments with minor-actinide (MA) fuel, and that of TEF-T is to perform irradiation tests using candidate materials installed in a lead-bismuth eutectic (LBE) target by injecting a 400-MeV proton beam under the condition of LBE flow and thermal field. In this report, the effect of the TEF-P reactor-physics experiments on the ADS nuclear characteristics is explained by using the cross-section adjustment method. Also, examples of the TEF-T neutron irradiation field are presented briefly.

2 Effect of experiments with TEF-P

2.1 Uncertainty reduction by the cross-section adjustment method

Since a detailed description of the cross-section adjustment method is given in the literature[1], a brief description is provided here. The posterior matrix $\mathbf{P}$ can be expressed as

$$\mathbf{P} = \mathbf{M} - \mathbf{M}\mathbf{G}^{\mathrm{T}} \left(\mathbf{G}\mathbf{M}\mathbf{G}^{\mathrm{T}} + \mathbf{V}\right)^{-1} \mathbf{G}\mathbf{M}, \tag{1}$$

where $\mathbf{M}$ is a prior covariance matrix, which corresponds to the JENDL-4.0 covariance data, $\mathbf{G}$ and $\mathbf{M}$ denote a sensitivity coefficient matrix and an experimental uncertainty matrix for a series of reactor-physics experiments, respectively. Multiplying Eq. (1) by the ADS sensitivity matrix $\mathbf{G}_{\mathrm{ADS}}$, which was obtained in

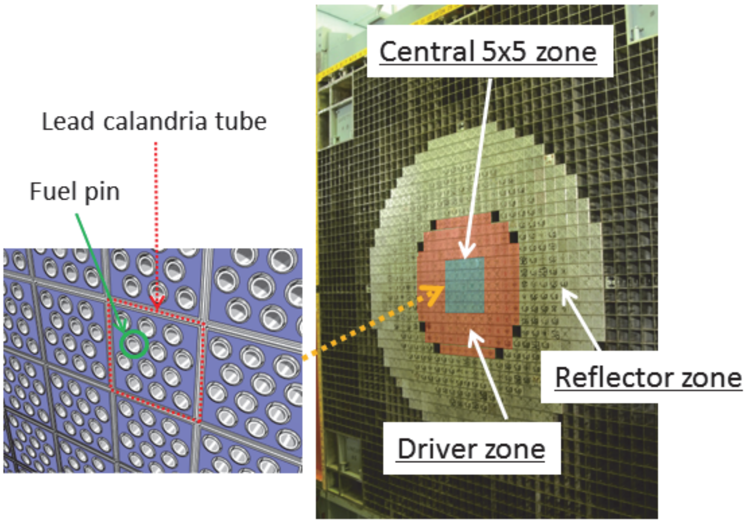

Figure 1: Image of TEF-P core.

a previous work [2, 3], from the left and right sides, the ADS uncertainty after adjustment, $U_{\mathrm{ADS}}^{\mathrm{after}}$, is given by

$$\begin{aligned} U_{\mathrm{ADS}}^{\mathrm{after}} &= \mathbf{G}_{\mathrm{ADS}}\mathbf{P}\mathbf{G}_{\mathrm{ADS}}^{\mathrm{T}} \\ &= \mathbf{G}_{\mathrm{ADS}}\mathbf{M}\mathbf{G}_{\mathrm{ADS}}^{\mathrm{T}} - \mathbf{G}_{\mathrm{ADS}}\mathbf{M}\mathbf{G}^{\mathrm{T}}\left(\mathbf{G}\mathbf{M}\mathbf{G}^{\mathrm{T}}+\mathbf{V}\right)^{-1}\mathbf{G}\mathbf{M}\mathbf{G}_{\mathrm{ADS}}^{\mathrm{T}} \\ &= U_{\mathrm{ADS}}^{\mathrm{before}} - \Delta U_{\mathrm{ADS}}, \end{aligned} \tag{2}$$

where $U_{\mathrm{ADS}}^{\mathrm{before}}$ is the ADS uncertainty before adjustment and ΔU_{ADS} is the reduction of ADS uncertainty. By using Eq. (2), the effect of the experiments with TEF-P can be estimated from the viewpoint of the uncertainty induced by nuclear data.

2.2 Calculation conditions

The analyses were performed using a reactor physics calculation code system, MARBLE, which is a framework system based on the deterministic models [6]. Here, the JENDL-4.0 nuclear data library [4] with 70-energy-group structure was employed for the analyses. The JENDL-4.0 covariance data were processed to 70-energy-group with NJOY [5]. The experiments were assumed to be conducted using TEF-P, whose structure is based on the Fast Critical Assembly (FCA). The image of TEF-P core is illustrated in Figure 1. In the central 5×5 zone, a lead calandria tube cased with stainless steel is inserted in each grid tube, and a mixed MA and Pu fuel pin is loaded in each guide hole in the calandria tube. Here, it was assumed that the fuel component was the same as the real ADS except for curium isotopes, the amount of loaded MA was ∼30 kg, and the number of fuel pins was 600.

In this study, we assumed five kinds of experiments, *i.e.*, totally 23 experiments, as listed in Table 2.1. The sensitivity matrix of the series of experiments, $\mathbf{G}$, was calculated by the sensitivity analysis code based on the perturbation theory, SAGEP [7], which is implemented in MARBLE. The experimental uncertainty $\mathbf{V}$ was deduced from the experience of similar experiments conducted at FCA. Here, the ADS target parameters are prodigality and coolant void reactivity.

2.3 Results and discussion

Figure 2 shows a breakdown of the uncertainty in criticality. From the result of the cross-section adjustment, it was found that, by conducting the all assumed experiments listed in Table 2.1, the total criticality

Table 2.1: Assumed experiments

Experiments	
Criticality experiment	build a critical core
Reaction rate ratio experiment	measure reaction rate ratios to ^{239}Pu fission **case:** capture–^{237}Np, ^{241}Am, fission–^{237}Np, ^{241,242m,243}Am, ^{238,240,241,242}Pu,^{244}Cm
Sample reactivity experiment	measure a sample reactivity worth **case:** ^{237}Np, ^{241,242m,243}Am, ^{240}Pu
Void reactivity experiment	measure a lead-void reactivity worth **case:** 3×3×15 cm, 3×3×30 cm, 3×3×45 cm voided
Fuel reactivity experiment	measure a fuel reactivity worth **case:** 1×1 (24 pins), 3×3 (216 pins), 5×5 (600 pins) removed

uncertainty of 1.0%, is reduced to 0.4% and the contributions of MA and Pu, which are main contributors, are significantly reduced. Here, some specific reaction contributions after adjustment become negative owing to the correlation of other reactions. Figure 3 shows a breakdown of the uncertainty in coolant void reactivity. As expected, the total coolant void reactivity uncertainty of 9.4% is dominated by the coolant material (*i.e.*, Pb and Bi), and the contributions of lead isotopes are reduced by conducting the assumed experiments. In this analysis, the use of ^{209}Bi was not considered for the experiments because of the difficulty in the treatment of LBE. Therefore, the contributions of ^{209}Bi are not reduced at all. This indicates that, to reduce this contribution, it is necessary to perform experiments using ^{209}Bi. More details on the results and discussion can be found in Ref. [8].

3 TEF-T irradiation field

In this section, the irradiation characteristics of TEF-T are briefly presented. The calculations were performed by the Monte Carlo particle transport code, PHITS [9]. A 250 kW proton beam accelerated by a 400-MeV accelerator is directed to the LBE target, where intense spallation neutrons and spallation products (SPs) are produced. As shown in Figure 4, unique neutron spectra ranging from 10^0 to 10^8 eV are expected to be obtained around the target. To make the best use of neutron fluxes for various purposes, we are considering that two pieces of apparatus, namely, a pneumatic tube and a neutron beam port are installed about 30 cm away and 650 cm away from the LBE target, respectively. As an example of the use of the neutron beam port, Figure 5 compares the neutron spectra with different experimental facilities [10, 11]. TEF-T is expected to provide neutron spectrum to users more intense than other facilities. Figure 6 illustrates a preliminary PHITS calculation model of TEF-T, including the neutron beam port. Here, the thickness of iron shielding around the target, which is 3 m thick, was optimized so that users can constantly access the multipurpose-use hall.

4 Summary and perspective

In this report, recent results of TEF were reviewed. Our future perspectives on the TEF construction are summarised as follows:

- Concrete design is in progress. A technical design report of TEF-T will be published in the near future.

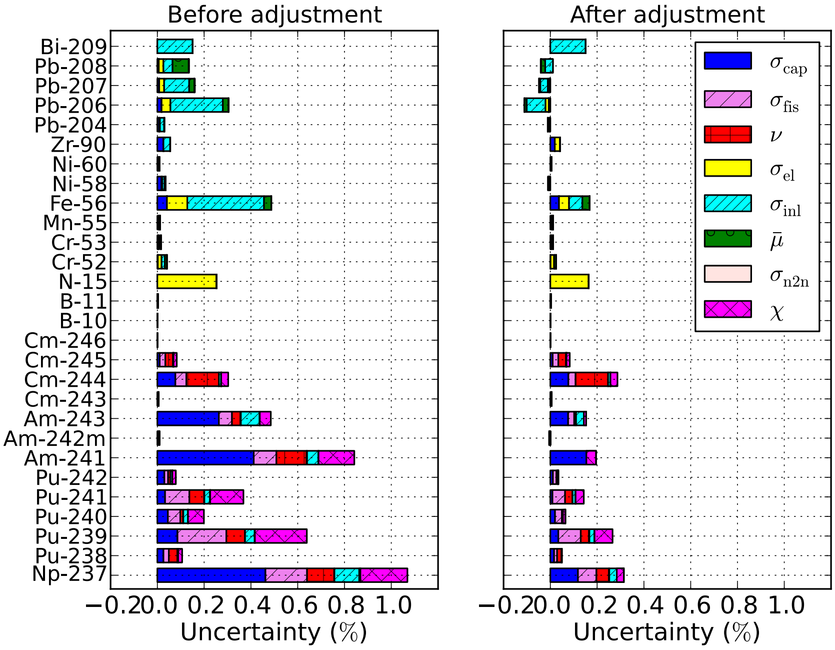

Figure 2: Breakdown of the criticality uncertainty before and after adjustment.

- From the viewpoint of the neutronics design, the treatment of MA fuel that generates radiation and nuclear heat and the SPs produced from the LBE target are the most challenging issues.
- A possibility to provide general-purpose spallation-neutron fields and a branched proton beam to a specific scientific program is under consideration.

References

[1] NEA/WPEC-26, ISBN 978-92-64-99053-1, (2008).

[2] H. Iwamoto, *et al.*, *J. Nucl. Sci. Technol.*, 50 (8), pp.856–862 (2013).

[3] H. Iwamoto, *et al.*, *Nucl. Data Sheets*, 118, pp.519–522 (2014).

[4] K. Shibata, *et al.*, *J. Nucl. Sci. Technol.* 48(1), pp.1–30 (2011).

[5] http://t2.lanl.gov/nis/codes/njoy99/index.html

[6] K. Yokoyama, *et al.*, Proceedings of PHYSOR2008 (CD-ROM), Interlaken, Switzerland (2008).

[7] A. Hara, *et al.*, JAERI-M 84-027 (1984).

[8] H. Iwamoto, *et al.*, JAEA-Research 2014-033 (2015).

[9] T. Sato, *et al.*, J. Nucl. Sci. Technol. 50:9, 913–923 (2013).

[10] Y. Iwamoto, *et al.*, *Nucl. Technol.*, 173 (2), pp.210–217 (2011).

[11] JEDEC Standard, JESD89A, (2006).

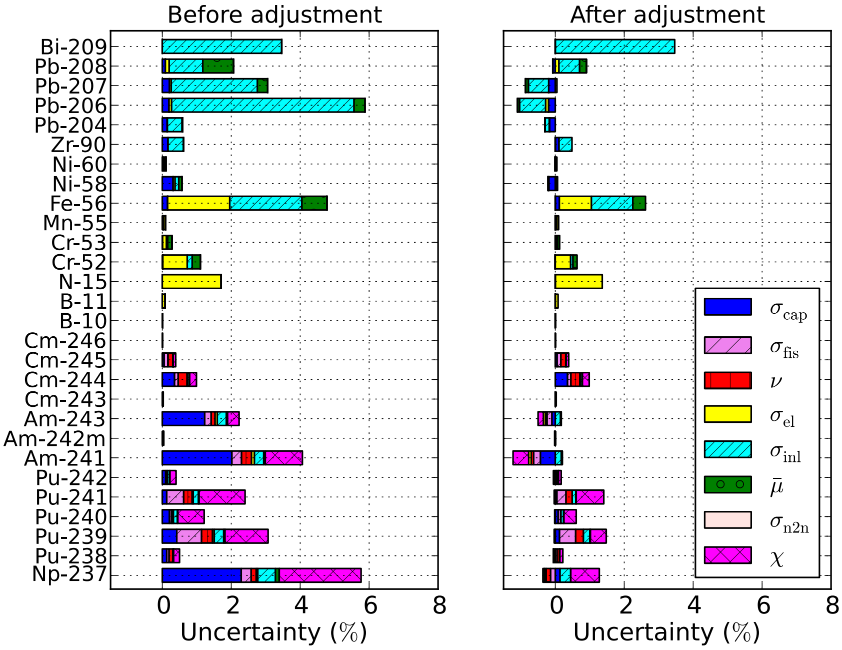

Figure 3: Breakdown of the coolant void reactivity uncertainty before and after adjustment.

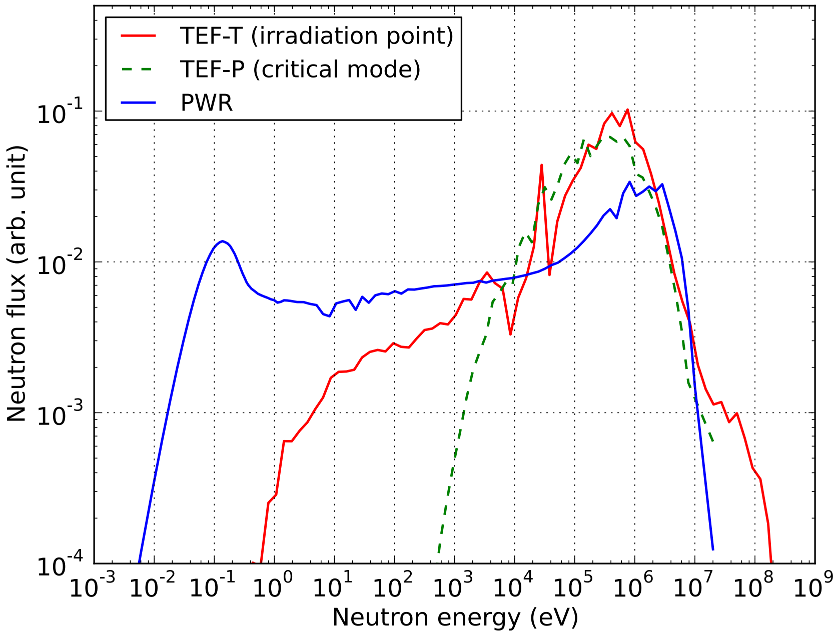

Figure 4: Comparison of neutron spectra.

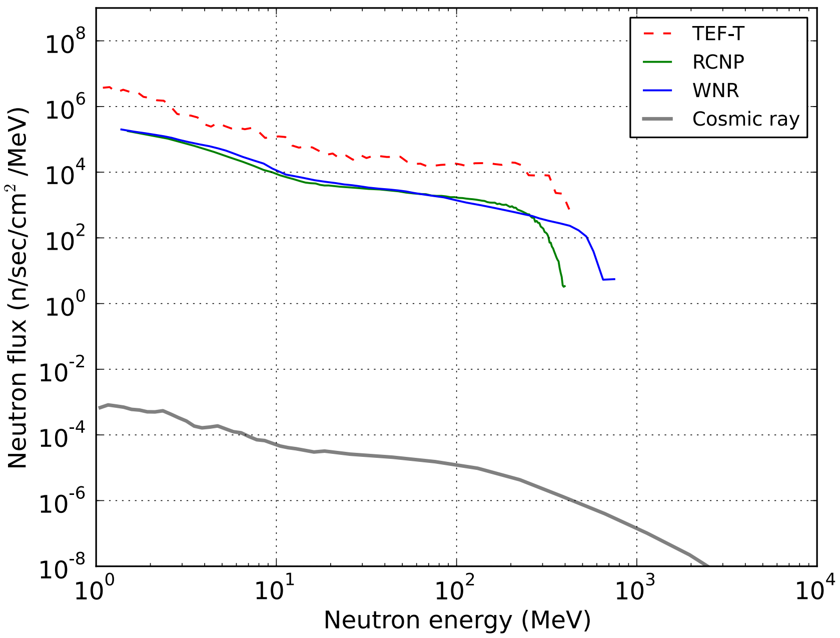

Figure 5: Comparison of neutron spectra.

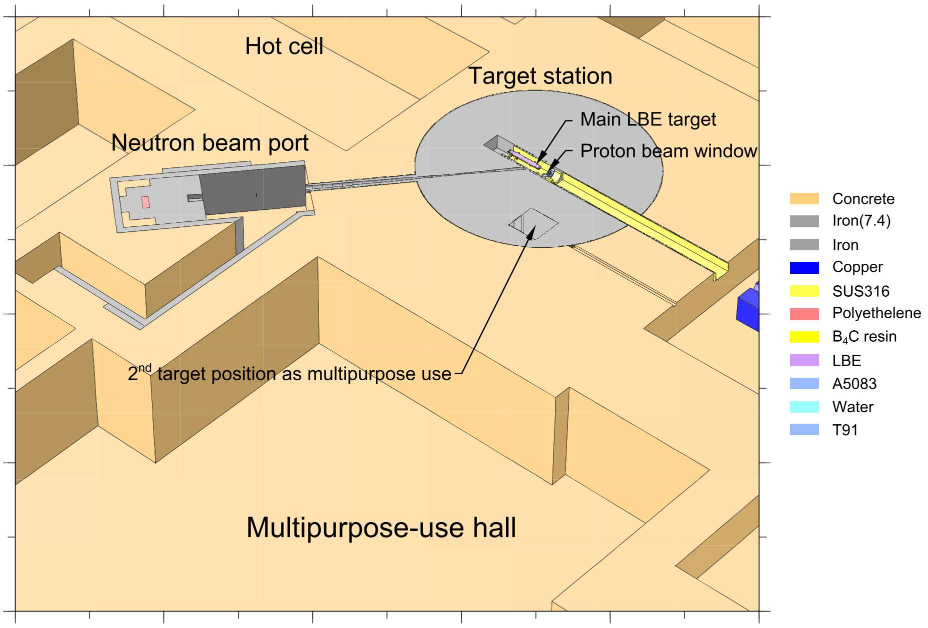

Figure 6: Preliminary PHITS calculation model.

15 Interaction cross sections using thick-target transmission method

Masayuki Aikawa[1], Shuichiro Ebata[1], Shotaro Imai[2]
[1] Faculty of Science, Hokkaido University, Sapporo 060-0810, Japan
[2] Institute for the Advancement of Higher Education, Hokkaido University, Sapporo 060-0817, Japan
e-mail: aikawa@sci.hokudai.ac.jp

The excitation functions of interaction cross sections are important for applications. The data of radioactive isotopes are few and insufficient since a huge experimental effort is required at each energy. We therefore proposed the thick-target transmission (T3) method to obtain the excitation functions of the interaction cross sections. The T3 method consists of iterative measurements of beam attenuations with only changing target thicknesses and no readjusting beam settings. In this paper, we perform a simulation of the ^{135}Cs-induced reaction on ^{12}C for interaction cross sections which are equivalent to inclusive cross sections for transmutation of nuclear wastes. The result shows that the T3 method seems to work well in real experiments.

An interaction cross section gives us valuable knowledge for nuclear radii in nuclear physics [1,2,3] and transmutation of nuclear wastes in nuclear engineering. Its excitation function is thus important, however the data of radioactive isotopes are few and insufficient since a huge experimental effort is necessary. Therefore, we proposed the thick-target transmission (T3) method to obtain the excitation functions of the interaction cross sections [4].

The T3 method can derive the excitation function through iterative measurements of beam attenuations with different target thicknesses. As shown in **Fig. 1 (a)** and **(b)**, we can measure the numbers of transmitted particles $N_{\mathrm{i}}(L+\Delta L)$ and $N_{\mathrm{i}}(L)$ at the downstream of the targets with thicknesses $L+\Delta L$ and L. From the two measurements, similar to the ordinary transmission method, the interaction cross section σ_I can be derived as

$$\sigma_I(L) = -\frac{1}{n_T \Delta L} \ln\left(\frac{N_{\mathrm{i}}(L+\Delta L)}{N_{\mathrm{i}}(L)}\right), \qquad (1)$$

where n_T is the number density of the target. In other words, $N_{\mathrm{i}}(L)$ passed through the moderator with the thickness L is available as a beam on the reaction target of the thickness ΔL as shown in **Fig. 1 (c)**. We performed a simulation with the Particle and Heavy Ion Transport code System (PHITS) [5] for the interaction cross sections of ^{135}Cs on ^{12}C. The cross sections are equivalent to inclusive cross sections of ^{12}C- induced transmutation reaction on ^{135}Cs.

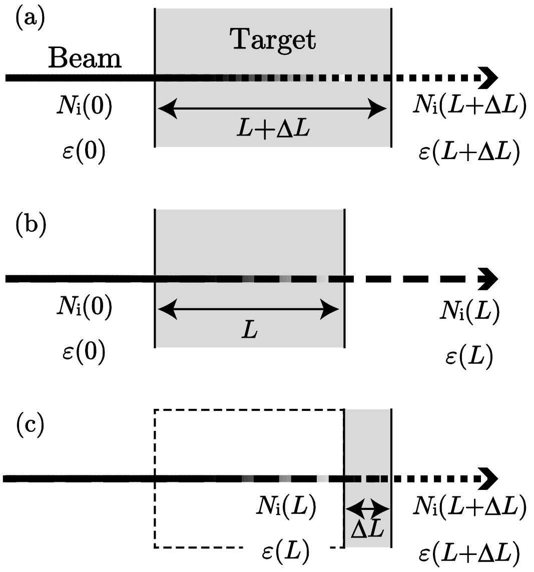

Fig. 1 Schematic of beam attenuations in the targets of the thicknesses (a) $L + \Delta L$ and (b) L. From the two cases, we can derive (c) the beam attenuation in the target ΔL.

Table 1 Simulation Parameters

Projectile	^{135}Cs	
Energy	100 MeV/nucleon	
Target	^{12}C	
Density	2.260 g/cm^3	
Foil thickness	0.02 cm	($0 \leq L \leq 0.16$ cm)
	0.004 cm	($0.16 \leq L \leq 0.2$ cm)
Trial number	10^5	

The parameters adopted in the simulation are listed in **Table 1**. Calculations with different target thicknesses were iteratively performed in the simulation. The beam attenuation and energy at the downstream of the target with each thickness were obtained in the simulation and shown as a function of the target thickness in **Fig. 2**. The interaction cross sections thus obtained from Eq. (1) are shown in **Fig. 3** with values intrinsically prepared in PHITS. The cross sections in the high energy region are well reproduced although discrepancy appears in the low energy region since the uncertainties are accumulated as the thickness increases.

In summary, based on the T3 method, we performed a simulation to derive the interaction cross section of ^{135}Cs on ^{12}C with PHITS, which shows the availability of the method. In future to propose more realistic experiments for other radioactive isotopes, we will construct and scrutinize the specifications of the method for them.

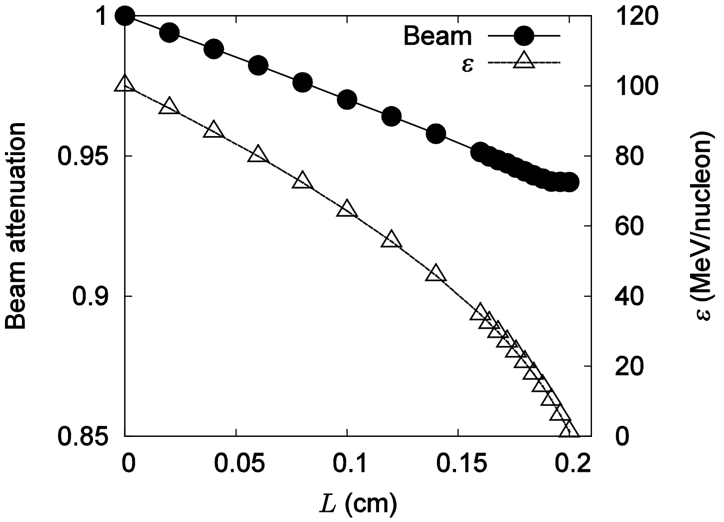

Fig. 2 The attenuation (solid line with solid circles) and energy (dotted line with open triangles) of the incident beam are shown as a function of the thickness of the target.

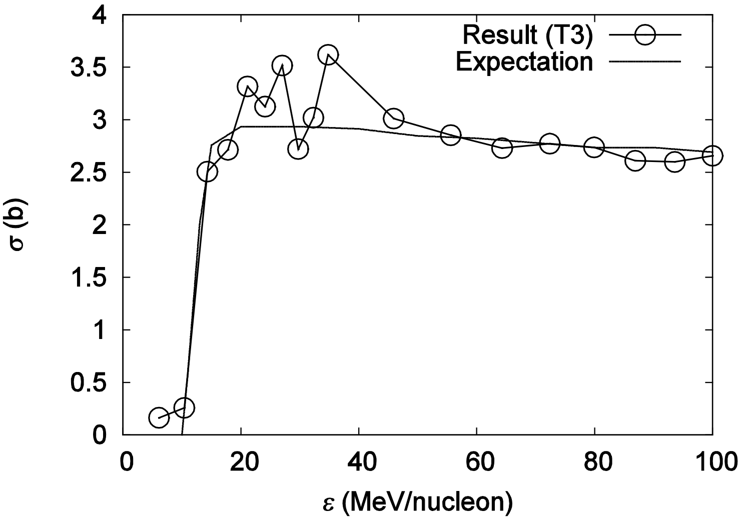

Fig. 3 Interaction cross section of ^{135}Cs on ^{12}C. The results of the PHITS simulation (solid line with open circles) are shown with expected values of PHITS (dotted-line).

Acknowledgement

This work was funded by ImPACT Program of Council for Science, Technology and Innovation (Cabinet Office, Government of Japan).

References

[1] I. Tanihata, H. Hamagaki, O. Hashimoto, S. Nagamiya, Y. Shida, N. Yoshikawa, O. Yamakawa, K. Sugimoto, T. Kobayashi, D.E. Greiner, N. Takahashi, Y. Nojiri, Phys. Rev. Lett. 55, 2676 (1985).

[2] A. Ozawa, O. Bochkarev, L. Chulkov, D. Cortina, H. Geissel, M. Hellstrom, M. Ivanov, R. Janik, K. Kimura, T. Kobayashi, A.A. Korsheninnikov, G. Munzenberg, F. Nickel, Y. Ogawa, A.A. Ogloblin, M. Pfutzner, V. Pribora, H. Simon, B. Sitar, P. Strmen, K. Summerer, T. Suzuki, I. Tanihata, M. Winkler, K. Yoshida, Nucl. Phys. A 691, 599 (2001).

[3] M. Takechi, M. Fukuda, M. Mihara, K. Tanaka, T. Chinda, T. Matsumasa, M. Nishimoto, R. Matsumiya, Y. Nakashima, H. Matsubara, K. Matsuta, T. Minamisono, T. Ohtsubo, T. Izumikawa, S. Momota, T. Suzuki, T. Yamaguchi, R. Koyama, W. Shinozaki, M. Takahashi, A. Takizawa, T. Matsuyama, S. Nakajima, K. Kobayashi, M. Hosoi, T. Suda, M. Sasaki, S. Sato, M. Kanazawa, A. Kitagawa, Phys. Rev. C79, 061601 (2009).

[4] M. Aikawa, S. Ebata, S. Imai, under submission.

[5] T. Sato, K. Niita, N. Matsuda, S. Hashimoto, Y. Iwamoto, S. Noda, T. Ogawa, H. Iwase, H. Nakashima, T. Fukahori, K. Okumura, T. Kai, S. Chiba, T. Furuta L. Sihver, J. Nucl. Sci. Technol. 50, 913 (2013).

16 Current status in development of new EXFOR editor

A. Sarsembayeva[1,*], S. Imai[2], S. Ebata[1], M. Chiba[3], K. Katō[1], N. Otuka[4], M. Aikawa[1]
[1]Faculty of Science, Hokkaido University, Sapporo 060-0810, Japan
[2]Institute for the Advancement of Higher Education, Hokkaido University, Sapporo 060-0817, Japan
[3]Sapporo-Gakuin University, Ebetsu 069-8555, Japan
[4]Nuclear Data Section, International Atomic Energy Agency, A-1400 Wien, Austria
[*] E-mail: aiganym@nucl.sci.hokudai.ac.jp

A new stand-alone type editor for EXFOR is being developed in Hokkaido University Nuclear Reaction Data Centre (JCPRG). The new editor is designed to allow compilers to save time and to avoid mistakes by using its advanced features. The features included in the latest release are described such as filterable and dynamic suggestion fields.

1. Introduction

The EXFOR (EXchange FORmat) database is a collection of experimental nuclear reaction data, maintained by the IAEA on behalf of the International Network of Nuclear Reaction Data Centres (NRDC). The Hokkaido University Nuclear Reaction Data Centre (JCPRG, formerly Japan Charged-Particle Nuclear Reaction Data Group) became a member of the NRDC Network [1] in the early 80s. Currently the 14 data centers worldwide of the NRDC collaborate mainly for collection, dissemination, compilation and exchange of experimental data by using the common EXFOR format.

In 1969, the NRDC decided to create the EXFOR format as the common format to exchange and store neutron-induced reaction data [2, 3]. In 1976 charged-particle and photon induced reaction data were added to EXFOR. Thus the current scope of the EXFOR database covers neutron-induced, charged particle induced and photonuclear data. It contains experimental nuclear reaction data including a well-defined range of parameters and numerical data.

JCPRG has an editor to compile such nuclear reaction data. The editor HENDEL was developed for compilation of experimental nuclear reaction data in NRDF (Nuclear Reaction Data File) and EXFOR formats [4]. It has been used as a standard compilation editor system at JCPRG since 2001 [5]. The main advantages of the HENDEL editor are 1) a web-based user interface, 2) easy in use, and 3) output in both formats EXFOR and NRDF.

In an EXFOR compilation workshop (6-10 Oct. 2014, Vienna) EXFOR compilers emphasized that it is important to develop an OS independent EXFOR editor system [6]. Motivated by the platform independent features of Java, the JCPRG embarked on a project to develop an advanced EXFOR editor for data compilation. The developing editor, called ForEX (For EXFOR) would address the growing needs of traditional EXFOR compilers as well as advanced functionalities. ForEX was designed by the influence of the HENDEL editor. Advanced features implemented in the program can allow compilers to save their time.

2. Method

In order to establish an OS independent EXFOR editor system, Java was selected as a programming language for ForEX. Java is an OS independent platform and distributed free of charge. Many functions provided in Java are available for usability: 1) Collapsible/expandable item, 2) Add/remove buttons, 3) Filterable suggestion field, 4) Text filtering for a table, and 5) Dynamic suggestion.

In addition to the new functions, some external tools such as DANLO and CHEX should be available in ForEX. DANLO is a tool to extract a dictionary of codes in EXFOR and utilized for ForEX. CHEX is a checking program of the EXFOR format. These softwares are prepared by IAEA NDS, and very useful and valuable to manipulate directly in the editor.

3. Result & Discussion

The following functions were implemented for the usability. Java is basically an OS independent platform, however, tests on each OS may be necessary. At present, the test was only performed in Microsoft Windows and Linux, and will be performed in Mac OS in near future.

1) Collapsible/expandable item

Many kinds of information and data are required to input for each keyword. For instance, the reaction information consists of data on projectile, target, emitted particles and so on. However, during input of the other data, the reaction information is unnecessary to see. Therefore, the collapsible/expandable function for each item is implemented. This function makes the screen space more efficient and better visualized as shown in Fig. 1. If the button at the right side of each item is selected, all fields in the item to input can be collapsed and expanded. This function can reduce complexity for users.

2) Add/remove buttons

Similar to the concept of collapsible/expandable items, the number of input areas must be minimum at first. The areas can be added/removed interactively by buttons as shown in Fig. 2. If the “+” button is clicked, additional line is prepared for another data input. On the other hand, the "-" button can be clicked when the line is unnecessary for data input.

Figure 1 Example of collapsible/expandable items for Bib section. The buttons at right sides of items enable us to collapse and expand data input/select areas.

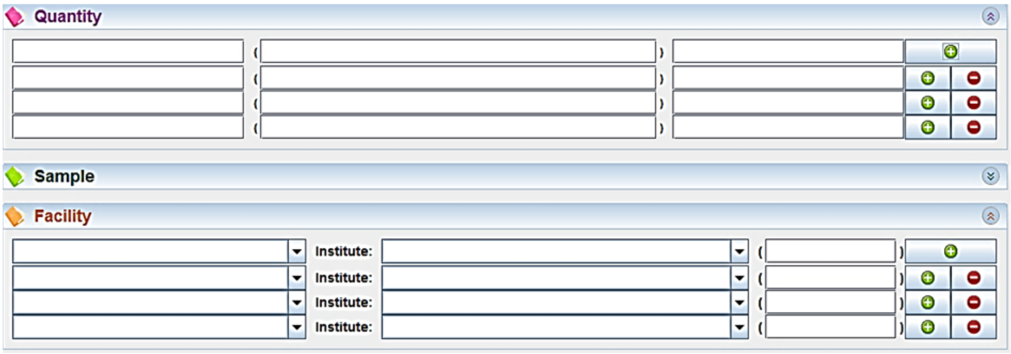

Figure 2 Buttons to add/remove input areas. In the right sides, there are "+" and "-" buttons to add and remove lines to input data.

3) Filterable suggestion field

There are a lot of codes for some keywords. The selection of the correct code is very difficult task for compilers. It is very rare for the compilers to know the exact codes to express the information to input. Therefore, the compiler should be supported by a function of automatic completion. It is implemented by filterable suggestion fields to allow compilers to save time and avoid mistakes. The field shows suggestions interactively according to the part of input words as shown in Fig. 3.

4) Text filtering

Similar to the concept of the filtering suggestion fields, the codes can be suggested by a keyword input. There are so many similar codes, especially related to reactions. With text filtering, an appropriate list of reaction codes can be obtained as shown in Fig. 4. If we input "CUM" which means a code to express a cumulative reaction, we can obtain a list including the keyword.

5) Dynamic suggestion field

There are several classification of codes, such as “Journal” and “Progress Report” in reference codes. It is easier to separate codes and to prepare the individual lists for compilers. This can be implemented by introducing dynamic suggestion fields as shown in Fig. 5. The fields enable compilers to reduce mistakes.

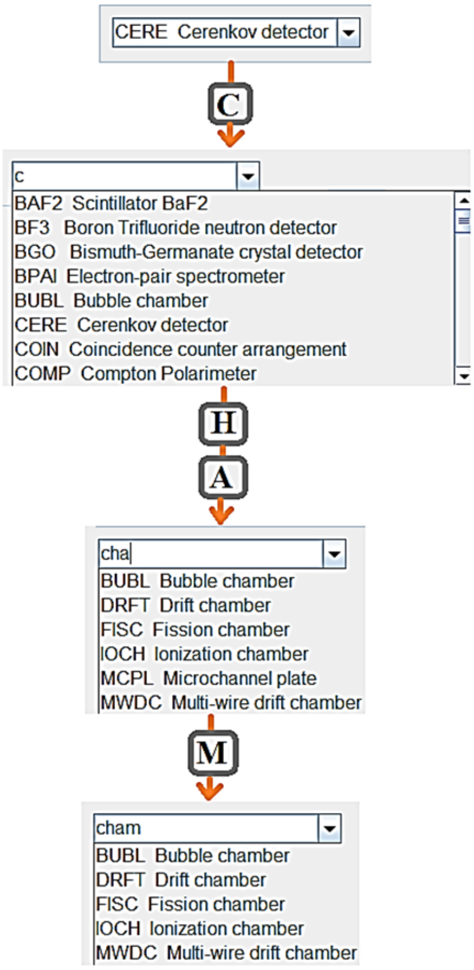

Figure 3 The example of suggestion field implemented for Detector field. The codes were suggested interactively by the part of the input word.

6) External tools

ForEX is connected with external tools, DANLO and CHEX. When the DANLO button is clicked, a new dictionary can be selected and its contents can be extracted for ForEX.

4. Summary

A new EXFOR editor system, ForEX, is being developed by Java as a standalone application. ForEX can provide an environment for compilation of numerical data with its bibliographic and experimental information in the EXFOR format. In this paper we presented various novel functionalities implemented in the program; 1) Collapsible/expandable item, 2) Add/remove buttons, 3) Filterable suggestion field, 4) Text filtering for a table, and 5) Dynamic suggestion. In addition, some external tools can directly be manipulated in the editor. Execution of the program was only tested in Windows and Linux and will also be tested in Mac OS. We will finalize the EXFOR output part at the earliest period. Moreover we plan to provide implementation of "Import" function, which allows to load existing EXFOR entries to further edit in ForEX.

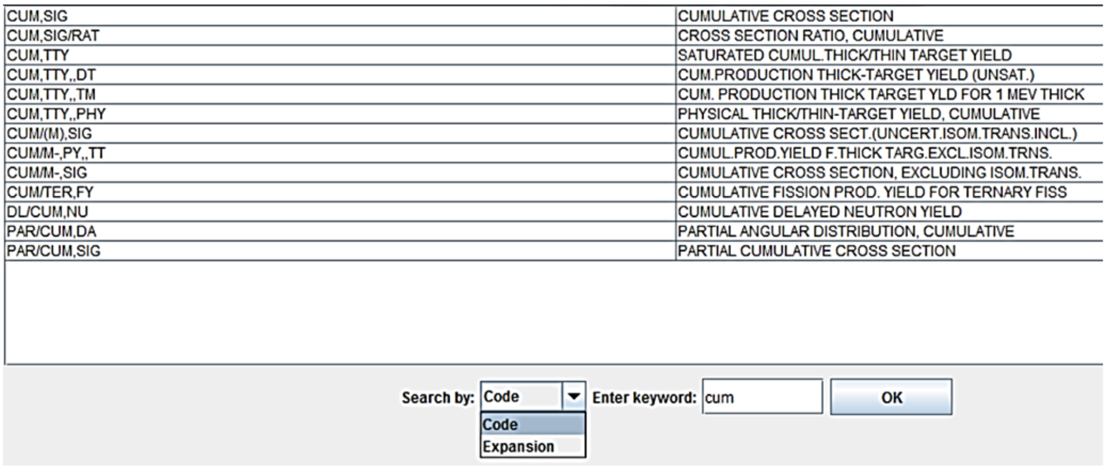

CUM,SIG	CUMULATIVE CROSS SECTION
CUM,SIG/RAT	CROSS SECTION RATIO, CUMULATIVE
CUM,TTY	SATURATED CUMUL.THICK/THIN TARGET YIELD
CUM,TTY,,DT	CUM.PRODUCTION THICK-TARGET YIELD (UNSAT.)
CUM,TTY,,TM	CUM. PRODUCTION THICK TARGET YLD FOR 1 MEV THICK
CUM,TTY,,PHY	PHYSICAL THICK/THIN-TARGET YIELD, CUMULATIVE
CUM/(M),SIG	CUMULATIVE CROSS SECT.(UNCERT.ISOM.TRANS.INCL.)
CUM/M-,PY,,TT	CUMUL.PROD.YIELD F.THICK TARG.EXCL.ISOM.TRNS.
CUM/M-,SIG	CUMULATIVE CROSS SECTION, EXCLUDING ISOM.TRANS.
CUM/TER,FY	CUMULATIVE FISSION PROD. YIELD FOR TERNARY FISS
DL/CUM,NU	CUMULATIVE DELAYED NEUTRON YIELD
PAR/CUM,DA	PARTIAL ANGULAR DISTRIBUTION, CUMULATIVE
PAR/CUM,SIG	PARTIAL CUMULATIVE CROSS SECTION

Search by: Code

Enter keyword: cum

Figure 4 Filterable reaction code

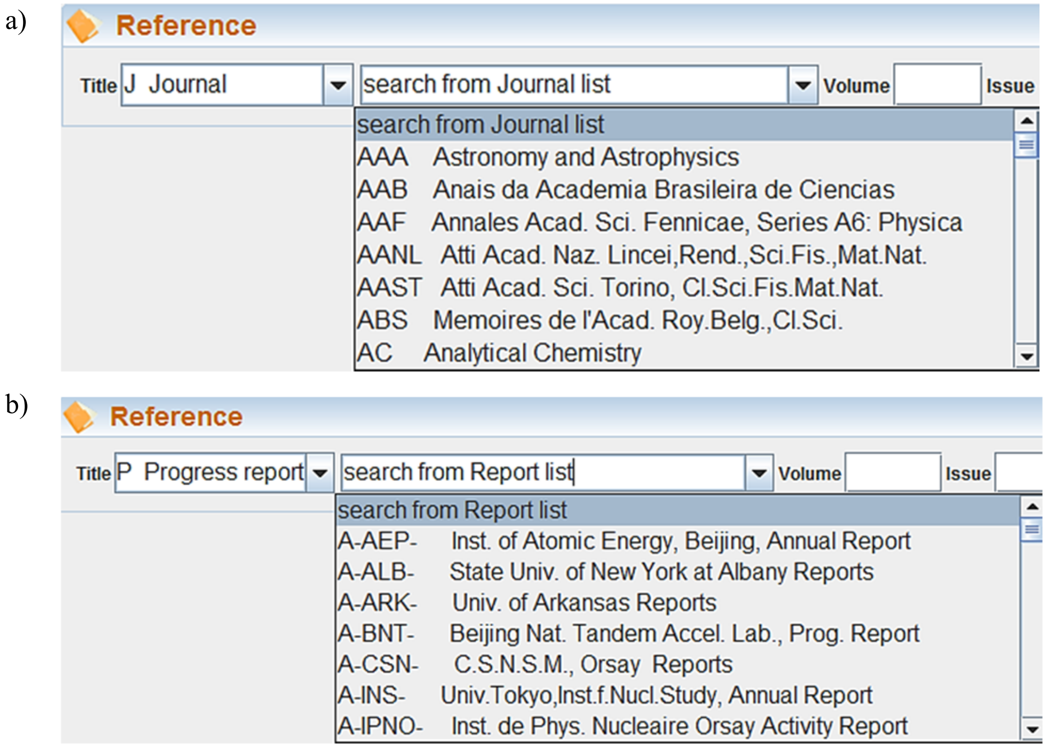

a)

Reference

Title: J Journal

search from Journal list

search from Journal list	
AAA	Astronomy and Astrophysics
AAB	Anais da Academia Brasileira de Ciencias
AAF	Annales Acad. Sci. Fennicae, Series A6: Physica
AANL	Atti Acad. Naz. Lincei,Rend.,Sci.Fis.,Mat.Nat.
AAST	Atti Acad. Sci. Torino, Cl.Sci.Fis.Mat.Nat.
ABS	Memoires de l'Acad. Roy.Belg.,Cl.Sci.
AC	Analytical Chemistry

b)

Reference

Title: P Progress report

search from Report list

search from Report list	
A-AEP-	Inst. of Atomic Energy, Beijing, Annual Report
A-ALB-	State Univ. of New York at Albany Reports
A-ARK-	Univ. of Arkansas Reports
A-BNT-	Beijing Nat. Tandem Accel. Lab., Prog. Report
A-CSN-	C.S.N.S.M., Orsay Reports
A-INS-	Univ.Tokyo,Inst.f.Nucl.Study, Annual Report
A-IPNO-	Inst. de Phys. Nucleaire Orsay Activity Report

Figure 5 The example of dynamic suggestion fields implemented for: a) Journal, and b) Progress report

References

[1] Nuclear Reaction Data Centre. Available from: http://www.jcprg.org/.

[2] Lorenz A. Report of the Fifth Four-Centre Meeting. NDS IAEA (VIENNA); 1969 Dec. 29 p. Report No.: INDC(NDU)-16/N.

[3] Otuka N, Dupont E, Semkova V, et al., Towards a More Complete and Accurate Experimental Nuclear Reaction Data Library (EXFOR): International Collaboration Between

Nuclear Reaction Data Centres (NRDC). Nucl. Data Sheets. 2014 Jun; 120: 272-76.
[4] Web-based Editor for Nuclear Data. Available from: http://www.jcprg.org/hendel/
[5] Otuka N, Noto H, Ohnishi A, Kato K. Development of Web Editor for Charged-Particle Nuclear Reaction Data. NDS IAEA (VIENNA),2002 Aug.,162p. Rep. No. INDC(NDS)-0434.
[6] Semkova V, Pritychenko B. The Experimental Nuclear Reaction Data Database. NDS IAEA (VIENNA); 2014 Dec. 46 p. Report No.: INDC(NDS)-0672.

17 Intranuclear cascade model for alpha induced reactions at incident energies 50-150 MeV

M J Kobra*, T Mori and Y Uozumi
Department of Applied Quantum Physics and nuclear Engineering
Kyushu University, 744, Motooka, Nishi-ku, Fukuoka 819-0395, Japan
email: mjkobra@yahoo.com

The Intranuclear Cascade (INC) model with the inclusion of collective excitation, trajectory deflection and transmission coefficient successfully predicts low-energy (p, p'x) reactions over a wide range of targets. Taking into account nucleon correlations, INC model can predict fragment emissions considerably well up to ^{4}He. In this report, INC has been improved to give accounts for α-particle induced reactions between 50-150 MeV of incident energies. Although JQMD and INCL are two widely used models for nucleus/light ion induced reactions in Particle and Heavy Ion Transport Code System, PHITS, both of them are known to show low predictive power for (α, α'x) reaction. As the consequence of including the correlation for incident α-particle, the predictive powers were improved significantly for (α, α'x) reactions. Although the direct reaction was ignored in this work, closer agreements with experiments were achieved for other α-induced reactions.

1. Introduction:

The intra-nuclear cascade model (INC) coupled with evaporation model is one of the most powerful tools to describe nuclear spallation reactions. The reasons and motivations for studying spallation reactions are manifolds. The advent of accelerator-driven systems (ADS), growing development of radioactive beams and the relevance in astrophysics, protection against radiation near accelerators and space missions, cosmic ray physics, planetary science etc. have renewed strong interest to study spallation reactions. There exist many INC and de-excitation models. Many efforts have been devoted to improve the accuracy of the theoretical tools. We are interested here in the INC model developed at Kyushu University and implemented in the particle and heavy ion transport code system (PHITS) [1].

In our previous works, the INC model has been successfully extended toward proton productions [2], and cluster productions [3,4] induced by protons of energies above 200 MeV or higher. More recently, we have successfully made extension of the INC model to the lower beam energies, around 50 MeV [5,6] by including collective excitations, trajectory deflections and barrier transmission coefficients. However, this improvement was carried out for only (*p*, *p'x*) reactions. For broadening the applicability of transport code, further extension towards cluster induced reactions is crucial.

The INC model assumes that nuclear reactions can be described by sequential nucleon-nucleon (*NN*) collisions inside the nucleus and that all nucleons other than the colliding pair behave as spectators.

Considering indirect pickup and knockout processes i.e. by the inclusion of nucleon correlations in target nucleus, INC model predicted cluster emission up to ^{4}He reasonably well.

To broaden the applicability of PHITS, it is highly desirable that model should be capable of describing light cluster like alpha induced reactions. For simulating light ion or nucleus induced reactions, quantum molecular dynamics (JQMD) and Liège intranuclear cascade model (INCL) model are used in PHITS. Although these models give reasonable accounts of (α, p'x) reactions, their prediction on other reactions such as (α, α'x) reactions are poor.

In our present study, the INC model is extended for cluster induced reactions by including nucleon correlations for incident particle. Here we restrict ourselves for alpha induced reactions for the incident energy 50-150 MeV. The extended INC model is validated via comparison with experimental data.

2. Overview of model

The present study was carried out by extending the INC model code investigated in Ref. [4, 5], where details of the model were described. Therefore, its main features are only briefly presented here. The present model describes the time-dependence of many-particle system. For target nucleus, initial nucleon positions are randomly distributed inside a sphere with nuclear radius R_0 and diffuseness a. They were given by $R_0 = \left(0.978 + 0.0206 A^{1/3}\right) A^{1/3}$ fm, and $a = 0.54$ fm, respectively. Each nucleon is treated as spinless particles, and is given position and momentum randomly. However, target nucleons stay at the initial location before being struck out over the Fermi sea by the *NN* collision. The nucleon above the Fermi sea is assumed to travel inside the nucleus freely. When two nucleons *i* and *j* approach to each other within a distance equivalent to the nucleon–nucleon cross section, σ_{NN}:

$$r_{ij} < \sqrt{\frac{\sigma_{NN}}{\pi}} ,$$

they have a chance to undergo a collision. The occurrence of collisions is judged from Pauli blocking, which forbids collisions leading to nucleons having momenta smaller than the Fermi momentum. The scattering angle is determined randomly to reproduce experimental angular distributions in a way that conserves energy and momentum. Nucleons under the Fermi sea are treated as spectators and are not traced in terms of their positions. A nucleon reaching the nuclear surface is assumed to be emitted when its energy is higher than the threshold. Reflection or refraction by the changing nuclear potential is not included. The model assumes the nucleus to be at equilibrium when all of the cascade particles that are not emitted fall below the threshold energies.

Cluster productions in target nucleus are considered in two ways, namely, through initial-state and final-state interactions, which are responsible for the knockout and indirect-pickup processes, respectively. Though direct nuclear reaction is important, we ignored it. For the knockout calculation, the existence of a cluster state is assumed under the initial-state interaction in the target nucleus. A composite of two nucleons forms satisfying $r_{nm} \le \lambda_i$, here r_{nm} is distance between n-th and m-th nucleon. If two nucleons are found near n-th nucleon, that is, $r_{nm} \le \lambda_i$ and $r_{nl} \le \lambda_{nl}$, a cluster having a mass of 3 is assumed to be produced. Similarly, we treat a cluster knockout up to an α particle. During transportation of a cluster inside the nucleus, the break up process is ignored. Priority of cluster productions is ordered as ^{4}He > (^{3}He or triton) > deuteron.

The final-state correlation is responsible for the indirect pickup or coalescence process. Through this process, a cluster is produced when two or more nucleons are found within a limited phase space in the final state. Here, we assume that an outgoing cluster is formed by nucleons excited above the Fermi level. The cluster forms when,

$$r_{nm}p_{nm} \le \lambda_f$$

where, r_{nm} and p_{nm} represents the distances between nucleons in phase-space. Cluster formation up to alpha particle is considered in this process.

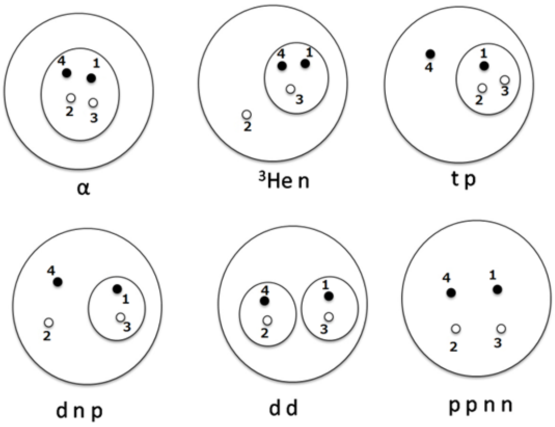

Figure 1. Six particle states of incident alpha particle.

In the present work, we added breakup of incident alpha by including nucleon correlations. This is the main difference in our present calculations with nucleon induced reactions. For alpha induced reactions there may have six particle states as shown in Figure 1 and can be expressed as

$$\psi_\alpha = c_1|\alpha\rangle + c_2|{}^3Hen\rangle + c_3|tp\rangle + c_4|dnp\rangle + c_5|dd\rangle + c_6|ppnn\rangle$$

At the end of the cascade phase, the static phase of nuclear reactions is computed by the generalized evaporation model GEM code. Information about residual nuclei at the end of INC calculation is transferred to the evaporation stage of GEM.

3. Results and discussion

Figs 1-4 show the calculated differential cross-sections（DDX）spectra and a comparison with experimental data for alpha induced reactions. In order to avoid overlap, factors indicated in figures are multiplied. Closed circles indicate experimental data taken from EXFOR [7]; solid line, dotted and short-dashed histograms are the present INC, INCL and JQMD calculation results respectively. The contribution of evaporation model, GEM, has been included on each calculation result followed by cascade state.

3.1 Alpha productions

The INC model including nucleon correlations for incident alpha particle was verified for alpha production. Calculated DDXs for 140-MeV ^{27}Al(α, α'x) reactions are compared with experimental data together with JQMD and INCL, and the comparison for 58.8-MeV ^{54}Fe (α,α'x) reactions are displayed in Figure 2. The observed angles are 30º and 60º for the both cases. The INC model shows reasonable agreement with the experimental data where peak in the highest energy region corresponds to nuclear elastic scattering, and broad peak in low energies are attributed to the evaporation. In contrast, other two models (INCL and JQMD) fail to explain these reactions. It is noted that only evaporation components are presented by INCL and JQMD model in the 58.8-MeV reaction.

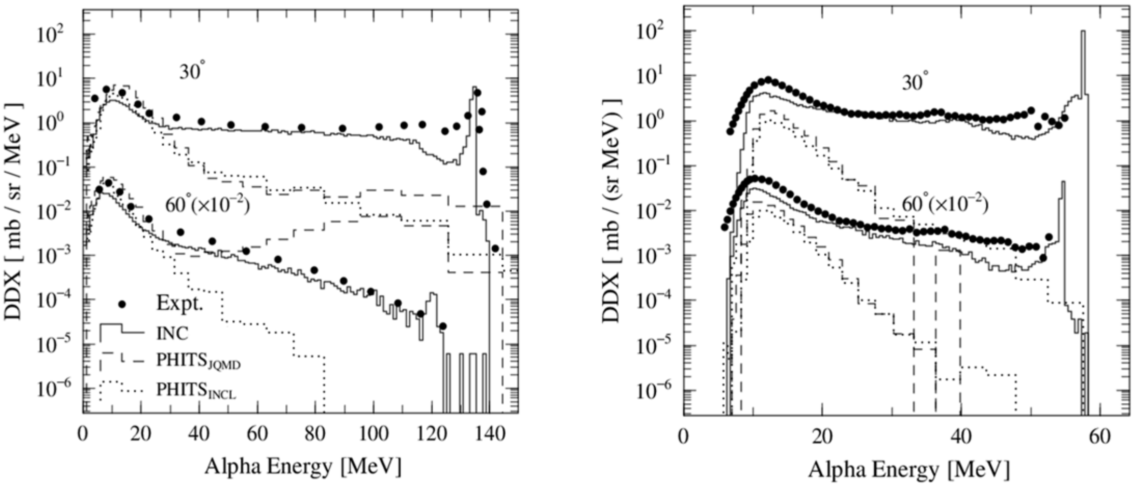

Figure 2. Comparison of DDXs spectra of 140-MeV ^{27}Al(α,α'x) (left) and 58.8-MeV ^{54}Fe(α,α'x) (right) reactions between experiments, and codes implemented in PHITS: JQMD and INCL model, and present INC model. Factors in parentheses are multipliers to avoid pile up. Solid circles are experimental data; solid line, dotted and short-dashed histograms are the INC, INCL and JQMD calculation results respectively.

3.2 Test of present model with other reactions

In this section we will discuss the results of INC considering incident alpha breakup, and the comparison for (α, dx), (α, ^{3}Hex), (α, px) and (α, tx) reactions on ^{27}Al together with experimental data and other models are shown in Figure 3-4. Unlike others' cluster induced reaction calculations, nucleon correlations have been included for incident alpha particles in present INC calculations. Present INC results shown by solid lines are in good agreement in low-energy region. However, the highest ends of spectra are underestimated. These high-energy spectra are governed by the direct reactions which are not presently considered in the INC model. That is, unlike INCL or JQMD model there is a scope for improving the calculation results for INC, because we have already succeded in including the direct (p,d) reaction.

Unfortunately, there are remarkably few alpha induced data in this incident energy region. For this reason we expect comprehensive experimental data.

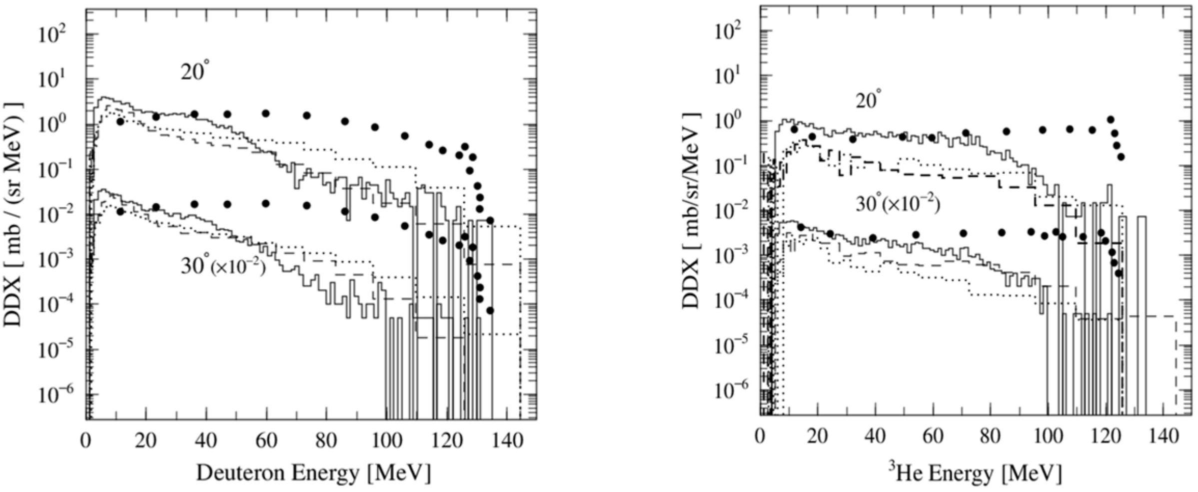

Figure 3. Same as Figure 2 but for ^{27}Al(α,dx) (left) and ^{27}Al(α,^{3}Hex) (right) at incident energy 140MeV.

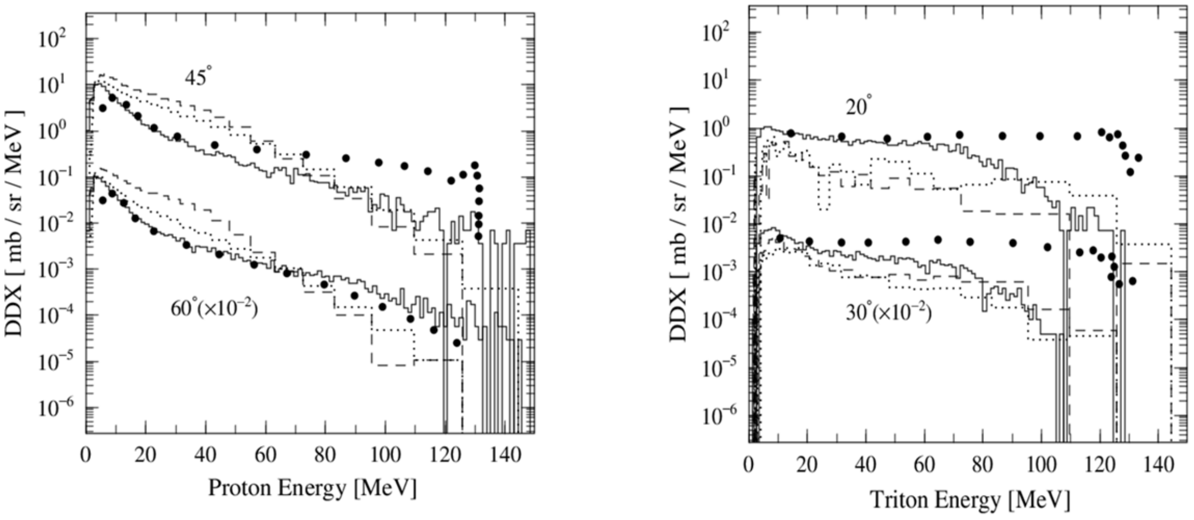

Figure 4. Same as Figure 2 but for ^{27}Al(α,px) (left) and ^{27}Al(α,tx) (right) at incident energy 140 MeV.

4. Conclusion

INC model was extended to incorporate nuclear correlations at incident alpha particle. Alpha production DDXs spectra for 50- and 140- MeV alpha-nucleus interactions were investigated on ^{27}Al and ^{54}Fe target respectively. The present model reproduced experimental alpha DDXs spectra reasonably well and better than other models (INCL and JQMD) in PHITS. The extended INC model was also verified for proton, deuteron, triton, ^{3}He emission DDXs spectra at 140-MeV alpha particle on ^{27}Al. The calculated spectra showed closer agreement except high energy region as direct reactions has not been considered.

In near future we plan to extend INC for direct alpha induced reactions. It should be noted that comprehensive experimental data are essential for this extension.

Acknowledgements
One of the authors, M.J.K., is indebted to the support from the Yoshida Scholarship Foundation.

References

[1] K. Niita, T. Sato, H. Iwase, H. Nose, H. Nakashima, L. Silver: “PHITS-a particle and heavy ion transport code system,” Radiation Measurement, 41, nos, 7-8, 1080-1090 (2006).

[2] H. Iwamoto, M. Imamura, Y. Koba, Y. Fukui, G. Wakabayashi, Y. Uozumi, T. Kin, Y Iwamoto, S. Hohara, M. Nakano: “Proton-production double-differential cross sections for 300-MeV and 392-MeV proton-induced reactions,” Phys. Rev. C 82, 034604 (2010).

[3] Y. Uozumi: “Intranuclear cascade model for cluster production”, Proceedings of the 2010 Symposium on Nuclear Data, JAEA-Conf 2011-002, pp.65−70 (2011).

[4] Y. Uozumi, Y, Sawada, A. Mzhavia, S. Nogamine, H.Iwamoto, T. Kin, S. Hohara, G. Wakabayashi, M. Nakano: “Deuteron-production double-differential cross sections for 300- and 392-MeV proton-induced,” Phys. Rev. C 84, 064617 (2011).

[5] Y. Uozumi, T. Yamada, S. Nogamine, M. Nakano: “Intranuclear cascade model including collective excitations and trajectory deflections for (p, p'x) reactions around 50 MeV,” Phys. Rev. C 86, 034610 (2012).

[6] Y. Uozumi, T. Yamada, M. Nakano: “Intranuclear cascade model for 50-MeV-region (p,p’x) reactions over a wide target mass range,” Jour. Nucl. Sci. Tech. 52, 264 (2015).

[7] EXFOR Experimental Nuclear Reaction Data, https:// www-nds.iaea.org/exfor/exfor.htm

18 Microscopic nuclear structure calculation for nuclear data evaluation of various nuclei produced via nuclear transmutation of long-lived fission products

N. Furutachi, F. Minato and O. Iwamoto
Nuclear Data Center, Japan Atomic Energy Agency, Tokai-mura, Ibaraki 319-1195, Japan
e-mail: furutachi.naoya@jaea.go.jp

When performing nuclear data evaluation, we have to depend on a certain theoretical model to compensate and predict data points at which no experimental data exist. Such a complementation with a theoretical model usually requires several nuclear structure parameters, which are estimated by experimental findings in general. However, even those parameters have to be predicted by a nuclear structure theory for some nuclei. Such a theoretical prediction becomes more important as we go to nuclei apart from the stability line on the nuclear chart, e.g. nuclei produced via nuclear transmutations. In this work, we therefore have calculated the nuclear structure parameters needed for the nuclear data evaluation by using Hartree-Fock-Bogoliubov theory. In this work, we discuss the deformation parameters and the nuclear level densities as the nuclear structure inputs. The reproduction power of our calculation and its interaction dependence are discussed.

1. Introduction

To establish the nuclear transmutation system for the long-lived fission products (LLFPs), it is desired to improve precision of its simulation calculation by taking into account all the possible reaction pass. To achieve this, nuclear data of various nuclei produced via the nuclear transmutation of LLFPs are needed. However, it is expected that unstable nuclei with no available experimental data are produced via the nuclear transmutation, and their nuclear data are usually insufficient. For the nuclear data evaluation of such nuclei, the structure parameters used for nuclear reaction calculation are often obtained with phenomenological models, which are basically adjusted to existing experimental information of stable nuclei. However, it has been claimed that its applicability to unstable nuclei far from the stability line on the nuclear chart is not obvious.

Our aim is to predict the structure parameters used in the nuclear data evaluation for various nuclei that have no or scarce experimental information, which are expected to be produced via the transmutation of ^{79}Se, ^{93}Zr, ^{107}Pd and ^{135}Cs. To account for transmutations using nuclear reactions such as spallation reactions, structure parameters of a wide range of nuclei are needed. For this purpose, we have calculated the deformation parameter and the nuclear level density (NLD) using a microscopic nuclear many-body theory. In this report, we discuss the reliability of our method by investigating the capability of our method to reproduce the experimentally known structure parameters and its dependence on the used effective interaction in $30 \leqq Z \leqq 56$ nuclei. As for the deformation parameter, our predictions for the odd nuclei are also shown to discuss the importance of the microscopic calculation. Hartree-Fock-Bogoliubov (HFB) theory was used for the calculation of both the deformation parameter and the NLD, and the microscopic statistical method [1,2,3] was applied for the case of the NLD.

Section 2 illustrates the theoretical framework used in this study, and sec. 3 discusses the obtained results. Finally, we summarize in sec. 4.

2. Theoretical framework

We calculated nuclei with atomic mass $30 \leqq Z \leqq 56$ including even-odd and odd-odd nuclei by HFB theory. HFBTHO code [3] was used for the calculation, in which axial- and time-reversal symmetries are assumed. For the calculation of odd-even and odd-odd nuclei, the blocking of quasi-particle states with the equal filling approximation is introduced. Several sets of the Skyrme forces were tested to find an appropriate one for the present purpose, and in this report, we show the results of SkM* [5], SLy4[6]. The pairing interaction we used is the mixed type pairing force given by

$$V_{pair}^{(n,p)} = V_0^{(n,p)} \left(1 - \frac{1}{2}\frac{\rho_0(\boldsymbol{r})}{\rho_c}\right) \delta(\boldsymbol{r} - \boldsymbol{r}'),$$

where $V_0^{(n,p)}$ is the pairing strength for neutrons (n) or protons (p), $\rho_0(\mathbf{r})$ the isoscalar local density, and ρ_c the saturation density fixed at 0.16 fm^{-3}. For SLy4 force, V_0^n and V_0^p are −325.2500 MeV and −340.0625 MeV, respectively For SkM* force, we adopted two pairing strength parameter sets, which are referred to as SkM* P1 and P2. For SkM* P1, V_0^n and V_0^p are −262.5 MeV and −340.0625 MeV, respectively, and for SkM* P2, they are −212.2 MeV and −272.05 MeV, respectively. The pairing strength of P1 reproduces the global trend of the pairing gap, while that of P2 is weakened to investigate its effect on the deformation parameter and the NLD. The constant cutoff energy $\varepsilon_{cut} = 60$ MeV is adopted for all pairing forces.

The NLD is calculated by the microscopic statistical method with the finite temperature HFB calculation. The formalism used in this study is basically the same with that used in the study of Demetriou and Goriely [2]. To see the effect of the vibrational collective enhancement, NLD was multiplied by the approximated form of the vibrational collective enhancement factor [3]

$$K_{vib} = \exp(0.0555A^{3/2}T^{4/3}) \ .$$

3. Results and discussion

3.1 Deformation parameter

In Fig.1, the deformation parameters of even-even Se, Kr, Sr and Zr isotopes using Sly4 and SkM* with two different pairing strength parameters are shown. The results are compared with the β_2 values derived from the experimental B(E2) values, which are taken from NuDat2 [7], and another HFB calculation with BSk14 force [8] taken from RIPL-3 database [9]. We found the strong dependence of the deformation parameter on the used interactions. In Se and Kr, while spherical solutions disagreed significantly with the experimental ones are obtained with SLy4 at N=40 and 42 due to the sub shell closure of the neutron, large deformations are found with SkM* for these nuclei. For Sr and Zr, most of the isotopes are spherical with SLy4. Overall agreement with the experiments is better in case of SkM* force. The pairing strength also changes the deformation significantly. In Kr and Sr, the deformation disappears suddenly at N=44 with SkM* P1, while it decreases gradually towards N=50 with SkM*P2. Because the spherical and the deformed states are energetically close to each other in these isotopes, the order of these states can be inverted easily with a change of pairing strength. As a consequence, a moderate agreement with the experiments of whole 30≦Z≦56 nuclei is achieved with SkM* P2. The gradual change of the deformation is consistent with the tendency of the experiments.

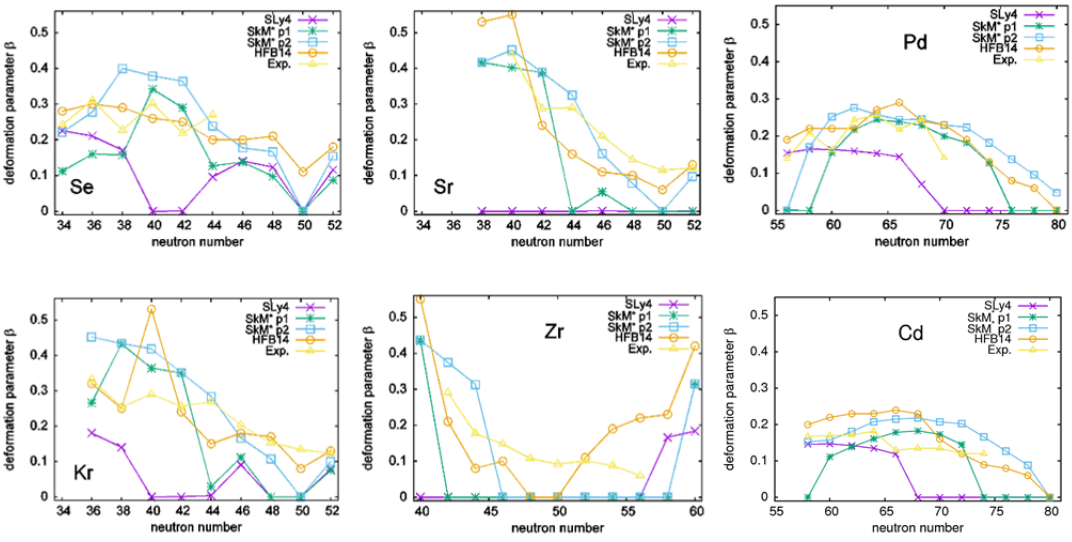

Fig. 1 Absolute values of deformation parameter β_2 of even-even Se, Kr, Sr, Zr, Pd and Cd isotopes.

The deformation parameters have been also obtained for odd nuclei. In Fig. 2, those of Se(Z=34), Br(35), Zr(40), and Nb(41) are shown; Br and Nb are neighbors of Se and Zr with respect to the proton number, respectively. We can see that the addition of one proton or one neutron to even-even nucleus causes non-monotonic modification to the deformation. Especially, the one additional nucleon inverts the oblate and prolate deformations around N=37 of Se and Br, and the spherical and deformed states around N=58 of Zr and Nb. It is difficult to expect such complicated change of the deformation in empirical way, and therefore, the microscopic calculation of the deformation parameter of odd nuclei is needed.

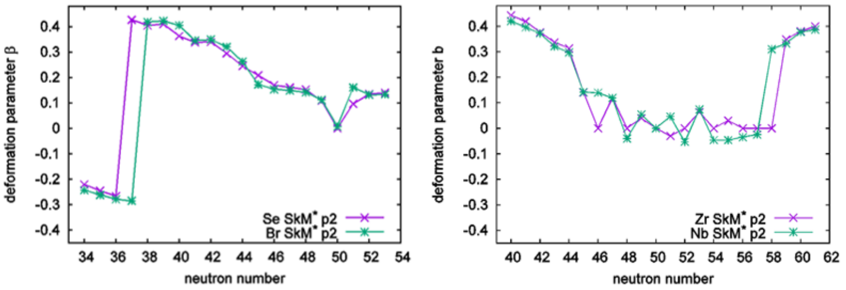

Fig. 2 Deformation parameter β_2 of Se, Br, Zr and Nb isotopes.

3.2 Nuclear level density

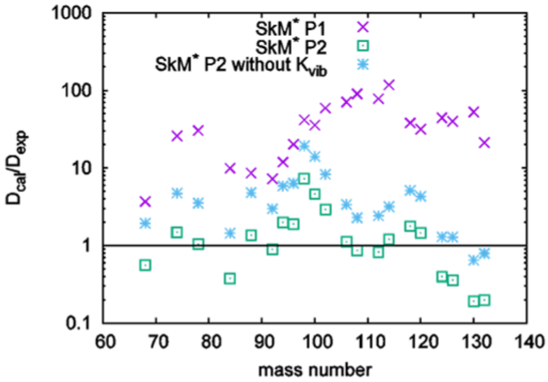

Fig. 3 s-wave neutron resonance spacing normalized to the experimental value.

To discuss the reproducibility of the NLD quantitatively, we compare the calculated s-wave neutron resonance spacing D_0 derived from the NLD with that of the experiment. Fig. 3 shows the calculated D_0 normalized to the experimental data. The experimental data are taken from RIPL-3 database, and available for 21 nuclei in $30 \leqq Z \leqq 56$ even-even isotopes. While the results with SkM* P1 significantly overestimate the experimental values, SkM* P2 shows a better agreement with the experiments. Since the pairing correlation lowers the ground state energy, the NLD with a stronger pairing force is likely to be smaller than that with a weaker one at the same excitation energy, despite the pairing correlation vanishes at high excitation energy. The vibrational collective enhancement factor K_{vib} increases the NLD by a factor of approximately three, which results in a better agreement with the experiments. The root-mean-square deviation defined as

$$f_{rms} = exp\left(\sqrt{\frac{1}{N}\sum_{i=1}^{N} ln^2 \frac{D_{cal}^{i}}{D_{exp}^{i}}}\right)$$

is 2.5 and 32.5 for 21 nuclei with SkM* P2 and P1, respectively. Since the NLD is directly affected by the strength of the pairing force for the reason mentioned above, further improvement of f_{rms} value may be achieved by a fine tuning of the pairing strength. Although the NLD is adjustable with the pairing strength, it should be noted that the weaker pairing strength is also supported by the calculation of the deformation parameters as explained in sec.3.1.

4. Summary

We calculated the deformation parameters and the NLDs of 30≦Z≦56 isotopes with Skyrme-HFB theory, in order to use them for the nuclear data evaluation of nucleus with no available experimental data in future. To discuss the reliability of the theoretical prediction, the calculated results were compared with the available experimental data, and the interaction dependence was investigated as well.

We found that the strength of the pairing force affects significantly both the deformation parameter and the NLD. Due to the shift of the ground state energy, the s-wave neutron resonance spacing D_0 is directly affected by the strength of the pairing force. On the other hand, size of the difference between the deformation parameters obtained with two different pairing strengths depends on nuclei. If the spherical and the deformed states are energetically close, the deformation parameter can be changed sensitively. The better agreements with the experiments were achieved both in the deformation parameter and the NLD calculations when we used SkM* P2. We obtained the result that the consistent description of two different physical quantities was achieved with the same microscopic theoretical framework and the effective nuclear force. This fact gives a certain validity of the present method to the predictions of unstable nuclei in which no experimental data exist, and we plan to study them in future.

Acknowledgment

This work was funded by ImPACT Program of Council for Science, Technology and Innovation (Cabinet Office, Government of Japan) .

References

[1] S. Goriely, “A new nuclear level density formula including shell and pairing correction in the light of a microscopic model calculation,” Nucl. Phys., A605, pp.28-60 (1996).

[2] P. Demetriou, S. Goriely, “Microscopic nuclear level densities for practical applications,” Nucl. Phys., A695, 95 (2001).

[3] F. Minato, “Nuclear level densities with microscopic statistical method using a consistent residual interaction,” J. Nucl. Sci. Technol., 48, pp.984-992 (2011).

[4] M.V. Stoitsov, N. Schunck, M. Krtelainen, N. Michel, H. Nam, E. Olsen, J. Sarich, S. Wild, “Axially deformed solution of the Skyrme Hartree-Fock-Bogolyubov equations using the transformed harmonic oscillator basis,” Comput. Phys. Comm. 184, 1592 (2013).

[5] E. Chabanat, P. Bonche, P. Haensel, J. Meyer, R. Schaeffer, “ A Skyrme parametrization from subnuclear to neutron star densities Part II. Nuclei far from stabilities,” Nucl. Phys., A635, 231 (1998).

[6] J. Barterl, P. Quentin, M. Brack, C. Guet, H.-B. Hakansson, “Towards a better parametrization of Skyrme-like effective forces: a critical study of the SkM force,”, Nucl. Phys., A386, 79 (1982).

[7] NuDat2, http://www.nndc.bnl.gov/nudat2/

[8] S. Goriely, M. Samyn, J. M. Pearson, “Further explorations of Skyrme-Hartree-Fock-Bogliubov mass formulas. VII. Simultaneous fits to masses and fission barriers,” Phys. Rev. C75, 064312 (2007).

[9] RIPL-3, https://www-nds.iaea.org/RIPL-3/

19 Isotopic distribution of ^{235}U + n $\rightarrow$ ^{236}U at low E* using 4D-Langevin calculation

Chikako ISHIZUKA[1,a], Satoshi CHIBA[1], Alexander V. KARPOV[2], and Yoshihiro ARITOMO[3]
[1]Research Laboratory for Nuclear Reactors, Tokyo Institute of Technology, 2-12-1-N1-9,
Ookayama, Meguro-ku, Tokyo, 152-8550, Japan,
[2]Flerov Laboratory of Nuclear Reactions, Joint Institute for Nuclear Research, 141980, Dubna,
Moscow region, Russia,
[3]Graduate School of Science and Engineering, Faculty of Science and Engeineering, KINDAI University,
2-3-1 Kowakae, Higashiosaka, Osaka 577-8502, Japan
[a]Email:chikako@nr.titech.ac.jp

Measurements of the isotope distribution of fission fragments are still challenging at low excitation energies and play a key role to understand the fission mechanism. Such quantities are vital for applications. In this study, fragment distributions from the fission of U isotopes at low excitation energies are studied using the Langevin model. The potential energy surface is derived from two center shell model including the shell and pairing corrections. In order to calculate charge distribution of fission fragments, we introduce a new parameter η_Z as their charge asymmetry, in addition to three parameters describing nuclear shape, z as a distance between two centers of mass, δ as fragment deformation, and η_A as a mass asymmetry. Using this model, we calculated the isotopic distribution of ^{236}U for the n-induced process ^{235}U + n → ^{236}U at low excitation energies. Consequently, we found that the current model can well reproduce isotopic fission-fragment distribution which can be compared favorably with major libraries.

1.Introduction

Prediction of the fission properties of exotic heavy systems is crucial not only to extract the information on the charge equilibrium, but also to examine astrophysical models of supernova explosions and/or a site for the rapid neutron capture process. In the high burn-up nuclear and light water reactors, information on minor actinides also plays a key role for their safety. However, the experimental data on the fragment charges are still limited compared to the mass and TKE data, although measurements of isotopic yield using the inverse kinematics have made great progress [1]. Our aim is to understand how the charge of fission fragments are distributed at pre-scission stage, and to develop a theoretical model, and to provide high quality data for minor actinides, theoretically. The Langevin model is suitable method to track the dynamical history of a system with only a few essential variables, which can give us an intuitive image of a fissioning nucleus. In the past decades, the charge distribution of a fission has been discussed from the view point of charge equilibrium. Such discussion was revived quite recently [2, 3] within the Langevin models. Difference between the current work and other recent works relating to the fission properties based on the Langevin model [2, 3], is the way of the charge mode. We consider the charge mode simultaneously with other degrees of freedom within unified computational scheme solving a system of coupled equations. Another important feature of the present model is that the microscopic shell effects are essential part of our model that is very important for the considered energy region. In this paper, we extend our model [4] in order to treat the charge mode that allows the isotope yield calculation.

2. Model

We solve the time evolution of a shape of a compound nucleus by solving the following Langevin equations, where variable $q1$, $q2$, $q3$, and $q4$ correspond to z (the distance between two center of masses), δ (deformation), η_A (mass asymmetry), and $\eta_{Z,}$(charge asyymetry), respectively.

$$
\begin{aligned}
\dot{q}_i &= m^{-1}_{ij} \\
\dot{p}_i &= -\frac{\partial V}{\partial q_i} - \frac{1}{2}\frac{\partial}{\partial q_i} m^{-1}_{jk} p_j p_k - \gamma_{ij} m^{-1}_{ij} p_k + g_{ij} R_j(t)
\end{aligned}
$$

Basically, for the potential energy V, we use a similar potential as in the three dimensional case [4]. The difference in the potential, between the three dimensional case and the current model, is the fluctuation around the expectation value of the charge asymmetry. We have solved the Langevin equations with the charge asymmetry around the expectation value by using the potential as follows. The coefficient of the fluctuation-potential term can be derived from the Harmonic approximation. Potential terms relating to the charge asymmetry, are symmetry energy and the Coulomb energy. Then we can obtain the analytical expression for the coefficient $C_{<Z>}$ with the assumption of homogeneous charge spheres,

$$
C_{\eta_Z} = \left.\frac{\partial^2 V}{\partial \eta_Z^2}\right|_{\eta_Z = <\eta_Z>}
$$

as derived in [5, 6].

As we mentioned in the previous section, in order to treat low-energy fission, we include quantum corrections in the potential. For the shell correction, we adopt the Strutinsky method. The BCS pairing effect is also included. We use the Ignatyuk's values for the coefficient.

$$
\begin{aligned}
V &= V_{LD} + (V_{Shell} + V_{Pair}) \exp\left(-\frac{aT^2}{E_d}\right) + \frac{l(l+1)\hbar^2}{2I} \\
&= V(q_i, <\eta_Z>) + \frac{C_{\eta_Z}}{2}(\eta_Z - <\eta_Z>)^2
\end{aligned}
$$

Here, note that the liquid-drop model (the original potential used in [4]) presumes the Unified Charge Distribution (UCD). As already discussed in early 80s [9], the expectation value of the charge asymmetry is not that of the UCD. Deviation from the UCD has been observed. Then, the whole potential of the present model can be expressed using the potential relating to the liquid-drop potential, the fluctuation around the the UCD, and the charge deviation from the UCD.

$$V = V(q_i, <\eta_Z>_{UCD}) + \frac{C_{\eta_Z}}{2}(\eta_Z - <\eta_Z>)^2 - \frac{C_{\eta_Z}}{2}(<\eta_Z>_{UCD} - <\eta_Z>)^2$$

Another extension of the Langevin model is the transport coefficient. For the mass mode [4], we use the same one as the three dimensional calculations. The Werner-Wheeler approximation for the inertial mass, and the Wall and Window formula for the friction tensor. For the charge mode [5, 6], we neglect the off-diagonal components. Here, note that we assume the evolution of the charge mode starts just after the neck appearance in a compound nucleus. For the mass tensor of the charge mode, we approximate a nuclear shape near the scission point as two spheres connected by a circular hole with radius r_N. The mass tensor can be described as

$$m_{ij} = \begin{pmatrix} m_{11} & m_{21} & m_{31} & 0 \\ m_{12} & m_{22} & m_{32} & 0 \\ m_{13} & m_{23} & m_{33} & 0 \\ 0 & 0 & 0 & m_{\eta_Z\eta_Z} \end{pmatrix} \qquad m_{\eta_Z\eta_Z} = \frac{m}{3\pi\rho}\frac{ZA^2}{N}\frac{(l+2r_N)}{r_N^2}$$

$$\gamma_{ij} = \begin{pmatrix} \gamma_{11} & \gamma_{21} & \gamma_{31} & 0 \\ \gamma_{12} & \gamma_{22} & \gamma_{32} & 0 \\ \gamma_{13} & \gamma_{23} & \gamma_{33} & 0 \\ 0 & 0 & 0 & \gamma_{\eta_Z\eta_Z} \end{pmatrix} \qquad \gamma_{\eta_Z\eta_Z} = \frac{4m}{9\rho}\frac{AZ}{N}[N\bar{v}_p + Z\bar{v}_n]\frac{1}{\Delta\sigma}$$

Thus, the time evolution of variables for the mass mode and for the charge mode are coupled only through the potential, because the transport coefficients are independent for each mode.

3.Results and Analysis

In this section, we show properties of obtained fission-fragments using the Langevin model with the charge fluctuation for ^{236}U at E*= 20MeV which corresponds to n+^{235}U at En = 14MeV. The current mass distribution reproduces the peak position and width of the experimental data as well as the result only with the mass mode. It means that the current modification (including the charge mode simultaneously with the mass mode) keeps the gross feature of the fissioning system, though the statistics of current calculation is not sufficient compared to the three dimensional case.

In Fig.1 and Fig. 2, we show our results on the isotopic fission yields. We found that the peak position and the curvature of the obtained results can reproduce the experimental values for the wide range of proton numbers from Z=39 to Z=52, qualitatively and quantitatively. Symbols are common in Fig. 1 and 2. Red line with filled circle is our calculation on a log scale. Black line with open circle is the JENDL/FPY-2011 [8] for ^{236}U thermal-fission. Blue dashed line with open square is the JEFF-3.1.1 [12] for ^{236}U thermal-fission. Purple dashed-line with open triangle is the ENDF/B-VII [13] for ^{236}U thermal fission. Green dashed-line with open inverted triangle is the GEF [11] for ^{236}U thermal-fission, respective

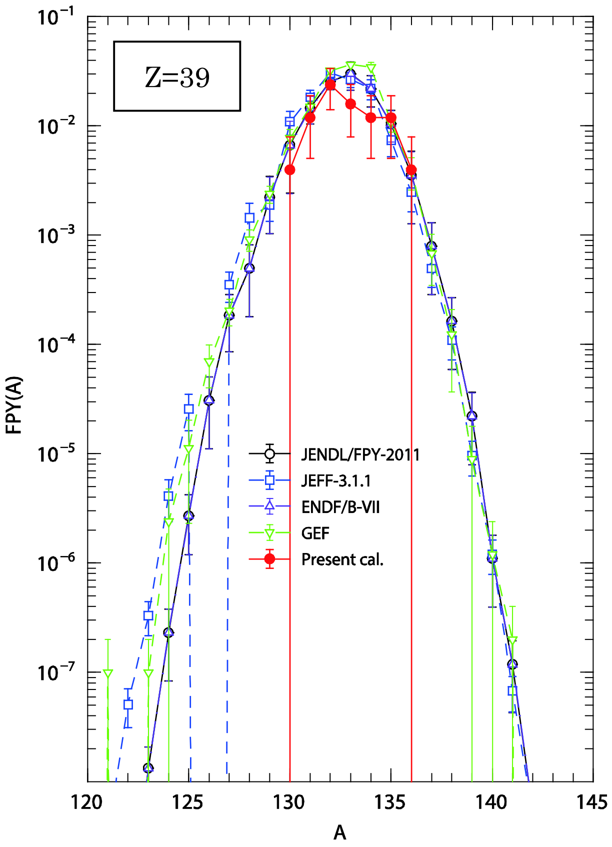

Figure 1. Isotope distribution for Z=52 derived from the current Langevin model. Red symbols are our calculation, other symbols are data from major libraries.

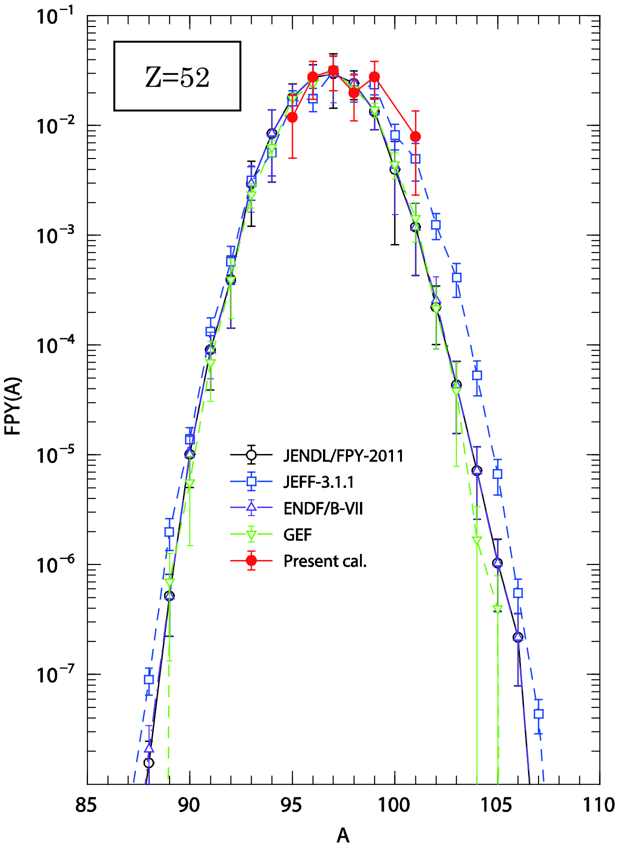

Figure 2. Isotope distribution for Z=52 derived from the current Langevin model. Symbols are the same as those in Fig.1.

4.Summary

In this paper, we extended our Langevin model based on the two-center shell-model parametrization by including the contribution from the fluctuation around the most stable charge asymmetry. We performed the Langevin calculation for the compound system of ^{236}U at E* = 20 MeV in terms of shape parameters, the mass asymmetry and the charge asymmetry simultaneously. We assumed the expectation value for the charge asymmetry including the charge deviation from the UCD as defined in [7]. As a result, our calculations showed good agreement with the isotope distributions of the major libraries, and that our model can provide sufficient accuracy to be compared to them, without any modification, qualitatively and quantitatively.

Acknowledgements

The present study comprises the results of the “Comprehensive study of delayed-neutron yields for accurate evaluation of kinetic of high-burn up reactors” entrusted to Tokyo Institute of Technology by the Ministry of Education, Culture, Sports, Science and Technology of Japan (MEXT).

References

[1] M. Caamano et al, PRC 88 (2013) 024605.

[2] K. Mazurek, C. Schmitt and P. N. Nadtochy, PRC 91 (2015) 041603(R).

[3] M. R. Pahlavani and S. M, Mirfathi, PRC 92 (2015) 024622.

[4] Y. Aritomo and S. Chiba, PRC 88 (2013) 044614 .

[5] A. V. Karpov and G. D. Adeev, EPJA 14 (2002) 169 .

[6] A. V. Karpov and G. D. Adeev, Phys. At. Nucl. 65 (2002) 1596.

[7] G. D. Adeev, Fiz. Elem. Chastis At. Yadara 23 (1992) 1572.

[8] K. Shibata, O. Iwamoto, T. Nakagawa, N. Iwamoto, A. Ichihara, S. Kunieda, S. Chiba, K. Futuraka, N.Otuka, T.Ohsawa, T.Murata, H.Matsunobu, A.Zukeran, S.Kamada, and J.Katakura, J. Nucl. Sci. Technol., 48(2011)1.

[9] R. K. Gaputa and D. R. Saroha RPC 30 (1984) 395 .

[10] A. C. Wahl, Atomic Data and Nucl. Data Tables 39 (1988) 1.

[11] K.-H. Schmidt, B. Jurado, Ch. Amouroux, JEFF-Report 24 (2014) 1.

[12] A. Santamarina et al., JEFF-Report 22 (2009) 1.

[13] M.B. Chadwick et al., Nucl. Data Sheets 112 (2011) 2887.

This is a blank page.

20 A way for synthesis of doubly magic superheavy nuclei, located in the center of Island of Stability

Y. Aritomo

Faculty of Science and Engineering, Kinki University, Higashi-Osaka, Osaka, Japan

Contact e-mail : aritomo@ele.kindai.ac.jp

Abstract

The possibility of synthesizing a doubly magic superheavy nucleus, $^{298}\mathrm{Fl}_{184}$, is investigated on the basis of fluctuation-dissipation dynamics. In order to synthesize this nucleus, we must generate more neutron-rich compound nuclei because of the neutron emissions from excited compound nuclei. The compound nucleus ^{304}Fl has two advantages to achieving a high survival probability. First, because of low neutron separation energy and rapid cooling, the shell correction energy recovers quickly. Secondly, owing to neutron emissions, the neutron number in the nucleus approaches that of the double closed shell and the nucleus attains a large fission barrier. Because of these two effects, the survival probability of ^{304}Fl does not decrease until the excitation energy E^*= 50 MeV. These properties lead to a rather high evaporation residue cross section.

1 Introduction

During the last thirty years, research for the synthesis of superheavy elements has progressed significantly and approaching to the ”Island of Stability” step by step [1]. In cold fusion reactions with Pb and Bi targets [2, 3], the heaviest element with $Z = 113$ was reported by RIKEN [4]. Another possibility is to use actinide nuclei as targets, and is called hot fusion reactions. Using the hot fusion reactions, production of new superheavy elements with Z=114, 115, 116, 117 and 118 has been reported by Flerov Laboratory of Nuclear Reactions (FLNR) [5]. Recently, other laboratories performed experiments by the hot fusion reaction and obtained results which were consistent with those by FLNR [6].

In order to realize the synthesis of superheavy elements, it is indispensable to clarify the fusion-fission mechanism, including a role of the nuclear structure of colliding nuclei and the deformation of them in the fusion process. To describe heavy-ion fusion reactions around the Coulomb barrier, we proposed a model which combines the coupled-channels approach and a fluctuation-dissipation model for dynamical calculations [7]. Fusion-fission, quasi-fission and deep quasi-fission are separated as different Langevin trajectories on the potential energy surface.

Using the dynamical model, we discuss the possibility of synthesizing new superheavy elements. The neutron number of the compound nuclei which were produced so far is insufficient to reach the Island of Stability. In order to synthesize the double magic superheavy nucleus such as ^{298}Fl, we must generate more neutron-rich compound nuclei (for example ^{304}Fl) because of the neutron emissions from excited compound nuclei. Such neutron-rich compound nucleus has advantages to achieve a high survival probability in comparison with ^{292}Fl and ^{298}Fl. During the fusion-fission process, we take account of the neutron emission with Langevin calculation, and estimate the possibility of the production of such neutron rich compound nuclei.

The paper is organized as follows. In Sec. 2, we detail the framework of the model. We discuss the possibility of synthesizing superheavy nuclei at the center of Island of Stability in Sec. 3. In Sec. 4, we present a summary of this study and further discussion.

2 Model

For fusion process, we use the fluctuation-dissipation model and employ Langevin equations [8] to investigate the dynamics of the fission process. The nuclear shape is defined by the two-center parametrization [9, 10], which has three deformation parameters, z_0, δ, and α to serve as collective coordinates: z_0 is the distance between two potential centers, while $\alpha = (A_1 - A_2)/(A_1 + A_2)$ is the mass asymmetry of the two fragments, where A_1 and A_2 denote the mass numbers of heavy and light fragments [8]. The symbol δ denotes the deformation of the fragments. The detail of the definition is explained in Ref [8]. We assume in this work that each fragment has the same deformation. This constraint should be relaxed in the future work since the deformations of the heavy and light fragments in the fission of U region are known to be different from each other. In order to reduce the computational time, we employ the coordinate z defined as $z = z_0/(R_{CN}B)$, where R_{CN} denotes the radius of a spherical compound nucleus and B is defined as $B = (3+\delta)/(3-2\delta)$. We use the neck parameter $\epsilon = 0.35$ for the fission process. The three collective coordinates may be abbreviated as q, $q = \{z, \delta, \alpha\}$. For a given value of a temperature of a system, T, the potential energy is defined as a sum of the liquid-drop part $V_{\rm LD}$ and a microscopic part $E^0_{\rm shell}$ [8].

The multidimensional Langevin equations [8] are given as

$$\begin{aligned}\frac{dq_i}{dt} &= \left(m^{-1}\right)_{ij} p_j,\\ \frac{dp_i}{dt} &= -\frac{\partial V}{\partial q_i} - \frac{1}{2}\frac{\partial}{\partial q_i}\left(m^{-1}\right)_{jk} p_j p_k - \gamma_{ij}\left(m^{-1}\right)_{jk} p_k + g_{ij} R_j(t),\end{aligned} \tag{1}$$

where $i = \{z, \delta, \alpha\}$ and $p_i = m_{ij} dq_j/dt$ is a momentum conjugate to coordinate q_i. The summation is performed over repeated indices. In the Langevin equation, m_{ij} and γ_{ij} are the shape-dependent collective inertia and the friction tensors, respectively. The wall-and-window one-body dissipation is adopted for the friction tensor. A hydrodynamical inertia tensor is adopted with the Werner-Wheeler approximation for the velocity field. The normalized random force $R_i(t)$ is assumed to be that of white noise, *i.e.*, $\langle R_i(t)\rangle$=0 and $\langle R_i(t_1)R_j(t_2)\rangle = 2\delta_{ij}\delta(t_1 - t_2)$. The strength of the random force g_{ij} is given by Einstein relation $\gamma_{ij}T = \sum_k g_{ij} g_{jk}$. The fission events are determined in our model calculation by identifying the different trajectories in the deformation space. We consider the neutron emission in our calculation. However, we only take into account the decrease in the excitation energy of the system by neutron emission, not the change in the potential energy surface, as our first step.

For fission process, we employ the Smoluchowski equation, which is expressed as follows:

$$\frac{dq}{dt}P(x,l;t) = \frac{1}{\mu\beta}\frac{\partial}{\partial x}\left\{\frac{\partial V(x,l;t)}{\partial x}P(x,l;t)\right\} + \frac{T}{\mu\beta}\frac{\partial^2}{\partial x^2}P(x,l;t), \tag{2}$$

$P(x,l;t)$ denotes the probability distribution in the collective coordinate space. The first term on the right hand side of the Smoluchowski equation is the potential term and the second term is the diffusion term. The coordinate x is defined as $x = R_{c/m.} - \frac{3}{4}r_0 A^{1/3}$ so that $x = 0$ corresponds to the spherical shape, where $R_{c.m.}$ denotes the separation distance between the mass centers of two incident nuclei or the nascent fission fragments, A the mass number of the nucleus, and $r_0 = 1.16$ fm. The angular momentum of the system is expressed by l. Both the inertia mass m and the reduced friction β are assumed to be independent of the shape of nucleus in the present calculations. The parameter μ is taken to be the reduced mass for the symmetric separation and β

is taken to be 5×10^{21} s^{-1} which is consistent with the value of the one-body dissipation in a series of shapes. Here, it is mentioned that $V(x, l; t)$ is a function of x, l and t. The time dependence enters through the time dependence of the temperature T of the system. The detail is denoted in the reference [11].

3 Synthesis of superheavy nuclei

In order to synthesize the doubly magic nucleus $^{298}\mathrm{Fl}_{184}$ by hot fusion reactions, we must fabricate a more neutron-rich compound nucleus of $N > 184$ because of the neutron emissions from the excited compound nucleus. Here, we discuss the decay process mainly.

Taking into account the neutron emissions, we investigate the possibility of synthesizing $^{298}\mathrm{Fl}_{184}$. The neutron separation energy depends on the neutron number. The neutron separation energies averaged over four successive neutron emissions $\langle Bn \rangle$ for the isotopes with Z = 114. We use the mass table in Ref. [12]. $\langle Bn \rangle$ values of A=292, 298, and 304 are 6.43, 5.25, and 4.06 MeV, respectively. With increasing neutron number of the nucleus, the neutron separation energy becomes low. Therefore many neutrons evaporate easily from the neutron-rich compound nuclei.

Because of rapid neutron emissions, the cooling speed of the compound nucleus is very high. Using the statistical code SIMDEC [11, 13], we obtained that the excited compound nucleus of A= 304 cools rapidly and the fission barrier recovers at a low excitation energy. Moreover, owing to the neutron emissions, the neutron number of the deexciting nucleus with A = 304 approaches that of a nucleus with the double closed shell Z = 114, N = 184. The shell correction energies V_{shell} of the A = 304 (N = 190) nucleus is smaller than that of the A = 298 (N = 184) [12].

In the deexciting process of the nucleus with A=304 (N=190), the neutron number approaches N=184 because of neutron emission. At a high initial excitation energy, the neutron number of the compound nucleus quickly approaches $N \sim 184$, which is that of a neutron closed shell. This indicates the rapid appearance of a large fission barrier. The compound nucleus with ^{304}Fl has two advantages for attaining a high survival probability. First, because of the low neutron separation energy and rapid cooling, the shell correction energy recovers quickly. Secondly, because of neutron emissions, the number of neutrons in the nucleus approaches that in the double closed shell, and a high shell correction energy is attained.

Generally, at a high excitation energy, the recovery of the shell correction energy is delayed. On the other hand, at a low excitation energy, the shell correction energy is established. The restoration of the shell correction energy is increasingly delayed with increasing excitation energy. Using the Smoluchowski equation, we calculate the survival probability, which is denoted in Fig. 1. With increasing excitation energy, the survival probability decreases drastically. However, for ^{304}Fl, the situation is opposite. At an excitation energy of 50 MeV, the fission barrier recovers faster than in the cases with lower excitation energies. The reason is the double effects, that is to say, the rapid cooling and rapid approach to $N \sim 184$. The survival probability of ^{304}Fl is denoted in Fig. 1. It is highly interesting that the excitation function of the survival probability has a flat region around $E^* = 20 \sim 50$ MeV. At $E^* = 50$ MeV, the survival probability of ^{304}Fl is three orders magnitude larger than that of ^{298}Fl. For reference, the survival probability of ^{300}Fl is denoted in Fig. 1.

For the ideal combinations for synthesizing the compound nucleus ^{304}Fl, the fusion probabilities for each system are shown in Fig. 2, which were calculated using the Langevin equation,

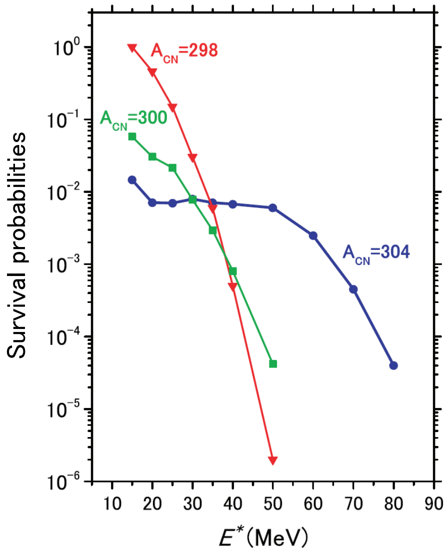

Figure 1: Survival probabilities for ^{298,300,304}Fl, calculated using the one-dimensional Smoluchowski equation.

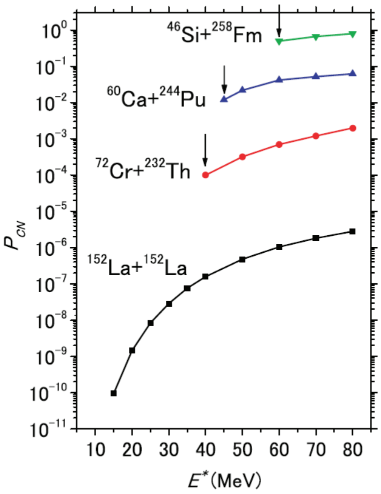

Figure 2: Fusion probabilities for each ideal system leading to the compound nucleus ^{304}Fl, which were calculated using the three-dimensional Langevin equation. For the reaction ^{152}La + ^{152}La, it was calculated using the one-dimensional Smoluchowski equation. The arrows denote the corresponding Bass potential barriers [14].

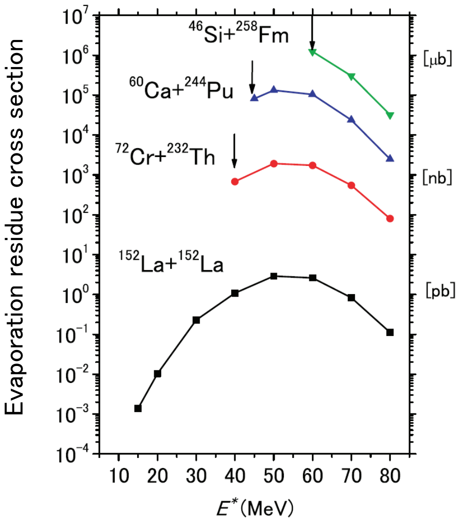

Figure 3: Excitation function of the evaporation residue cross section for each reaction forming the nuclei with Z=114.

except for the reaction ^{152}La+^{152}La. This symmetric reaction system with extremely low fusion probability is applied to the one-dimensional Smoluchowski equation. The combinations of the projectile and target are indicated in Fig. 2. The corresponding Bass potential barriers are denoted by the arrows [14]. We show the fusion probabilities above the barrier, because we use the classical models. To multiply the fusion probability with the survival probability of ^{304}Fl in Fig. 1, we obtain the evaporation residue cross section of superheavy elements, as shown in Fig. 3. The cross section is rather high. It is expected that neutron-rich isotopes are more favorable for the enhancement of the evaporation residue cross section. Thus, an investigation of the experimental feasibility of obtaining neutron-rich superheavy elements is an extremely urgent subject.

4 Summary

In this study, using the three-dimensional Langevin equation for the fusion process and the one-dimensional Smoluchowski equation for the survival process, we investigated the possibility of synthesizing the doubly magic superheavy nucleus $^{298}\mathrm{Fl}_{184}$. The compound nucleus ^{304}Fl has two advantages to achieving a high survival probability. First, because of small neutron separation energy and rapid cooling, the shell correction energy recovers quickly. Secondly, owing to neutron emissions, the neutron number of the nucleus approaches that of the double closed shell. Because of these two effects, the excitation function of the survival probability of ^{304}Fl has a flat region around $E^* = 20 \sim 50$ MeV. These properties lead to a rather high evaporation residue cross section.

References

[1] W.D. Myers and W.J. Swiatecki, *Nucl. Phys.* **81**, 1 (1966); A. Sobiczewski, F.A. Gareev, and B.N. Kalinkin, *Phys. Lett.* **22**, 500 (1966).

[2] Yu.Ts. Oganessian, *Lecture Notes in Physcs* (Springer Heidelberg) **33**, 221 (1975).

[3] S. Hofmann and G. Munzenberg, *Rev. Mod. Phys.* **72**, 733 (2000).

[4] K. Morita *et.al.*, *J. Phys. Soc. Jpn.* **73**, 2593 (2004); *J. Phys. Soc. Jpn.* **81**, 103201 (2012).

[5] Yu.Ts. Oganessian *et.al.*, *Nature* **400**, 242 (1999); *Phys. Rev. Lett.* **83**, 3154 (1999); *Phys. Rev. C* **76**, 011601 (2007); *Phys. Rev. Lett.* **104**, 142502 (2010).

[6] S. Hofmann *et.al.*, *Eur. Phys. J. A* **31**, 251 (2007); L. Stavsetr *et.al.*, *Phys. Rev. Lett.* **103**, 132502 (2009); P.A. Ellison *et.al.*, *Phys. Rev. Lett.* **105**, 182701 (2010); Ch.E. Dullmann *et.al.*, *Phys. Rev. Lett.* **104**, 252710 (2010).

[7] Y. Aritomo, K. Hagino, K. Nishio and S. Chiba, *Phys. Rev. C* **85**, 044614 (2012).

[8] Y. Aritomo and M. Ohta, *Nucl. Phys. A* **744**, 3 (2004).

[9] J. Maruhn and W. Greiner, *Z. Phys.* **251**, 431 (1972).

[10] K. Sato, A. Iwamoto, K. Harada, S. Yamaji, and S. Yoshida, *Z. Phys. A* **288**, 383 (1978).

[11] Y. Aritomo, T. Wada, M. Ohta, and Y. Abe, *Phys. Rev. C* **59**, 796 (1999).

[12] P. Möller, J.R. Nix, W.D. Myers, and W.J. Swiatecki, *Atomic Data and Nuclear Data Tables* **59**, 185 (1995).

[13] M. Ohta, *Proceedings on Fusion Dynamics at the Extremes* (World Scientific, Singapore, 2001), p.110.

[14] R. Bass, *Nuclear Reactions with Heavy Ions* (Springer, Berlin, 1980).

21 Comparison of several state-of-the-art deexcitation models coupled with an intranuclear-cascade model for proton-induced reactions at intermediate energies

M.Hagiwara[1)], D.Mancusi[2)], A. Boudard[2)], J. Cugnon[3)] and S. Leray[2)]

[1)] High Energy Accelerator Research Organization, KEK, Oho 1-1, Tsukuba-shi,
Ibaraki-ken 305-0801
[2)] CEA, Centre de Saclay, IRFU/Service de Physique Nucléaire
[3)] Fundamental Interactions in Physics and Astrophysics, University of Liège
e-mail: hagi@post.kek.jp

We have calculated cross-sections for proton-induced reactions producing residues heavier than α-particle at intermediate energies from 10 to 1000 MeV using several state-of-the-art deexcitation models (ABLA07, GEMINI++, SMM+GEM) coupled with the Liège Intranuclear Cascade model (INCL4.6). Typical calculation results on excitation functions, mass and charge yields, and isotopic distributions are presented in comparison with the relevant experimental data. All the models used in this study generally reproduces experimental data for wide incident energy and target mass ranges, but several discrepancies between the models were found in the comparison of cross-sections producing light-fragments and multi-neutrons.

1. Introduction

In the last few decades, there have been the growing interest and development among applications of accelerator handing particle beam with intermediate energies from tens of MeV to GeV for not only traditional nuclear physics experiments but also industrial and medical applications such as accelerator-based neutron sources, particle radiotherapy, generator of radiopharmaceuticals in positron emission tomography (PET) and so on [1]. These application technologies require a reliable and convenient tool to compute nuclear reactions as a key parameter for the design of experimental equipment and the detailed analysis. In 2010, the International Atomic Energy Agency (IAEA) organized a benchmark test of the physics models used in high-energy transport codes to identify the reason of success or deficiency of the models describing spallation reactions at intermediate energies [2]. In the competition, 17 models, all of which were coupling of a dynamical reaction model (intra-nuclear cascade, quantum molecular dynamics …) and statistical-decay deexcitation model, were participated and one remarkable outcome pointed out the overall high-quality level of some models such as the Liège intra-nuclear cascade model (INCL) [3] for a dynamical reaction model, and ABLA07 [4], GEMINI++ [5] and SMM [6] for a deexcitation model. In the previous paper, on the other hand, we incorporated the statistical multi-fragmentation model of SMM into the generalized evaporation model (GEM) [7] and improved the prediction accuracy of double differential cross-sections in the spallation reaction induced by several GeV protons [8].

In this paper we compared excitation functions, mass and charge yields, and isotopic distributions for several targets induced by protons between relevant experimental data and the three deexcitation models (ABLA07 [4], GEMINI++ [5], SMM+GEM [8]) by coupling with a fixed intra-nuclear cascade model (the latest version of the Liège intra-nuclear cascade model; INCL4.6) [2] to check the prediction accuracy and the difference between the deexcitation models.

2. Model overview

To focus on deexcitation models, we will limit our description on the physics models used in this paper to the deexcitation part by directing the reader to refer the relevant publications describing each model. The ABLA07 model [4] developed at GSI (Darmstadt, Germany) contains a multi-fragmentation submodule, which is triggered only if the temperature of the compound nucleus exceeds a mass-dependent freezeout threshold. The excitation energies of the resulting fragments are determined by assuming thermal equilibrium at the freeze-out temperature. Subsequent deexcitation is quantitatively described by the Weisskopf-Ewing evaporation formalism [9]. During secondary deexcitation, emission of any stable nucleus up to half the mass of the compound nucleus is possible. The GEMINI++ model, developed by R. J. Charity [5], describes nuclear deexcitation in terms of binary decays. Multi-fragment events can be produced by sequences of binary fragment emissions. Emission of light particles ($Z < 4$ by default) is described by the Hauser-Feshbach evaporation formalism [10]. Emission of fragments ($Z > 3$) is described by Moretto’s conditional-saddle-point formalism [11] with Sierk’s finite-range barriers [12]. GEM, developed by Furihata, describes nuclear deexcitation on the basis of the Weisskopf-Ewing evaporation formalism [9] with sophisticated parameterizations and allows the particle emission up to Mg in the evaporation stage. Since the original GEM model did not support for a multi-fragmentation process, the statistical multi-fragmentation model of SMM [6] have been incorporated in GEM + SMM models [8].

3. Comparison of calculation results

Figure 1 and 2 illustrate excitation functions of ^{27}Al(p,^{7}Be), ^{27}Al(p,^{22}Na), ^{nat}Cu(p,^{56}Co), ^{nat}Cu(p,^{62}Zn), ^{nat}Cu(p,^{63}Zn) and ^{nat}Cu(p,^{65}Zn) reactions calculated by three deexcitation models (SMM+GEM, ABLA07 and GEMINI++) coupled with INCL4.6 in comparison with experimental data [13-18]. All the models used in the comparison generally reproduces experimental data from threshold energies to 100 MeV, but rather large discrepancies between the models were found in the cross-sections of light-fragment emission for ABLA07 and multi-neutron emission such as ^{63}Cu(p,2n)^{62}Zn for all models.

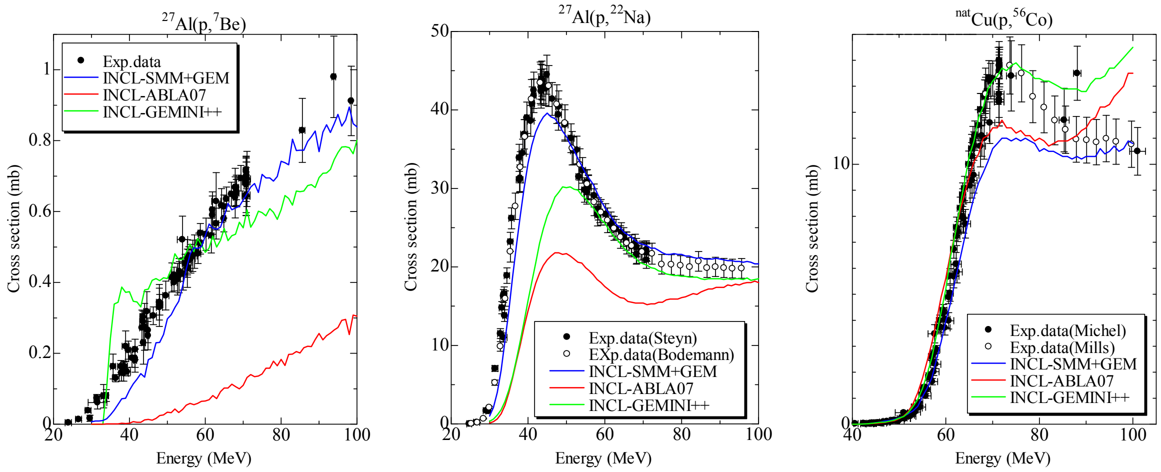

Fig.1 (Color online) Excitation functions of ^{27}Al(p,^{7}Be), ^{27}Al(p,^{22}Na) and ^{nat}Cu(p,^{56}Co) calculated by three deexcitation models (SMM+GEM, ABLA07 and GEMINI++ coupled with INCL4.6 in comparison with experimental data [13-16]. Calculation results of SMM+GEM, ABLA07 and GEMINI++ are indicated by blue, red and green lines, respectively. Experimental data are indicated by black symbols.

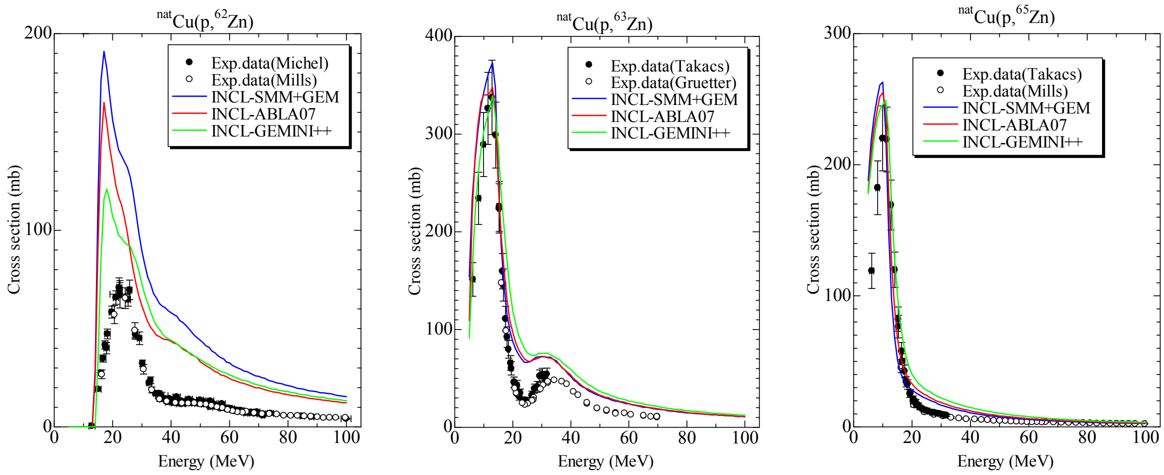

Fig.2 (Color online) Same as in Fig. 1 but for ^{nat}Cu(p,^{62}Zn), ^{nat}Cu(p,^{63}Zn) and ^{nat}Cu(p,^{65}Zn) reactions experimental data from Ref. [14-18].

Figure 3 illustrate mass and charge distribution of ^{56}Fe(p,x) at 1 GeV calculated by GEM with/without SMM coupled with INCL4.6 in comparison with experimental data [19]. The both calculation results generally agree with the experimental data. The enhancement of light fragment emission due to SMM appeared in the calculation results with SMM+GEM in the range of mass from 10 to 25 and the range of charge from 4 to 11. Figure 4 illustrates isotope distribution of ^{56}Fe(p,x) at 1 GeV calculated by GEM with/without SMM coupled with INCL4.6 in comparison with experimental data [19]. The both calculation results generally agree with the experimental data same as in Fig. 3. The enhancement of fragment emission due to SMM appeared in the calculation results with SMM+GEM from beryllium to neon. The calculation results with ABLA07 and GEMINI++ showed similar to those with SMM+GEM.

4. Conclusion

We have calculated cross-sections for proton-induced reactions producing residues heavier than α-particle at intermediate energies from 10 to 1000 MeV using several state-of-the-art deexcitation models (ABLA07, GEMINI++, SMM/GEM) coupled with the Liège Intranuclear Cascade model (INCL4.6). Typical calculation results on excitation functions, mass and charge yields, and isotopic distributions are illustrated in comparison with the relevant experimental data. All the models used in this study generally reproduce experimental data for wide incident energy and target mass range, but several discrepancies between the models were found in the cross-sections of light-fragment emission and multi-neutron emission at the low incident energies.

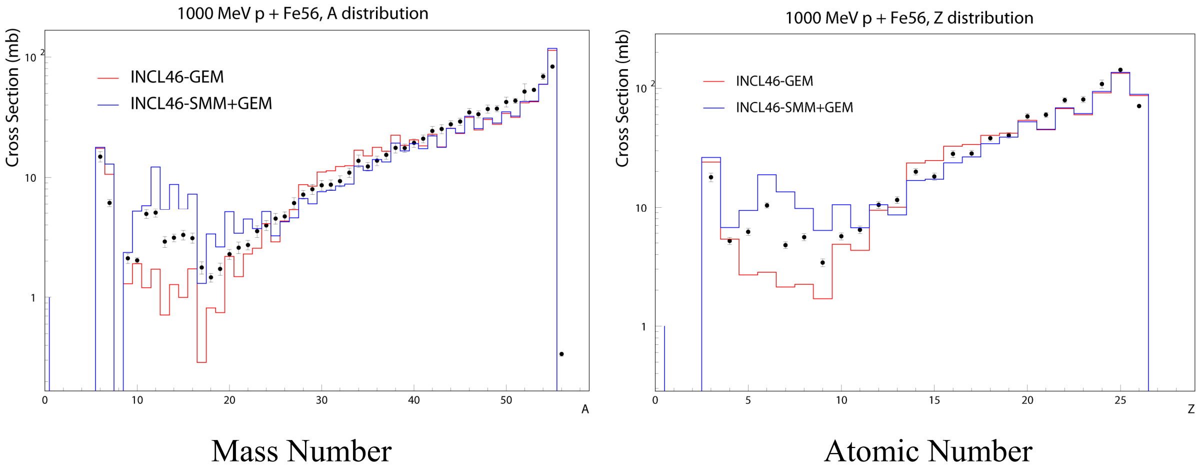

Fig.3 (Color online) Mass and charge yield for ^{56}Fe induced by 1 GeV proton in comparison between experimental data [19] (symbols), original INCL4.6+GEM (red lines) and INCL4.6 + SMM+ GEM (blue lines)

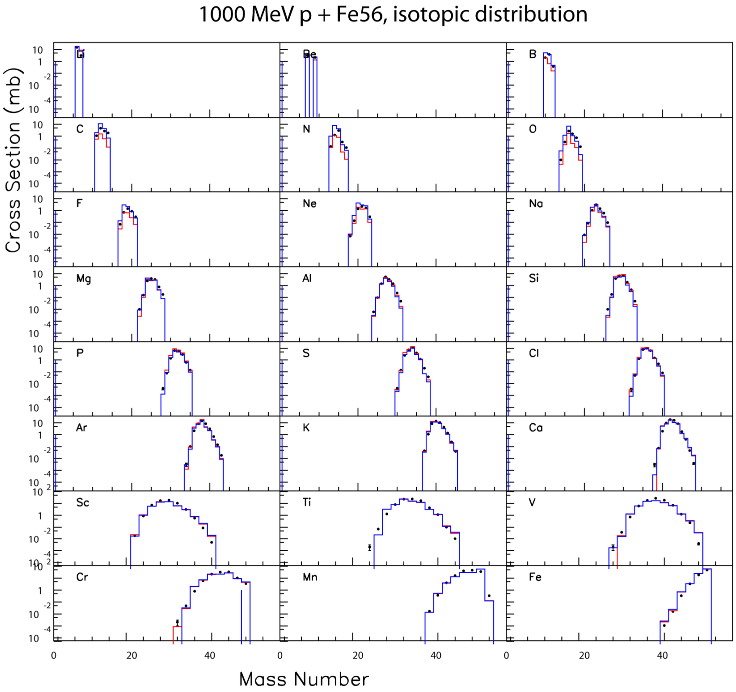

Fig.4 (Color online) Isotopic distribution for ^{56}Fe induced by 1 GeV proton in comparison between experimental data [19] (symbols), original INCL4.6+GEM (red lines) and INCL4.6 + SMM+GEM (blue lines).

Acknowledgements

The authors wish to thank the members of SPhN (Nuclear Physics Department) in CEA-Saclay for their help to perform this study. This study was partly supported by the KEK fellowship for research abroad at FY2013 and JSPS "KAKENHI (25871111).

REFERENCES

[1] Filges D, Goldenbaum F. Handbook of Spallation Research: Theory, Experiments and Applications: Berlin: Wiley VCH; 2010.

[2] S. Leray, J.-C. David, M. Khandaker, G. Mank, A. Mengoni, N. Otsuka, D. Filges, F. Gallmeier, A. Konobeyev, and R. Michel, J. Korean Phys. Soc. 59, 791 (2011); “IAEA benchmark of spallation models,” official web site, [http://www-nds.iaea.org/spallations].

[3] A. Boudard, J. Cugnon, J.C. David, S. Leray, D. Mancusi, Phys. Rev. C. 2013 Jan; 87:014606.

[4] A. Kelic, M. V. Ricciardi, and K.-H. Schmidt, in Joint ICTPIAEA Advanced Workshop on Model Codes for Spallation Reactions (IAEA, Trieste, Italy, 2008), p. 181.

[5] R. J. Charity, in Joint ICTP-IAEA Advanced Workshop on Model Codes for Spallation Reactions (IAEA, Trieste, Italy, 2008), p. 139.

[6] J. P. Bondorf, et. all, Phys. Rep. 257, 133 (1995).

[7] S. Furihata, Nucl. Instrum. Methods B 171, 251 (2000).

[8] M. HAGIWARA, et. all, Proceedings of the 2013 Symposium on Nuclear Data; November 14-15, 2013, pp.63-68.

[9] V. F. Weisskopf and D. H. Ewing, Phys. Rev. 57, 472 (1940).

[10] W. Hauser and H. Feshbach, Phys. Rev. 87, 366 (1952).

[11] L. G. Moretto, Nucl. Phys. A 247, 211 (1975).

[12] A. J. Sierk, Phys. Rev. Lett. 55, 582 (1985).

[13] R. Bodemann, H. J. Lange, I. Leya, R. Michel, T. Schiekel, R. Rösel, U. Herpers, H. J. Hofmann, B. Dittrich, M. Suter, W. Wölfli, B. Holmqvist, H. Condé and P. Malmborg, Nucl. Instrum. Meth. B 82 (1), 9-31 (1993).

[14] R. Michel, R. Bodemann, H. Busemann, R. Daunke, M. Gloris, H. J. Lange, B. Klug, A. Krins, I. Leya, M. Lüpke, S. Neumann, H. Reinhardt, M. Schnatz-Büttgen, U. Herpers, T. Schiekel, F. Sudbrock, B. Holmqvist, H. Condé, P. Malmborg, M. Suter, B. Dittrich-Hannen, P. W. Kubik, H. A. Synal and D. Filges, Nucl. Instrum. Meth. B 129 (2), 153-193 (1997).

[15] G. F. Steyn, S. J. Mills, F. M. Nortier, B. R. S. Simpson and B. R. Meyer, International Journal of Radiation Applications and Instrumentation. Part A. Applied Radiation and Isotopes 41 (3), 315-325 (1990).

[16] S. J. Mills, G. F. Steyn and F. M. Nortier, International Journal of Radiation Applications and Instrumentation. Part A. Applied Radiation and Isotopes 43 (8), 1019-1030 (1992).

[17] A. Grütter, Nucl Phys A 383 (1), 98-108 (1982).

[18] S. Takács, F. Tárkányi, M. Sonck and A. Hermanne, Nucl. Instrum. Meth. B 188 (1–4), 106-111 (2002).

[19] E. Le Gentil, T. Aumann, C. O. Bacri, J. Benlliure, S. Bianchin, M. Böhmer, A. Boudard, J. Brzychczyk, E. Casarejos, M. Combet, L. Donadille, J. E. Ducret, M. Fernandez-Ordoñez, R. Gernhäuser, H. Johansson, K. Kezzar, T. Kurtukian-Nieto, A. Lafriakh, F. Lavaud, A. Le Fèvre, S. Leray, J. Lühning, J. Lukasik, U. Lynen, W. F. J. Müller, P. Pawlowski, S. Pietri, F. Rejmund, C. Schwarz, C. Sfienti, H. Simon, W. Trautmann, C. Volant and O. Yordanov, Phys Rev Lett 100 (2), 022701 (2008).

22

Nuclear Data Adjustment with Integral Data Sensitive to Fast Neutron Energy Range

Go CHIBA
Graduate School of Engineering, Hokkaido University
Sapporo, Hokkaido, 060-8628 Japan
e-mail: go_chiba@eng.hokudai.ac.jp

Nuclear data given in several modern evaluated nuclear data files are adjusted with integral data sensitive to fast neutron energy range. It is shown that C/E values of these integral data become close to unity through the nuclear data adjustment. This improvement is observed regardless of the original nuclear data files. On the other hand, the adjusted nuclear data significantly depend on the original one; the adjusted nuclear data do not converge to unique value for all the evaluated nuclear data files.

1. Introduction

The modern evaluated nuclear data files, such as JENDL-4.0, ENDF/B-VII.1 and JEFF-3.2, show excellent performance in fast reactors neutronics parameters prediction even though there are significant dispersions in some nuclear data among the different files[1][2][3]. Nuclear data given in the evaluated nuclear data files can be further improved by the nuclear data adjustment technique with available integral data[4]. It is expected that the additional information, i.e., the integral data, might provide us knowledge on true values of nuclear data.

In the present study, nuclear data given in several evaluated nuclear data files are adjusted with several integral data sensitive to fast neutron energy range. The nuclear data adjustment is carried out for each of three modern nuclear data files, JENDL-4.0, ENDF/B-VII.1 and JEFF-3.2, and then dependence of adjusted nuclear data on the original nuclear data files is examined.

2. Concerned integral data

Fourteen criticality data and 18 reaction rate ratios data are utilized in the present nuclear data adjustment. Those integral data with their specific indices are listed in **Table1**.

3. Numerical procedure

Calculation-to-Experiment (C/E) values of the integral data are obtained through deterministic calculations with a code system CBZ, which is being developed at the Hokkaido University. Neutron energy is discretized to 175 groups. The energy group structure is almost similar with the well-known VITAMIN-J one. Numerical errors of the deterministic calculation, i.e., differences to reference continuous-energy Monte Carlo solutions, are less than 0.1% for criticality and 1% for reaction rate ratios except the Big-Ten criticality. In the Big-Ten criticality calculation, a correction factor to reduce the numerical errors induced by CBZ calculations is applied. Seventy-group sensitivities of neutronics parameters with respect to nuclear data are calculated with the (generalized) perturbation theory-based functionality of CBZ. Nuclear data adjustment is carried out with the obtained C/E values, sensitivities and covariance data of nuclear data. Note that adjustment on inelastic scattering cross sections is done not for each excitation level but for total reaction, so secondary neutron energy distributions of total inelastic scattering reactions are invariant through the adjustment.

Table 1 Integral data utilized in cross section adjustment. ”Ref.” stands for reflector, and “F28”, “F25”, “F37”, “F23” and “F49” stand for fission reactions of U-238, U-235, Np-237, U-233 and Pu-239, respectively.

Index	Name	Index	Name
1	Jezebel	15	F28/F25 in Godiva
2	Jezebel-Pu	16	F37/F25 in Godiva
3	Jezebel-233	17	F23/F25 in Godiva
4	Godiva	18	F49/F25 in Godiva
5	Flattop-Pu	19	F28/F25 in Jezebel
6	Flattop-U	20	F37/F25 in Jezebel
7	Flattop-233	21	F23/F25 in Jezebel
8	Big-ten	22	F49/F25 in Jezebel
9	Thor (HEU w Th Ref.)	23	F28/F25 in Jezebel-233
10	PMF010 (Pu w NU Ref.)	24	F37/F25 in Jezebel-233
11	U3MF002-1 (U-233 w HEU Ref.)	25	F28/F25 in Flattop-U
12	U3MF002-2 (U-233 w HEU Ref.)	26	F37/F25 in Flattop-U
13	U3MF003-1 (U-233 w NU Ref.)	27	F23/F25 in Flattop-U
14	U3MF003-2 (U-233 w NU Ref.)	28	F49/F25 in Flattop-U
		29	F28/F25 in Flattop-Pu
		30	F37/F25 in Flattop-Pu
		31	F28/F25 in Flattop-233
		32	F37/F25 in Flattop-233

4. Covariance data of nuclear data

Covariance data of the following 10 nuclides are considered: Th-232, U-233, -234, -235, -238, Np-237, Pu-239, -240, -241 and -242. In JENDL-4.0, covariance data of reaction cross sections, nu-bar, mu-bar and fission spectrum are given. In ENDF/B-VII.1, covariance data of mu-bar and fission spectrum are not given for some nuclides, so JENDL-4.0 evaluations are adopted to these data. In calculations with JEFF-3.2, the covariance data given in ENDF/B-VII.1 are used since covariance data are quite few in JEFF-3.2.

5. Numerical results

Firstly, C/E values before and after adjustment are shown. **Figure 1** shows C/E values of the criticality data. While those before adjustment disperse to some extent, those after adjustment are quite close to unity. **Figure 2** shows C/E values of the reaction rate ratio data. Through the adjustment C/E values become close to unity like the criticality data. C/E values of F28/F25 reaction rate ratios obtained with JEFF-3.2 are larger than others before the adjustment because U-238 fission cross section evaluations of JEFF-3.2 are somewhat different from the others.

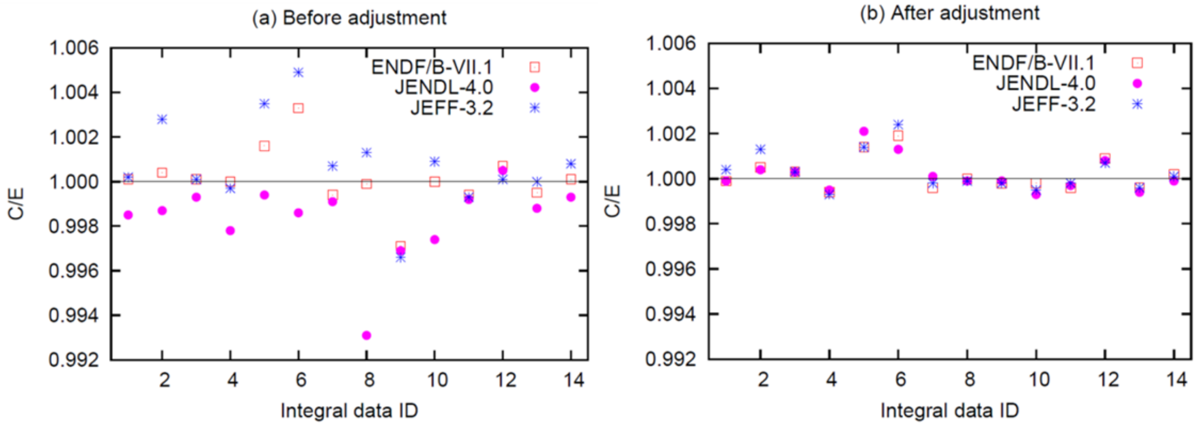

Fig. 1　C/E values of criticality data

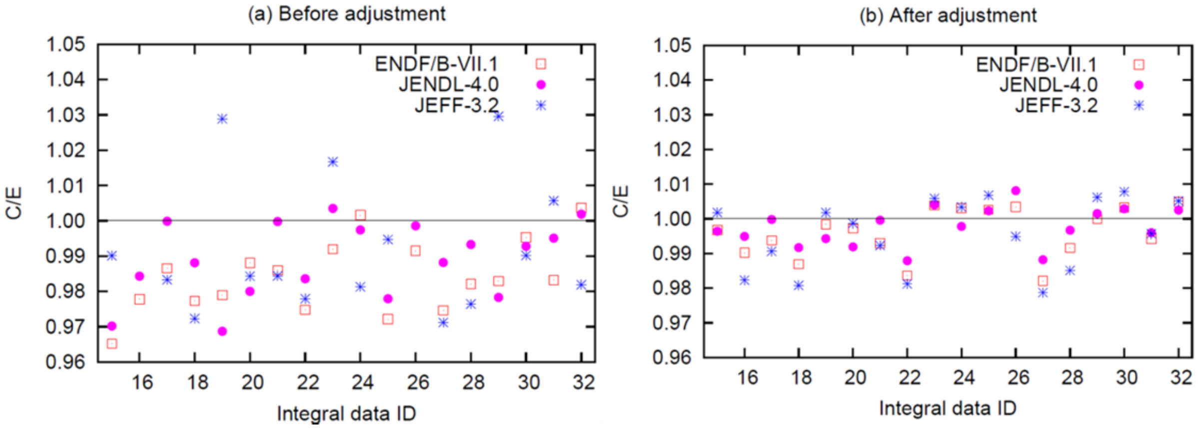

Fig. 2　C/E values of reaction rate ratio data

Next, changes in several nuclear data through the adjustment are shown. **Figures 3 to 5** show inelastic scattering cross sections of U-235, U-238 and Pu-239, respectively.

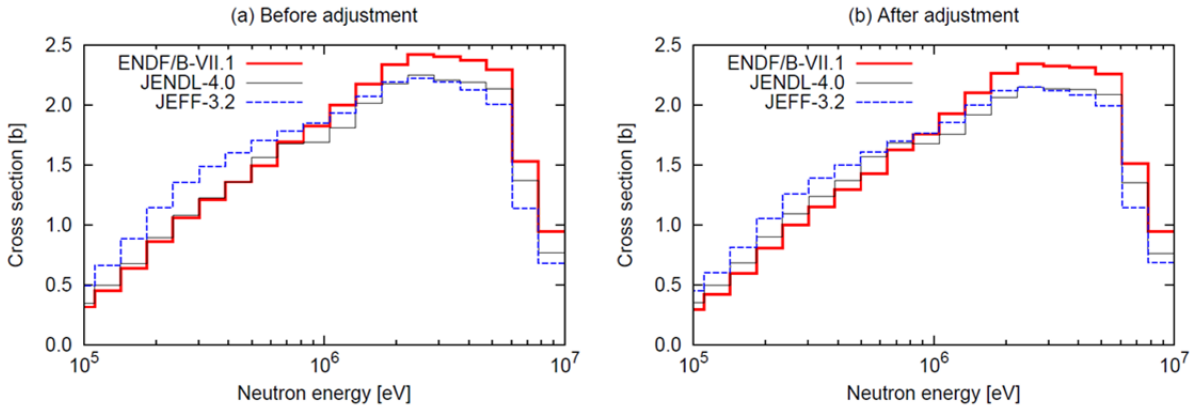

Fig. 3　Inelastic scattering cross section of U-235

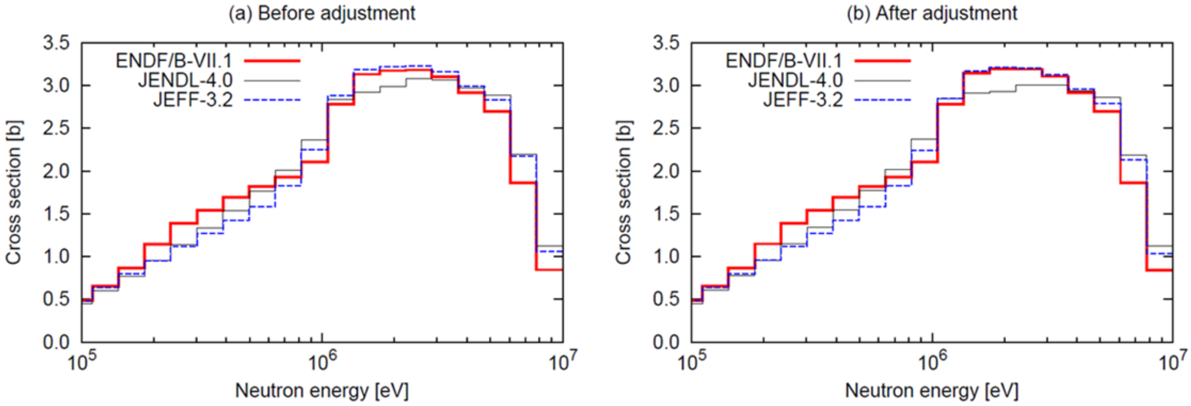

Fig. 4 Inelastic scattering cross section of U-238

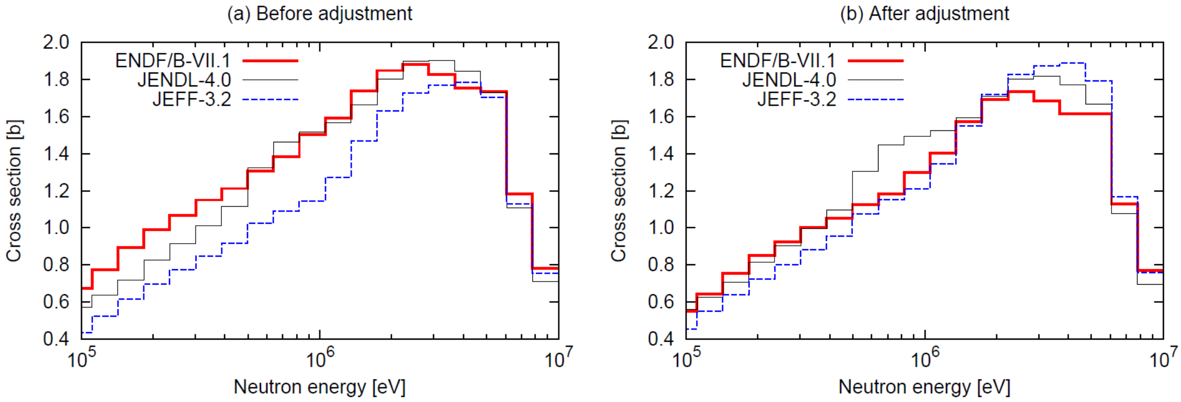

Fig. 5 Inelastic scattering cross section of Pu-239

Figures 6 to 8 show fission cross sections of U-235, U-238 and Pu-239, respectively. As described earlier, the difference in the U-238 fission cross section among JEFF-3.2 and the others significantly affects the F28/F25 reaction rate ratios. Note that the standard cross section is coincident or similar with the ENDF/B-VII.1 and JENDL-4.0 evaluations for the U-238 fission cross section.

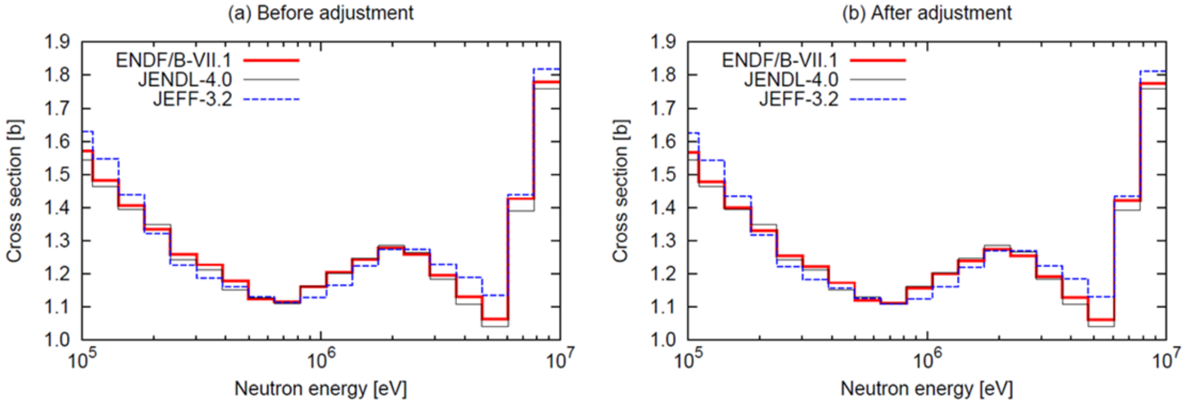

Fig. 6 Fission cross section of U-235

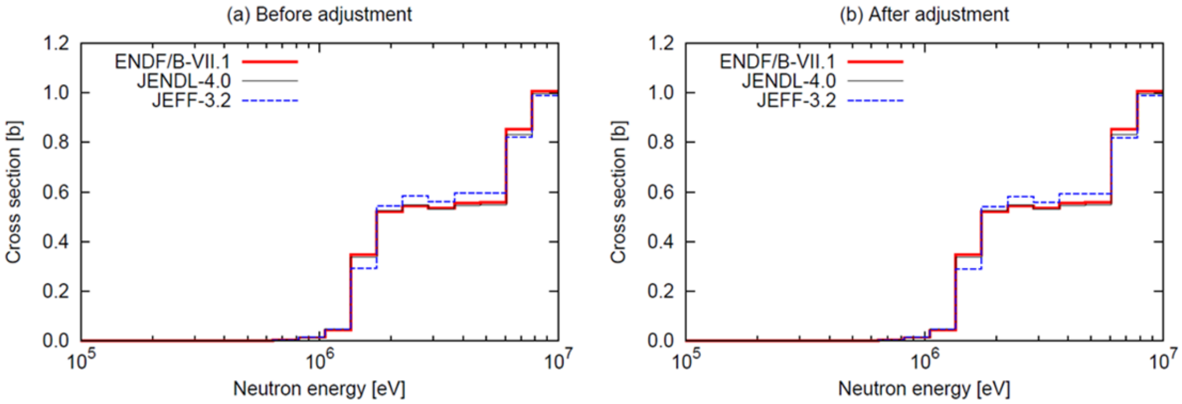

Fig. 7　Fission cross section of U-238

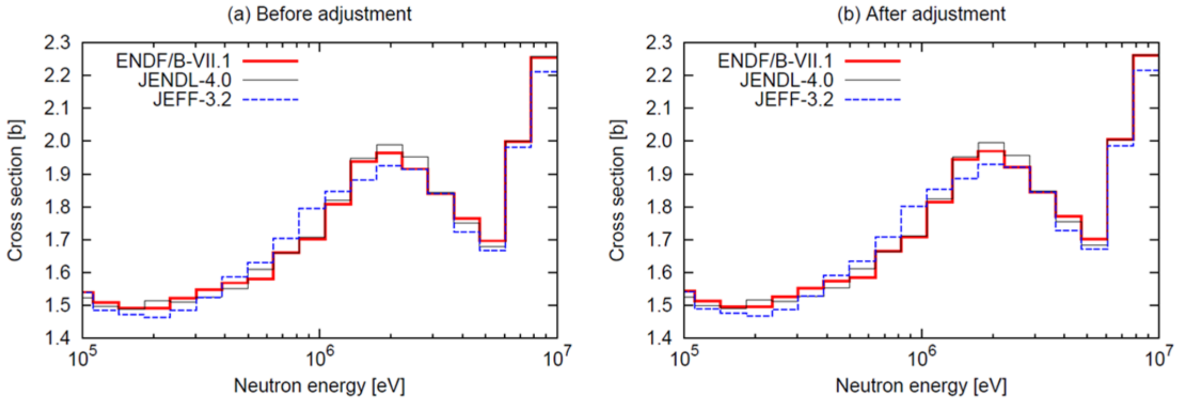

Fig. 8　Fission cross section of Pu-239

Figures 9 and 10 show fission spectra of U-235 and Pu-239, respectively.

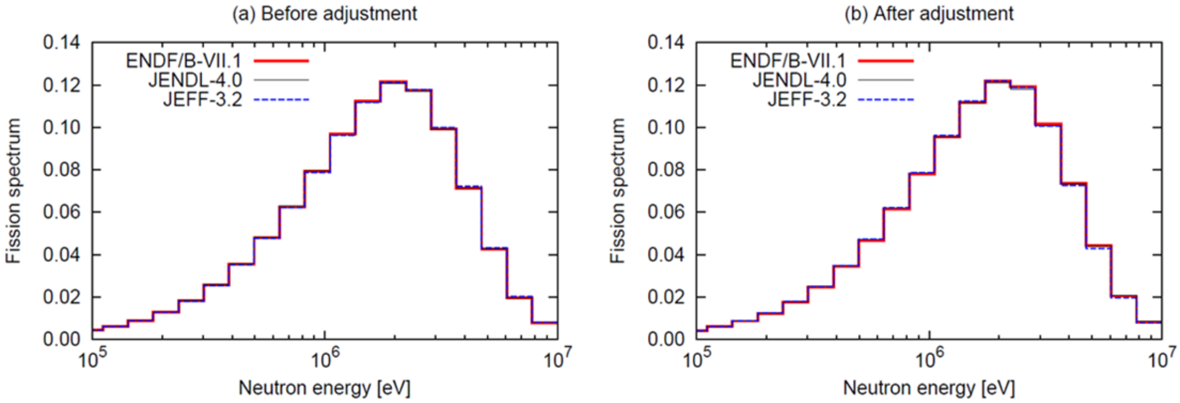

Fig. 9　Fission spectrum of U-235

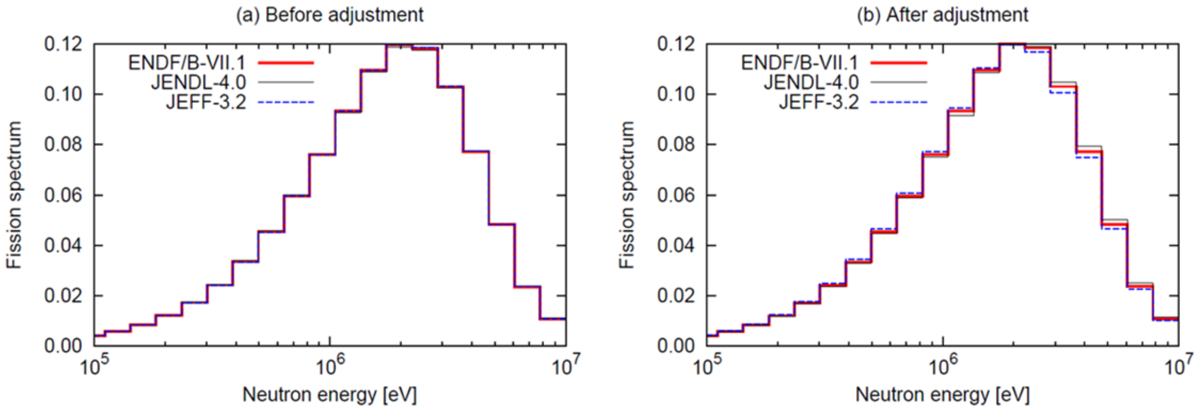

Fig. 10 Fission spectrum of Pu-239

6. Conclusion

Nuclear data given in several modern evaluated nuclear data files are adjusted with integral data sensitive to fast neutron energy range. It has been shown that C/E values of these integral data become close to unity through nuclear data adjustment. This improvement is observed regardless of the original nuclear data files. On the other hand, the adjusted nuclear data significantly depend on the original one; the adjusted nuclear data do not converge to unique value for all the evaluated nuclear data files.

References

[1] A.C. Kahler, et al.: *Nucl. Data Sheets*, **112**, 2997 (2011).

[2] S.C. van der Marck: *Nucl. Data Sheets*, **113**, 2935 (2012).

[3] Summary report: Technical meeting on inelastic scattering and capture cross-section data of major actinides in the fast neutron region, INDC(NDS)-0597, International Atomic Energy Agency, (2012).

[4] M. Ishikawa, et al.: "Development of a unified cross section set ADJ2000 based on adjustment technique for fast reactor analysis," *Proc. Inc. Conf. on Nuclear Data for Sci. and Technol.*, ND2001, Vol. 2, 1073 (2002).

23 Preliminary Calculation with JENDL-4.0 for Evaluation of Dose Rate Distribution in the Primary Containment Vessel of the Fukushima Daiichi Nuclear Power Station

Keisuke OKUMURA
Collaborative Laboratories for Advanced Decommissioning Science, Japan Atomic Energy Agency
Tokai-mura, Naka-gun, Ibaraki-ken 319-1195 Japan

It is important to know the dose rate distribution in the primary containment vessel (PCV) to consider decommissioning strategy of the Fukushima Daiichi nuclear power station. However, the radioactive source distribution has not been clarified yet. The radiation source distribution in PCV was estimated by the help of fuel burn-up calculation, activation calculation of structural materials, and results of severe accident analysis. Finally, the dose rate distribution was calculated by photon transport calculation at each process of the decommissioning. For the above calculations, the nuclear data based on JENDL-4.0 was used.

1. Introduction

In order to examine the decommissioning strategy of the Fukushima-Daiichi Nuclear Power Station (1F), it is important to know the distribution of the radiation sources and dose rate distribution in the primary containment vessel (PCV) to ensure worker’s safety by performing appropriate radiation shielding. There are three kinds of radiation sources in PCV. They are a) fuel debris, b) structures in PCV contaminated with Cs emitted at the 1F accident, and c) activated structures irradiated during normal reactor operation before the accident. In order to establish the evaluation method of the dose rate distribution in PCV, a preliminary calculation was carried out with JENDL-4.0[1] in the following way.

1) burnup calculation to obtain fuel composition at the time of accident, 2) activation calculation for the structural materials including impurities, 3) estimation of Cs contamination in PCV from a result of severe accident analysis, 4) decay calculation of radioactive nuclides in PCV, 5) photon transport calculation to obtain dose rate distribution.

2. Radiation Sources

(1) Fuel debris

The burned fuel composition was evaluated with the use of JENDL-4.0 and an inventory calculation code MOSRA-Superbacon which can consider the three-dimensional burnup and axial void distributions [2]. For the structure materials such as fuel cladding, channel box, spacers, and top and bottom nuzzles of a fuel assembly, additional activation calculations were carried out by using ORIGEN2[3] and revised data library ORLIBJ40[4] based on JENDL-4.0 and JEFF-3.0/A[5]. The important impurities[6] in each structure material were taken into account in the activation calculation. After the isotopes of fuels and structures were mixed, highly volatile nuclides such as Cs, I, and noble gas (Xe, Kr, etc.) isotopes were all released. Since there are so many radioactive nuclides in the fuel debris, the radiation source of the fuel debris was modeled by the photon source with the eighteen-group structure of ORIGEN2. Figure 1 shows the time change of the radiation source of the fuel debris for the Unit 2 of 1F. The intensity and the photon spectrum of the fuel debris don't change drastically after 2020, because of decay of short-lived radioactive nuclides. In this study, radiation source of fuel debris was represented by the photon source at the time of Apr. 2020 in Fig.1.

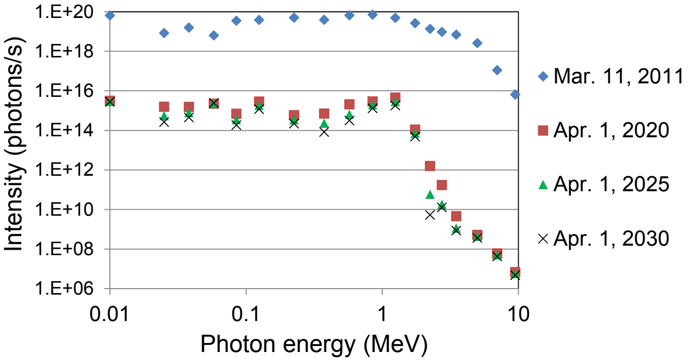

Fig.1 Calculated photon source of fuel debris (Unit 2 of 1F, high volatile FPs are all released.)

(2) ^{60}Co source due to activation of core internals

The radiation source due to activation of core internals such as upper lattice plate and shroud was roughly estimated by the ORIGEN2 calculation. The one-group cross section data of ORIGEN2 was newly generated for each structure from the multi-group activation cross section library MAXS2015[7] and 200-group neutron spectrum obtained by one- or two-dimensional core calculation for the Unit 2 of 1F (1F2) by using the MOSRA-Light code[8]. In the ORIGEN2 calculation, only ^{59}Co of about 0.14 wt% in stainless steel was considered as an impurity in the core internals, because we know ^{60}Co from ^{59}Co(n,γ) reaction is a main contributor to this kinds of radiation source. Based on the activation calculation for about 11 years after the change of core-internals of 1F2, radiation source of ^{60}Co was estimated as 1.7×10^{15} Bq in Apr. 2020. This value has, however, large uncertainty due to many assumptions.

(3) Cs contamination

Since there was no reliable information on radiation source of Cs contaminations in PCV and reactor pressure vessel (RPV), we assumed a radiation source distribution of ^{137}Cs on the basis of a preliminary result obtained by a sever accident (SA) analysis[9] by JAEA. The radioactivity of ^{134}Cs was neglected from the radiation sources because the contribution of ^{134}Cs to the dose rate is sufficiently small compared with that of ^{137}C in 2010 or later. The result of the SA analysis for Cs distribution has a still large uncertainty, but it seems enough to get a qualitative result in this study.

3. Method of Dose Rate Calculation

The calculation of the dose rate distribution in PCV was carried out by using the particle transport simulation code system PHITS[10] based on the Monte Carlo method. The dose rate (exactly, ambient dose equivalent rate) was evaluated by Eq.(1).

$$D(\vec{r}) = \int H^{*10}(E) \emptyset(\vec{r}, E) dE \tag{1}$$

Where, $H^{*10}(E)$ is the flux-to-dose equivalent rate conversion coefficients based on ICRP-74, and $\emptyset(r, E)$ is a photon flux internally obtained by PHITS.

Figure 2 shows the cylindrical model of PCV with the radiation sources for the PHITS calculation. Here, we model the 800MWe grade Mark-I type BWR, which corresponds to the Unit 2 or Unit 3 of 1F. It simulates a situation in which the shield plug, PCV head, RPV lid are dismounted for the fuel debris retrieval.

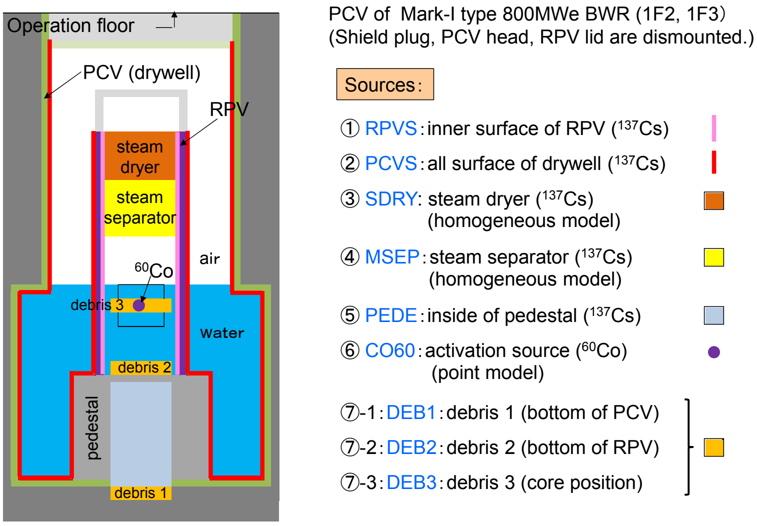

Fig.2 Cylindrical model of PCV and considered photon source distribution for PHITS calculation

To investigate the sensitivity of each radiation source to the dose rate distribution, we considered nine kinds of photon sources: ^{137}Cs on the surfaces of RPV (referred to as ①RPVS) and PCV (②PCVS), ^{137}Cs inside of the steam dryer (③SDRY), steam separator (④MSEP) and pedestal of RPV(⑤PEDE), ^{60}Co in RPV (⑥CO60) which is modeled by a point source, fuel debris at the bottom of the drywell (⑦DEB1), bottom of the RPV(⑧DEB2) and center of the core position (⑨DEB3). The dose rate distribution $D(\vec{r})$ is evaluated as follows,

$$D(\vec{r}) = \sum_{i=1}^{9} \{S_i d_i(\vec{r})\} \tag{2}$$

where, S_i is the intensity of the i-th photon source, $d_i(\vec{r})$ is the dose rate distribution obtained by PHITS for the i-the source with a unit intensity. This method is convenient to understand the contribution of each source for $D(\vec{r})$ when the uncertainty of S_i is large and frequently reevaluated.

As shown in Fig.3, the PHITS calculation was performed for the several cases corresponding to the decommissioning method: (a) Full submersion method, (b) Dry method, (c) Partial submersion method, and (d) situation when both of the steam-dryer and water-steam-separator are dismounted in the Dry method.

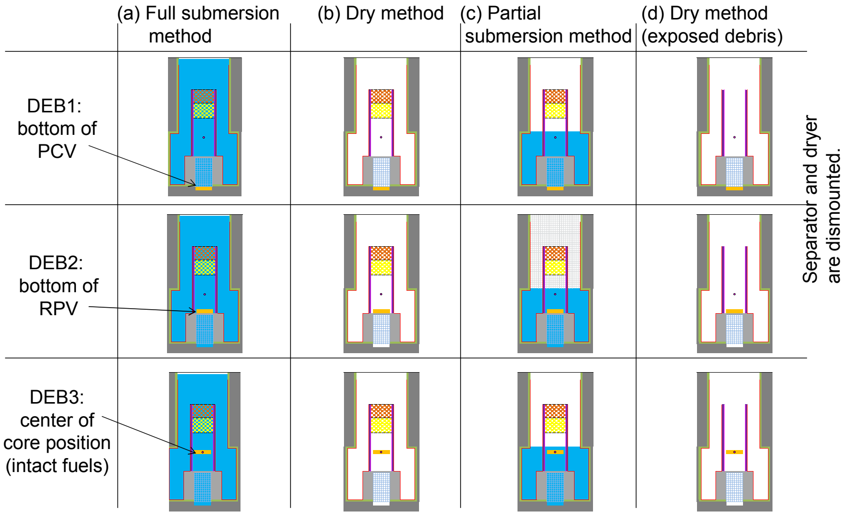

Fig. 3 Calculation cases corresponding to the decommissioning methods (a)-(d)
(water level : (a) top of PCV, (b) no water, (c) upper core position, (d) no water)

4. Result and Discussion

The source dependent dose rate distribution $S_i d_i(\vec{r})$ in each case is shown in Figs.4-7. The left side of each dose rate map corresponds to the top of PCV. From these figures, we can say as follows.

(a) Full submersion method

This method is ideal from the view point of radiation shielding and protection of scattering of radioactive fine particles, if the structural strength of the fully submerged PVC is sufficient, and if the prevention of the re-criticality of the intact fuels in RPV is possible.

(b) Dry method

The radiation sources of ‘PCVS’ (surface of PCV), ‘SDRY’(steam-dryer)’, and ‘RPVS’ (surface of RPV) have a possibility of large contribution to the dose around the operation floor. On the other hand, the radiation from the fuel debris is expected to be shielded by the RPV wall and the upper structures in RPV.

(c) Partial submersion method

Dose rate around the operation floor is almost the same as that of the Dry method, because the upper part of the dose rate is mainly due to the radiation sources ‘PCVS’, ‘SDRY’ and ‘RPVS’. The radiation of fuel debris deeply submerged in the water is not sensitive to the dose rate in the upper air region. It can be said that the measured dose rates by the robot in Unit 1 (B1 investigation) [11] is mainly due to the Cs contamination of the drywell.

(d) Dry method (Exposed debris)

It has a possibility that all of radiation sources including the fuel debris contribute to the dose rate around the operation floor, when the upper steam-dryer and water-steam-separator are dismounted. In this situation, Cs contamination inside of RPV is important and it should be well investigated before decommissioning.

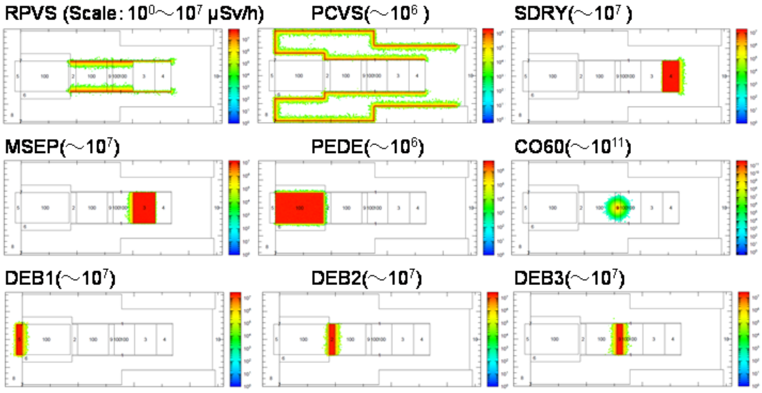

Fig. 4 Source dependent dose rate distribution in PCV for case (a) Full submersion method

(Note: Although the upper scale limit for ‘CO60’ is the largest, this is because activated core-internals are modeled by a point source for simplicity.)

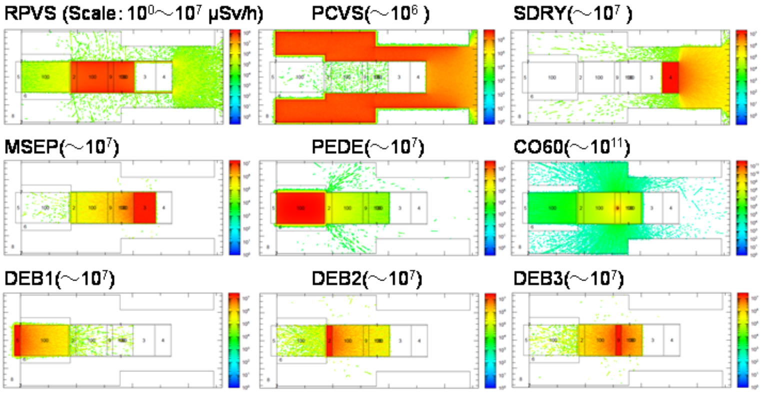

Fig. 5 Source dependent dose rate distribution in PCV for case (b) submersion method

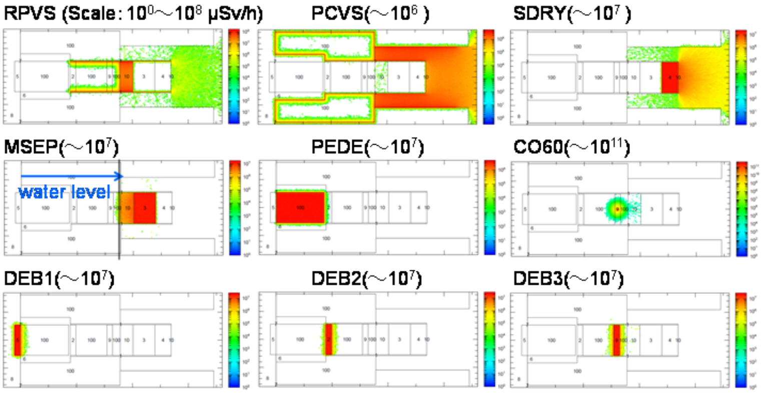

Fig. 6 Source dependent dose rate distribution in PCV for case (c) Partial submersion method

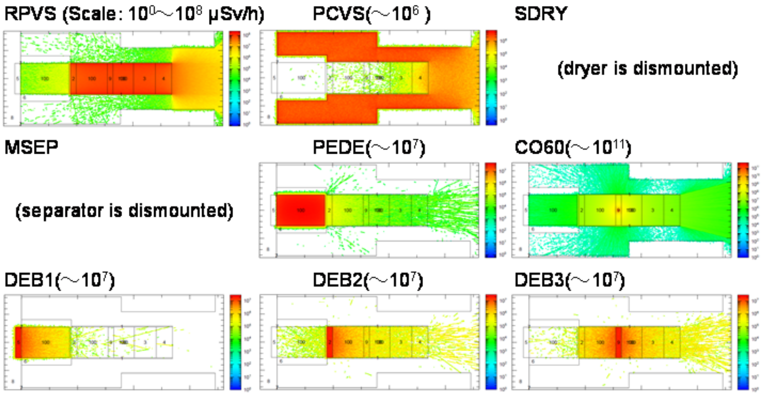

Fig. 7 Source dependent dose rate distribution in PCV for case (d) Dry method

5. Afterword

Through the present study, data and method were developed for future detailed analysis. The data are mainly based on JENDL-4.0. Although this study is qualitative, the result indicates useful information to consider decommissioning strategy of 1F and to improve prediction accuracy of the dose rate distribution. A quantitative evaluation is currently under way by using recent results of SA analyses and a more precise three-dimensional model of PCV.

References

[1] K. Shibata, O. Iwamoto, T. Nakagawa, *et al.*, “JENDL-4.0: A New Library for Nuclear Science and Engineering,” J. Nucl. Sci. Technol. 48[1], 1 (2011).

[2] K. Okumura, K. Kojima, T. Okamoto, *et al.*, “Nuclear Data for Severe Accident Analysis and Decommissioning of Nuclear Power Plant,” JAEA-Conf 2013-002, pp.15-20 (2013).

[3] A.G. Croff, “ORIGEN2: A Versatile Computer Code for Calculating the Nuclide Compositions and Characteristics of Nuclear Materials,” Nucl. Technol. 62, 335 (1983).

[4] K. Okumura, K. Sugino, K. Kojima, *et al.*, “A Set of ORIGEN2 Cross Section Libraries Based on JENDL-4.0: ORLIBJ40,” JAEA-Data/Code 2012-032 (2013) [in Japanese].

[5] J-Ch. Sublet, A. J. Koning, R.A. Forrest, J. Kopecky, “The JEFF-3.0/A Neutron Activation File - EAF-2003 into ENDF-6 format -,” JEFDOC-982, OECD/NEA (2003).

[6] K. Yamamoto, K. Okumura, K. Kojima, T. Okamoto, “Main Generation Pathways of Activation Products for In-core Structure Materials,” JAEA-Research 2013-038 (2014) [in Japanese].

[7] K. Okumura, K. Kojima, K. Tanaka, “Development of multi-group neutron activation cross-section library for decommissioning of nuclear facilities,” JAEA-Conf 2015-003, pp.43-47 (2016).

[8] K. Okumura, “High Speed Three-Dimensional Nodal Diffusion Code for Vector Computers,” JAERI-Data/Code 98-025 (1998).

[9] Y. Maruyama, Private communication (2014).

[10] T. Sato, K. Niita, N. Matsuda, et al., “Particle and Heavy Ion Transport Code System PHITS, Version 2.52,” J. Nucl. Sci. Technol. 50, pp.913-923 (2013).

[11] http://www.tepco.co.jp/en/decommision/planaction/pcv/index-e.html

24 Uncertainty Quantification of Decay Heat Regarding Thorium Fuel

Takanori Kajihara, Go Chiba, and Tadashi Narabayashi

Division of Energy and Environmental Systems, Hokkaido University
Kita13 Nishi8, Kita-ku, Sapporo, Hokkaido, Japan
e-mail: kajihara@eng.hokudai.ac.jp

Recently, thorium fuel has strengthened its presence as an important alternative resource for nuclear fuel. Several pioneering works for reactor physics simulation have been conducted by several countries. One of the most important physical quantities for accident analyses and spent fuel management is decay heat. For the practical thorium fuel usage, uncertainty quantification of decay heat is also essential because nuclear data of thorium-fuel-related nuclides have relatively greater uncertainty compared to conventional-fuel-related ones. This study numerically calculates the decay heat and the uncertainty of decay heat for thorium fuel. As a result, we clarify that the uncertainty of decay heat as for Th fuel is greater than that for conventional fuels from 100,000 seconds to 0.4 years of cooling time and after 1,000 years of cooling time. In the case of pure Th-^{233}U fuel, the uncertainty after 100 years of cooling time is very large: approximately 4 % in 20 GWd/t burn-up and 10 % in 60 GWd/t burn-up. We also identify that the dominant factor of high decay heat uncertainty in Thorium Fuel cycles is capture cross-section of Th-232.

1 Introduction

Recently, thorium has been much acknowledged as an important resource for nuclear fuel. However, the nuclear characteristics of thorium fuels are not so well unraveled compared to conventional fuels. Vast evaluation of reactor physics quantities is necessary to realize thorium fueled reactors. There are some previous works of reactor physics simulation of Thorium Fuel Cycles(ThFCs) for the case of heavy water reactors in Canada[1, 2, 3]. In the European Union, ThFCs of light water reactors have been mainly studied in France. There are some studies of pressurized water reactor neutronic characteristics with thorium fuel[4, 5, 6]. In Japan, there is a ThFCs research of decay heat[7], which is one of the important physical quantities for both accident and nuclear waste analyses.

However, compared to the conventional fuel simulation, the uncertainty of decay heat induced by nuclear data can be greater in the case of thorium fuel because it has to consider the uncertainty of thorium-series nuclides. Hence, uncertainty quantification of decay heat for thorium fuel is essential for high credibility. The motivation of this study is to clarify the uncertainty of decay heat through the comparison between Th and conventional fuels, and identify the causal nuclides inducing high uncertainty of decay heat. It can ascertain the feasibility of the system of ThFCs.

2 Calculation Condition

We calculate decay heat and uncertainty of decay heat for three compositions of Th fuel in PWR. These fuels are Th-^{235}U[8], Th-Pu[9], and Th-^{233}U[10] whose components are shown in **Table 1**. The burn-up of fuel is set 20 GWd/t and 60GWd/t. Linear power density during irradiation is 170 W/cm. The fuel depletion calculation and sensitivity calculation are conducted in pin cell system with CBZ, a general-purpose deterministic reactor physics calculation code system[11]. A burn-up equation is solved by a new numerical method of the matrix exponential, a Mini-Max Polynomial Approximation (MMPA) method[12]. Sensitivities of decay heat are obtained by burn-up sensitivity calculation based on the generalized perturbation theory, and uncertainties are calculated by error propagation calculation using burn-up sensitivity[13, 14]. We adopt JENDL-4.0, JENDL/FPD-2011, and JENDL/FPY-2011[15] as nuclear data, and also use JEFF-3.1.1[16] for complimenting the FPs, which are not included in JENDL.

Table 1: Initial fuel composition

	composition ratio[wt%]				
Nuclide	UO_2	MOX	Th-^{235}U	Th-Pu	Th-^{233}U
Th-232	-	-	75	95.5	96.25
U-233	-	-	-	-	3.75
U-235	4.1	0.18	4.875	-	-
U-238	95.9	89.82	20.125	-	-
Pu-238	-	0.2	-	0.045	-
Pu-239	-	5.5	-	2.79	-
Pu-240	-	2.5	-	1.08	-
Pu-241	-	0.9	-	0.36	-
Pu-242	-	0.6	-	0.025	-
Am-241	-	0.3	-	-	-

3 Result and Discussion

First, we simulate the case of short cooling time (0.1 - 100,000 seconds) after irradiation. **Figures 1** and **2** show relative uncertainties of Th-^{233}U and Th-Pu fuels in 20GWd/t burn-up respectively. Left side figures represent five components of uncertainty: cross section, decay energy, fission yield, half-life, and branching ratio. Right side figures represent comparison between Th fuels and conventional fuels: UO_2 and MOX fuels. In the short cooling time cases, the uncertainties of all Th fuels do not change significantly till about 1,000 seconds of cooling time when we compare them with that of UO_2 and MOX fuels. The result of Th-^{235}U case is similar to those of Th-^{233}U case. Dominant source of increasing uncertainty is cross-section of a few nuclides. Around 10,000 seconds, capture cross-section of Th-232 is main source of uncertainty according to a sensitivity analysis.

Next, we calculate the case of long cooling time (0.1 - 1,000 years). **Figures 3**, **4**, and **5** show relative uncertainties of Th-^{235}U, Th-^{233}U, and Th-Pu fuels in 20GWd/t burn-up respectively. Left side figures represent components and right side figures represent comparison with conventional fuels. When we see the longer cooling time scale, the uncertainties are greater at the early part and around 1,000 years of cooling time. In both areas, the influence of uncertainties induced by cross section is significant. The contributed nuclides through early part are Th-232

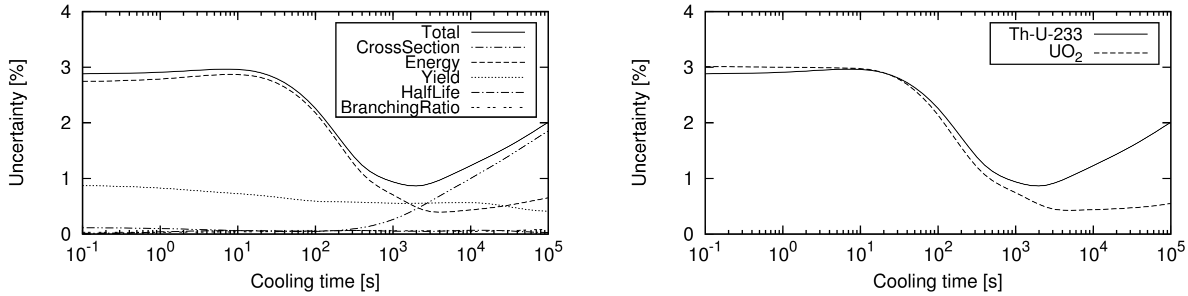

(a) uncertainty component

(b) comparison with UO$_2$ fuel

Figure 1: Th-U-233 decay heat uncertainty in 20GWd/t burn-up.

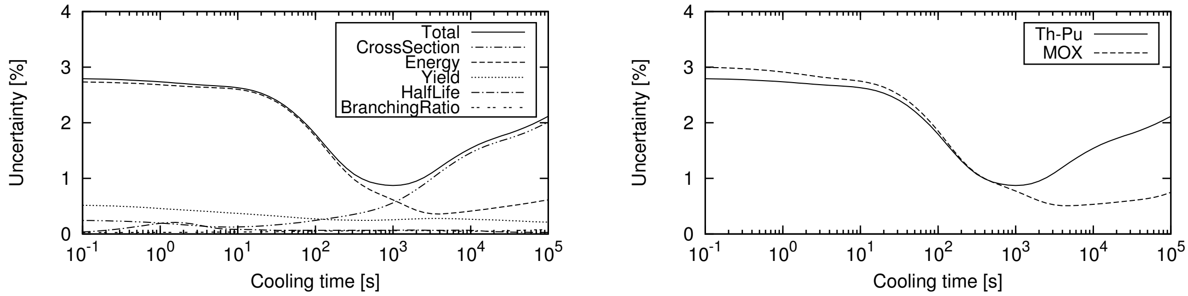

(a) uncertainty component

(b) comparison with MOX fuel

Figure 2: Th-Pu decay heat uncertainty in 20GWd/t burn-up.

in all cases. In the case of Th-^{233}U, uncertainties after 100 years are large, which is the influence of Th-232. On the other hand, the uncertainty of Th-Pu fuel is slightly greater compared with a MOX fuel. These gaps are induced by the capture and fission cross-sections of Th-232 at 10 years and capture cross-section of Th-232 at 300 years.

Figures 6 and **7** show relative uncertainty of Th-^{235}U and Th-^{233}U in the burn-up of 60GWd/t. In the case of high burn-up fuel, 60GWd/t, the gap between Th-fuels and conventional fuels become much larger. The uncertainty of Th-^{235}U fuel reaches about 4% at 1,000 year, and that of Th-^{233}U fuel reaches about 10% at 1,000 year. The main factors with high contribution to the uncertainty are capture cross-section of Th-232. The contribution of the capture and fission cross-section of U-233 is only 5% of total cross-section-induced uncertainty. It indicates that obtaining the additional data of capture cross-section of Th-232 can reduce uncertainty of decay heat in THFCs significantly.

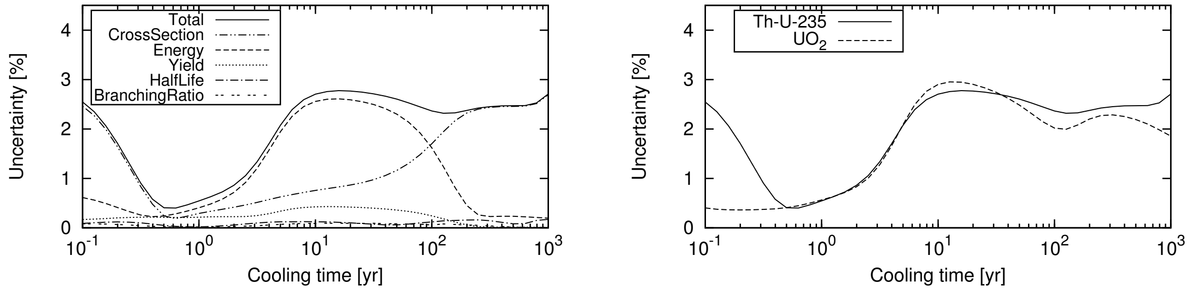

(a) uncertainty component

(b) comparison with UO$_2$ fuel

Figure 3: Th-U-235 decay heat uncertainty in 20GWd/t burn-up.

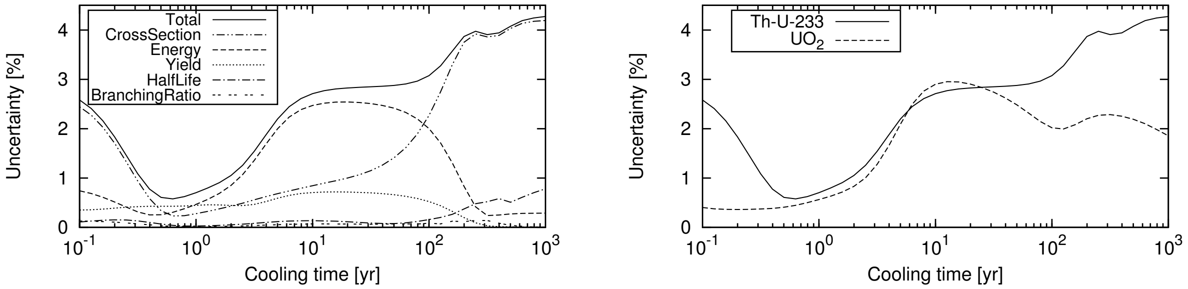

(a) uncertainty component (b) comparison with UO$_2$ fuel

Figure 4: Th-U-233 decay heat uncertainty in 20GWd/t burn-up.

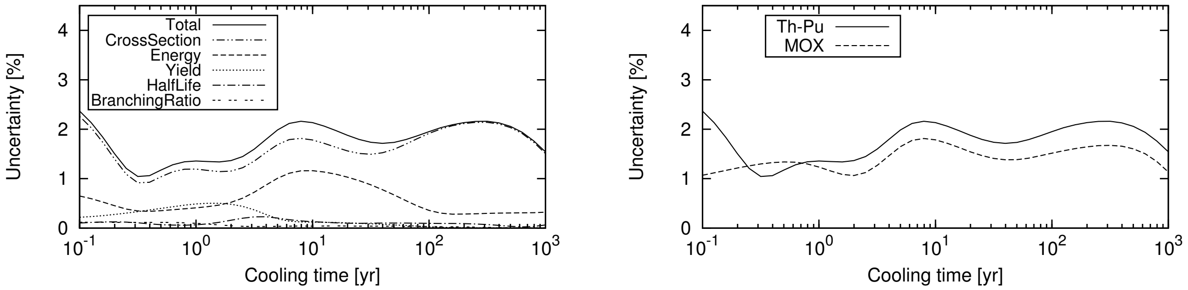

(a) uncertainty component (b) comparison with MOX fuel

Figure 5: Th-Pu decay heat uncertainty in 20GWd/t burn-up.

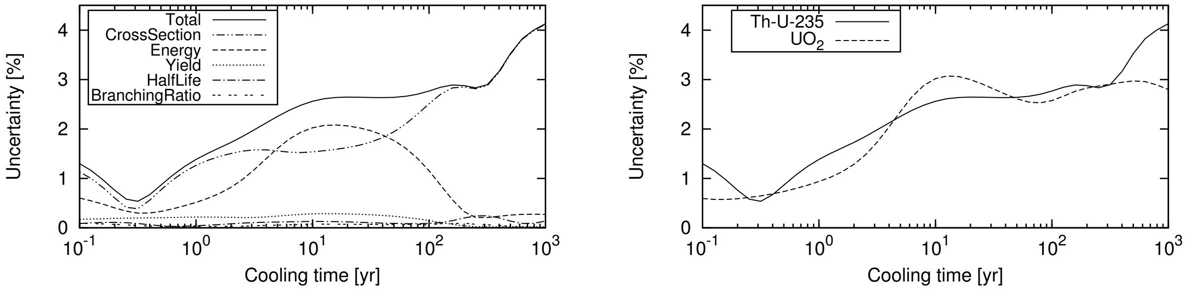

(a) uncertainty component (b) comparison with UO$_2$ fuel

Figure 6: Th-U-235 decay heat uncertainty in 60GWd/t burn-up.

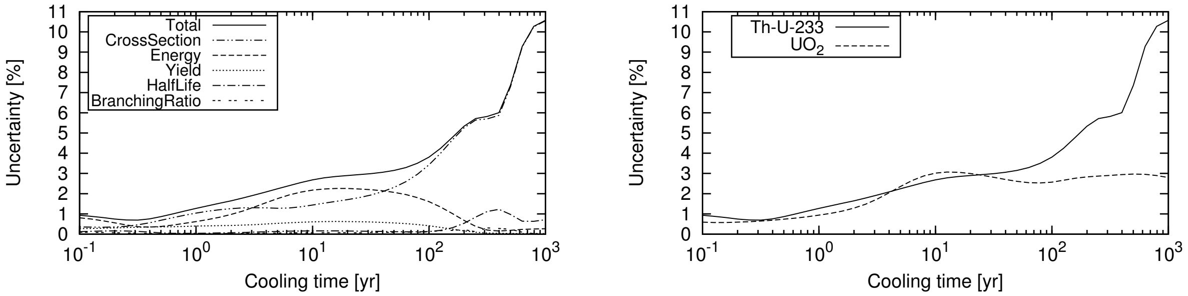

(a) uncertainty component (b) comparison with UO$_2$ fuel

Figure 7: Th-U-233 decay heat uncertainty in 60GWd/t burn-up.

4 Conclusion

Through the uncertainty quantification of decay heat regarding thorium fuels, we have clarified the difference between Th fuel and conventional fuel. It is relatively high from 100,000 seconds to 0.4 years and after 100 years. We have also identified that desirable nuclear data to reduce the uncertainty of decay heat are capture cross-section of Th-232.

References

[1] D.V. Antiparmakov, New Capabilities of the Lattice Code WIMS-AECL. Proc. of PHYSOR 2008; 2008 Sep.14-19; Interlaken(Switzerland).

[2] T. Liang *et al.*, Improvement and Qualification of WIMS Utilities. Proc. of 29th CNS annual Conf.; 2008; Tronto(Canada).

[3] W. Shen *et al.*, Evolution of Computer Codes for CANDU Analysis. Proc. of PHYSOR 2010; 2010 May. 9-14; Pittsburgh(U.S.).

[4] IAEA, Thorium Fuel Utilization: Options and Trends. IAEA-TECDOC-1319. Viena. IAEA; 2003. pp.185-197.

[5] European Commission, Thorium as a Waste Management Option. Report EUR-19142. Brussels. EC; 2000.

[6] IAEA, Role of Thorium to Supplement Fuel Cycles of Future Nuclear Energy Systems. Report NF-T-2.4. Viena. IAEA; 2012. pp.38-48.

[7] M. Usui *et al.*, Decay Heat Analysis of Thorium Fuel Used in a Light Water Reactor. Proc. of AESJ 2012 Autumn; 2012 Sep.19-21; Hiroshima(Japan).[in Japanese].

[8] X. Zhao *et al.*, A PWR Thorium Pin Cell Burnup Benchmark. Proc. of PHYSOR2000; 2000 May 7-11; Pittsburgh(U.S.).

[9] IAEA, Potential of Thorium Based Fuel Cycles to Constrain Plutonium and Reduce Long Lived Waste Toxicity. IAEA-TECDOC-1319. Viena. IAEA; 2002.

[10] H. Yamana *et al.*, Recent Research Trends of Thorium Fuel Cycle, Nihon-Genshiryoku-Gakkai Shi(J. At. Energy Soc. Jpn.). 2005; 47(12) [in Japanese].

[11] G. Chiba *et al.*, Uncertainty Quantification of Neutronic Parameters of Light Water Reactor Fuel Cells with JENDL-4.0 Covariance Data. J. Nucl. Sci. Technol. 2013 Jul; 50:751-760

[12] Y. Kawamoto *et al.*, Numerical Solution of Matrix Exponential in Burn-up Equation Using Mini-max Polynomial Approximation. Ann. Nucl. Energy. 2015; 80 .

[13] T. Takeda *et al.*, Burnup Sensitivity Analysis in a Fast Breeder Reactor Part I: Sensitivity Calculation Method with Generalized Perturbation Theory. Nucl. Sci. Soc. 1985; 91 .

[14] T. Kajihara *et al.*, Uncertainty Quantification of Nuclear Reactor Decay Heat. Proc. of RPHA 2015; 2015 Sep. 16-18; Jeju(Korea).

[15] J. Katakura, JENDL FP Decay Data File 2011 and Fission Yields Data File 2011. JAEA-Data/Code 2011-025. 2011.

[16] A. Santamaria *et al.*, The JEFF-3.1.1 nuclear data library. OECD/NEA Data Bank. 2009.

This is a blank page.

25 A function formation of source neutron production by the ^{9}Be + p reaction at 7 MeV at RANS

Yasuo Wakabayashi[1], Atsushi Taketani[1], Yoshimasa Ikeda[1], Takao Hashiguchi[1],
Tomohiro Kobayashi[1], Sheng Wang[2, 1], Mingfei Yan[2, 1], Masahide Harada[3],
Yujiro Ikeda[3, 1] and Yoshie Otake[1]
[1]RIKEN Center for Advanced Photonics, RIKEN
[2]School of Energy and Power Engineering, Xi'an Jiaotong University
[3]J-PARC Center, Japan Atomic Energy Agency
E-mail : y.wakabayashi@riken.jp

A function to give the neutron energy spectrum and angular distribution in the ^{9}Be + p reaction with less than 12 MeV of incident proton energy has been newly formed and implemented in simulation codes in order to calculate the source neutron spectrum of RIKEN Accelerator-driven compact Neutron Source (RANS). The function was created by fitting available experimental data for neutron production with thin beryllium target at low energy proton beams, which were referred from ENDF and ENSDF data bases. For confirmation of the fitting function, the neutron energy spectra produced by the ^{9}Be + p reaction with thick beryllium target were compared with two experimental data and MCNPX calculation.

1. Introduction

Neutrons with wide energy range from cold- to fast-neutron are used for not only the fundamental researches but also various applications. As one of application, fast neutron can be used for non-destructive inspection of large concrete structure, such as highways, bridges and boating docs. Thermal neutrons are used for neutron radiography, so called neutron scattering experiments, etc, for various materials sciences. To meet increasing demands for neutron, RIKEN Accelerator-driven compact Neutron Source (RANS)1) has been constructed and operated since 2013. At RANS, protons of 7 MeV are injected to a 300-um-thick target to generate neutrons via the ^{9}Be + p reaction. Then, most of their energy is slowed down to be thermal neutrons through a 4-cm-thick polyethylene moderator. Still there should be a fraction of fast neutron remained. These fast- and thermal-neutrons extracted from the moderator are transported through a neutron guide hole to the camera box where a sample is located. It is essential to know neutron energy spectrum and angular distribution of the ^{9}Be + p reaction with thick beryllium target for not only characterizing RANS but also a development of compact neutron source. In particular, the neutron spectrum flux is key information of the experiment. To simulate the neutron yields, the simulation codes such as MCNPX2), PHITS3), and GEANT44) have been used. However, these simulations have not always reproduced the experimental data5) well at an energy region such less than 10 MeV, because nuclear reaction models of these simulators are optimized at more than 100 MeV. To obtain reliable neutron spectrum for RNAS, we have made newly a dedicated function based on existing experimental data using the ^{9}Be + p reaction with thin beryllium targets6–11). In this paper, we describe the procedure to form the function and the adequacy of the function is verified by comparing the calculation with implemented function and experimental measurement.

2. Method

To make the function for the neutron yield generated by the ^{9}Be + p reaction, the experimental data using thin beryllium targets6-11) were obtained from EXFOR12) and ENSDF13) data bases. These incident proton energies (E_p) were less than 18 MeV. For thin target experiment, a total cross section ($\sigma(E_p)$) at certain E_p is represented as

$$\sigma(E_p) = \int \frac{d\sigma(E_p)}{d\Omega} = \iint \frac{d^2\sigma(E_p)}{d\ \Omega d\mathrm{E_n}}$$

where dσ, Ω , and $\mathrm{E_n}$ indicate differential cross section, solid angle, and neutron energy, respectively. From this equation, angular distribution against the reaction angle (θ) in the ^{9}Be + p reaction should be determined as a function of E_p , and also the neutron energy spectrum can be decided as a function of E_p and θ considering kinematics and reaction Q-value. For thick target experiment, the total neutron yield is obtained by integrating that of thin target experiments, that is, $\int \sigma(E_p)dE_p$. From this relation, we adopt three functions for total cross section, angular distribution, and energy spectrum.

Firstly, the total cross sections (TCS) are fitted up to E_p = 12 MeV by a formula,

$$\mathrm{TCS}\ (E_p) = [\mathrm{a}] \cdot {E_p}^{[\mathrm{b}]} \cdot e^{-[\mathrm{c}]\cdot E_p} \cdot ln(E_p - [\mathrm{d}]) + \text{Breit-Wigner(1peak)} + \text{Gaussian(3peaks)} \quad (1),$$

where [a] – [d] are constant. The result is shown in Fig. 1.

As second step, angular distributions (ACS) at several E_p as shown in Fig. 2 are fitted by Legendre polynomial expanded up to third order,

$$\mathrm{ACS}(\theta) = \Sigma\, \mathrm{A_j}\, \mathrm{P_j}(\cos\theta)$$
$$= \mathrm{TCS}(E_p) \cdot \mathrm{C} \cdot (\,[\mathrm{e}] + [\mathrm{f}](\cos\theta) + [\mathrm{g}](\cos\theta)^2 + [\mathrm{h}](\cos\theta)^3) \qquad (2),$$

where [e] – [h] are the fitting parameters obtained by interpolating between E_p = 2.56 and 18 MeV as function of "E_p", and "C" is a normalization factor, which adjust an integration of ACS(θ) to TCS(E_p) at certain E_p. The results of our function are drawn in Figure 2.

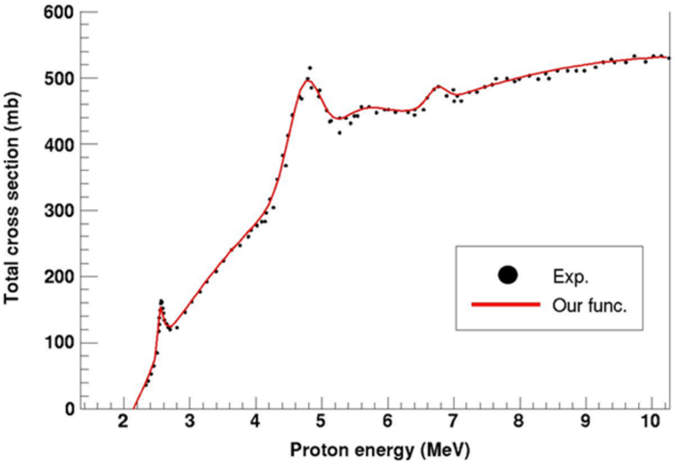

Figure 1 : Total cross section of neutron produced by the ^{9}Be + p reaction with thin beryllium target. Experimental data from references[6, 7] are used.

As final step, the neutron energy spectra (ECS) of experimental values plotting in Fig.3 are fitted by a formula consists of continuum part and peaks of transitions from the excited states in ^{10}B to the ground and excited states in ^{9}B.

ECS(En) = Continuum + Peaks of transition to ground state, 1st Ex, and 2nd Ex in ^{9}B

$$= \mathrm{ACS}(\theta) \cdot \{\,[1]/\,(1 + \mathrm{e}^{\frac{\mathrm{En}-[2]}{[3]}} + [4] \cdot log[([5]-\mathrm{En})^2 + 1]\,)/(1 + \mathrm{e}^{\frac{\mathrm{En}-\mathrm{En\_max}}{0.001}}) + [6] \cdot \mathrm{e}^{-\left(\frac{\mathrm{En}-[7]}{[8]}\right)^2} + [9] \cdot \mathrm{e}^{-\left(\frac{\mathrm{En}-[10]}{[11]}\right)^2} + [12] \cdot \mathrm{e}^{-\left(\frac{(\mathrm{En}-[13])}{[14]}\right)^2}\} \qquad (3),$$

where [1] – [14] are the fitting parameters as the function of "E_p" to reproduce the energy spectrum and "En" represents neutron energy. This function used the maximum neutron energy (En_max) from kinematics between E_p and θ considering Q-value of ^{9}Be + p reaction.

Then, we can get total cross section, angular distribution, and neutron energy spectrum at certain E_p and θ. To obtain thick target yield of neutron, the Monte Carlo calculation is performed by incorporating our function and the energy loss calculation in the target material by SRIM code[14)]. Our function needs only E_p and target thickness as input parameters. At this moment, this calculation is done by ROOT framework[15)].

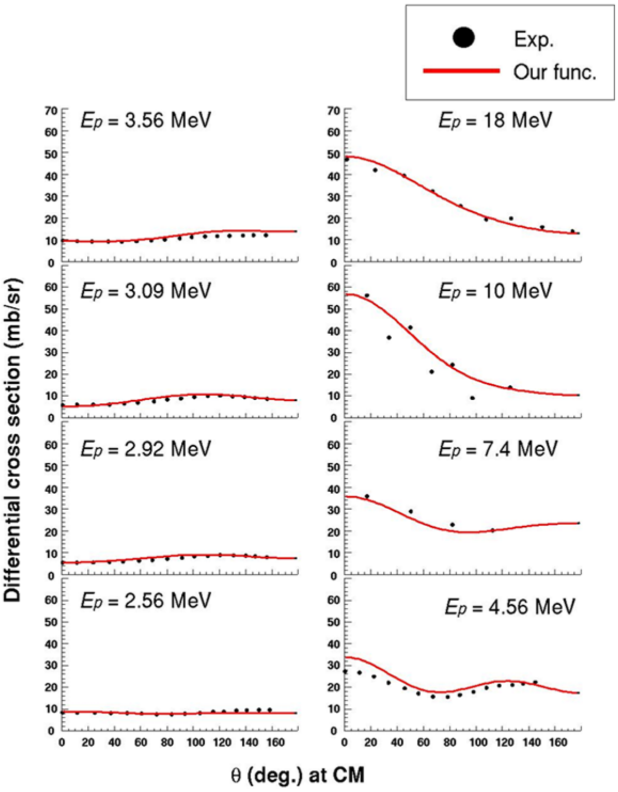

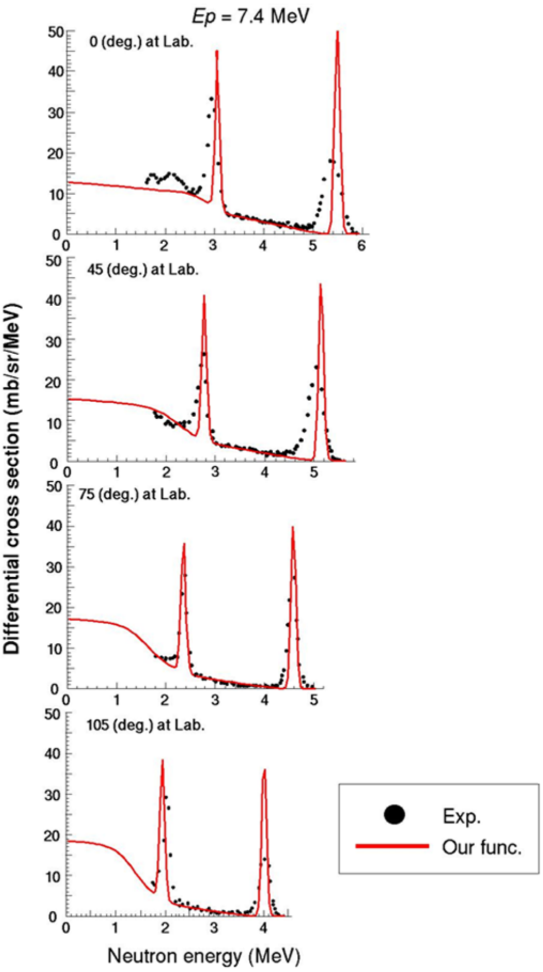

Figure 2 : Angular distribution of neutron with thin target. The experimental data[8-11)] and our function are compared.

Figure 3 : Neutron energy spectrum in laboratory system with thin target. Black dots indicate the experimental data[9)].

3. Result

In order to evaluate our fitted function, the neutron energy spectra are compared with those of experimental data [5)] and MCNPX ver. 2.7.0 with Bertini model as shown in Fig. 4. The experimental conditions were E_p = 11 MeV and 2-mm-thick beryllium target. The neutron energy spectra were measured from 0.5 MeV up to 9 MeV. Our function generally well reproduces the experimental spectra at each angle in comparison with MCNPX calculation, though the higher energy region has some discrepancy. Especially, they agree very well on the energy regions from 1 MeV to 7 MeV. Another experimental data[16)] with E_p =

4 MeV and 0.25- or 0.5-mm-thick beryllium target which covers neutron energy from 0.1 MeV up to 2.2 MeV is also compared in Fig. 5. Our calculation agrees well up to the highest energy at each angle. However it overestimates in the low energy region such as less than 0.3 MeV. This discrepancy is caused by lack of data points for low energy region of neutron energy spectra in referred thin target experiments[9, 10]. It will be resolved by referring thick target experiment measured until low neutron energy.

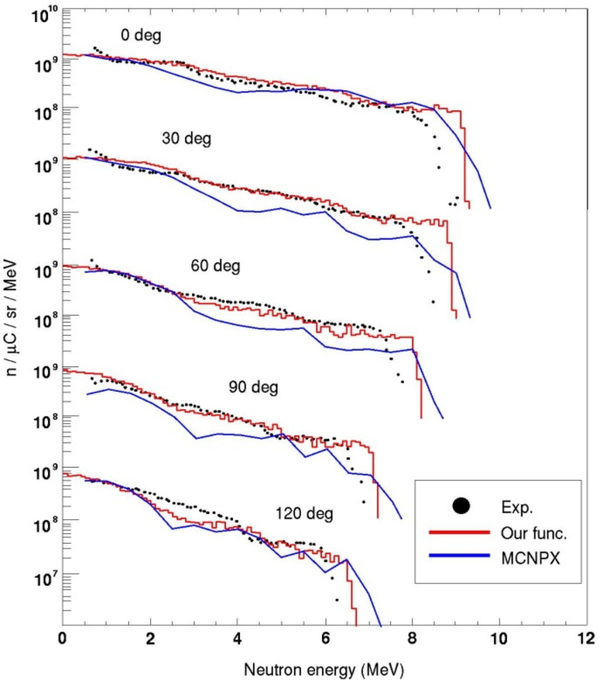

Figure 4 : Neutron energy spectrum in laboratory system with thick beryllium target. Black dots indicate the experimental data[5].

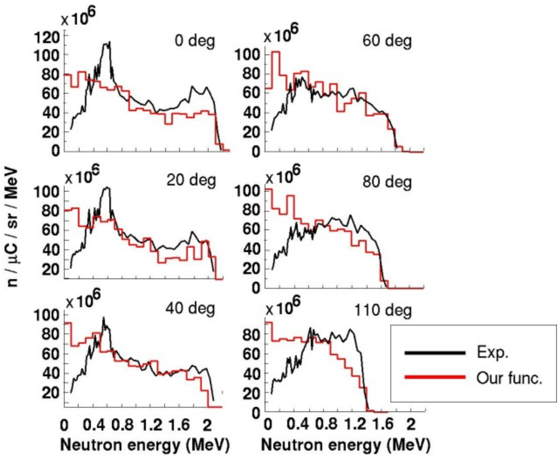

Figure 5 : Neutron energy spectrum in laboratory system with thick beryllium target. Black line is the experimental data[16].

4. Summary

We made the original function to reproduce energy spectra and angular distributions of neutrons produced by the ^{9}Be + p reaction for RANS from existing experimental results. The neutron energy spectra calculated by this function were compared with experimental data and MCNPX. The neutron energy spectra by the function agree fairly well with experimental data except for discrepancy at low energy less than 0.3 MeV and high energy larger than 7 MeV. We confirmed validity of the method with the function based on experimental base nuclear data to simulate the p-Be source neutron production and the approach could be applicable to other reaction, such as p-Li, d-Be, etc., as far as suitable number of valid experimental data exist.

References

[1] Y. Otake, Rev. Laser Engineering, **43**, vol. 2, p.71 (2015).
[2] M. B. Chadwick *et al*., Nucl. Sci. Eng. **131**, p.293 (1999).
[3] K. Niita *et al*., JAEA-Data/Code 2010-022 (2010).
[4] http://geant4.cern.ch
[5] S.Kamada, Jour. Of Korean Phys. Soc. **59**, p.1676 (2011).
[6] J.H.Gibbons and R.L.Macklin, PR **114**, p.571 (1959).
[7] J.K.Bair *et al*., NP **53**, p.209 (1964).
[8] J.B.Marion *et al*, PR **103**, p.713 (1956).
[9] R.W.Bauer *et al*., NP **56**, p.117 (1964).
[10] Y. Iwamoto *et al*., NIM A**598**, p.687 (2009).
[11] V.V.Verbinski *et al*., PR **177**, p.1671 (1969).
[12] http://www.nndc.bnl.gov/exfor/exfor.htm
[13] http://www.nndc.bnl.gov/ensdf/
[14] J.F.Ziegler *et al*, The stopping and Range of Ions in Solids, Pergamon Press, 1985
[15] https://root.cern.ch
[16] W.B.Howard *et al*., Nuclear Science and Engineering, Vol.**138**, p.145 (2001).

26 Evaluation of Neutron Cross Sections of ^{93}Nb in the Energy Range between 10^{-5} eV and 20 MeV

Akira ICHIHARA
Nuclear Data Center, Japan Atomic Energy Agency
Tokai-mura, Naka-gun, Ibaraki-ken, 319-1195, Japan
e-mail: ichihara.akira@jaea.go.jp

Neutron cross sections of ^{93}Nb in JENDL-4.0 were reexamined in the incident energy (E_n) range between 10^{-5} eV and 20 MeV. Resonance parameters were assessed by referring to the published experimental and recommended data. Above the resonance region, cross sections were calculated using the CCONE system. We adjusted spin cutoff factors in nuclear level densities to reproduce measured cross sections for metastable state production (MSP). The obtained MSP cross section for the (n,n') reaction was in good agreement with the experimental data compared with the evaluated data in JENDL/A-96.

1. Introduction

In 2015 we started a new activity for the next version of Japanese Evaluated Nuclear Data Library, JENDL-4.0. The next JENDL is planned to contribute to nuclear transmutation for the disposal of nuclear wastes. The evaluation activity will be focused on structural materials in atomic energy power plants, and metastable state production (MSP) data will be added to the library.

The ^{93}Nb isotope, whose isotopic abundance is 100 % in nature, is being employed in high-melting point alloys. Besides, ^{93}Nb is useful as a component of superconductor alloys in fusion reactors. Moreover, the reaction ^{93}Nb(n,n')^{93m}Nb is important as a long-term activation monitor in reactor dosimetry, owing to its long half-life (~16 y) and low threshold (~31 keV).

In this work, we investigated the resonance parameters in JENDL-4.0 on the basis of the experimental and recommended data. Also, for the incident neutron energy $E_n \geq 7$ keV, we calculated cross sections by the comprehensive nuclear data evaluation code CCONE [1]. It should be pointed out that enough MSP data are not provided in general purpose libraries such as ENDF/B-VII.1, JEFF-3.2 and JENDL-4.0. In JENDL-4.0, no MSP data is included for ^{93}Nb. Although MSP data are available in the activation library JENDL/A-96 [2], the appreciable deviation from measured data is observed in the ^{93}Nb(n,n')^{93m}Nb reaction. Thus we tried to reproduce the measured MSP cross sections.

2. Evaluation

(1). Resonance Parameters

The multilevel Breit-Wigner (MLBW) formula is used for thermal and resonance cross sections. A negative resonance parameter is applied to produce the thermal cross sections. In JENDL-4.0, total 194 resonance parameters have been compiled in the range from 35.9 eV to 7 keV. The resonance parameters by Drindak et al. [3] have been adopted up to 501 eV. These parameters are thought to be most accurate at present. In the range 501 eV $\leq E_n \leq$ 2.6 keV, we confirmed that most neutron and radiative widths $2g\Gamma_n$ and Γ_γ (g: statistical weight factor) agree with the recommended values of Mughabghab [4] within his estimated errors. In $2.6 \leq E_n \leq 7$ keV, the resonance parameters have been evaluated using the quantity $g\Gamma_n\Gamma_\gamma/\Gamma$ (Γ: total width) of Macklin [5]. The original data have been multiplied by 1.0737 according to the corrigendum.[6] Mughabghab adopts the original values of Macklin.[5] In JENDL-4.0, the resonance parameters were evaluated by using the corrected $g\Gamma_n\Gamma_\gamma/\Gamma$ values and the width parameters derived by Macklin,[5] Garg et al. [7] and Poittevin et al.[8] If their data are not available, the average radiative widths 0.172 and 0.212 eV were employed for the s- and p- wave resonances, respectively. To estimate unknown spin values of resonance states, the JCONV code [9] has been used.

(2). Theoretical Calculation

The ^{93}Nb data above the resonance region were calculated by the CCONE code [1]. Most parameter values applied were taken from our previous work [10]. The optical model potentials (OMP) for spherical nuclei were employed to obtain neutron elastic scattering cross sections and reaction cross sections for neutrons, protons, deuterons, tritons, ^{3}He and ^{4}He particles. In the statistical model computations, level density parameter values in [10] were utilized. Also, parameters in the γ-ray strength functions were taken from [10] except for ^{94}Nb. In ^{94}Nb, the γ-ray strength function was normalized to produce $2\pi\langle\Gamma_{\gamma0}\rangle/D_0 = 9.5 \times 10^{-3}$, where $\langle\Gamma_{\gamma0}\rangle$ is the average radiative width for s-wave resonances and D_0 is the s-wave average level spacing. In the preequilibrium computations based on two-component exciton model and the Kalbach pickup and knockout formulations [11], the parameters were adjusted to reproduce the preequilibrium spectra obtained in [10]. Moreover, contribution of inelastic scattering was supplemented with the distorted-wave Born approximation (DWBA) computation. The DWBA cross sections were calculated using deformation parameters and excitation energies suggested by Marcinkowski et al., ($\beta_{l=2}$=0.13, 0.95 MeV) and ($\beta_{l=3}$=0.18, 2.3 MeV) [12].

In our previous study [10], we concentrated our attention on the reproducibility of measured cross sections. There, deviations from measured MSP data were observed. We tried to reproduce measured MSP cross sections by adjusting spin cutoff factors in nuclear level densities. In the present calculation, the Mengoni-Nakajima factors [13] in the statistical model were multiplied by 1.2 and 1.1 for ^{93}Nb and ^{91}Nb, respectively. Moreover, in ^{93}Nb, the spin cutoff factor of the preequilibrium model was multiplied by 1.3.

3. Results

Figures 1 and 2 show the average total and capture cross sections in the range $2 \leq E_n \leq 8$ keV. The experimental data were obtained from the EXFOR data base [14], where the index "02 Grigoriev+" indicates the measurements by Grigoriev et al. in 2002. In Figs.1-2, the average cross sections which were evaluated using the original data of Macklin and the recommended data of Mughabghab are also shown by dotted lines. It is seen that the evaluated average cross sections lie near the measured data. If the original data of Macklin are employed, the resulting cross sections would be slightly lower than the JENDL-4.0 evaluations in the range $3 \leq E_n \leq 7$ keV.

Figure 3 shows the total cross section obtained from the spherical neutron OMP in [10]. It is seen that the experimental cross section is reproduced quantitatively. Neutron emission cross sections of this work were calculated by employing transmission coefficents derived from this OMP. Figure 4 shows the (n,n') cross sections, where the measured MSP data after 1980 are shown. The JENDL/A-96 evaluation seems to be appreciably lower than the measured data. The present MSP cross section is consistent with the measured data.

The evaluation of MSP cross sections for the (n,γ), (n,2n) and (n,3n) reactions are in progress.

4. Conclusion

We surveyed resonance parameters in JENDL-4.0 on the basis of the published experimental and recommended data. We confirmed how they were derived. It is noted that the original data of Macklin were multiplied by 1.0737 and applied to JENDL-4.0. Above the resonance region, the cross sections were calculated by the CCONE code. We adjusted spin cutoff parameters in nuclear level densities to reproduce the measured MSP cross sections. In the (n,n') reaction, we could obtain the MSP cross section which is in good agreement with the experiments compared with JENDL/A-96.

References

[1] O. Iwamoto et al., "The CCONE Code System and its Application to Nuclear Data Evaluation for Fission and Other Reactions", Nuclear Data Sheets **131**, 259 (2016).

[2] Y. Nakajima and JNDC WG on Activation Cross Section Data, *JENDL-Activation Cross*

Section File, JAREI-M 91-032, p.43, (1991).

[3] N. J. Drindak et al., “Neutron Capture and Transmission Measurements and Resonance Parameter Analysis of Niobium”, Nucl. Sci. Eng., **154**, 294 (2006).

[4] S. F. Mughabghab, *Atlas of Neutron Resonances*, Elsevier, Amsterdam, 2006.

[5] R. L. Macklin, “Neutron Capture Cross Section of Niobium-93 from 2.6 to 7 keV”, Nucl. Sci. Eng., **59**, 12 (1976).

[6] R.L. Macklin and R.R. Winters, “Stable Isotope Capture Cross Sections from the Oak Ridge Electron Linear Accelerator”, Nucl. Sci. Eng., **78**, 110 (1981).

[7] J.B. Garg et al., “Neutron Resonance Spectroscopy. V. Nb, Ag, I, and Cs”, Phys. Rev. **137**, B547 (1965).

[8] G.L. Poittevin et al., “Determination of the Strength functions S_0 and S_1 in Nb by Identification of the Nature of Neutron Resonances”, Nucl. Phys. **70**, 497 (1965).

[9] T. Nakagawa et al., “Auxiliary Programs for Resonance Parameter Storage and Retrieval system REPSTOR”, JAERI-Data/Code 99-030 (1999).

[10] A. Ichihara et al., “Calculation of Neutron Cross Sections on ^{93}Nb for JENDL-4”, J. Nucl. Sci. Technol., **45**, 793 (2008).

[11] C. Kalbach, “The Griffin Model, Complex Particles and Direct Nuclear Reactions”, Z. Phys. **A283**, 401 (1977).

[12] A. Marcinkowski et al., “Neutron Emission Cross Sections on ^{93}Nb and ^{209}Bi at 20 MeV Incident Energy”, Nucl. Phys. **A530**, 75 (1991).

[13]A. Mengoni and Y. Nakajima, “Fermi-gas Model Parametrization of Nuclear Level Density”, J. Nucl. Sci. Technol. **31**, 151 (1994).

[14]O. Schwerer, editor, *EXFOR Formats Description for Users (EXFOR Basics)*, IAEA-NDS-206, International Atomic Energy Agency (2008).

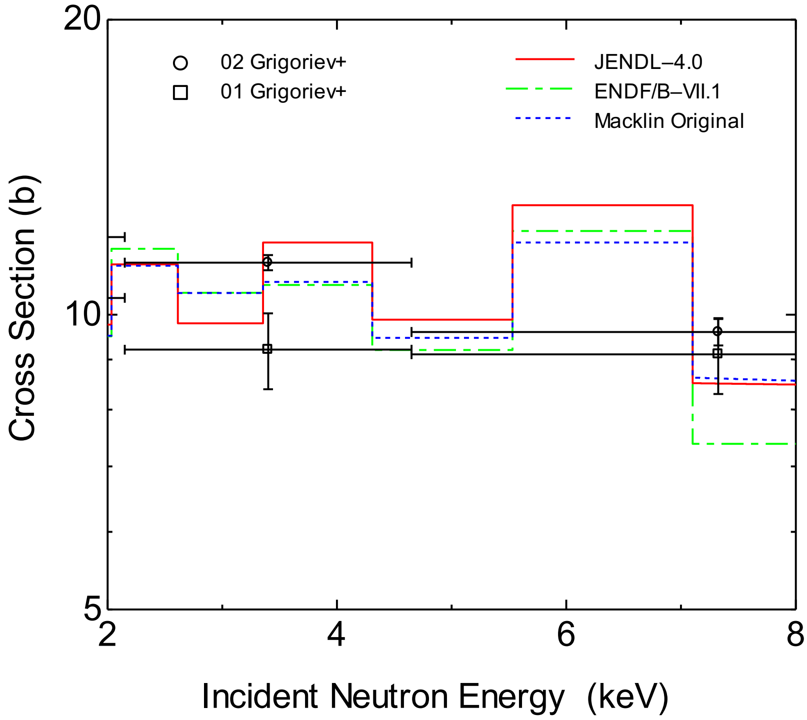

Fig.1 Average total cross section of ^{93}Nb evaluated from the resonance parameters.

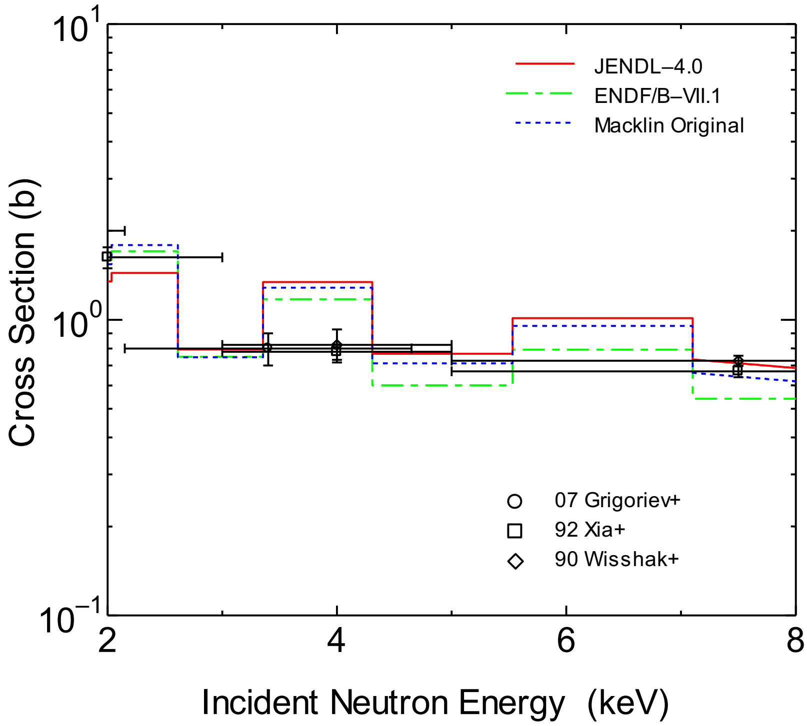

Fig.2 Average (n,γ) cross section of ^{93}Nb evaluated from the resonance parameters.

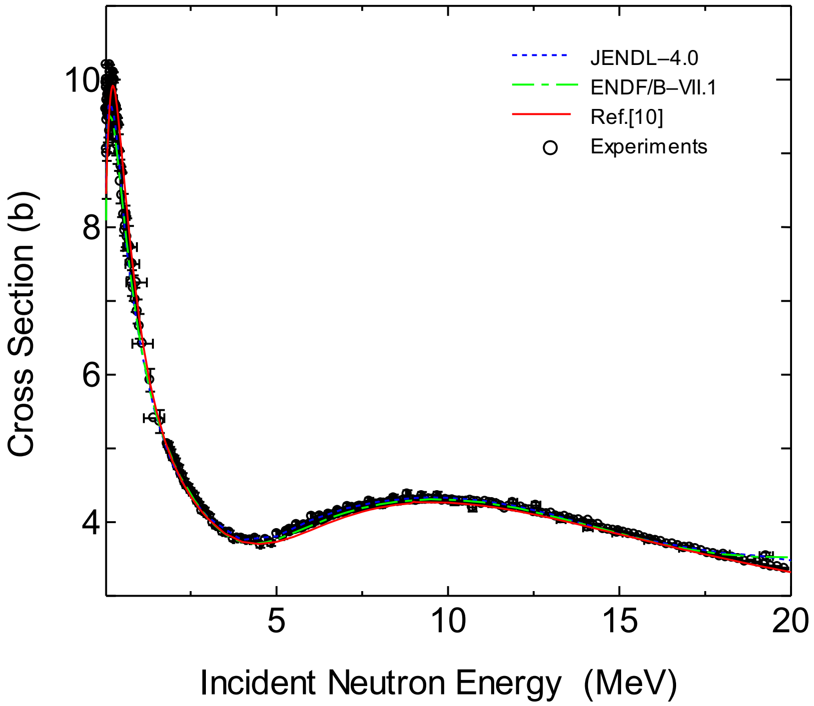

Fig.3 Total cross section of ^{93}Nb calculated with the optical model potential [10].

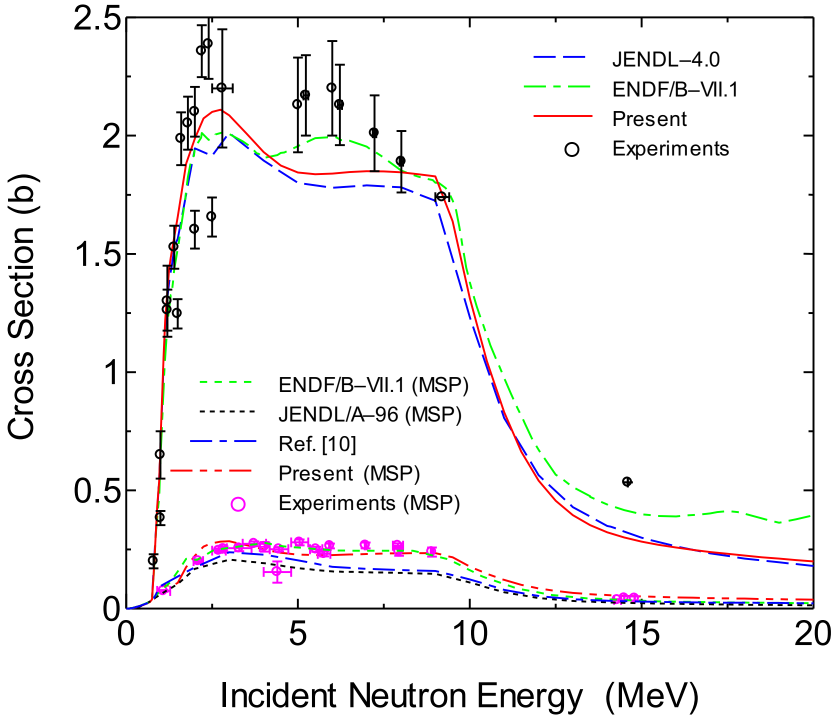

Fig.4 ^{93}Nb (n,n') cross section and the MSP component.

27 Evaluation of neutron nuclear data on copper isotopes by a consistent method

Shinsuke NAKAYAMA

Nuclear Data Center, Japan Atomic Energy Agency
2-4 Shirakata, Tokai-mura, Naka-gun, Ibaraki 319-1195, Japan
E-mail: nakayama.shinsuke@jaea.go.jp

Copper is an important element relevant to heat sink material for fusion reactors, structural material for accelerator-driven systems, and so on. In addition to more precise neutron nuclear data on copper isotopes, covariance data are currently required. Towards preparation of covariance data, we evaluated neutron nuclear data on ^{63,65}Cu by a consistent method. All cross sections and angular distributions for the neutron induced reactions on ^{63,65}Cu were consistently calculated using the CCONE code in the energy range from 50 keV to 20 MeV. The dispersive optical model potential was adopted with a couple-channel method for the interaction between neutron and ^{63,65}Cu. Compound, pre-equilibrium and direct processes were considered for calculation. The calculated results are in good agreement with measured data of cross sections as well as angular distributions for ^{63,65}Cu and natural targets.

1. Introduction

Copper is an important element relevant to heat sink material for fusion reactors, structural material for accelerator-driven systems, and so on. Therefore, more precise neutron nuclear data on copper isotopes are currently required. In addition, covariance data are also required to estimate uncertainties of various integral quantities obtained from calculation using the nuclear data. Covariance includes correlated uncertainties between different nuclear data, e.g. cross sections of different reactions. In evaluation on ^{63,65}Cu of JENDL-4.0 [1], the neutron total cross sections on ^{63,65}Cu were obtained from least-square fit to experimental data of natural Cu. In addition, the cross sections and angular distributions for several reactions were calculated by various computational codes such as SINCROS-II [2], GNASH [3] and so on. Towards preparation of covariance data, it is desirable that neutron nuclear data on ^{63,65}Cu are calculated by a consistent method, namely one code and consistent model input parameters. In the present study, we evaluate all cross sections, angular distributions for the neutron induced reactions on ^{63,65}Cu in the energy range from 50 keV to 20 MeV using only the CCONE code [4, 5], which was successfully applied to neutron nuclear data evaluation on various nuclei of JENDL-4.0.

2. Optical model calculation

In the present optical model calculation, the dispersive optical model potential (OMP) by Soukhovitskii et al. [6] with a couple-channel method was adopted for the interaction between neutron and ^{63,65}Cu. In the dispersive OMP, a connection between the real and imaginary parts of potential is given by the dispersion relation as described in Ref. [6]. This dispersive constraint helps us to reduce the number of parameters of OMP. This is favorable to evaluate covariance data by propagating uncertainties of model input parameters to those of cross sections. The parameters of OMP were decided based on the works by Hao et al. [7, 8]. The coupling scheme and deformation parameters are given in **Table 1**. The deformation parameters were decided so as to reproduce the measured total cross sections and elastic scattering angular distributions simultaneously.

Table 1. Coupling scheme and deformation parameters

	Coupled levels J^π (E_x in MeV)	β_2
^{63}Cu	$3/2^-$(g.s.), $5/2^-$(0.962), $7/2^-$(1.327)	-0.1788
^{65}Cu	$3/2^-$(g.s.), $5/2^-$(1.116), $7/2^-$(1.482)	-0.1542

The calculated neutron total cross sections on natural Cu are shown in **Figure 1** together with the evaluated data of JENDL-4.0, which were obtained from least-square fit to experimental data. In this figure, the total cross sections calculated using the spherical OMP of Koning and Delaroche [9] and the couple-channel OMP of Kunieda et al. [10] are shown, respectively. The present result is in better agreement with the experimental data than the ones using the two typical OMPs. **Figures 2 and 3** show the calculated neutron elastic scattering angular distributions on ^{63}Cu and ^{65}Cu, respectively. The elastic angular distributions of JENDL-4.0, ENDF/B-VII.1 [11], and JEFF-3.2 [12] are also shown. The present results reproduce the experimental data better than the other evaluated data.

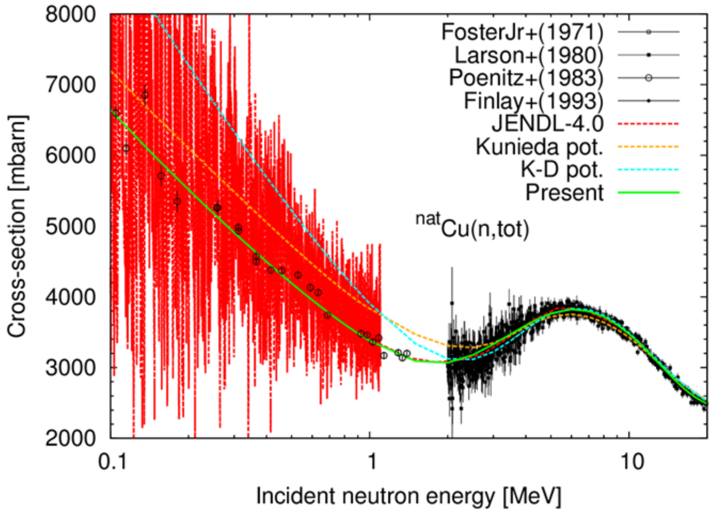

Figure1. Neutron total cross sections on natural Cu

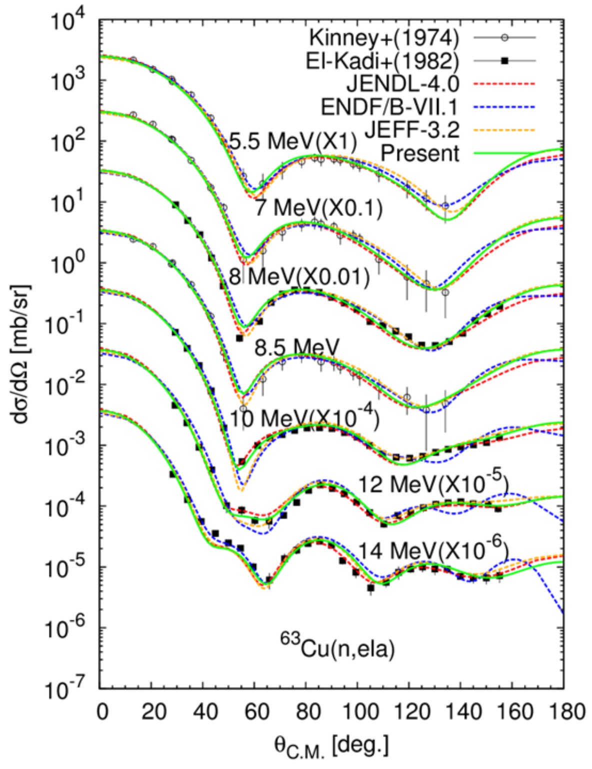

Figure 2. Neutron elastic scattering angular distributions on ^{63}Cu

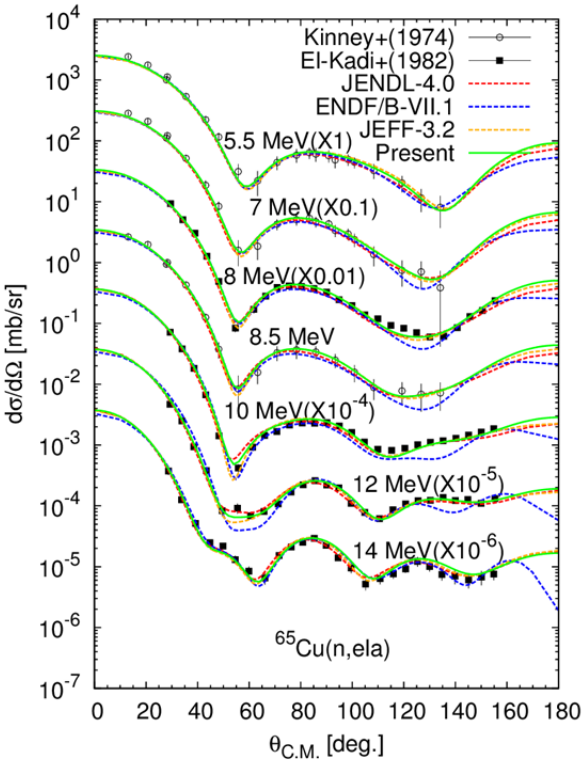

Figure 3. Same as Figure 2 but for ^{65}Cu

3. Evaluated results of reaction cross sections

In the present study, each reaction cross sections were calculated by the theoretical nuclear reaction models implemented in the CCONE code. Direct component of neutron inelastic scattering are calculated by the distorted wave Born approximation (DWBA). Cross sections of the equilibrium and pre-equilibrium decay processes are calculated by the Hauser-Feshbach statistical model and two component exciton models, respectively. In addition, information of discrete levels was taken from RIPL-3 [13]. Level density was adopted from the formulation of Mengoni and Nakajima [14]. The OMPs for the particles other than neutron were taken from Koning and Delaroche [9] for protons, An and Cai [15] for deuterons, Becchetti and Greenlees [16] for tritons and ^{3}He, and Avrigeanu et al. [17] for α-particle.

Figures 4 and 5 show the calculated neutron inelastic scattering angular distributions on ^{63}Cu and ^{65}Cu, respectively. It should be noted that the direct components of inelastic scattering corresponding to the second (J^{π}=5/2$^-$) and third (J^{π}=7/2$^-$) excited states were obtained from the couple-channel optical model calculation as shown in Table 1. Contributions from the first excited state were calculated by the DWBA and the deformation parameters β_2 were evaluated as 0.05 for both ^{63}Cu and ^{65}Cu. The present results reproduce the experimental data as well as the other evaluated data.

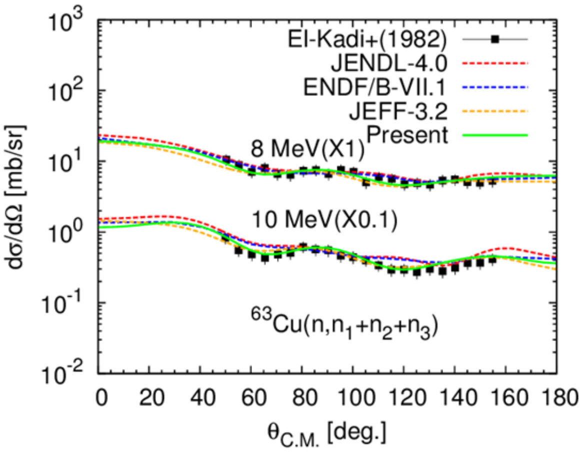

Figure 4. Neutron inelastic scattering angular distributions on ^{63}Cu

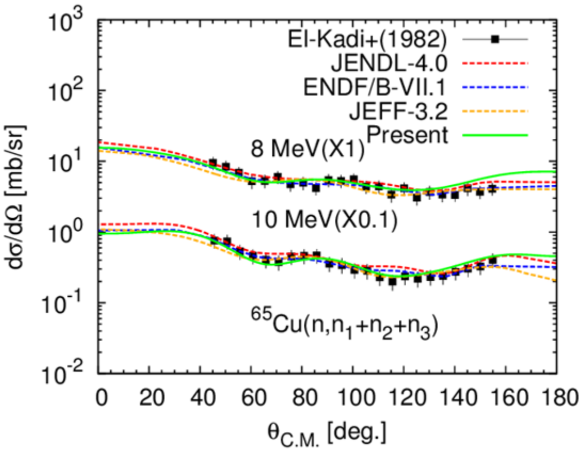

Figure 5. Same as Figure 4 but for ^{65}Cu

The calculated results of (*n*,*2n*) reactions on ^{63}Cu and ^{65}Cu are shown in **Figures 6 and 7**. As shown in Figure 6, the experimental data of ^{63}Cu(*n*,*2n*) cross sections have three trends in the high energy region although those of ^{65}Cu(*n*,*2n*) cross sections show good agreement with each other. We evaluated the cross sections of ^{63}Cu(*n*,*2n*) so as to reproduce the experimental data of $^{63,65,\mathrm{nat}}$Cu(*n*,*2n*) reactions consistently. As a result, the present evaluation of ^{63}Cu(*n*,*2n*) cross sections shows agreement with the data of ENDF/B-VII.1 and JEFF-3.2.

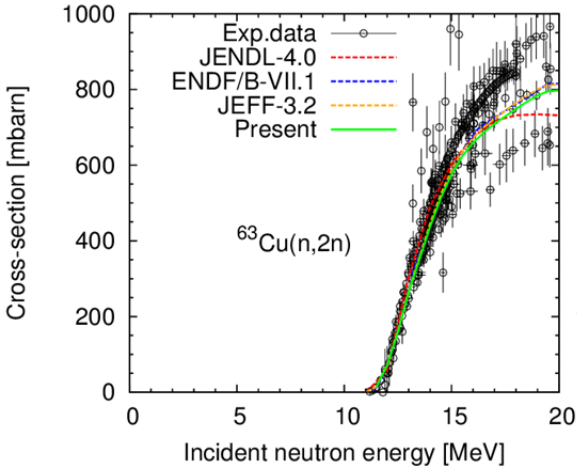

Figure 6. ^{63}Cu(*n*,*2n*) cross sections

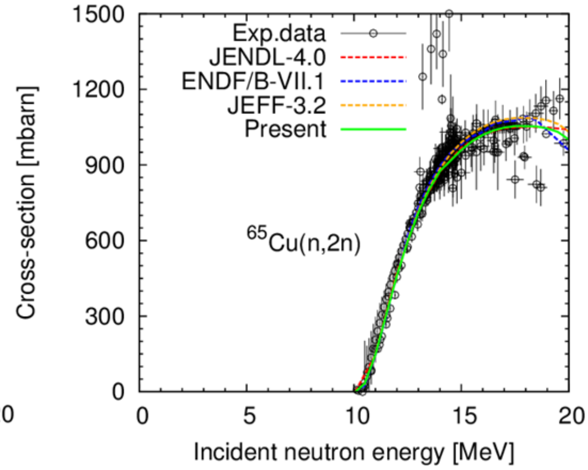

Figure 7. Same as Figure 6 but for ^{65}Cu

Figures 8 and 9 show the calculated radiative capture cross section of ^{63}Cu and ^{65}Cu, respectively. In addition, the calculated results of charged particle emission reactions are shown in **Figures 10 and 11**. As shown in these figures, the present results are in agreement with JEFF-3.2, which is the recently updated nuclear data library.

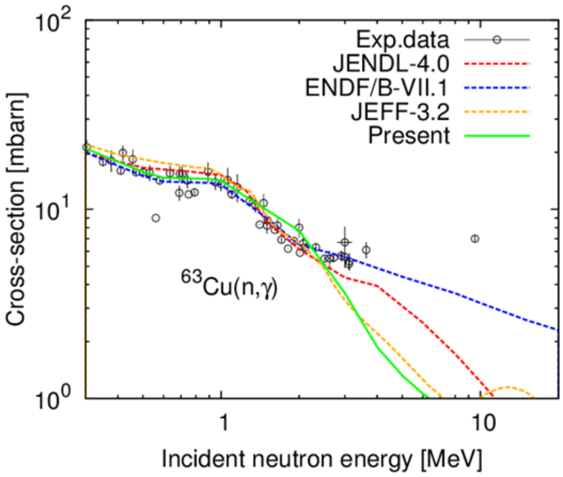

Figure 8. Radiative capture cross section of ^{63}Cu

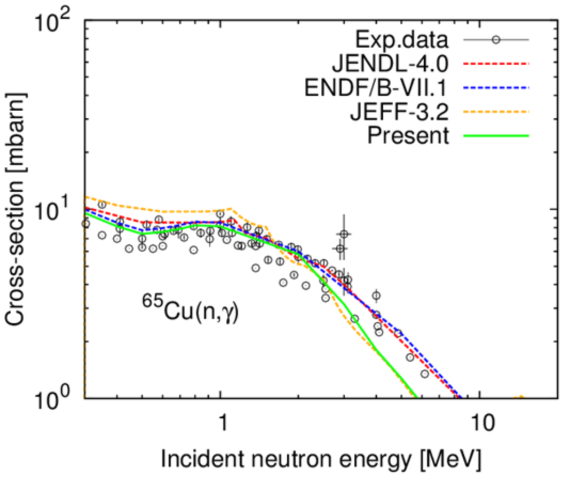

Figure 9. Same as Figure 7 but for ^{65}Cu

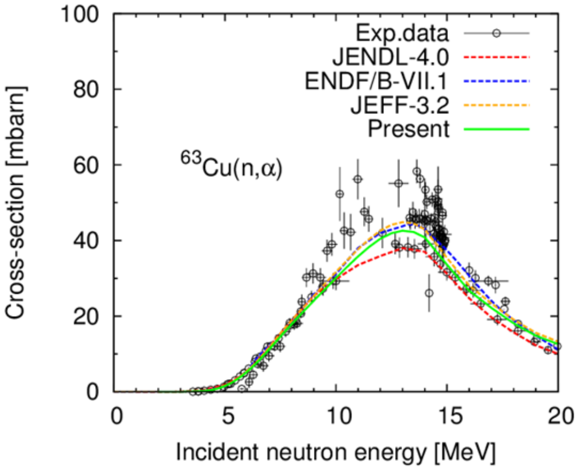

Figure 10. ^{63}Cu(n, α) cross sections

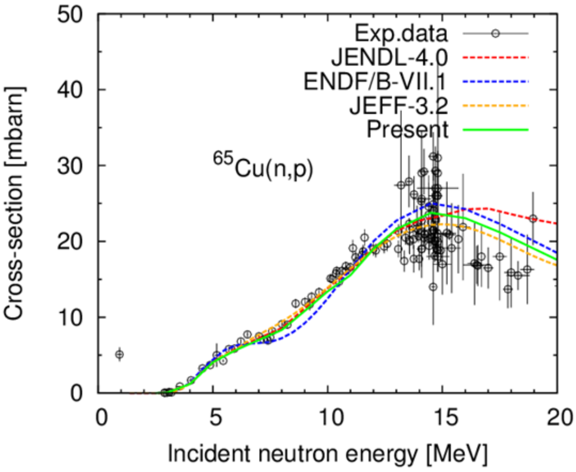

Figure 11. ^{65}Cu(n, p) cross sections

4. Summary and outlook

Towards preparation of covariance data, neutron nuclear data on ^{63,65}Cu were evaluated in the energy range from 50 keV to 20 MeV by using the CCONE code. The dispersive optical model potential was adopted with a couple-channel method for the interaction between neutron and ^{63,65}Cu. The consistently calculated results well reproduced the available measured cross sections and angular distributions. Based on these results, we plan to evaluate covariance data on copper isotopes in the fast energy region.

On the other hand, the resent benchmark experiment suggests that the neutron nuclear data on copper isotopes of JENDL-4.0 might have some problems in the low energy region [18]. Therefore, we will reevaluate nuclear data on copper isotopes in the low energy region, especially resonance data.

Acknowledgments

The author wish to thank the members of the Nuclear Data Center, Japan Atomic Energy Agency, for fruitful discussion and comments on this work.

References

[1] Shibata K, Iwamoto O, Nakagawa T, Iwamoto N, Ichihara A, Kunieda S, Chiba S, Furutaka K, Otuka N, Ohsawa T, Murata T, Matsunobu H, Zukeran A, Kamada S, Katakura. J. Nucl. Sci. Technol. 2011; 48:1-30.

[2] Yamamuro N. JAERI-M 1990; 90-006.

[3] Young PG, Arthur ED. 1977; LA-6974.

[4] Iwamoto O, J. Nucl. Sci. Technol. 2007; 44:687-697.

[5] Iwamoto O, Iwamoto N, Kunieda S, Minato F, Shibata S. Nucl. Data Sheets 2016; 131:259-288.

[6] Soukhovitskii ESh, Capote R, Quesada JM, Chiba S. Phys. Rev. C 2005; 72:024604.

[7] Hao L, Sun W, Soukhovitskii ESh. J. Phys. G Nucl. Part. Phys. 2008; 35:095103.

[8] Hao L, Sun W, Soukhovitskii ESh. JAEA-Conf 2009-004, pp.95-100.

[9] Koning AJ, Delaroche JP. Nucl. Phys. A 2003; 713:231-310.

[10] Kunieda S, Chiba S, Shibata S, Ichihara A, Soukhovitskii ESh. J. Nucl. Sci. Technol. 2007; 44:838-852.

[11] Chadwick MB, Herman M, Oblozinsky P, Dunn ME, Danon Y, Kahler AC, Smith DL, Pritychenko B, Arbanas G, Arcilla R, Brewer R, Brown DA, Capote R, Carlson AD, Cho YS, Derrien H, Guber K, Hale GM, Hoblit S, Holloway S, Johnson TD, Kawano T, Kiedrowski BC, Kim H, Kunieda S, Larson NM, Leal L, Lestone JP, Little RC, McCutchan EA. Nucl. Data Sheets 2011; 112:2887-2996.

[12] Pereslavtsev P, Fischer U, Konobeyev A, Sobes V, Leal L. Nucl. Data Sheets 2014; 118:158-160.

[13] Capote R, Herman M, Oblozinsky P, Young PG, Goriely S, Belgya T, Ignatyuk AV, Koning AJ, Hilaire S, Plujko VA, Avrigeanu M, Bersillon O, Chadwick MB, Fukahori T, Zhigang G, Yinl H, Kailas S, Kopecky J, Maslov VM, Reffo G, Sin M, Soukhovitskii ESh, Talou P. Nucl. Data Sheets 2009; 110:3107-3214.

[14] Mengoni A, Nakajima Y. J. Nucl. Sci. Technol. 1993; 31:151-162.

[15] An H, Cai C. Phys. Rev. C 2006; 73:054605.

[16] Becchetti FD Jr., Greenlees GW. 1969 Ann. Rept. J.H.Williams Lab. Univ. Minnesota

[17] Avrigeanu V, Hodgson PE, Avrigeanu M. Phys. Rev. C; 1994; 49:2136-2141.

[18] Kwon S, Sato S, Ohta M, Ochiai K, Konno C. Fusion Eng. Des.; 2016 *in press*.

28 ^{3}H Photonuclear Data Evaluation and Preliminary Study of Reduction of ^{3}H Density in Waste Water by Photon Irradiation

Toru Murata[1], Kazuaki Kosako[2], Nobuyuki Iwamoto[3],
[1]*Former JENDL Committee, Nuclear Science and Engineering Center, Japan Atomic Energy Agency, Tokai Ibaraki 319-1195, Japan*
[2]*Shimizu Corporation, 3-4-17 Etchujima, Koto-ku, Tokyo 135-8530, Japan*
[3]*Nuclear Data Center, Nuclear Science and Engineering Center, Japan Atomic Energy Agency, Tokai, Ibaraki 319-1195, Japan*

The nuclear data of photo-reactions on tritium (^{3}H) were evaluated using the moving deuteron model, which postulates that ^{3}H is a composite nucleus of deuteron and neutron. Experimental cross sections were reproduced well with the model. Feasibility to reduce ^{3}H density in a waste water using bremsstrahlung photons was estimated by Monte Carlo simulation. It is found that quite small depletion rate is obtained, and thus, this method does not seem to be feasible.

1 Introduction

Tritium (^{3}H) is a radioactive nuclide with the half-life of 12.32 years. It is generated by the ternary fission of ^{235}U and ^{239}Pu, and ^{6}Li(n,t) reaction in nuclear reactors. The waste water including ^{3}H, which is stored in the Fukushima dai-ichi nuclear power station, is increasing and has become problematic. It is needed to dispose ^{3}H which cannot be discriminated from ^{1}H and ^{2}H. One of the methods to resolve this issue is photodisintegration of ^{3}H into neutron, proton or deuteron. In order to estimate the feasibility, numerical simulations have to be done. However, the photonuclear data of ^{3}H have not been included in main nuclear data libraries, JENDL/PD-2004 [1], ENDF/B-VII.1 [2], KAERI [3] and TENDL-2014 [4].

Photoabsorption cross sections are the sum of ^{3}H$(\gamma,n)^{2}$H and ^{3}H$(\gamma,2n)^{1}$H reaction cross sections. Threshold energies for those reactions are 6.26 and 8.48 MeV, respectively. Experimental cross sections of the ^{3}H$(\gamma,n)^{2}$H, ^{3}H$(\gamma,2n)^{1}$H, and neutron production ^{3}H(γ,xn) reactions were measured by Faul et al. [5] using positron annihilation quasi-mono energetic photons of $E_\gamma = 5$ to 30 MeV and neutron multiplicity measurement with the ring ratio method of BF$_3$ neutron detectors embedded in a 61 cm cube paraffin moderator. In addition, the cross section of the ^{3}H$(\gamma,n)^{2}$H reaction was measured by Kosiek et al. [6] and Pfeiffer [7]. Both adopted differential bremsstrahlung methods for the reaction, and outgoing particles were detected by an E-ΔE semiconductor detectors telescope. Bösch et al. [8] used monoenergetic γ-radiation from neutron capture reactions on Ni, Fe and Ti. Skopik et al. [9] employed photon flux generated by bombarding a Ta target with an electron beam. The latter two experiments measured emitted neutrons and deuterons by a long counter and two positive-ion spectrometers, respectively.

2 ^{3}H Photonuclear Data Evaluation

2.1 Photonuclear Reaction Cross Sections

The reaction cross sections were derived by the following approach. Structure of ^{3}H was assumed to be a neutron plus a deuteron. Photon-induced reactions are initiated by photo-absorption of the deuteron. Since the deuteron is moving in the ^{3}H nucleus, balancing with the neutron,

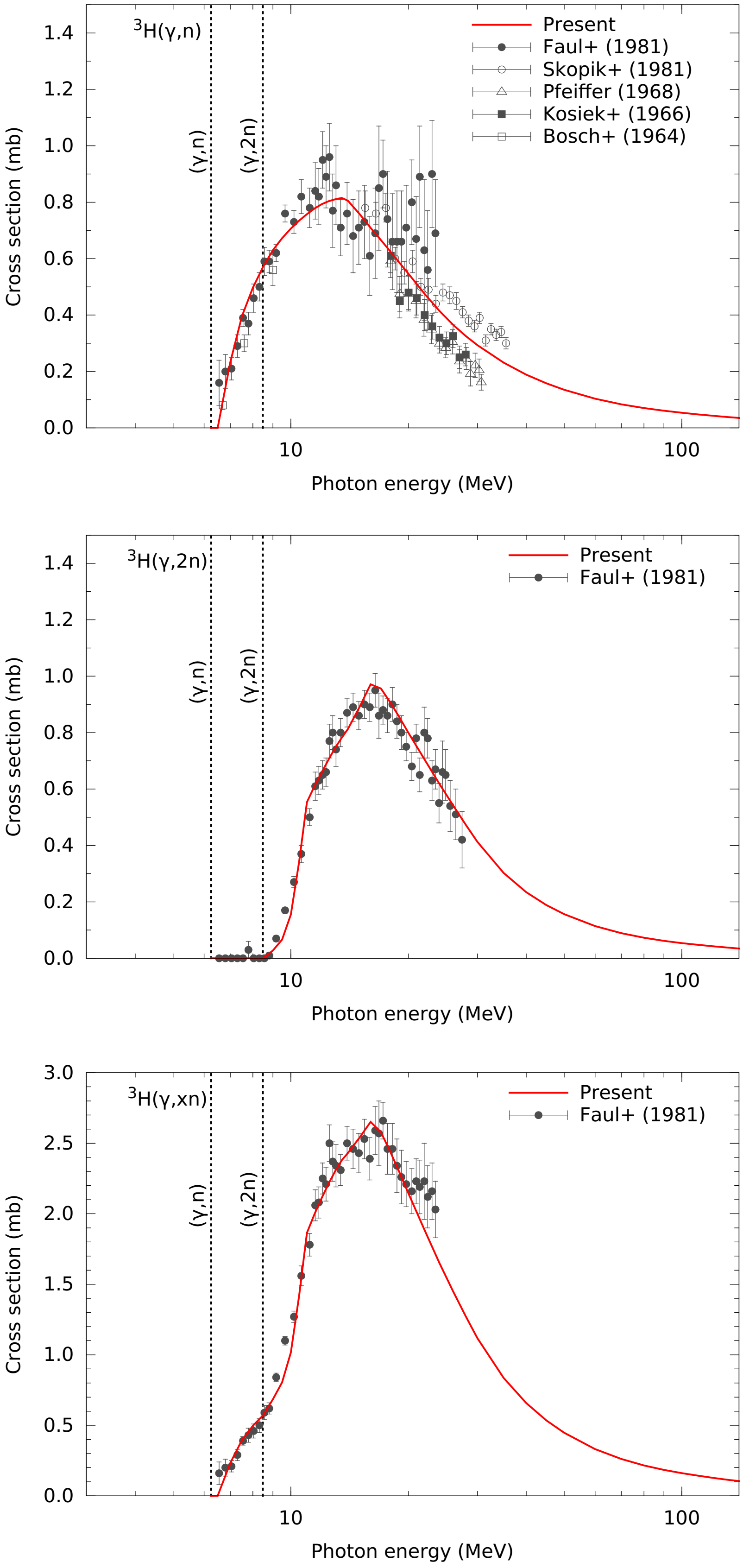

Figure 1: Evaluated results of the ^{3}H photonuclear reaction cross section. The threshold energies of $^3\mathrm{H}(\gamma, n)$ and $^3\mathrm{H}(\gamma, 2n)$ reactions are presented by each vertical line.

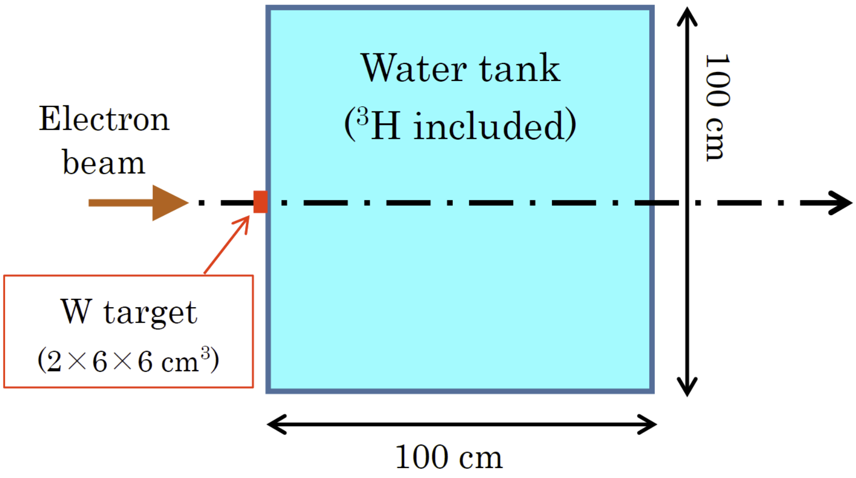

Figure 2: Calculation system of the water tank irradiated by the electron beam.

the energy of incident photons is modified due to the internal motion. The modification was, however, assumed to be small as $E'_\gamma = E_\gamma + \delta E$, where E_γ is the incident photon energy, δE is the energy shift parameter to reproduce experimental data (by ordinary $\delta E = 0$). The comparisons of calculated cross sections with experimental data are shown in **Fig. 1**, in which ^{3}H(γ, n), $(\gamma, 2n)$ and (γ, xn) reaction cross sections are illustrated. The present results well reproduce their experimental data.

2.2 Energy-Angular Distribution of Emitted Particles

The neutron production cross section is the sum of ^{3}H(γ, n) reaction and two times ^{3}H$(\gamma, 2n)$ reaction ones. The proton production cross section is the ^{3}H$(\gamma, 2n)^1$H reaction one. The energy-angular distributions of produced neutrons and protons were calculated with the moving deuteron model using the ^{2}H(γ, n) differential cross section and with 3-body break-up kinematics given by Ohlsen [10] using pure phase space formalism. The deuteron production cross section is the ^{3}H$(\gamma, n)^2$H reaction one. The angular distributions of a produced ^{2}H were given by the ^{2}H(γ, n) reaction with recoiled deuteron angles which were calculated with two body kinematics.

3 Estimation of ^{3}H Depletion by Photon Irradiation

The estimation of ^{3}H depletion by photon irradiation was performed on the basis of Monte Carlo simulation. The considered system was that an electron beam was irradiated into a W target set in front of a waste water tank in which ^{3}H was included (**Fig. 2**). The ^{3}H in the tank was bombarded with the photons generated by bremsstrahlung in the W target. The detailed calculation conditions were summarized below.

The reaction rate distributions of neutron and gamma-ray productions by the photonuclear reactions on ^{3}H are shown in **Fig. 3**. It is found that the produced neutrons and gamma-rays concentrate at the beam direction along the Y-axis. **Figure 4** illustrates the photon energy spectra at $0 - 5$ cm and $20 - 25$ cm in the tank at the beam direction from cells in the W target. The number of ^{3}H(γ, n) and ^{3}H$(\gamma, 2n)$ reactions is presented as a function of thickness in the tank in **Fig. 5**. According to the present simulation, the depletion rate results in 3×10^{-5} to 5×10^{-7} (yr^{-1}). It is, therefore, found that the ^{3}H amount reduced by this method is unexpectedly small.

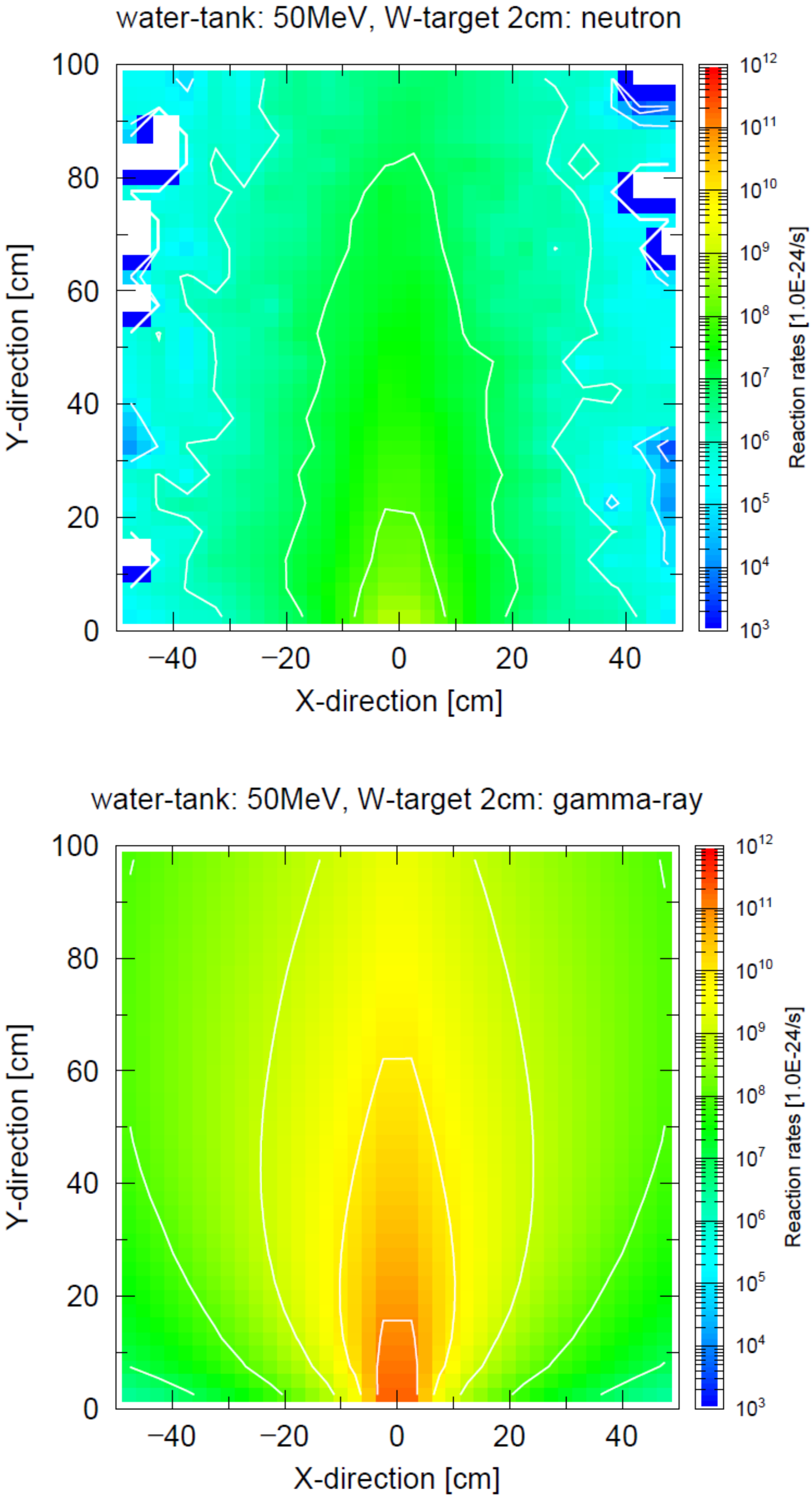

Figure 3: Reaction rate distributions of neutron and gamma-ray productions (top and bottom panels, respectively) in the water tank with the W target (2 cm-thickness) irradiated by the 50 MeV electrons (10 mA).

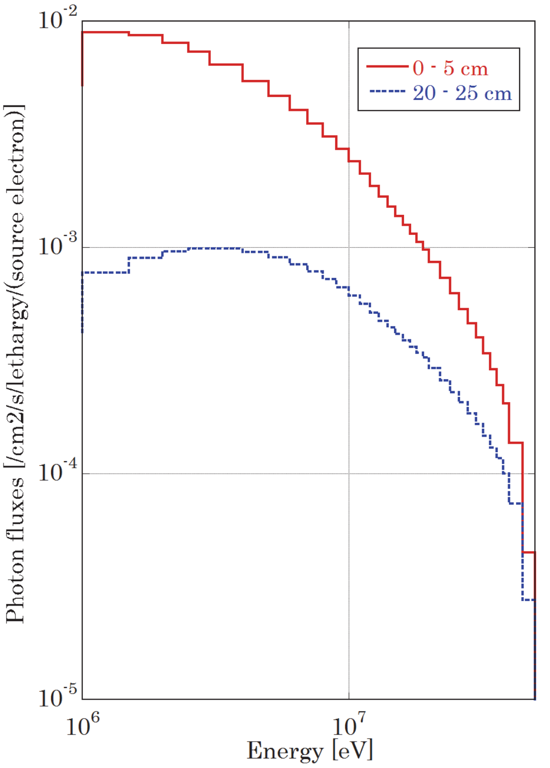

Figure 4: Photon energy spectra in the cells placed at 0-5 and 20-25 cm from the W target irradiated by the 50 MeV electrons.

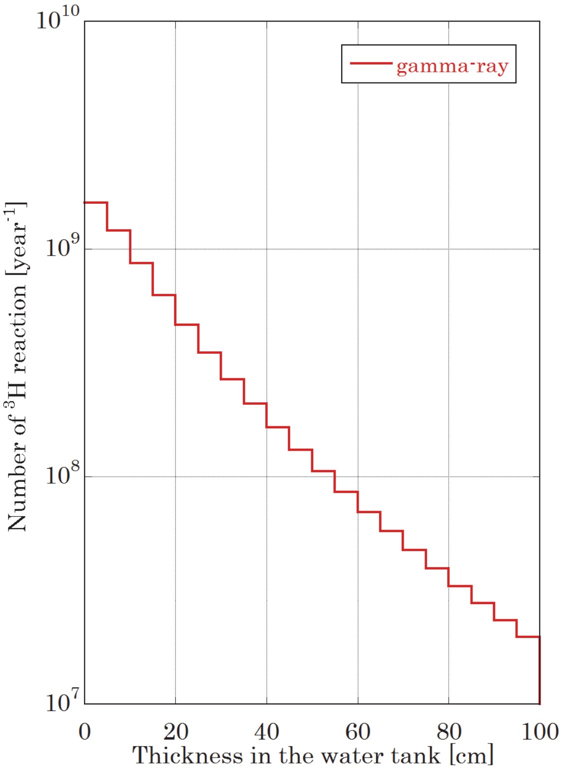

Figure 5: The number of ^{3}H(γ, n) and ^{3}H$(\gamma, 2n)$ reactions in the water tank in 1 year.

Calculation conditions:

- Calculation code: MCNP5
- Library: neutron-nuclear data (FSXLIB-J40), photo-atomic data (MCPLIB04), electron data (EL03), photonuclear data (LA150)
- Source: electron beam; 50 MeV and I_e=10 mA (6.24×10^{16} e/sec)
- Target: Tungsten ($2 \times 6 \times 6$ cm^3)
- Tank: cubic ($100 \times 100 \times 100$ cm^3) with carbon steel wall (1 cm-thickness), pure water (1.0 g/cm^3)
- Activity of ^{3}H: 10^5 Bq/cm^3 (number density 5.6×10^{13} cm^{-3})
- Reaction cross section: ^{3}H$(n, 2n)$ reaction data of ENDF/B-VII.1, ^{3}H photonuclear data of the present evaluation.

4 Summary

The photonuclear data of ^{3}H were evaluated on the basis of the moving deuteron model. The current results well reproduced the available experimental data. Feasibility study was done by the Monte Carlo simulation, in order to evaluate the reduction efficiency of ^{3}H density in waste water using bremsstrahlung photons. It is found that the obtained efficiency is quite low, and thus, this proposed method seems to be impractical.

References

[1] N. Kishida et al., Proc. of Int. Conf. on Nuclear Data for Science and Technology, 1, p.199 (2004).

[2] M.B. Chadwick et al., Nucl. Data Sheets, 112, 2887 (2011).

[3] Y.O. Lee, Y. Han, KAERI/TR-1512 (2000).

[4] A.J. Koning et al., TENDL-2014 (2014).

[5] D.D. Faul et al., Phys. Rev. C24, 849 (1981).

[6] R. Kosiek et al., Phys. Let. 21, 199 (1966).

[7] R. Pfeiffer, Z. Physik. 208, 129 (1968).

[8] R. Bösch et al., Phys. Let. 8, 120 (1964).

[9] D.M. Skopik et al., Phys. Rev. C24, 1791 (1981).

[10] G.G. Ohlsen, Nucl. Instr. Method, 37, 240 (1965).

29 Measurement of double differential (d,xn) cross sections for carbon at an incident energy of 100 MeV

Shouhei ARAKI[1], Yukinobu WATANABE[1], Mizuki KITAJIMA[1], Hiroki SADAMATSU[1],
Keita NAKANO[1], Tadahiro KIN[1], Yosuke IWAMOTO[2], Daiki SATOH[2], Masayuki HAGIWARA[3],
Hiroshi YASHIMA[4] and Tatsushi SHIMA[5]
[1]*Department of Advanced Energy Engineering Science, Kyushu University*
6-1 Kasuga, Fukuoka 816-8580, Japan
[2]*Japan Atomic Energy Agency (JAEA), 2-4 Shirakata, Tokai, Naka, Ibaraki 319-1195, Japan*
[3] *High Energy Accelerator Research Organization (KEK), 1-1 Oho, Tsukuba, Ibaraki 305-0801, Japan*
[4]*Research Reactor Institute, Kyoto University,*
2-1010 Asashiro-nishi, Kumatori, Sennan, Osaka 590-0494, Japan
[5]*Research Center for Nuclear Physics (RCNP), Osaka University,*
10-1 Mihogaoka, Ibaraki, Osaka 567-0047, Japan
E-mail: araki@aees.kyushu-u.ac.jp

Double differential cross sections (DDXs) of the C(d, xn) reaction at an incident energy of 100 MeV were measured at six angles (0°, 5°, 10°, 15°, 20°, and 25°) with NE213 liquid organic scintillators at the Research Center of Nuclear Physics (RCNP) in Osaka University. The neutron energy was determined by the time of flight method. The experimental results were compared with PHITS calculations, and it turned out that the calculation does not reproduce the experimental data satisfactorily well.

1. Introduction

Accelerator based neutron sources with deuteron beam are attractive for not only radiation damage evaluation for fusion materials [1] but also boron neutron capture therapy [2] and production of nuclear medicine [3], since deuteron induced reaction is capable of generating intensive neutron beam. Neutron production data from neutron converter materials such as Li, Be and C bombarded by deuteron are required for optimized design of accelerator based neutron sources. Experimental double differential cross sections (DDXs) for such neutron production are also important for understanding of the reaction mechanism and development of theoretical models. However, measurements of neutron production DDXs are scarce over a wide incident energy range. Particularly there is no experimental data above 40 MeV.

Under this situation, we have planned a series of measurements for neutron production DDXs. For Li, Be, C, Al, Cu, and Nb at an incident deuteron energy of 100 MeV, because a systematic (d,xp) data for Be, C, Al, Ni, Nb, Ta, Pb, and U is available at 100 MeV [4]. The DDXs data for both (d,xp) and (d,xn) reactions at same incident energy are expected to help the development of reliable theoretical models. In this report, we focus on the measurement of the DDXs for carbon. In addition, the experimental results are compared with the calculation using the PHITS code [5].

2. Measurement

The experiment was performed at the ring cyclotron facility of the Research Center for Nuclear Physics, Osaka University. The experimental setup was almost the same as used in the (p,xn) measurements [6-9].The experimental arrangement is shown in Fig. 1. A 102 MeV deuteron beam was forced on a 14 mg/cm^2-thick natural carbon target placed in the beam swinger magnet and delivered to a Faraday cup in a beam dump. The beam current and pulse interval were 5 to 60 nA and 910 ns, respectively. The time of flight (TOF) measurements were performed at 0°, 5°, 10°, 15°, 20° and 25° by moving the target along the beam trajectory in the swinger magnet.

Emitted neutrons were transported to the 100-m TOF tunnel through a movable collimator (10 cm × 12 cm). A clearing magnet installed in the collimator had a role to remove background components of charged particles. The TOF measurements were performed using two different sizes of NE213 liquid organic scintillators coupled to photomultiplier tubes in order to obtain the energy spectrum over a wide dynamic range with good energy resolution: one of them had 5.08 cm × 5.08 cm in diameter and length and the other had 12.7 cm × 12.7 cm in diameter and length, which are hereafter referred to as 2” and 5” NE213 detectors, respectively. At a certain angle, we measured two TOF spectra with the 2” NE213 detector placed at 7 m and with the 5” NE213 detector placed at 17 m from the target, respectively. The magnetic field of the clearing magnet influenced the photomultiplier tube in the case of the measurement at 7m.Therefore, the magnet was switched off and a 5 mm thick NE102A plastic scintillator was mounted as a veto detector in front of the liquid scintillator in order to tag the events induced by background charged particles.

The data acquisition system based on CAMAC and NIM modules was used. The integrated charges of total and slow components of current pulses from the NE213 detector was recorded by a charge sensitive Analog to Digital Converter (ADC) for Pulse Shape Discrimination (PSD). The detector signal and the chopper signal from the cyclotron provided the start and stop signal of a Time to Digital Converter (TDC) to obtain the TOF spectrum. For 7m measurement, the NE102A detector signal was also recorded by ADC. Finally, those data were taken in list mode.

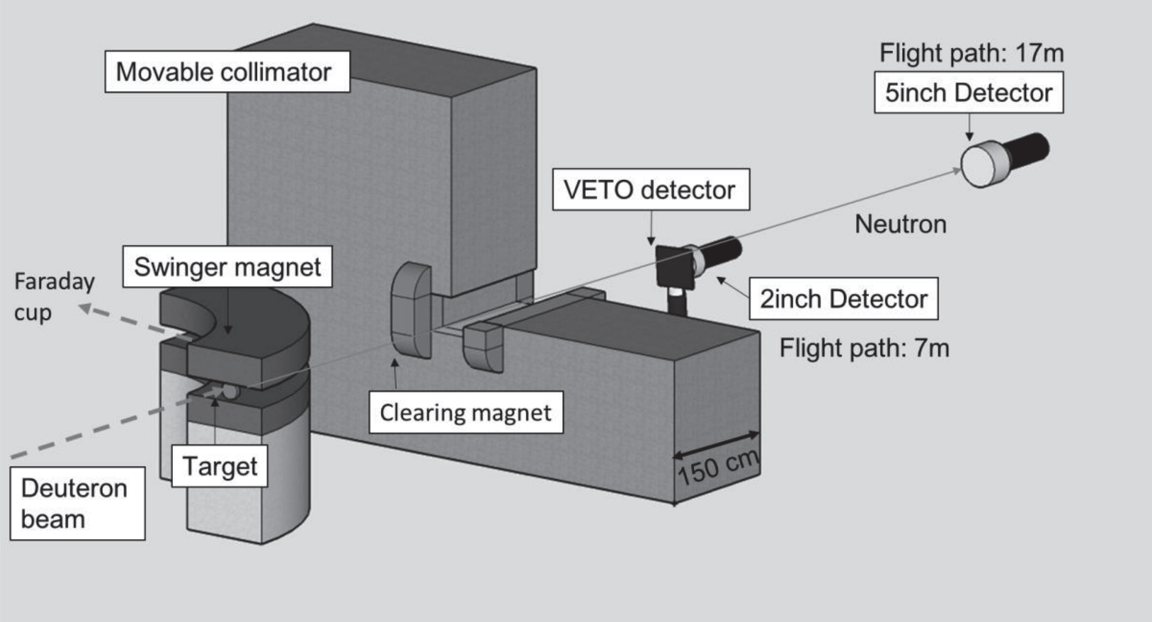

Fig. 1 Illustration of experimental setup

3. Data analysis

The energy threshold of the NE213 detector was adjusted using the Compton edge of the gamma-rays from ^{137}Cs and ^{241}Am/Be radioactive source. The thresholds of the 2” NE213 and 5” NE213 detectors were set to be 0.49 MeVee and 4.3MeVee, respectively, which correspond to 3 and 15 MeV of neutron energy, respectively.

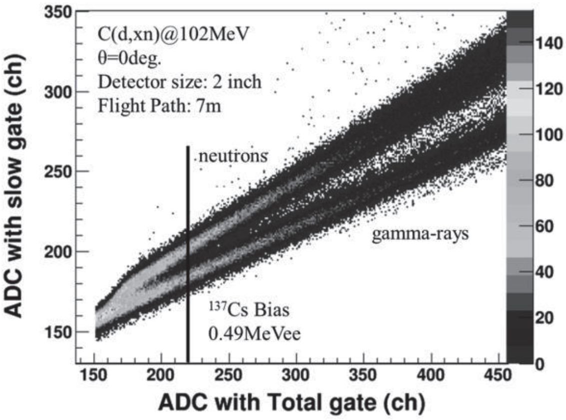

Fig.2 Two dimensional plot of neutrons and gamma rays discrimination using the two gate integration method.

In the low energy range ($\lesssim$15 MeV), the number of background gamma-rays events were comparable to that of neutron events. Therefore only the neutron events were distinguished from the gamma rays events by PSD using two gate integration method [10] in derivation of neutron TOF spectra from the 7 m measurement. The light output in total and slow components in the measurement with the 2”NE213 detector is shown in Fig. 2. The solid line seen on 220 channel indicated the Compton edge from ^{137}Cs gamma ray. Neutron events are clearly distinguished from the gamma ray events above 0.49 MeVee.

To obtain the absolute neutron flight time, the prompt gamma peak seen in the measured TOF spectrum was used as a reference point. The neutron energy was calculated from the flight time by the following equation:

$$E = m_n c^2 \Big/ \sqrt{1-\left(\frac{L}{L+ct}\right)^2} - m_n c^2 ,$$

where E is the neutron energy, m_n is the rest mass of neutron, c is the velocity of light, L is the flight path, and t is the time difference between the prompt gamma and neutron.

The energy spectrum was converted to DDXs using the neutron detection efficiency, the solid angle and the deuteron beam current. The efficiency was calculated by the SCINFUL-QMD code [11, 12]. The attenuation of neutron fluxes at 7 m and 17 m through air was estimated using the PHITS code with JENDL/HE-2007 [13]. Fig. 3 shows the estimated attenuation fraction of neutron fluxes at 7 m and 17 m as a function of neutron energy. The measured neutron flux was corrected by the energy-dependent attenuation fraction. Finally, two DDXs measured at 7 m and 17 m were merged at 15 MeV, that is, the DDXs measured at 7 m was adopted in the energy range less than 15 MeV and the one measured at 17 m was done above 15 MeV.

Uncertainties of the measurements are due to systematic and statistical errors. The estimated systematic errors are given in Table 1. The total systematic error depends mainly on the neutron detection efficiency.

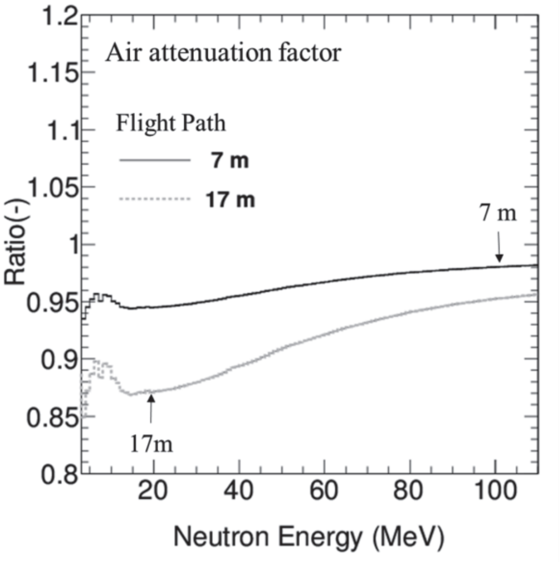

Fig. 3 Estimated attenuation fraction of neutron

Table 1. Estimation of systematic errors

Error origin	Error
Detection efficiency	15%
Gamma-ray rejection	2%
Solid angle	<1%
Beam integration	<1%
Correction of air attenuation	3%
Total systematic error	15.4%

4. Results and discussion

The experimental DDXs for carbon at 102 MeV are shown in Fig 4. It should be noted that the error bars indicates only the statistical error. A broad peak around half the incident energy and sharp peaks around 100 MeV are observed in all the measured energy spectra. The broad peak intensity decreases rapidly with increasing angle. This peak may correspond to neutron emission via elastic breakup and stripping reaction processes to continuum, since the deuteron is a very loosely bound system of a proton and a neutron. The sharp peaks around 100 MeV arise from stripping reaction process to discrete levels in the residual nucleus ^{13}N by the ^{12}C(d,n) reaction.

The PHITS calculation is also shown in Fig.4. In the calculation, the dynamical and subsequent evaporation processes were described with the intra-nuclear cascade of Liège (INCL) model [14] and the generalized evaporation model (GEM) [15], respectively. The calculations reproduce roughly the structure of broad peak due to elastic breakup and stripping reactions to continuum at very forward angles. However, the reproducibility of the shape and magnitude is not satisfactory. Further improvement of the INCL model will be necessary to obtain better agreement with the experimental data.

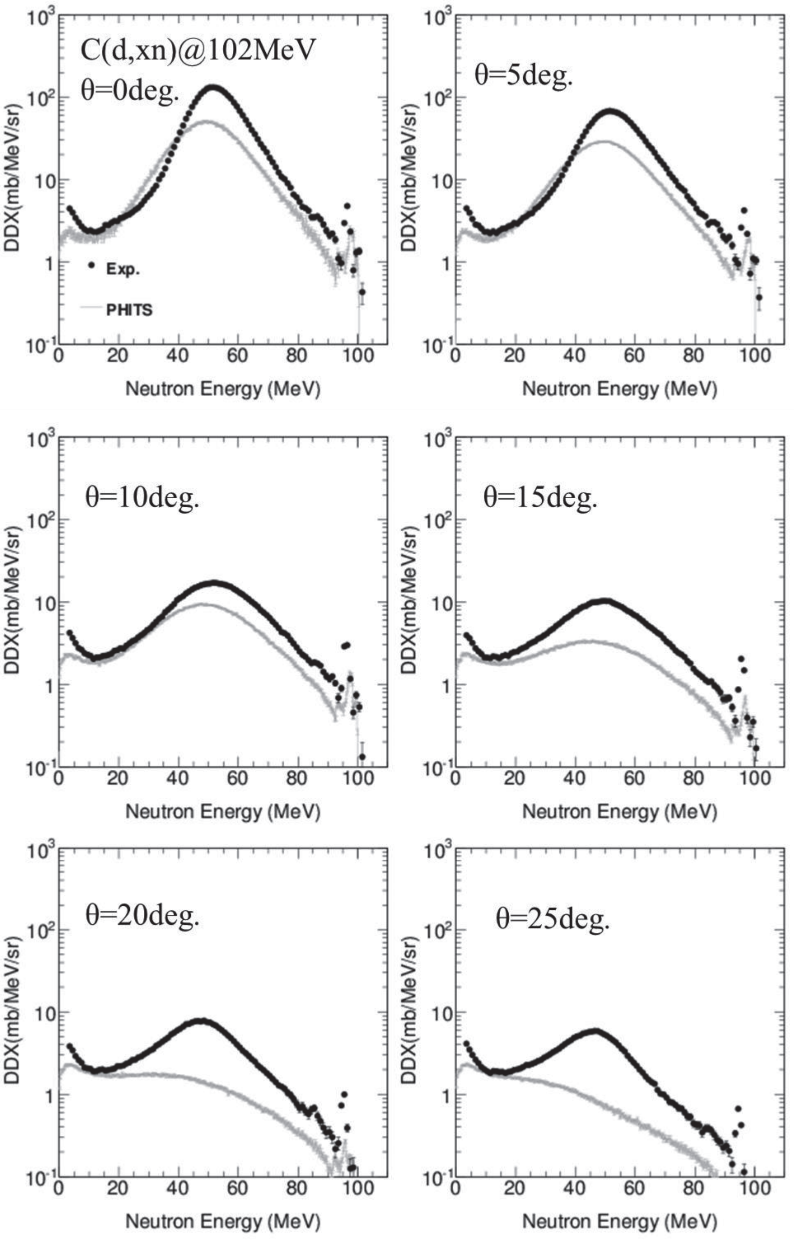

Fig. 4 Double differential cross sections of neutron production from carbon by 102MeV deuteron incidence. The experimental results are compared with the calculation results by PHITS code.

5. Summary and conclusion

We measured the double differential cross sections (DDXs) of 102 MeV (d,xn) reaction on C at six angles (0°, 5°, 10°, 15°, 20° and 25°) using the TOF method with two different sizes of NE213 liquid organic scintillators placed at 7 m and 17 m from the target. The neutron detection efficiencies were calculated by the SCINFUL-QMD code. The experimental DDXs after the correction of neutron attenuation in air were compared with the calculation using the INCL plus GEM models implemented in the PHTIS code. The model calculation does not reproduce the experimental DDXs satisfactorily well.

In the future, we plan to apply a code system based on alternative theoretical models [16, 17] to further model analysis of the experimental data in order to establish the most reliable theoretical model for nuclear data evaluation of deuteron induced neutron production.

Acknowledgment

The authors wish to thank the staff of RCNP for providing beams and for their assistance during the experiment. The research was partly funded by the Sasagawa Scientific Research Grant from The Japan Scientific Society.

References

[1] A. Moeslang, V. Heinzel H. Matsui, et al.: Eng, Des. 81, 106-112 (2006).
[2] S. Agosteoa, G. Curzioc, F. d'Erricoc, et al: Nucl. Instr. and Meth. A 476, 106-112 (2002).
[3] Y. Nagai, K. Hashimoto, Y. Hatsukawa et al.: J. Phys. Soc. Jpn. 82,064201 (2013).
[4] D. Ridicas, W. Mittig, H. Savajols, et al.: Phys. Rev. C 63, 014610 (2000).
[5] T. Sato, K. Niita, N. Matsuda, et al: J. Nucl. Sci. Technol. 50, 9, 913-923(2013).
[6] Y. Iwamoto, S. Taniguchi, N. Nakao, et al.:, Nucl. Inst. Method. in Phys. Res. A 598, 298 (2008).
[7] Y. Iwamoto, D. Satoh, M. Hagiwara, et al.: Nuclear Technol. 168, 340 (2009).
[8] Y. Iwamoto, M. Hagiwara, D. Satoh, et al.: Nucl. Inst. Method. in Phys. Res. A 629, 43 (2011).
[9] Y. Iwamoto, M. Hagiwara, T. Matsumoto, et al.: Nucl. Inst. Method. in Phys. Res. A 690, 10 (2012).
[10] M. Moszynski, G. J. Costa, G.Guillaume, et al: Nucl. Inst. Method. in Phys. Res. A 343, 563-572 (1994).
[11] D. Satoh, T. Sato, N. Shigyo, et al: JAEA-Data/Code 2006-023(2006).
[12] D. Satoh, T. Sato, A. Endo, et al: J. Nucl. Sci. Technol. 43, 714 (2006).
[13] Y. Watanabe, T. Fukahori, K. Kosako, et al, AIP Conference Proceedings769, 326 (2005).
[14] A. Boudard J. Cugnon, J.-C. David ,et al, Phys. Rev. C 87, 014606 (2013).
[15] S. Furihata: Nucl. Instr. and Meth. B 171, 251-258 (2000).
[16] S. Nakayama, S. Araki, Y. Watanabe, et al.: Energy Procedia 71, 219-227(2015).
[17] H. Kouno, Y. Watanabe, S. Nakayama, et al.: presented at this symposium (2015).

30 Theoretical model analysis of (*d,xn*) reactions on beryllium

Hiroshi KOUNO[1], Yukinobu WATANABE[1,*], Shinsuke NAKAYAMA[2],
Osamu IWAMOTO[2], Tao YE[3], Kazuyuki OGATA[4]
[1]*Department of Advanced Energy Engineering Science, Kyushu University, Japan*
[2]*Nuclear Science and Engineering Center, Japan Atomic Energy Agency, Japan*
[3]*Institute of Applied Physics and Computational Mathematics, China*
[4]*Research Center for Nuclear Physics, Osaka University, Japan*
[*]e-mail: watanabe@aees.kyushu-u.ac.jp

Neutron production from deuteron-induced reactions on beryllium is analyzed with theoretical model calculation considering elastic breakup process, stripping processes to both continuum and discrete states, and statistical decay process. The calculation results reproduce experimental thick target neutron yields from ^{9}Be(*d,xn*) reactions at incident energies up to 40 MeV generally well, except in the low emission energy region. The stripping process to continuum is found to be the most dominant reaction process.

1. Introduction

Accelerator-based neutron sources with deuteron beam draw attention as intensive neutron sources for various applications such as the International Fusion Materials Irradiation Facility (IFMIF) [1] and production of radioisotopes for Positron Emission Tomography (PET) [2]. For the development and design of deuteron accelerators, comprehensive and accurate nuclear data of deuteron-induced reactions are needed for neutron converter materials (Li, Be, C, etc.) and accelerator structure materials (Fe, Cr, Ni, etc.). Since it is impossible to produce the nuclear data based on measurements alone, theoretical model calculations which can complement experimental data play an important role.

We have developed a computational code system based on theoretical models for deuteron-induced reactions [3], and have demonstrated that the calculation using the code system reproduces experimental double differential (*d,xp*) cross sections in the incident energy range up to 100 MeV fairly well [4]. However, the code system have not been enough tested for (*d,xn*) reactions, which are important for the design of accelerator neutron sources, since there are few available experimental data of double differential (*d,xn*) cross sections. On the other hand, experimental data of Thick Target Neutron Yields (TTNYs) from the (*d,xn*) reactions exist to some extent. In the present study, thus, the code system is applied to analyses of the TTNYs from beryllium in order to validate the theoretical models employed.

2. Theoretical model of deuteron induced reactions

To describe deuteron-induced reactions, we have used some theoretical models as follows. Elastic breakup, which is the reaction that an incident deuteron breaks into a proton and a neutron, is calculated using the code based on the Continuum-Discretized Coupled-Channels method (CDCC) [5]. Then, the stripping reaction, in which either proton or neutron in deuteron is absorbed into the target and the remaining one is emitted, is calculated using the

DWUCK4 code based on conventional zero-range Distorted Wave Born Approximation (DWBA), or the Glauber model [6] for the transition to discrete states or continuum states of the residual nucleus, respectively. Finally, the statistical process is calculated using the Hauser-Feshbach and exciton models implemented in the CCONE code [7].

In the CDCC and the Glauber model calculations, the nucleon optical model potentials (OMPs) of the target nucleus are necessary. In the present work, we use the global potentials of Koning and Delaroche (KD) [8] at a half of the incident deuteron energy. In both the CCONE and DWBA calculations, the nucleon OMPs and the deuteron OMPs are necessary. In the CCONE calculation, the KD OMPs and the An and Cai (An-Cai) global OMPs [9] are used for nucleon OMPs and deuteron OMPs, respectively. In the DWBA calculation, the KD OMPs and the adiabatic OMPs [10] derived from the KD OMPs are used for nucleon OMPs in the exit channel and deuteron OMPs in the entrance channel, respectively. Note that these OMPs are the same as in our previous (*d,p*) analysis [4].

3. Optical potential of beryllium

In the CDCC calculation and the adiabatic OMPs, the KD OMPs are used as OMPs between the nucleon in deuteron and the target. However, the target nucleus, ^{9}Be, is a light nucleus and beyond the target mass range to which the KD OMPs is applicable. First of all, thus, we have validated the application of KD OMPs for ^{9}Be by the analysis of deuteron elastic scattering.

Figure 1 shows comparisons between experimental deuteron elastic scattering cross sections from ^{9}Be bombarded by deuterons at 7 [11], 15.8 [12], and 24 MeV [13] and the CDCC calculation. In addition, optical model calculations are performed using the DWUCK4 code with both the adiabatic OMPs based on the KD OMPs and the An-Cai global OMPs and compared with the experimental data and the CDCC calculation. At forward angles, three calculations reproduce the experimental data well to the same extent, whereas the agreement with the experimental data is not necessarily good at low incident energies of 7 and 15.8 MeV at large angles, because the contribution from compound elastic scattering is not included in the calculation. At the highest incident energy of 24 MeV, all the calculations reproduce the experimental data reasonably well over the whole angular region. Thus, the choice of OMPs used in the following (*d,n*) calculation is validated.

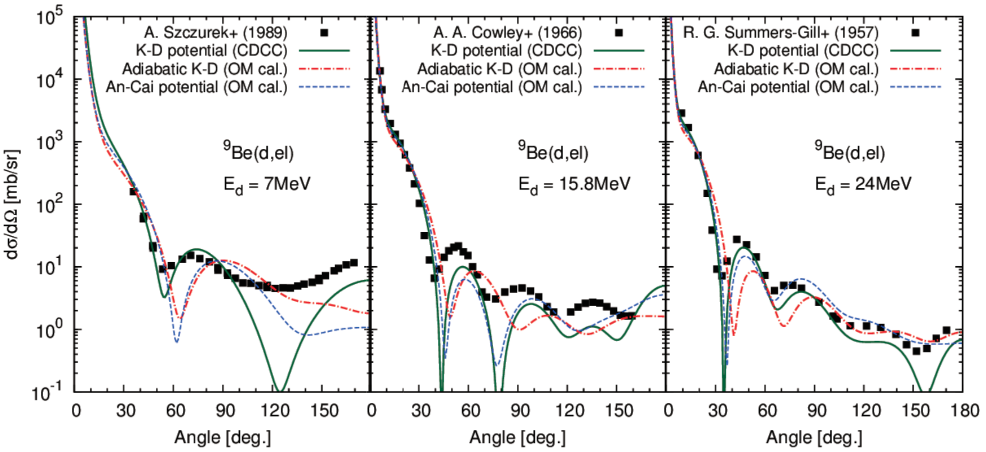

Fig. 1 Calculated and experimental differential cross sections of deuteron elastic scattering from ^{9}Be.

4. DWBA analysis of the (*d,n*)reaction

To calculate TTNYs from the ^{9}Be(*d,n*) reaction, we extract the spectroscopic factors (SFs) of single proton orbits in the residual nucleus ^{10}B which is necessary to determine the absolute value of differential cross sections calculated by the DWUCK4 code. The relation between the DWUCK cross section and the DWBA differential cross section for stripping reaction leading to the excited states *i* of residual nucleus is given by

$$\frac{d\sigma^{DWBA}_{boundi}}{d\Omega}\left(E_d\right)=\frac{D_0^{\ 2}}{10^4}\frac{2J_i+1}{2J_A+1}\frac{S_i}{2j+1}\frac{d\sigma^{DWUCK4}_{boundi}}{d\Omega}\left(E_d\right), \tag{1}$$

where E_d is the incident deuteron energy, D_0 is a constant used in zero-range approximation and the value is $D_0^2 = 1.50 \times 10^4$, J_A and J_i are the spins of the ground state of target nucleus and the *i*-th state of residual nucleus, respectively, S_i is the SF for each state, *j* is the intrinsic spin of transferred neutron, and $d\sigma^{DWUCK4}_{bound,i}/d\Omega$ is the differential cross section calculated with the DWUCK4 code. In this study, eight states from the ground state to 5.16 MeV level of residual nucleus ^{10}B are considered as discrete states in the exit channel.

Figure 2 shows comparisons of calculated and experimental differential cross sections for the transition to the ground and 0.718 MeV states of ^{10}B in the ^{9}Be(*d,n*)^{10}B reaction at incident energies from 7 to 25 MeV. The experimental data are taken from Refs. [14-16]. The calculation is composed of the direct DWBA component corresponding to stripping process and the statistical decay component calculated by the CCONE code. Each S_i of the SF is extracted by fitting the calculated cross section to the corresponding experimental data at forward angles for each incident energy.

In the early work of ^{12}C(*d,p*) reactions [4], we have reported that the S_i has an incident energy dependence given by

$$S_{i,k}\left(E_d\right)=F_i S_{C-12,1}\left(E_d\right), \tag{2}$$

where F_i is a scaling factor depending on the excited states *i* of residual nucleus *k*, and $S_{C\text{-}12,1}(E_d)$ is the incident energy dependence of the SF value which is determined by the ^{12}C(*d,p*)^{13}C$_{\text{g.s.}}$ reaction:

$$S_{C-12,1}\left(E_d\right)=-2.18\times10^{-6}E_d^{\ 3}+3.19\times10^{-4}E_d^{\ 2}-1.56\times10^{-2}E_d+8.20\times10^{-1} \tag{3}$$

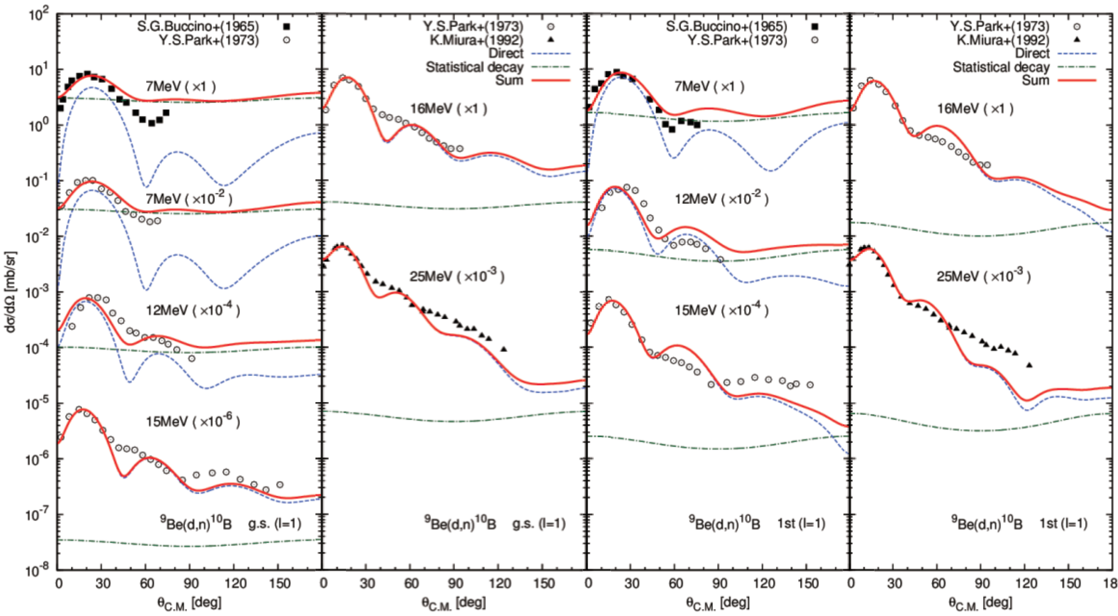

Fig. 2 Calculated and experimental differential cross sections from ^{9}Be(*d,n*) reactions.

In Fig. 3, the extracted SFs for the ground and 0.718 MeV states of ^{10}B are plotted as a function of incident energy and compared with the incident energy dependence given by Eqs. (2) and (3). The extracted SFs are not smooth and varied with incident energy. This behavior might be influenced by resonance structure seen in the low incident energy region [17]. To reduce the flucutation structure, the F_i in Eq. (2) is determined by fitting the experimental SFs as shown in Fig.3. The same approach is applied to the other discrete levels and finally the incident energy depedent SF of each excited state is determined for the DWBA calcultation for the stripping (*d,n*) reaction to discrete state.

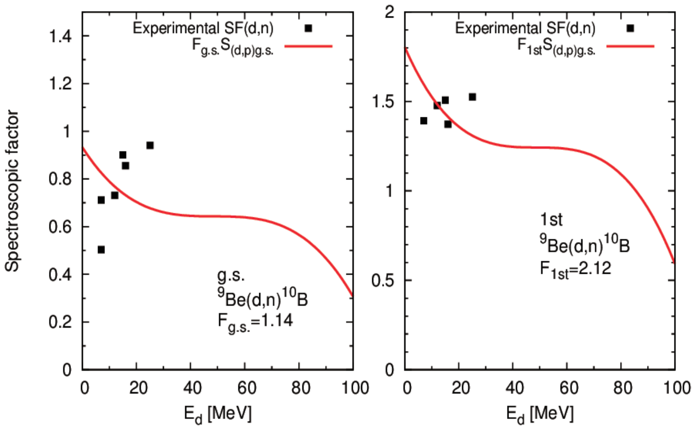

Fig. 3 Incident energy dependence of experimental SFs extracted from the ^{9}Be(*d,n*)^{10}B reaction.

5. Analysis of thick target neutron yields

5.1. Calculation method

The thick target neutron yields (TTNYs) is calculated using the following expression:

$$\frac{d^2Y}{dEd\Omega}(E_0) = N\int_0^{E_0} \frac{d^2\sigma}{dEd\Omega}(E_d)\left[\frac{dE_d}{dx}\right]^{-1} \exp\left(-\int_{E_d}^{E_0} \sigma_R(E')\left[\frac{dE'}{dx}\right]^{-1} dE'\right)dE_d\,, \tag{4}$$

where E_i is the incident deuteron energy, N is the atoms density of the target, $d^2\sigma/dEd\Omega$ is the calculated DDXs for the ^{9}Be(*d,xn*) reaction, E_d is the deuteron energy in the Be target, dE/dx is the deuteron stopping power, and σ_R is the deuteron total reaction cross section of ^{9}Be. The deuteron stopping power and total reaction cross sections are calculated with the SRIM-2010 code [18] and the CCONE code, respectively.

5.2. Results and discussion

Figure 4 show comparisons between the calculated and experimental TTNYs from ^{9}Be bombarded by deuterons of 7 [19], 14.8 [20] and 40MeV [21] at 0 degree. The calculation results with the Monte Carlo particle transport calculation code PHITS [22] are also plotted with the dashed lines. The TTNYs calculated with the present theoretical model reproduce both the shape and magnitude of the experimental spectra better than the PHITS calculation. Especially, the present model calculations are in better agreement with the experimental data than the PHITS calculation in the high neutron energy region where the stripping reaction processes to discrete states are predominant. This indicates that the present DWBA calculation with the incident energy dependent spectroscopic factors is reasonable.

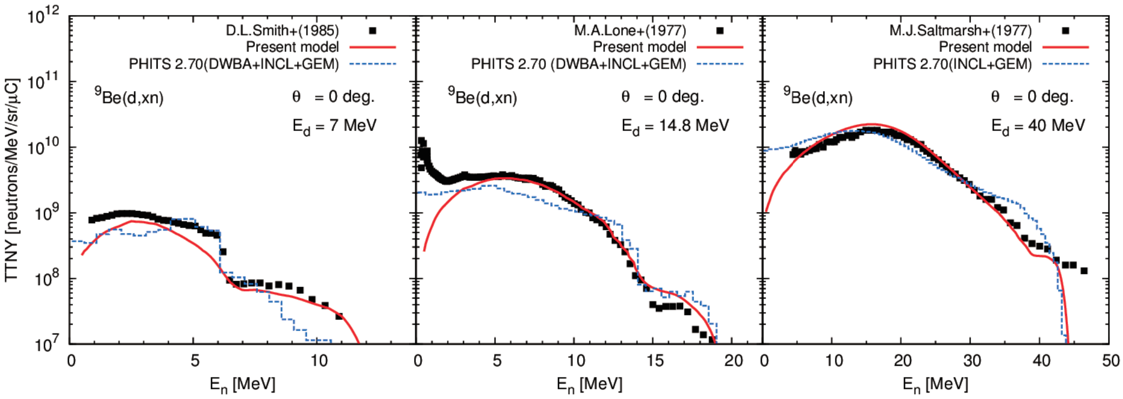

Fig. 4 Calculated and experimental TTNYs for ^{9}Be(*d,xn*) reaction at 7, 14.8 and 40 MeV.

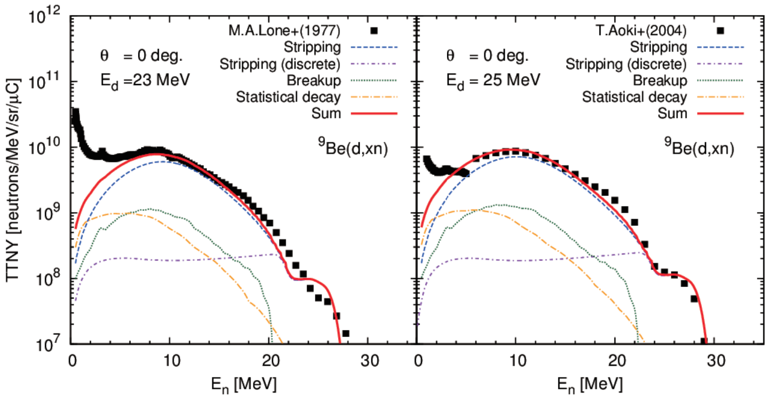

Fig. 5 Calculated and experimental TTNYs for ^{9}Be(*d,xn*) reaction at 23 and 25 MeV.

Experimental TTNYs from ^{9}Be bombarded by deuterons of 23 [20] and 25MeV [23] are compared with the present model calculation in Fig. 5. The calculated TTNY is decomposed into three components corresponding to the following reaction processes: the stripping process, the elastic breakup process, and the statistical decay process. It is found that the stripping process is the most dominant process in deuteron-induced reactions at these incident energies. The bump structure around 10 MeV seen in the experimental spectra is reproduced fairly well by the Glauber model calculation to describe the stripping process to continuum. The statistical decay process has a large contribution in the low neutron energy region below 5 MeV. However, the calculation is not in satisfactory agreement with the experimental spectra. This might be because any particle emissions from discrete states in residual nuclei are not allowed in the present CCONE code for statistical decay calculations. For instance, the following reaction path is one of the candidate neutron decays from discrete levels in the residual nucleus ^{9}Be after deuteron inelastic scattering:

$$^{9}\mathrm{Be} + d \rightarrow {}^{9}\mathrm{Be}^{*} + d$$

$$^{9}\mathrm{Be}^{*} \rightarrow {}^{8}\mathrm{Be}^{*} + n$$

We plan to apply a sequential decay model [24] to consider such the sequential neutron decay from the discrete levels and examine whether the underestimation seen in the low emission energy region is improved or not in our future work.

6. Conclusion

The theoretical model code system dedicated for deuteron-induced reactions was applied to calculate thick target neutron yields (TTNYs) for the ^{9}Be(*d,xn*) reaction at incident energies up to 40 MeV. The spectroscopic factors necessary in the calculation of the stripping process to discrete states were determined from the DWBA analysis. The model calculation results reproduced the experimental TTNYs generally well, except in the low emission energy region where underestimation was seen in the statistical decay component. Through the model analysis, it was found that the stripping process to continuum described by the Glauber model is the most dominant neutron emission process.

References

[1] A. Moeslang, V. Heinzel, H. Matsui, M. Sugimoto, Fusion Eng. Des., 81, 863 (2006).

[2] T. Kin, Y. Nagai, N. Iwamoto, F. Minato, O. Iwamoto, Y. Hatsukawa, M. Segawa, H. Harada, C. Konno, K. Ochiai and K. Takakura, J. Phys. Soc. Jpn, 82, 034201 (2013).

[3] S. Nakayama, S. Araki, Y. Watanabe, O. Iwamoto, T. Ye and K. Ogata, Energy Procedia, 71, 219 (2015).

[4] S. Nakayama and Y. Watanabe, J. Nucl. Sci. Thechnol., 53, 89 (2016).

[5] M.Yahiro, K. Ogata, T. Matsumoto and K. Minomo, Prog. Theor. Exp. Phys. 2012, 01A206, (2012).

[6] T. Ye, S. Hashimoto, Y. Watanabe, K. Ogata and M. Yahiro, Phys. Rev. C84, 054606 (2011).

[7] O. Iwamoto, N. Iwamoto, S. Kunieda, F. Minato, and K. Shibata, Nucl. data Sheet, 131, 259 (2016).

[8] A. J. Koning and J. P. Delaroche, Nucl. Phys., A713, 231 (2003).

[9] H. An and C. Cai., Phys. Rev., C73, 054605 (2006).

[10] D. G. Madland, Proc. Specialists' Meeting on Preequilibrium Nuclear Reactions, 103, Semmering, Austria, 10-12 Feb (1988).

[11] A. Szczurek, K. Bodek, J. Krug, W. Lübcke, H. Rühl, M. Steinke, M. Stephan, D. Kamke, W. Hajdas, L. Jarczyk, B. Kamys, A. Strzalkowski, and E. Kwasniewicz, Z. Phys. A, 333, 271 (1989).

[12] A. A. Cowley, G. Heymann, R. L. Keizer and M. J. Scott, Nucl. Phys., 86, 363 (1966)

[13] R. G. Summers-Gill, Phys. Rev., 109, 1591 (1958).

[14] S. G. Buccino and A. B. Smith, Phys. Lett., 19, 234 (1965).

[15] Y. S. Park, A. Niiler and R. A. Lindgren, Phys. Rev., C8, 1557 (1973).

[16] K. Miura, A. Sato, S. Mori, Y. Takahashi, T. Nakagawa, T. Tohei, T. Niizeki, S. Hirasaki, G. C. Jon, K. Ishii, H. Orihira and H. Ohnuma, Nucl. Phys., A539, 441 (1992).

[17] J. R. Davis and G. U. Din, Nucl. Phys. A179, 101 (1972).

[18] J. Z. Ziegler, M. D. Ziegler, and J. P. Biersack, Nucl. Instr. and Meth., B268, 1818 (2010).

[19] D. L. Smith, J. W. Meadows and P. T. Guenther, Nucl. Instr. and Meth. A241, 507 (1985).

[20] M. A. Lone, C. B. Bigham, J. S. Fraser, H. R. Schneider, T. K. Alexander, A. J. Ferguson and A. B. Mcdonald, Nucl. Instr. and Meth., 143, 331 (1977).

[21] M. J. Saltmarsh, C. A. Ludemann, C. B. Fulmer et al., Nucl. Instr. and Meth. 145, 81 (1977).

[22] T. Sato, K. Niita, N. Matsuda et al., J. Nucl. Sci. Technol. 50, 913 (2007).

[23] T. Aoki, M. Hagiwara, M. Baba, M. Sugimoto, T. Miura, N. Kawata and A. Yamadera, J. Nucl. Sci. Thechnol., 41, 399 (2004)

[24] T. B. Beynon and B. S. Sim, Ann. Nucl. Energy 15, 27 (1988).

31 Measurements of neutron production double-differential cross-sections and thick target neutron yields on carbon bombarded with 430 MeV/nucleon carbon ions

Yutaro Itashiki[1], Youichi Imahayashi[1], Nobuhiro Shigyo[1], Yusuke Uozumi[1],
Daiki Satoh[2], Tsuyoshi Kajimoto[3], Toshiya Sanami[4],
Yusuke Koba[5], Naruhiro Matsufuji[5]
[1]Kyushu University, Fukuoka, 819-0395, Japan
[2]Japan Atomic Energy Agency, Tokai, 319-1195, Japan
[3]Hiroshima University, Higashi-Hiroshima, 739-8527, Japan
[4]High Energy Accelerator Research Organization, Tsukuba, 305-0801, Japan
[5]National Institute of Radiological Sciences, Chiba, 263-8555, Japan
e-mail: itashiki@kune2a.nucl.kyushu-u.ac.jp

Neutron production double-differential cross-sections (DDXs) and thick target neutron yields (TTNYs) for carbon bombarded with 430 MeV/nucleon carbon ions were measured by the time-of-flight method with NE213 liquid organic scintillators at six angles of 15, 30, 45, 60, 75, and 90°. The experimental data were compared with calculated results by PHITS and Geant4. It is found that PHITS reproduced the experimental data better than Geant4.

1. Introduction

The carbon ion therapy is one of the effective treatment because of high curability and minimal invasiveness. In National Institute of Radiological Sciences (NIRS), the number of patients receiving carbon ion therapy from June 1994 to March 2014 was 8227 [1]. However, the patients could have a risk to get a secondary cancer in the long term. There were several reports about lifetime cancer risk due to secondary neutrons in proton therapy [2-4]. The particle transport Monte Carlo simulation code is one of useful tools to estimate the risk. However, the code has not been validated sufficiently for the heavy ion reaction because experimental data are scarce.

We previously measured neutron production DDXs on a carbon bombarded with 290 MeV/nucleon carbon ions [5]. Then, we confirmed the Monte-Carlo simulation code PHITS [6] reproduced the experimental data. In this article, we report the neutron production DDXs and TTNYs on a carbon bombarded with 430 MeV/nucleon carbon ions that are maximum energy beam in the therapy performed in NIRS. Then, the experimental data are compared with calculated results by Monte Carlo simulation codes such as PHITS and Geant4 [7].

2. Experiment

The experiment was performed at PH2 beam line of HIMAC facility in NIRS. The experimental set-up was similar to that in our previous paper [5]. **Figure 1** illustrates a schematic view of the experimental set-up.

Two sizes of graphite targets whose dimensions were 5 cm × 5 cm × 1 cm and 5 cm × 5 cm × 22 cm for neutron production DDXs and TTNYs measurements, respectively, were irradiated with 430 MeV/nucleon carbon beam. A 0.5 mm thick NE102A plastic scintillator (Beam pick up detector) was placed in front of the target to monitor beam intensity. Neutrons produced in the target were measured with two sizes of NE213 liquid organic scintillators located at six angles of 15, 30, 45, 60, 75, and 90°. A 5.08 cm long one (Small neutron detector) was used to obtain neutron spectra from 1 - 10 MeV and a 12.7 cm long one (Large neutron detector) was used above 5 MeV. The 2 mm thick NE102A scintillators (Veto detector) to discriminate charged particles were set in front of the neutron detectors.

Kinetic energies of neutrons were determined by the time-of-flight (TOF) method. Flight path lengths from the target were set to 1.0 - 2.5 m for the small neutron detectors and 1.6 - 3.9 m for the large neutron detectors.

Background neutrons were estimated by a measurement with iron shadow bars between the target and the neutron detectors. Neutrons emitted from the target to the neutron detectors directly were obtained by subtracting neutrons for the background measurement from neutrons for a measurement without the shadow bars.

An electronic circuit for data acquisition consisted of NIM and CAMAC modules. The data was acquired event-by-event. Light outputs of the neutron detector, the veto detector, and the beam pick up detector were registered with analog-to-digital converters (ADCs) and time difference between signals of the neutron detector and the beam pick up detector was registered with a time-to-digital converter (TDC).

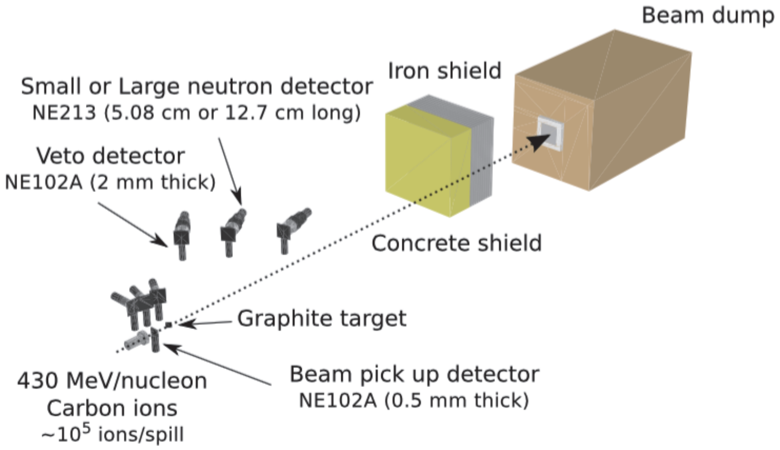

Fig. 1. Schematic view of the experimental set-up at PH2 beam line of HIMAC facility in NIRS

3. Analysis

Figure 2 shows inverse TOF spectrum for the large neutron detector at 15°. TDC of the horizontal axis is time difference between start signal of the neutron detector and stop signal of the beam pick up detector. A peak corresponding to prompt γ-ray events appeared at 3140 ch. Neutron kinetic energy E_n was determined by using the following formula:

$$E_\mathrm{n} = \frac{m_n c^2}{\sqrt{1-\left(\frac{L}{ct_{n-\gamma}+L}\right)^2}} - m_n c^2 \qquad (1)$$

where m_n is rest mass of neutron, L is distance from the target to the neutron detector, c is velocity of light and $t_{n-\gamma}$ is difference of flight time between the prompt γ-ray peak and neutron.

Non-charged particle events as neutrons and γ-rays in **Fig. 2** were extracted by using light output spectrum of the veto detector in **Fig. 3**. Events below 125 ch were non-charged particle events.

Neutron events were retrieved by using two-dimensional histogram of light outputs for the neutron detector in **Fig. 4**. The horizontal axis of the histogram as ADC total and the vertical axis of the histogram as ADC slow are integrated value of signal for the neutron detector and integrated value of delayed part of the signal, respectively. In this figure, events painted red were extracted as neutron events.

Neutron detection efficiency of the neutron detector was estimated by using SCINFUL-QMD code [8, 9]. **Figure 5** indicates the neutron detection efficiencies for small and large neutron detectors in this analysis.

Neutron production DDXs obtained by the small and large neutron detectors were adopted below and above 5 MeV, respectively. TTNYs obtained by the small and large neutron detectors were adopted below and above

20 MeV, respectively.

Since the carbon target for neutron production DDXs measurement was not very thin, an effect of multiple scattering in the target was not negligible. In this analysis, the effect was estimated by using the simulation code PHITS. Neutron production DDXs were obtained through multiplying experimental neutron production DDXs by ratio of calculated result for 5 cm × 5 cm × 0.01 cm target rotated 45° to the beam axis to calculated result for 5 cm × 5 cm × 1 cm target rotated 45° to the beam axis.

The uncertainty of the experimental data mainly results from statistical errors and the uncertainty of the neutron detection efficiency. For the neutron detection efficiency, we estimated an uncertainty at 15% in the whole energy region.

4. Simulation

Neutron production DDXs and TTNYs were calculated with PHITS and Geant4. The versions of these codes are PHITS 2.76 and Geant4 10.1, respectively. Two sizes of carbon targets which dimensions were 0.01 cm × 0.01 cm × 0.01 cm and 5 cm × 5 cm × 22 cm were irradiated with 430 MeV/nucleon carbon beam for neutron production DDX and TTNY calculations. As nucleus-nucleus collision model, PHITS and Geant4 adopt JQMD and G4QMD, respectively. For total cross sections of nucleus-nucleus collision, PHITS and Geant4 used KU-ROTAMA model [10] and Glauber model with Gribov corrections [11], respectively.

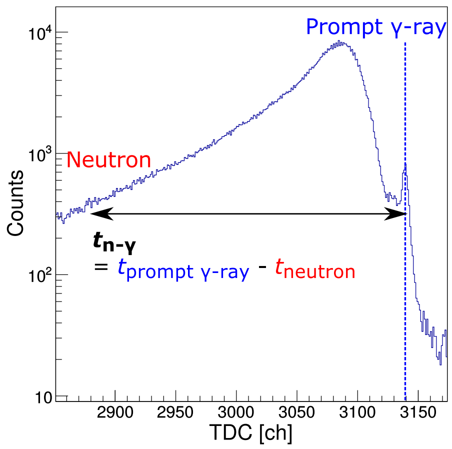

Fig. 2. Inverse TOF spectrum for the large neutron detector at 15°.

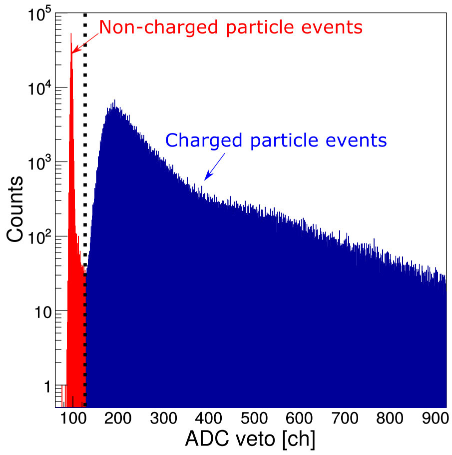

Fig. 3. Light output spectrum for the veto detector at 15°.

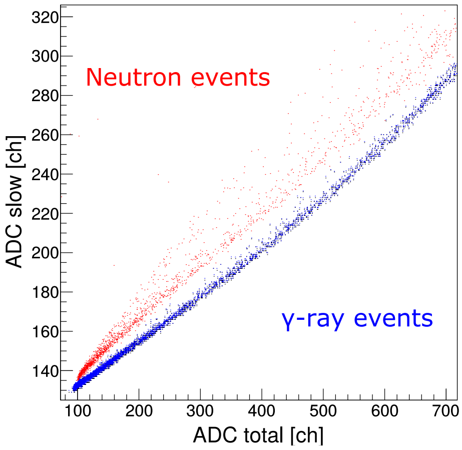

Fig. 4. Two-dimensional histogram of the light output for the neutron detector at 15°.

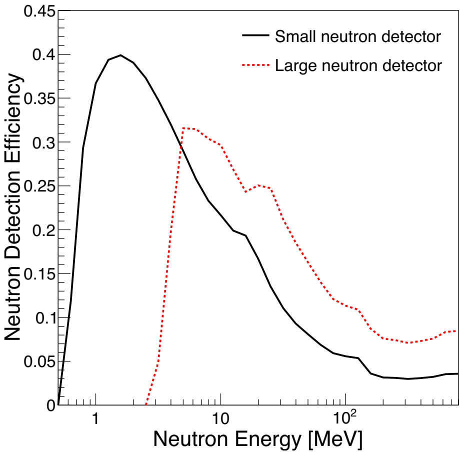

Fig. 5. Neutron detection efficiencies for small and large neutron detectors calculated by SCINFUL-QMD code.

5. Results and Discussion

Figure 6 shows neutron production DDXs for carbon bombarded with 430 MeV/nucleon carbon ions after the multiple scattering correction at six angles of 15, 30, 45, 60, 75, and 90°. Neutron production DDXs calculated by PHITS and Geant4 are shown with the experimental data. The experimental data below 3 MeV at 15 and 45° were not smooth because ratio of background neutrons to foreground neutrons was relatively large. We confirmed the experimental data were smooth in the other energy region. Geant4 underestimated the experimental data at 15 and 30° in the energy region from 20 to 300 MeV.

Figure 7 indicates TTNYs for carbon bombarded with 430 MeV/nucleon carbon ions at six angles of 15, 30, 45, 60, 75, and 90°. TTNYs calculated by PHITS and Geant4 are shown with the experimental data. The experimental data were smooth in the whole energy region.

Figure 8 presents angular distributions of the ratio of neutron production cross-sections integrated in the whole energy region calculated by PHITS and Geant4 to the experimental data. PHITS reproduced a shape of the angular distributions well. **Figure 9** illustrates angular distributions of the ratio of TTNYs integrated in the whole energy region calculated by PHITS and Geant4 to the experimental data. Both PHITS and Geant4 reproduced a shape of the angular distributions well. However, both calculations overestimated the experimental data in magnitude where such tendency is more clear in the Geant4 calculation.

Figure 10 shows angular distributions of the ratio of neutron production cross-sections integrated from 20 to 300 MeV calculated by PHITS and Geant4 to the experimental data. From this figure, we can see QMD model adopted in PHITS and Geant4 because most of the neutrons above 20 MeV are produced by the QMD model. An upper limit of the integral was set to 300 MeV because we confirmed Geant4's underestimation at 15 and 30° in the energy region below 300 MeV. PHITS (squares) reproduced a shape of angular distributions, while Geant4 (triangles) underestimated the experimental data by 50% and 35% at 15 and 30°, respectively.

We assume Geant4's underestimation at 15 and 30° are caused by a difference of inelastic collisions in the two-body collision term adopted in between G4QMD and JQMD. When nucleon-nucleon inelastic collision occurs in the two-body collision term, baryonic resonances ($\Delta(1232)$, $N^*(1440)$ and so on) are produced. **Table 1** shows a comparison of the two-body collision term adopted in JQMD and G4QMD. The number of successful inelastic collisions in G4QMD is about one hundredth of that in JQMD.

We suppose two reasons for the difference. The first reason is a difference of inelastic collision cross-sections in the two-body collision term adopted in between JQMD and G4QMD. According to this table, we can see the inelastic collision cross-section for G4QMD is about one third of that for JQMD because the number of all inelastic collisions is mainly determined by inelastic collision cross-sections. The second is a difference of algorithm in the case of not satisfying energy conservation before and after two-body collision. In JQMD algorithm, a momentum in the center mass of system after two-body collision is adjusted and momentum coordinates are resampled for satisfying energy conservation. On the other hand, in G4QMD algorithm, a channel of two-body collision is resampled. We confirmed two-body inelastic collision was much more difficult to satisfy energy conservation than two-body elastic collision and most of the inelastic collisions were replaced by the elastic collisions. Therefore, most of the inelastic collisions are rejected in G4QMD.

Solid circles in **Fig. 10** are angular distributions of when inelastic collisions never occur in the two-body collision term adopted in JQMD. We confirmed PHITS without two-body inelastic collision (circles) reduced neutron production cross-sections by 40% and 30% at 15 and 30°, respectively.

Figure 11 shows angular distributions of the ratio of neutron production cross-sections integrated from 1 to 20 MeV calculated by PHITS and Geant4 to the experimental data. Neutrons in this energy region are produced by both QMD model and GEM. PHITS (squares) reproduced a shape of angular distributions, while Geant4 (triangles) overestimated the experimental data at 60, 75, and 90°. A shape of angular distributions of Geant4 was similar to that in **Fig. 10** because angular distributions of neutrons produced by the G4QMD process did not reproduce the experimental data in both energy regions. Solid circles are angular distributions of when inelastic collisions never occur in the two-body collision term adopted in JQMD. The shape of angular distributions by PHITS (circles) was close to that by Geant4 (triangles).

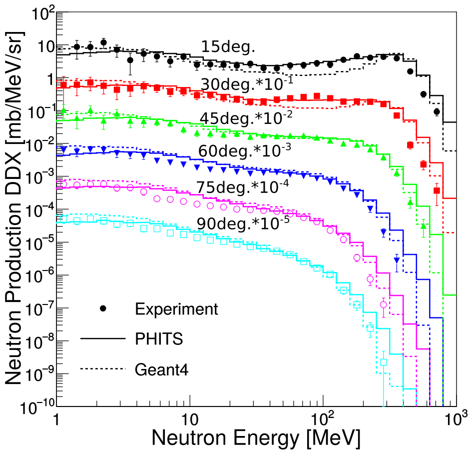

Fig. 6. Neutron production DDXs for 430 MeV/nucleon C +C reaction at 15, 30, 45, 60, 75, and 90°.

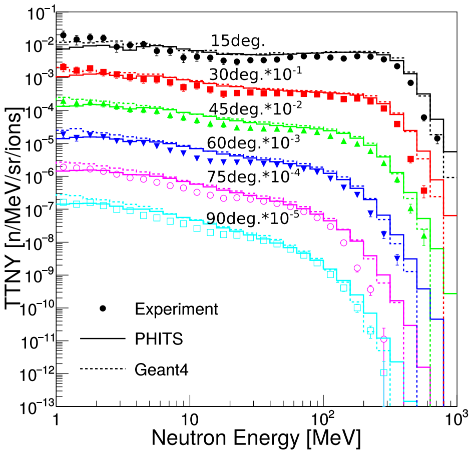

Fig. 7. TTNYs for 430 MeV/nucleon C + C reaction at 15, 30, 45, 60, 75, and 90°.

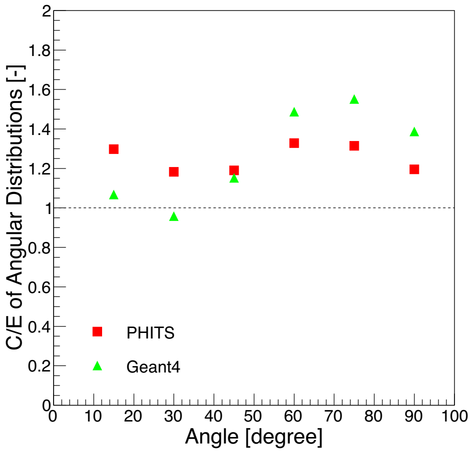

Fig. 8. Angular distributions of the ratio of neutron production cross-sections in the whole energy region calculated by PHITS and Geant4 to the experimental data.

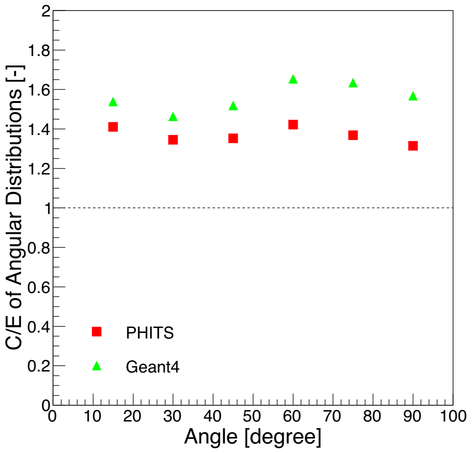

Fig. 9. Angular distributions of the ratio of TTNYs in the whole energy region calculated by PHITS and Geant4 to the experimental data.

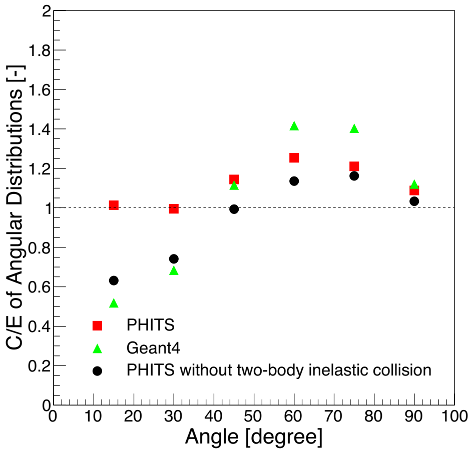

Fig. 10. Angular distributions of the ratio of neutron production cross-sections integrated from 20 to 300 MeV calculated by PHITS and Geant4 to the experimental data.

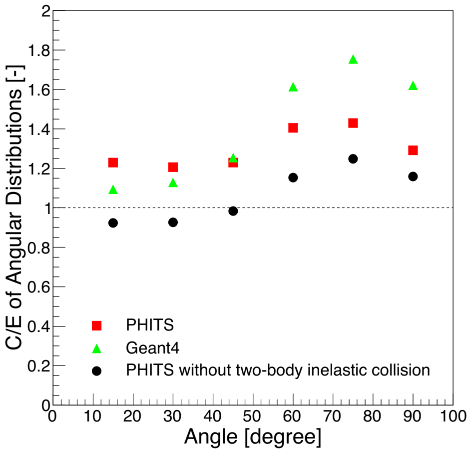

Fig. 11. Angular distributions of the ratio of neutron production cross-sections integrated from 1 to 20 MeV calculated by PHITS and Geant4 to the experimental data.

	All collisions		Successful collisions	
	Elastic	Inelastic	Elastic	Inelastic
JQMD	12.66	1.08	10.02	0.99
G4QMD	11.95	0.39	7.38	0.01

Table 1. Comparison of the two-body collision term adopted in JQMD (PHITS) and G4QMD (Geant4). All collisions are the mean number of elastic and inelastic collisions per QMD event and determined by cross-sections. Successful collisions are the mean number of elastic and inelastic collisions per QMD event satisfying the energy conservation law and the Pauli's exclusion law.

6. Conclusion

Neutron production DDXs and TTNYs for carbon bombarded with 430 MeV/nucleon carbon ions were measured at PH2 beam line of HIMAC facility in NIRS. We obtained the DDXs and TTNYs above 1MeV at six directions of 15, 30, 45, 60, 75, and 90°. The experimental data were compared with calculated results by PHITS and Geant4. PHITS reproduced the experimental data better than Geant4.

We confirmed PHITS was able to reproduce neutron production for carbon-carbon reaction more precisely than Geant4. However, more various researches are required to improve precision of neutron dose estimation and evaluation. In the future work, it is desirable to estimate lifetime cancer risk in the carbon therapy by using Monte Carlo simulation codes.

Acknowledgements

This work was performed as a Research Project with Heavy Ions at NIRS-HIMAC. We would like to express our thanks to the members of the Accelerator Engineering Corporation for technical assistance.

References

[1] http://www.nirs.go.jp/hospital/result/pdf/2014_03.pdf
[2] Agosteo S, et al., Radiotherapy and Oncology, 48 (1998), 293-305.
[3] Brenner DJ, Hall EJ, Radiotherapy and Oncology, 86 (2008), 165-170.
[4] Uwe S, Roger H, frontiers in Oncology, 5:235 (2015).
[5] Sato T, et al., J. Nucl. Sci. Technol., 50:9 (2013), 913-923.
[6] Satoh D, et al., Nucl. Inst. Meth., A644 (2011), 59-67.
[7] Agostinelli S, et al., Nucl. Inst. Meth., A506 (2003), 250-303.
[8] Satoh D, et al., JAEA-Data/Code 2006-023, 2006.
[9] Satoh D, et al., J. Nucl. Sci. Technol., 43 (2006), 714.
[10] Iida K, et al., J. Phys. Soc. Japan, 76 (2007), 044201.
[11] Franco V., Phys. Rev., 175 (1968), 1376.

32 Evaluation of Neutron Spectrum at KURRI-LINAC for Nuclear Data Measurement

Naoki TAKAYAMA[a*], Souichiro OKAZAKI[a],
Jun-ichi HORI[b], Tadafumi SANO[b], Ken NAKAJIMA[b]
[a] *Department of Nuclear Engineering, Kyoto University*
Nishi-Kyoku Kyoto-shi, Kyoto 615-8540, Japan
[b] *Research Reactor Institute, Kyoto University*
Kumatori-cho, Sennan-gun, Osaka 590-0494, Japan
*E-mail: takayama.naoki.46r@st.kyoto-u.ac.jp

In order to obtain the neutron spectrum for resonance cross section measurement, we evaluated the moderator geometry used for the pulsed neutron source at the Linac of Kyoto University Research Reactor Institute (KURRI-LINAC). We used three cylindrical moderator tanks (30, 20, 15cm in diameter) and an octagonal moderator tank named "pacman" (10cm in thickness), to vary the neutron spectrum. From the viewpoint of resonance cross section measurement, the neutron spectra, fluxes and background effects were investigated in this study. As a result, we found that the cylindrical tank with 15cm diameter was the best geometry among four types of moderators for the cross section measurements of resonance energy region.

1. Introduction

The nuclear data with high accuracy is required for the various research fields such as nuclear engineering, space physics and so on. In particular, cross sections of thermal and resonance energy regions were important for nuclear reactor design. The Time-of-flight (TOF) method is often used in resonance cross section measurement. At the KURRI-LINAC, a Ta target was irradiated by electron beam to generate a pulsed neutron for the TOF measurement. This pulsed neutron source is coupled with a water moderator to produce wide energy rage of neutrons (white neutrons) from thermal to MeV region. Thus, by changing the moderator geometry, we can vary the neutron spectrum depending on the purpose of experiment.

In this study, we have investigated the change of neutron spectrum using different moderator geometries to obtain a suitable spectrum for the measurement of resonance cross section. In general, we use an octagonal moderator tank named "pacman" (10cm in thickness) for the measurement of thermal and resonance cross sections as shown in Fig.1. In addition to the pacman, three cylindrical moderators with different diameter, as shown in Fig.2, were investigated for this study.

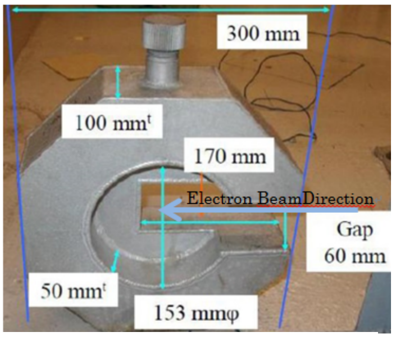

Fig. 1 Pacman moderator

Fig. 2 Cylindrical moderator

2. Experiments

The neutron spectrum for each moderator was obtained by measuring prompt gamma-ray from the ^{10}B(n, αγ) reaction with the TOF method (^{10}B run). The enriched ^{10}B pellet (8mm×22mmØ, 96.96wt%) was used as the sample. The leakage neutrons from the sample were compensated by the coefficient r of Eq. (1) to obtain a precise gamma-ray count.

$$r = \frac{1}{(1-e^{-n\sigma_t})} \times \frac{\sigma_t}{\sigma_c} , \qquad (1)$$

where n is the surface density of the ^{10}B sample [atoms/cm^2],

σ_t and σ_c are the microscopic cross sections of total and capture reactions [cm^2]. The schematic diagram of the experiment is shown in Fig.3. As shown in the figure, the ^{10}B sample was located at the distance of 10m from the Ta target. Prompt gamma-rays from ^{10}B sample were measured by the BGO detector (2inch×2inchØ), which was located at the 120mm away from the sample.

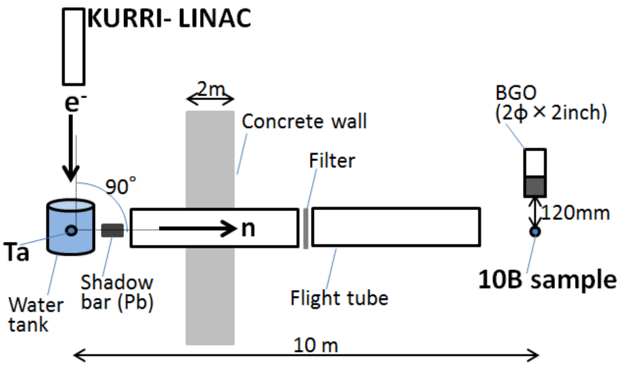

Fig.3 Schematic diagram of the TOF experiment

Table 1 Resonance Filters

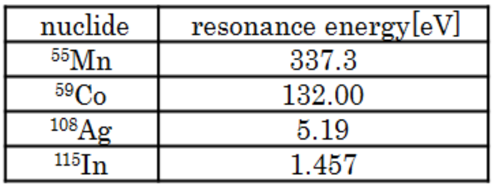

nuclide	resonance energy[eV]
^{55}Mn	337.3
^{59}Co	132.00
^{108}Ag	5.19
^{115}In	1.457

Table 2 Electron Beam Conditions

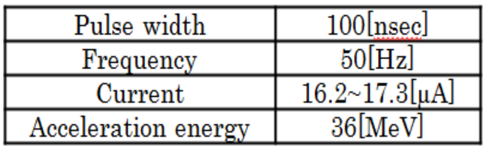

Pulse width	100[nsec]
Frequency	50[Hz]
Current	16.2~17.3[μA]
Acceleration energy	36[MeV]

The background component in the TOF spectrum consisted of natural gamma and neutron radiations, bremsstrahlung (gamma) radiations from the Ta target, scattered neutrons and gamma-rays, gamma-rays caused by the ^{1}H(n, γ)^{2}H reaction and so on. In order to evaluate the background, we performed the measurement with the black resonance method (filter run). In this method, the black resonance filters shown in Table 1 were inserted between the flight tubes as shown in Fig.3. The bottoms of the resonance dips in the obtained TOF spectrum were fitted to the following equation$^{1)}$, which represented the background spectrum.

$$y_B(t) = a_1 + a_2\exp(-a_3 t), \qquad (2)$$

where t is the time-of-flight [s], a_1, a_2 and a_3 are constants. In addition to this measurement, we also measured the neutron spectrum without the sample (blank run) to investigate the effect of scattered gamma-rays from the target.

The electron beam conditions in the experiments are shown in Table 2, and the measurement time for the cylindrical tanks and the pacman were 30minutes and 60minutes, respectively.

3. Results

The TOF spectra with background fitting curve obtained by the ^{10}B run, the filter run and the blank run are showed in Fig.4. The counts have been normalized by measurement time. We obtained the neutron spectra by subtracting the background from the measured TOF spectra as shown in Fig.5. For the background in this study, we used the larger values among the background fitting curve and the spectrum of the blank run.

4. Discussion

As shown in Fig.4, there exists the difference between fitting curve and the spectrum of blank run, and the difference increases with moderator thickness. Additionally, the difference varies with time. Hence, we assumed that the main factor of the difference between those backgrounds was the 2.2MeV gamma-rays caused by neutron capture reaction of hydrogen in the moderator and scattered by the sample. We calculated the time dependence of capture reactions using MVP$^{2)}$ code with JENDL-4.0$^{3)}$ library. The calculated results were shown in Fig.6 compared with the experimental results. In order to obtain the experimental results, the gamma-ray counts of fitting curve and blank run were bunched, respectively, per 10 micro seconds, and the differences between the two bunched data were calculated. The horizontal axis (life time) in the figure means the time to capture reaction from the neutron generation. These calculated results show the similar trend with the

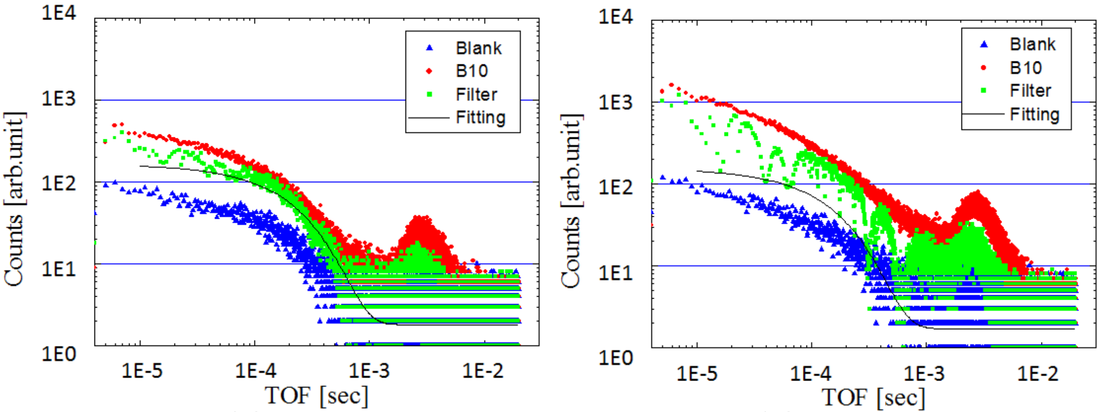

(a) ϕ=30cm (b) ϕ=20cm

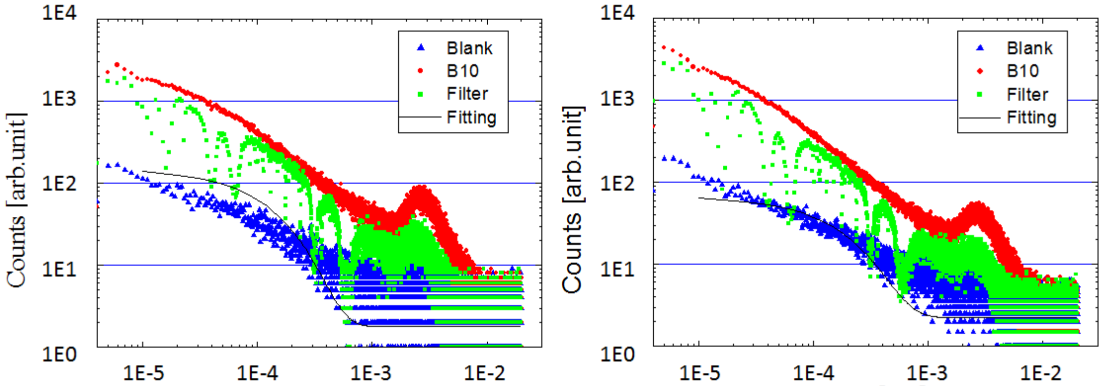

(c) ϕ=15cm (d) pacman

Fig.4 TOF spectrum for different moderators

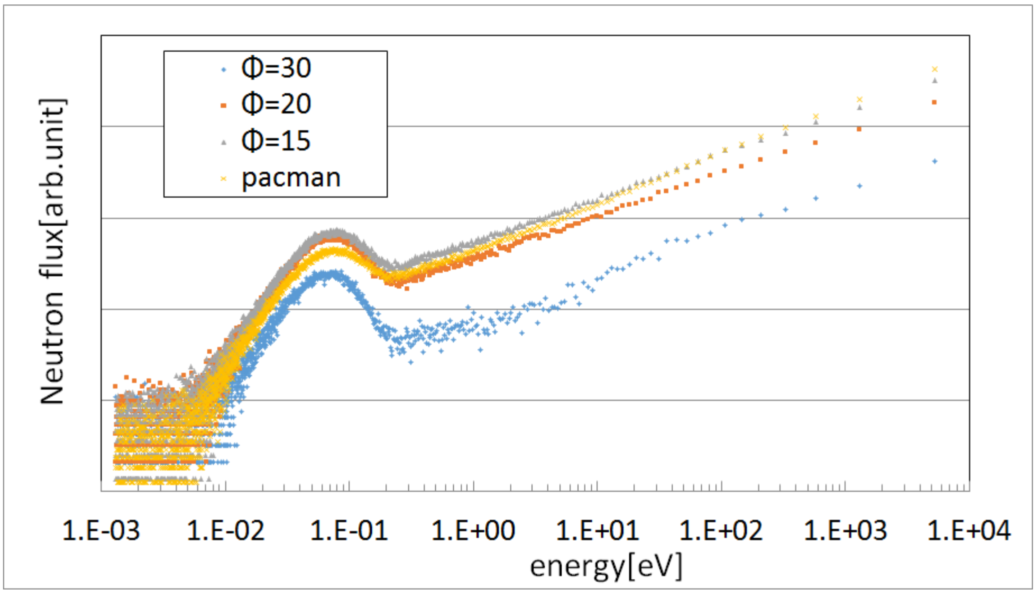

Fig.5 Neutron spectra

experimental ones. In addition, the time when the neutron capture reaction significantly decrease almost corresponds to the time that fitting curve starts to overlap with the blank run as seen in Fig.4. Therefore, it seems that the main component of time-dependent background difference was considered to be caused by the 2.2MeV gamma-rays from the hydrogen capture reaction.

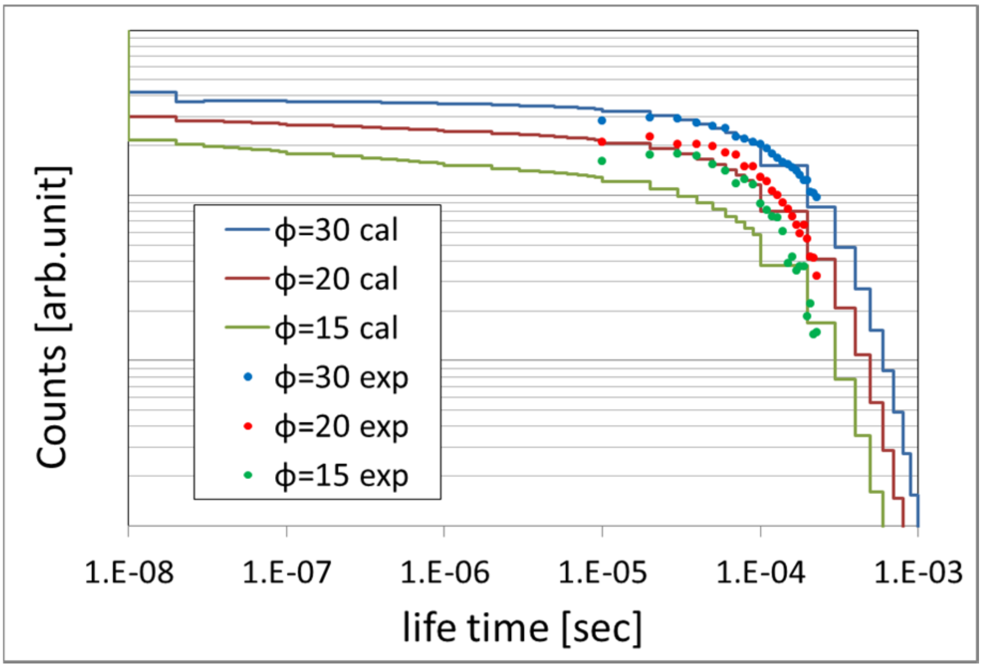

Fig.6 Time distribution of the events that neutron is captured in the moderator

Using the obtained neutron spectra, we calculated neutron spectrum indexes ($\equiv \int_{epi} \Phi(E)dE / \int_{all} \Phi(E)dE$), relative neutron fluxes and background fluxes integrated for the epi-thermal region. The results are shown in Fig.7. We defined that the epi-thermal region was 0.3~1000eV.

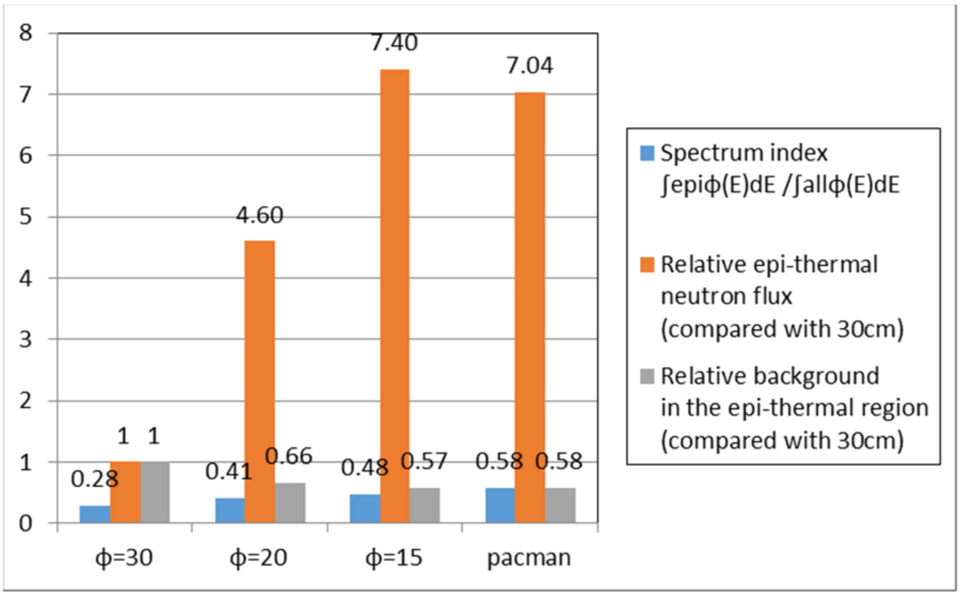

Fig.7 Neutron source performance

As seen in the figure, the epi-thermal neutron flux and the spectrum index for the cylindrical tanks increase by decreasing the tank diameter from 30cm to 20cm and 15cm. On the other hand, the background flux in the epi-thermal region decreases by decreasing the tank diameter. Thus, the 15cm-diameter tank gives the largest epi-thermal neutron flux and the lowest background in the cylindrical tanks. In comparison with the pacman moderator, the epi-thermal neutron flux of the 15cm-tank is larger than the pacman, although the spectrum index of the pacman is larger. It means that moderator thickness of the pacman is not enough for the epi-thermal neutron production. Consequently, it is concluded that the cylindrical tank with 15cm diameter is the best moderator for the resonance cross section measurement among the moderators investigated in the present study.

5. Conclusion

In order to obtain the neutron spectrum for resonance cross section measurement, we experimentally evaluated the moderator performance of four geometries at the KURRI-LINAC. We compared the neutron spectrum, flux and background for each moderator to evaluate the performance. From the view point of the epi-thermal neutron flux and background, the cylindrical tank with the diameter of 15cm shows best performance among the moderators investigated in the present study. In order to obtain more excellent moderator geometry for the measurement of the resonance capture cross section, the further study is necessary including the quantitative analysis on the background treatment.

References

1) O. Shcherbakov, K. Furutaka, S. Nakamura, H. Sakane, K. Kobayashi, S. Yamamoto, J. Hori, and H. Harada: "Measurement of Neutron Capture Cross Section of ^{237}Np from 0.02 to 100eV, " J. Nucl. Sci. Technol., **42**(2), 135-144 (2005).

2) Y. Nagaya, K. Okumura, T. Mori, M. Nakagawa: "MVP/GMVP II : General Purpose Monte Carlo Codes for Neutron and Photon Transport Calculations based on Continuous Energy and Multigroup Methods," JAERI 1348 (2005).

3) K. Shibata, O. Iwamoto, T. Nakagawa, N. Iwamoto, A. Ichihara, S. Kunieda, S. Chiba, K. Furutaka, N. Otuka, T. Ohsawa, T. Murata, H. Matsunobu, A. Zukeran, S. Kamada, and J. Katakura: "JENDL-4.0: A New Library for Nuclear Science and Engineering," J. Nucl. Sci. Technol. 48(1), 1-30 (2011).

This is a blank page.

33

Measurement of gamma-ray spectra from proton-Lithium nuclear reactions for development of a BNCT neutron source

Tatsuhiro SAITO*, Tatsuya KATABUCHI, Masayuki IGASHIRA, Shotaro YANAGIDA,
Tomohiro OKAMIYA, Brian HALES, Seigo UMEZAWA
Research Laboratory for Nuclear Reactors, Tokyo Institute of Technology
2-12-1-N1-26, Ookayama, Meguro-ku, Tokyo 152-8550, Japan
*e-mail: saito.t.aq@m.titech.ac.jp

For development of a neutron source for boron neutron capture therapy (BNCT) using the neutron production reaction ^{7}Li(p,n)^{7}Be, γ-ray spectra from a thick Li target irradiated with a proton beam near the neutron threshold energy were measured. Gamma-rays from the ^{7}Li(p,p'γ)^{7}Li and ^{7}Li(p,γ)^{8}Be reactions were observed. These γ-rays have a possible impact on patient dose in BNCT. The present γ-ray spectra can be used to determine γ-ray production yields that are necessary for patient dose evaluation.

1. Introduction

Boron neutron capture therapy (BNCT) has been proven to be effective treatment for infiltrating cancers such as glioblastoma. BNCT has been practiced using neutron beams from nuclear reactors. To deploy more BNCT facilities, accelerator BNCT projects are ongoing across the world.

The ^{7}Li(p,n)^{8}Be reaction is one of the best candidate neutron production reactions for accelerator-based BNCT. Required incident proton energy is less than 3 MeV, thus leading to compact BNCT irradiation system utilizing a small accelerator such as a radio-frequency quadrupole. Previous feasibility studies showed that the available neutron flux from the ^{7}Li(p,n)^{8}Be reaction is enough for BNCT [1]. However, one must consider two γ-ray production reactions ^{7}Li(p,p'γ)^{7}Li and ^{7}Li(p,γ)^{8}Be. Gamma-rays from these simultaneous reactions might affect patient dose. The ^{7}Li(p,p' γ)^{7}Li reaction emits a 478-keV γ-ray in deexcitation from the first excited state of ^{7}Li. The ^{7}Li(p,γ)^{8}Be reaction emits considerably high-energy gamma-rays up to around 18 MeV. The current available nuclear data of the γ-ray production reactions, used as calculation inputs in dose evaluations, are not satisfactory. The ^{7}Li(p,γ)^{8}Be cross section has been measured up to only 1.5 MeV, much lower than the neutron production threshold of 1.880 MeV. Angular distributions of both the ^{7}Li(p, γ)^{8}Be and ^{7}Li(p, p'γ)^{7}Li reactions have never been measured systematically in the relevant energy region. Isotropic angular distributions were inevitably assumed in the previous dose evaluations. This nuclear data situation motivated us to perform the present measurement. In the present work, we measured γ-ray spectra from a thick target irradiated with a proton beam at proton energies near the neutron threshold of the ^{7}Li(p,n)^{8}Be reaction .

2. Experiments

We made a Li target with an enough thickness to stop the incident protons. The thickness of the Li target was 300 μm while the penetration range of the proton in solid Li is 150 μm at 2 MeV. The diameter of the Li target was 20 mm. The Li target was fabricated on a cupper backing (30 mm diam). Experiments were carried out in the Research Laboratory for Nuclear Reactors of the Tokyo Institute of Technology. The Li target was bombarded with a proton beam form a 3-MV Pelletron accelerator. Gamma-rays were detected with an anti-Compton NaI(Tl) spectrometer placed at 0°. Measurements were made at incident proton energies of 1.870 and 1.670 MeV, which are 10 and 210 keV below the threshold of ^{7}Li(p,n)^{7}Be reaction. The proton beam current was kept at around 1 μA to avoid a high counting rate of the NaI(Tl) detector causing a large dead time. The typical counting rate was about 5 kcps.

3. Results

The obtained pulse-height spectra are shown in Fig.1. Natural background was already subtracted from the pulse-height spectra. The strong 478-keV gamma-rays from the ^{7}Li(p,p'γ)^{7}Li reaction dominated the total counting rate. Two high energy peaks from 14 MeV to 17MeV are gamma-rays from the ^{7}Li(p,γ)^{8}Be reaction. Our preliminary analysis showed that the yield of the ^{7}Li(p,p' γ)^{7}Li reaction was about 30% smaller than a thick target yield used in previous dose evaluation [1]. For the ^{7}Li(p,γ)^{8}Be reaction, the yield was about 25% smaller than a value calculated from previous cross section data [2].

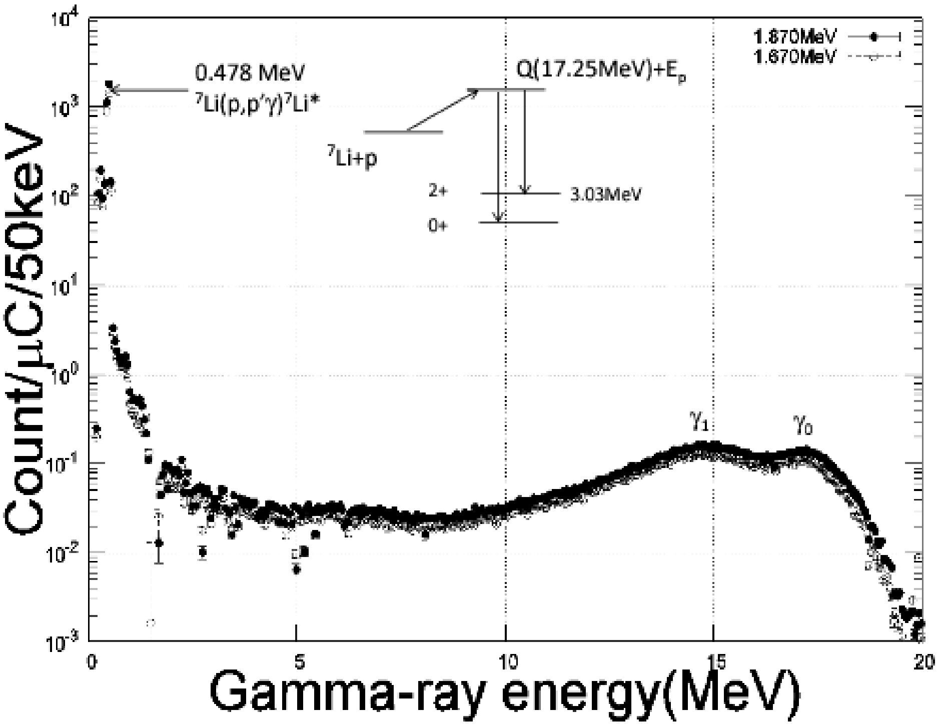

Fig. 1. Pulse height spectra.

4. Conclusion

We measured the γ-ray spectra from a thick Li target irradiated with a proton beam near the neutron threshold energy. Emitted gamma rays were detected with anti-Compton NaI(Tl) spectrometer at an angle of 0°. Data analysis to determine the thick target yields is underway. The γ-ray production yields can be used for patient dose evaluation in BNCT. In addition, we are planning to measure the angular distributions of the γ-ray production yields.

References

[1] C.L.Lee and X. –L.Zhou, A Monte Carlo dosimetry-based evaluation of the ^{7}Li(p,n)^{7}Be reaction near threshold for accelerator boron neutron capture therapy. Med. Phys. 27, 192-202 (2000).

[2] D.Zahnow, C.Anglo et al, The S(E) factor of ^{7}Li(p,γ)^{8}Be and consequences for S(E) extrapolation in ^{7}Be(p,γ_0)^{8}B. Z, Phys.A. 351, 229-236 (1995).

34 Measurement of the keV-Neutron Capture Cross Sections and Capture Gamma-ray Spectra of Cs-133 and I-127

Seigo UMEZAWA*, Masayuki IGASHIRA, Dominic MORARU, Tatsuya KATABUCHI,
Shotaro YANAGIDA, Tomohiro OKAMIYA
Research Laboratory for Nuclear Reactors, Tokyo Institute of Technology
O-okayama, Meguro-ku, Tokyo 152-8550, Japan
*E-mail: umezawa.s.aa@m.titech.ac.jp

The neutron capture cross sections and capture γ-ray spectra of ^{133}Cs and ^{127}I at incident neutron energies from 15 to 100 keV have been measured by the time-of-flight method. Capture γ-rays were detected with an anti-Compton NaI(Tl) γ-ray spectrometer, and the pulse-height weighting technique was applied to observed pulse-height spectra to derive capture yields. The capture cross sections of ^{133}Cs and ^{127}I were obtained with errors of about 5% using the standard capture cross section of ^{197}Au. The obtained cross sections were compared with evaluated values in JENDL4.0 and ENDF/B-VII.1. The capture γ-ray spectra of ^{133}Cs and ^{127}I were derived by unfolding the pulse height spectra.

1. Introduction

Management of radioactive waste from nuclear power plants is a key issue to continue nuclear energy production in the future. Currently-planned geological disposal is controversial because long-lived nuclides existing in spent nuclear fuel require very long-term management. In order to solve the issue, researchers have suggested nuclear transmutation systems that transmute long-lived nuclides to shorter-lived or stable species via neutron-induced reactions. Study of the nuclear transmutation systems is still in a stage of conceptual design. Accurate nuclear data such as reaction cross sections of long-lived fission products (LLFP) and minor actinides are necessary for the design of the nuclear transmutation systems.

In the present work, we measured the neutron capture cross sections of ^{133}Cs and ^{127}I. These neutron capture cross sections are needed to design a system to transmute the LLFP nuclides ^{135}Cs ($T_{1/2}$ = 2.3 M year) and ^{129}I ($T_{1/2}$ = 15.7 M year) because LLFPs exist together with their stable isotopes in spent nuclear fuel. The neutron capture cross sections of both

LLFPs and their stable isotopes are required unless isotope separation is carried out. In addition, we measured the neutron capture γ-ray spectra of ^{133}Cs and ^{127}I, which give more information on reaction mechanism of the neutron capture process.

2. Experimental Procedure and Data Analysis

Detail of experimental procedure has been described elsewhere1). Only a brief description is given in this report. Experiments were performed using the 3MV Pelletron accelerator at the Research Laboratory for Nuclear Reactors at the Tokyo institute of Technology. A pulsed neutron beam was generated via the ^{7}Li(p,n)^{7}Be reaction induced by a pulsed proton beam from the Pelletron accelerator. The pulse width was 1.5 ns and the repetition rate was 4 MHz. The time-of-flight (TOF) method was employed to deduce the incident neutron energy. Neutrons were detected with a ^{6}Li glass scintillator placed at a flight distance of 30 cm. The energy of the incident neutrons distributed from a few keV to 100 keV. The flight path length from the neutron source to the sample was 12 cm. Neutron capture γ-rays emitted from the samples were detected with an anti-Compton NaI(Tl) spectrometer2). The natural isotope abundance of ^{133}Cs and ^{127}I is 100%. Isotopically-enriched samples were not needed. Samples in chemical forms CsI, PbI_2 and Pb were used. Combing experimental results from three samples, contributions from Cs, I and Pb to neutron capture yields can be separated. After background subtraction, a pulse-height weighting technique3) was applied to derive the capture yields of Cs and I. The absolute cross sections were determined from standard measurements of a gold sample, based on the well-known cross section of ^{197}Au(n,γ)^{198}Au4).

The capture γ-ray spectra of ^{133}Cs and ^{127}I were derived by unfolding the net pulse height spectra with detector response functions.

3. Results and Discussion

The capture cross sections of ^{133}Cs and ^{127}I at neutron energies from 15 to 100 keV were derived with errors of about 5%. In Fig. 1 and Fig. 2, the present results are shown together with evaluated cross sections in JENDL-4.05,6) and ENDF/B-VII.17,8). The evaluated cross sections were averaged in the same energy bins as the present experimental data for comparison. For ^{133}Cs, the evaluated cross sections of JENDL4.0 are larger than the present results by 6-8%. The evaluated cross sections of ENDF/B-VII.1 are smaller than the present results by 13-16%. For ^{127}I, the evaluated cross sections and the present data disagree at the lowest and highest energy points. It seems that energy dependence is different between the evaluations and the present results. The obtained capture γ-ray spectra of ^{133}Cs and ^{127}I are shown in Fig.3 and Fig.4.

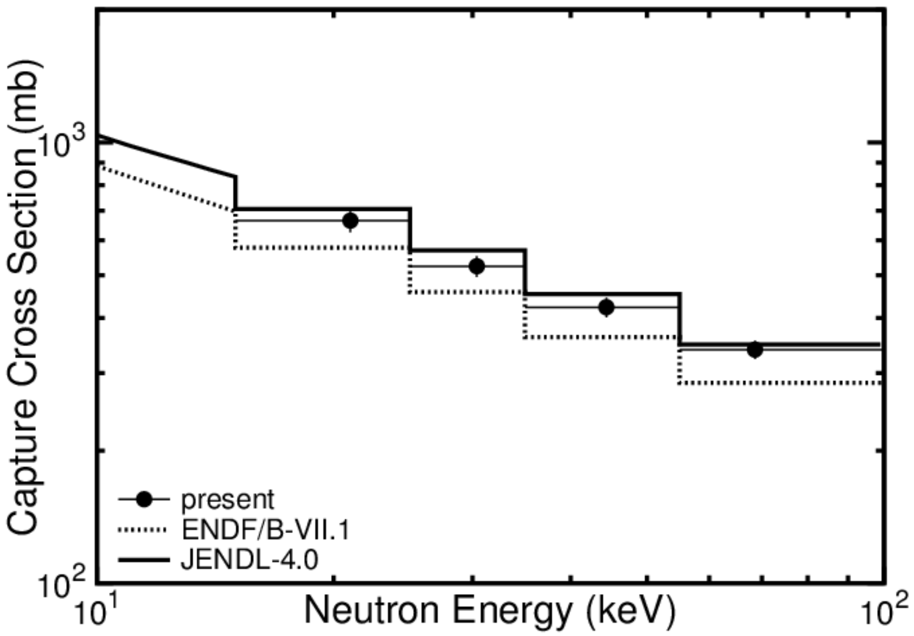

Fig.1 Neutron cross sections of ^{133}Cs. The present results (solid) are compared with evaluations of JENDL-4.0 and ENDF/BVII.1.

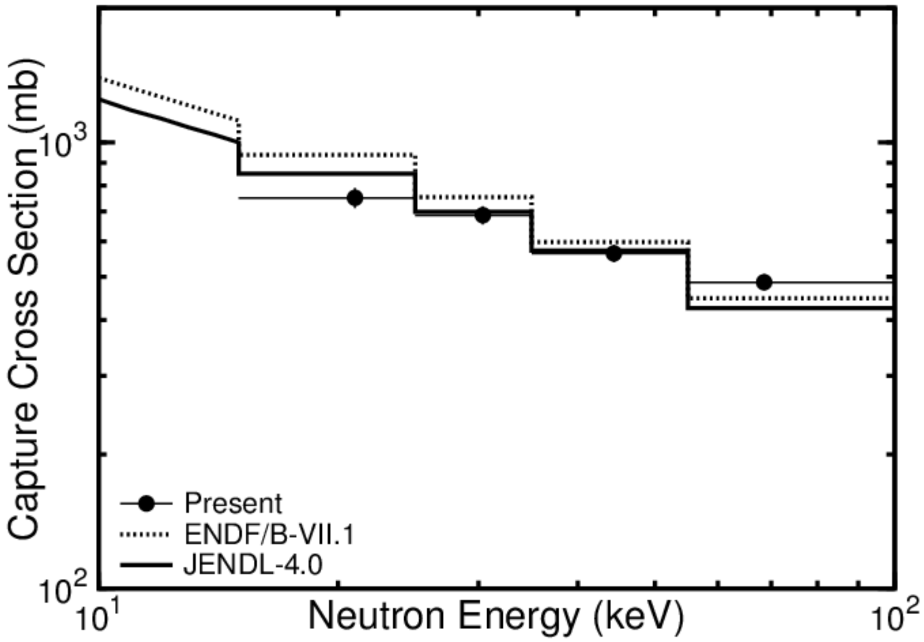

Fig.2 Neutron cross sections of ^{127}I. The present results (solid) are compared with evaluations of JENDL-4.0 and ENDF/BVII.1.

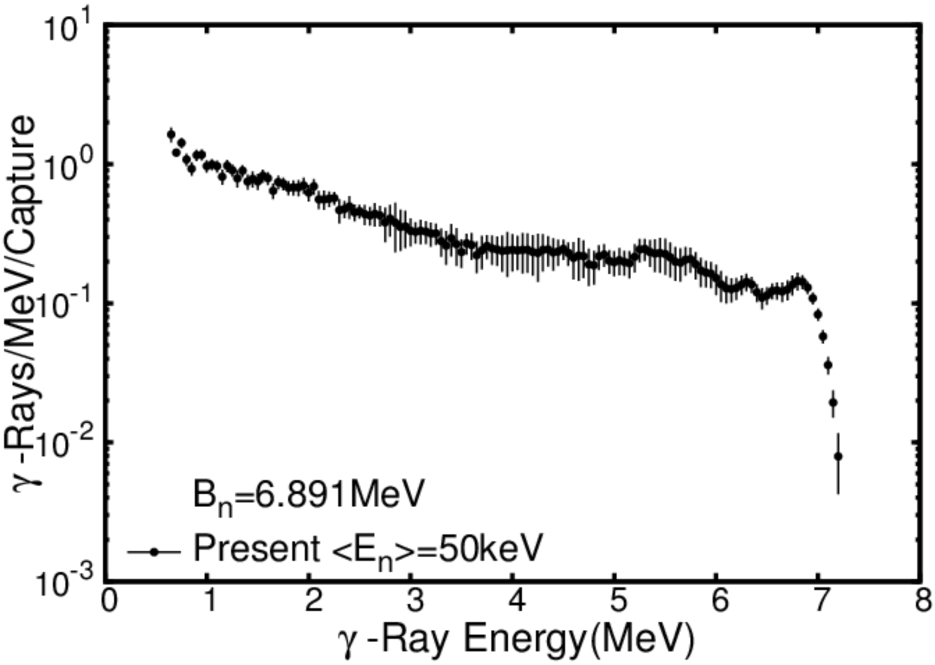

Fig.3 Neutron capture γ-ray spectrum of ^{133}Cs.

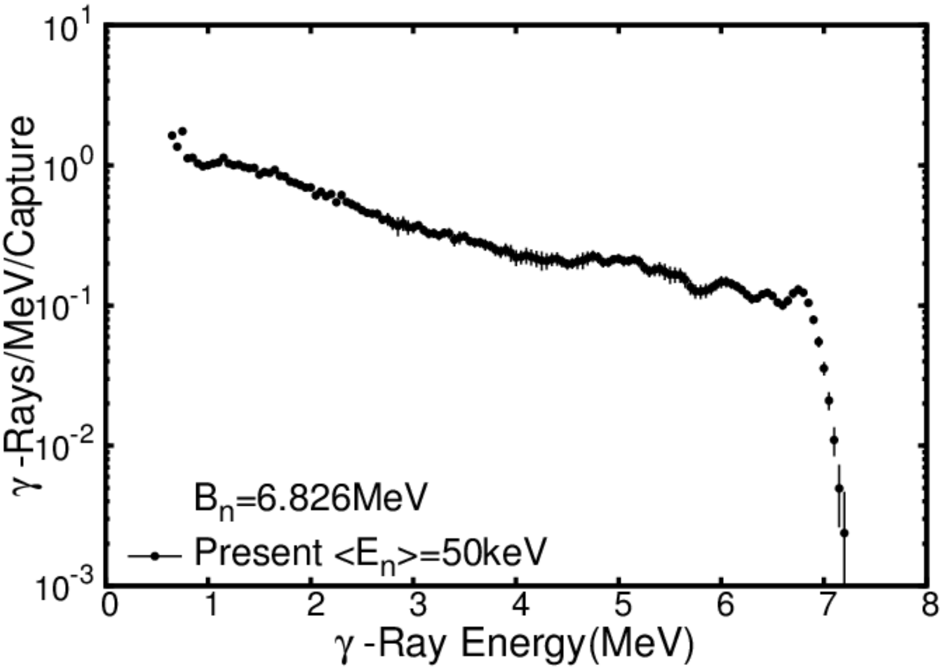

Fig.4 Neutron capture γ-ray spectrum of ^{127}I.

4. Conclusions

The capture cross sections and capture γ-ray spectra of ^{133}Cs and ^{127}I were measured at incident neutron energies from 15 to 100 keV by the TOF method. A pulse-height weighting technique was applied to derive capture yields. The capture cross sections of ^{133}Cs and ^{127}I were obtained with errors of about 5% based on the standard capture cross sections of ^{197}Au.

The evaluated cross sections disagree with the present results at some energy points. Reevaluation of the capture cross sections of ^{133}Cs and ^{127}I including the present results is necessary. The capture γ-ray spectra of ^{133}Cs and ^{127}I were derived by unfolding the pulse-height spectra.

References

1) S. Mizuno, M. Igashira and K. Masuda, "Measurements of keV-neutron capture cross sections and capture gamma-ray spectra of 161,162,163Dy," *J. Nucl. Sci. Technol.*, **36**, 493-507 (1999).
2) M. Igashira, H. Kitazawa, N. Yamamuro, "A heavy shield for the gamma-ray detector used in fast-neutron experiment," Nucl. Instrum. Methods, **A245**, 432-437 (1986).
3) R.L. Macklin and J. H. Gibbons "Capture-cross-section studies for 30-220 keV neutrons using a new technique," *Phys. Rev.*, **159**, 1007-1012(1967).
4) ENDF/B-VII.1 data file for ^{197}Au(MAT=7925), evaluated by P.G. Young (1991).
https://www-nds.iaea.org/exfor/servlet/E4sGetTabSect?SectID=2287532&req=14938&PenSectID=2305057
5) JENDL-4.0 data file for ^{133}Cs(MAT=5525), evaluated by N. Iwamoto (2010).
http://wwwndc.jaea.go.jp/cgi-bin/UNZIP_jendl.cgi?lib=J40&iso=Cs133
6) JENDL-4.0 data file for ^{127}I(MAT=5325), evaluated by JNDC FP Nuclear data W. G. (2009).
http://wwwndc.jaea.go.jp/cgi-bin/UNZIP_jendl.cgi?lib=J40&iso=I127
7) ENDF/B-VII.1 data file for ^{133}Cs(MAT=5525), evaluated by Mughabghab (2011).
https://www-nds.iaea.org/exfor/servlet/E4sGetTabSect?SectID=2271212&req=14942&PenSectID=2288737
8) ENDF/B-VII.1 data file for ^{127}I(MAT=5325), evaluated by Young (2011).
https://www-nds.iaea.org/exfor/servlet/E4sGetTabSect?SectID=2269757&req=14943&PenSectID=2287282

This is a blank page.

35 Measurement of the Cl-35(n,γ) reaction cross section in ANNRI at J-PARC

Kaoru Y. HARA[1)*], Nobuya FUJII[1)], Takashi KAMIYAMA[1)], Yuki NARITA[1)],
Hirotaka SATO[1)], Shoji NAKAMURA[2)], and Yosuke TOH[2)]

1) Faculty of Engineering, Hokkaido University, Sapporo 060-8628, Japan
2) Nuclear Science and Engineering Center, Japan Atomic Energy Agency, Ibaraki-ken 319-1195, Japan
*e-mail: hara.kaoru@eng.hokudai.ac.jp

The measurements of the neutron capture cross section of ^{35}Cl were performed using an NaI(Tl) detector in ANNRI at J-PARC. The measured pulse height and TOF spectra for NaCl samples are reported with the calculated pulse height spectra.

1. Introduction

A long-lived nucleus ^{36}Cl (half-life 3×10^5 yr) is a radioactive product in low-level radioactive wastes. It is produced by the neutron capture reaction of a stable nucleus ^{35}Cl, which is an impurity in a coolant of nuclear reactor and structural material of accelerator facility such as water and concrete. While the neutron capture cross section of ^{35}Cl is required to evaluate the production yields of the ^{36}Cl nuclei, the available data are scarce in the neutron energy region from 0.03 eV to 1 keV.

The previous data of the neutron capture cross section of ^{35}Cl are shown in Fig. 1, where the evaluated cross section of JENDL-4.0 [1] is also shown by the solid line. The datum at the thermal neutron energy (square [2]) was measured with the activation method in the NRX reactor by detecting the β-rays emitted from the ^{36}Cl nuclei. Other datum at the thermal neutron energy (triangle [3]) was determined from some γ-ray intensities which were measured with the prompt γ-ray activation method at the IEA–R1 reactor facility. In the keV neutron energy region, the data (circle [4] and cross [5]) were derived using the resonance parameters, which were measured with the neutron time-of-flight (TOF) method at the ORELA accelerator facility. These previous data are the Maxwellian averaged cross sections.

To obtain the neutron capture cross section of ^{35}Cl in the energy region below 1 keV, the neutron time-of-flight (TOF) measurements were performed using sodium chloride (NaCl) samples. In this work, we report the measured pulse height and TOF spectra for the NaCl samples with the calculated pulse height. The pulse height spectra due to each nucleus in NaCl were calculated with the PHITS code in order to estimate the background components in the experiment.

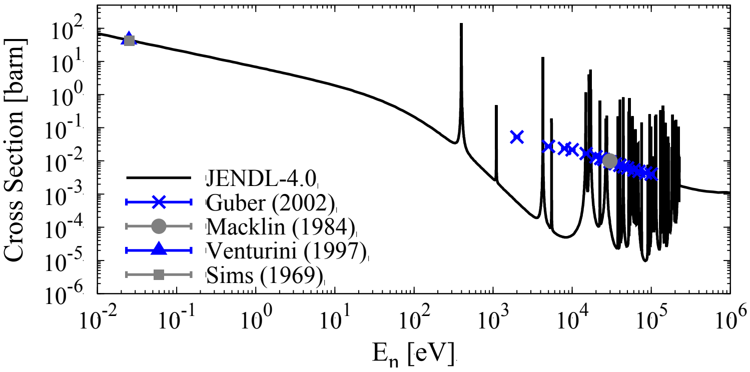

Figure 1: Neutron capture cross section of ^{35}Cl

2. NaCl sample

A solid sample of chemical compound is used in the measurements of the ^{35}Cl(n,γ) reaction since it is difficult to prepare a chlorine gas sample with sufficient density. In our experiment, NaCl was used as the sample, where the NaCl powder was molded into a disk with the weight of 0.15 g and the diameter of 1 cm. While the stable isotope of sodium is only ^{23}Na, the stable isotopes of chlorine are ^{35}Cl and ^{37}Cl. The natural abundances of ^{35}Cl and ^{37}Cl are 76% and 24%, respectively. Therefore, the ^{23}Na and ^{37}Cl nuclei, which are involved in the NaCl sample, contribute to the background of the TOF measurements. We prepared the 99% isotopically enriched ^{35}Cl sample to reduce the background due to ^{37}Cl. We also prepared the 98% enriched ^{37}Cl and natural Cl samples to distinguish the background due to ^{37}Cl and ^{23}Na.

For comparison, the evaluated neutron capture cross sections of ^{35,37}Cl and ^{23}Na in JENDL-4.0 are shown in Fig. 2(a) by the solid, dot-dashed, and dotted lines, respectively. Below 10 eV, the capture cross sections of ^{23}Na and ^{37}Cl are approximately 1% smaller than the one of ^{35}Cl. The capture cross section of ^{35}Cl begins to deviate from a 1/v-law above 10 eV and is comparable with the one of ^{23}Na at 1 keV. In addition, the evaluated neutron elastic cross sections of ^{35,37}Cl and ^{23}Na in JENDL-4.0 are shown in Fig. 2(b) by the solid, dashed, and dotted lines, respectively. The neutron elastic scattering on the sample induces the γ-ray of background since the scattered neutron interacts with the materials of detectors and radiation shields around the sample. Although the background composition depends on not only these cross sections but also the detection efficiencies, the pulse height spectra, and the materials, it is expected to be increase with the neutron energy from Fig. 2.

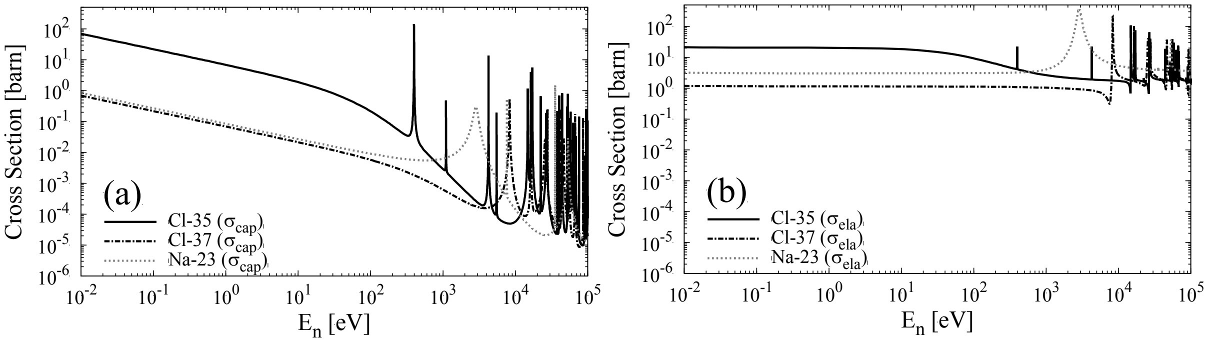

Figure 2: Neutron capture cross sections (a) and neutron elastic cross sections (b) of ^{35,37}Cl and ^{23}Na in JENDL-4.0.

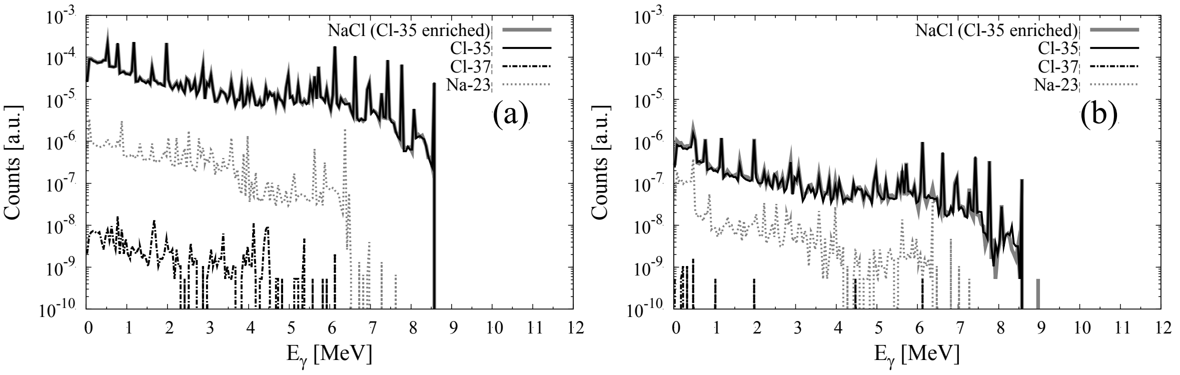

Figure 3: Calculated pulse height spectra for the natural NaCl sample at the incident neutron energies of 25 meV (a) and 100 eV (b).

3. Calculated pulse height spectra using the PHITS code

To estimate the degree of background composition, the pulse height spectra for the ^{35}Cl-enriched NaCl sample were calculated using the PHITS code [6]. At the incident neutron energies of 25 meV and 100 eV, the calculated pulse height spectra are shown in Fig. 3 (a) and (b), respectively. The gray solid, black solid, dot-dashed, and dotted lines present the pulse height spectra for NaCl, ^{35}Cl, ^{37}Cl, and ^{23}Na, respectively. In the simulation, the pencil-like neutron beam with the diameter of 1 cm irradiated the sample and induced the neutron nuclear reactions such as the ^{35}Cl(n,γ) reaction, where the γ de-excitation model EBITEM [7] was used i.e. “igamma = 3”. The NaCl sample with the diameter of 1 cm and the weight of 0.15 g were defined. An NaI(Tl) detector was only defined here because of the computation time, although there are two NaI(Tl) detectors in the experimental setup (Fig. 4) as described in the next section. The tally cell for the γ-ray energy deposit was set in an crystal of NaI(Tl) scintillator that was located at the direction of 90° with respect to the neutron beam axis.

As shown in Fig. 3, the dominant component of the pulse height spectrum of the NaCl sample results from ^{35}Cl. The background due to ^{37}Cl is negligible since ^{37}Cl was depleted in NaCl. On the other hand, the background due to ^{23}Na relatively increases with the incident neutron energy. As compared with Fig. 3(a), the obvious peak emerges on the pulse height spectra of ^{23}Na below 0.5 MeV in Fig. 3(b). The peaks arise from the ^{10}B(n,$\alpha\gamma$)^{7}Li reaction with the elastic scattering neutrons because the boron is involved in the neutron shields around the detector. When the discrimination level of the pulse height is set at 0.9 MeV (or 0.3 MeV), the background components due to ^{23}Na are approximately 1% (or 1%) and 4% (or 7%) of the NaCl spectra at the incident neutron energies of 25 meV and 100 eV, respectively. To reduce the background component, the higher discrimination level would be preferable in the data analysis.

4. Experimental Setup

The measurements of the neutron capture cross section of ^{35}Cl were performed in the Accurate Neutron-Nucleus Reaction measurement Instrument (ANNRI) at the Japan Proton Accelerator Research Complex (J-PARC). The pulsed neutrons were provided from the Japan Spallation Neutron Source (JSNS) at J-PRAC. The neurons were produced by bombarding a mercury target with the 3-GeV proton beam and slowed down in a liquid hydrogen moderator. The proton beam power was about 400 kW. The repetition rate of the proton beam pulses was 25 Hz. The neutron beam irradiated the sample in the experimental area 2 of ANNRI. The neutron flight path length between the moderator and the sample was 28 m. The prompt γ-rays emitted in the neutron capture reaction were measured by the NaI(Tl) detector with the TOF method. The experimental setup of the detector is shown in Fig. 4. Two NaI(Tl) detectors with the anti-Compton suppress plastic detectors, were located at angles of 90° and 125° with respect to the neutron beam axis [8]. The volumes of NaI(Tl) scintillators were 33 cm in diameter × 20 cm in length (90° detector) and 20 cm in diameter × 20 cm in length (125° detector). In this experiment, the 90° detector was only used. The detectors were surrounded by the borated rubber, borated polyethylene, cadmium, lead, enriched ^{6}LiH, and enriched ^{6}Li$_2$CO$_3$ to shield the neutron and γ-ray backgrounds. As described above, the enriched ^{35}Cl, ^{37}Cl, and natural Cl samples in chemical form of NaCl were used. In addition, the natural carbon and enriched ^{10}B samples were used for the evaluation of background due to the scattering neuron on the sample and the determination of neutron beam flux, respectively.

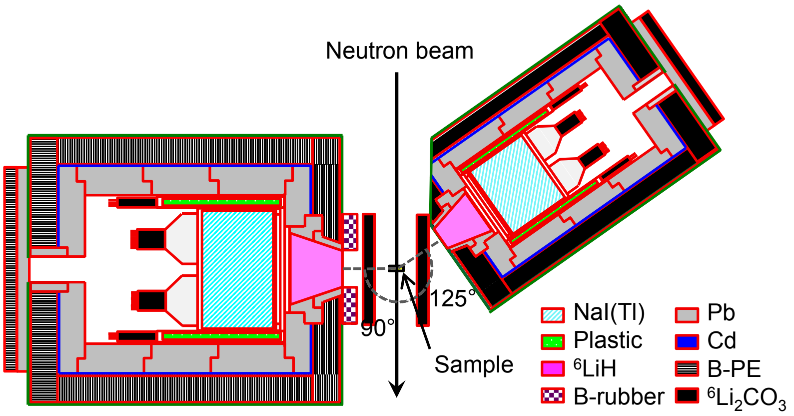

Figure 4: Experimental setup of the NaI(Tl) detectors in ANNRI at J-PARC

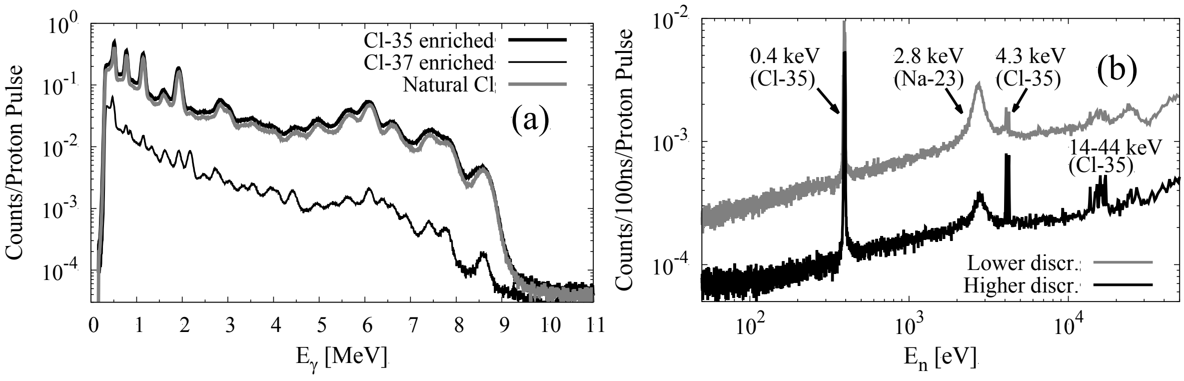

Figure 5: Measured pulse height spectra (a) and neutron TOF spectra (b)

5. Measured pulse height spectra and neutron TOF spectra

The measured pulse height spectra of the enriched ^{35}Cl, enriched ^{37}Cl, and natural Cl samples are shown in Fig. 5(a) by the solid, thin solid, gray solid lines, respectively. The spectrum of the natural Cl sample is similar to the one of the enriched ^{35}Cl sample since the dominant component of these spectra arose from the ^{35}Cl(n,γ) reaction. The spectrum of the enriched ^{37}Cl sample is of various compositions due to ^{35,37}Cl and ^{23}Na. In the three pulse height spectra, the 0.5-MeV peaks which are considered to be resulting from the ^{10}B(n,αγ)^{7}Li reaction with the scattering neutron are observed. In accordance with the consideration, at the lower and higher discrimination levels for the pulse heights, the neutron TOF spectra of the enriched ^{35}Cl sample are plotted by the gray solid and solid lines in Fig. 5(b), respectively, where the lower and higher discrimination levels are about 0.3 and 0.9 MeV, respectively. While the 0.4-keV and 4.3-keV resonances of ^{35}Cl and the 2.8-keV resonance of ^{23}Na are observed in the both TOF spectra, the resonances of ^{35}Cl can be enhanced in comparison with the 2.8-keV resonance of ^{23}Na in the TOF spectrum at the higher discrimination level.

6. Conclusion

The measurements of the neutron capture cross section of ^{35}Cl were performed using the NaI(Tl) detector in ANNRI at J-PARC. The enriched ^{35}Cl, ^{37}Cl, and natural Cl samples in chemical form of NaCl were used. The pulse height and TOF spectra for the NaCl samples were obtained. The background compositions in the experiment were estimated by utilizing the calculation of the pulse height spectra with the PHITS code.

Acknowledgments

The work is supported by JSPS KAKENHI Grant Number 26820411.

References

[1] Shibata K, Iwamoto O, Nakagawa T, Iwamoto N, Ichihara A, Kunieda S, Chiba S, Furutaka K, Otuka N, Ohsawa T, Murata T, Matsunobu H, Zukeran A, Kamada S, Katakura J. JENDL-4.0: a new library for nuclear science and engineering. J Nucl Sci Technol. 2011;48:1-30.

[2] Sims GHE and Juhnke DG. The thermal neutron capture cross section and resonance capture integral of ^{35}Cl for (n,γ) and (n,p) reactions. J. Inorg. Nucl. Chem. 1969;31:3721-3725.

[3] Venturini L and Pecequilo BRS. Thermal neutron capture cross-section of ^{48}Ti, ^{51}V, ^{50,52,53}Cr and ^{58,60,62,64}Ni. Appl. Radiat. Isot. 1997;48:493-496.

[4] Macklin RL. Resonance neutron capture by ^{35,37}Cl. Phys. Rev. 1984;C29:1996-2000.

[5] Guber KH, Sayer RO, Valentine TE, Leal LC, Spencer RR, Harvey JA, Koehler PE, and Rauscher T. New Maxwellian averaged neutron capture cross sections for ^{35,37}Cl. Phys. Rev. 2002;C65:058801-1-4.

[6] Sato T, Niita K, Matsuda N, Hashimoto S, Iwamoto Y, Noda S, Ogawa T, Iwase H, Nakashima H, Fukahori T, Okumura K, Kai T, Chiba S, Furuta T and Sihver L. Particle and Heavy Ion Transport Code System PHITS, Version 2.52. J. Nucl. Sci. Technol. 2013;50:913-923.

[7] Ogawa T, Hashimoto S, Sato T, and Niita K, Development of gamma de-excitation model for prediction of prompt gamma-rays and isomer production based on energy-dependent level structure treatment. Nucl. Instr. Methods. 2014;B325:35-42.

[8] Katabuchi T, Matsuhashi T, Terada K, Arai T, Furutaka K, Hara KY, Harada H, Hirose K, Hori J, Igashira M, Kamiyama T, Kimura A, Kino K, Kitatani F, Kiyanagi Y, Koizumi M, Mizumoto M, Nakamura S, Oshima M, and Toh Y. Pulse-width analysis for neutron capture cross-section measurement using an NaI(Tl) detector. Nucl. Instr. Meth. 2014;A764:369-377.

36 Neutron and X-ray imaging measurements by using a composite source system at Hokkaido University

Kaoru Y. HARA[1)*], Hisao TAIRA[1)†], Hirotaka SATO[1)], Takashi KAMIYAMA[1)],
Takenao SHINOHARA[2)]

1) Faculty of Engineering, Hokkaido University, Sapporo 060-8628, Japan
2) J-PARC Center, Japan Atomic Energy Agency, Ibaraki-ken 319-1195, Japan
† Present address: Hokkaido University of Education, Sapporo 002-8501, Japan
*e-mail: hara.kaoru@eng.hokudai.ac.jp

By using a composite source system of thermal neutron and keV X-ray, we performed neutron and X-ray imaging measurements at the 45-MeV electron linear accelerator facility in Hokkaido University. The neutron and X-ray transmission images for a same sample were obtained without change of a detector setup on the beam line.

1. Introduction

For a complementary imaging using a difference between the penetration abilities of neutron and X-ray, a composite source system of thermal neutron and several hundred keV X-ray has been constructed at the 45-MeV electron linear accelerator facility of Hokkaido University. The source system provides the alternative beam of neutron and X-ray by switching the production target onto the electron beam axis. The energy distributions of the beams were calculated with the PHITS code [1], where JENDL4.0 was used to the neutron cross-section data [2]. We reported about the simulations in the previous proceedings [3]. In this work, we reported the measurements of the transmission images for the neutron and X-ray beams using the source system.

2. Composite source system of thermal neutron and keV X-ray

As shown in Fig. 1, the composite source system mainly consists of production targets, a moderator, reflectors, and radiation shields. The horizontal sectional views of the neutron and X-ray production targets are shown in the upper and lower insets of Fig. 1, respectively. The X-ray production target is a copper plate. The 9-MeV electron beam irradiates the copper plate in order to produce a few hundred keV bremsstrahlung photons. The bremsstrahlung photons which are emitted into the perpendicular direction with respect to the electron beam axis are used as the X-ray beam. On the other hand, the neutron production target is an assembly of a tungsten disc and two lead blocks. In this target, the bremsstrahlung photons are produced by hitting the tungsten disc with the 34-MeV electron beam and used to induce the photonuclear reaction of lead. The fast neutrons, which are produced by the photonuclear reaction of lead, are moderated in the polyethylene moderator surrounded with the graphite reflectors. The thermal neutrons which are emitted into the perpendicular direction with respect to the electron beam axis are used as the thermal neutron beam. The source system can provide the alternative beam of neutron or X-ray by moving up (or down) the stage of source system i.e. the vertical level of production targets.

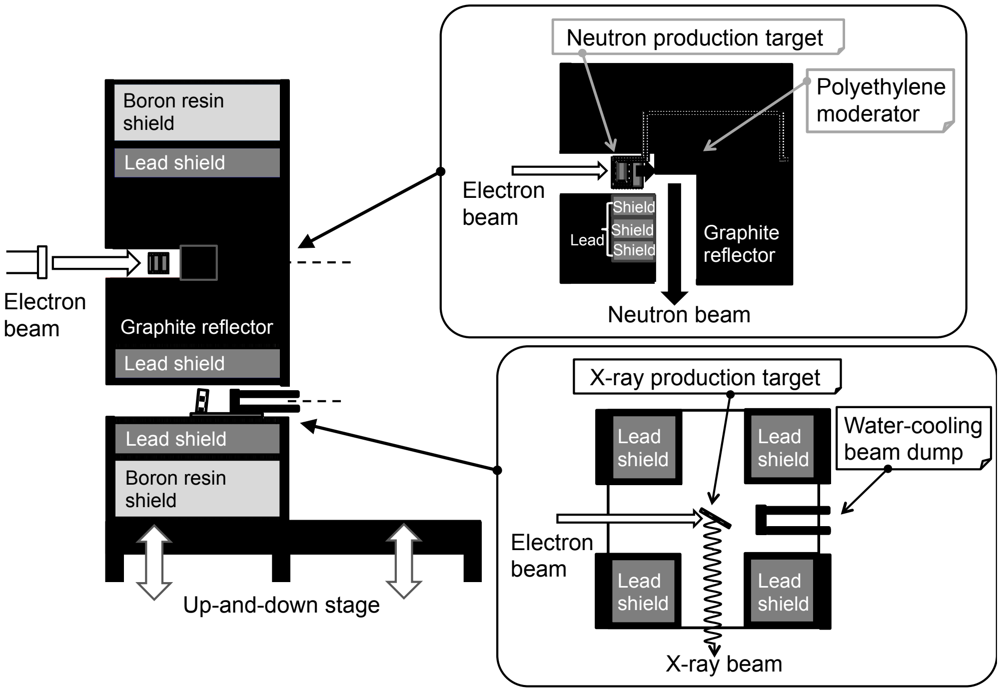

Figure 1: Hokkaido University neutron and X-ray source

3. Neutron and X-ray imaging measurements

By using the composite source system, the transmission images for the neutron and X-ray beams were measured without change of a sample and detector position. In the neutron and X-ray imaging measurements, the detector based on a vacuum-tube type neutron color image intensifier (NCII; TOSHIBA, Ultimage^{TM}-nγ-04) [4] was applied to the both beams for the purpose of dual-use. The schematic view of detector system is shown in Fig. 2. The input window of NCII was composed of a Gd_2O_3 layer, which was evaporated on an Al plate, CsI scintillator, and photocathode. In order to efficiently detect the incident neutrons, the neutrons were dominantly converted to internal conversion electrons through the neutron capture reaction of gadolinium. The conversion electrons yielded fluorescence photons in the CsI scintillator and these fluorescence photons produced photoelectrons in the photocathode. Although the thickness of CsI (50 μm) was optimized for a neutron imaging, we applied the NCII not only to the neutron imaging but also to the X-ray imaging because the CsI scintillator can partially detect with the X-rays. The succeeding process after the production of photoelectrons was same for either incident beam. The photoelectrons were accelerated and focused by using the electrodes of vacuum tube to project on a output screen made from a Y_2O_2S:Eu scintillator. The visible photons which were emitted from the output screen were collected to a image recorder through the optical lens and mirror. A digital photographic camera (CANON, EOS 5D Mark II) was used as the image recorder. The sample was an LED flashlight involving a nickel-metal hydrogen (NiMH) rechargeable cell. The each measurement time was three minutes.

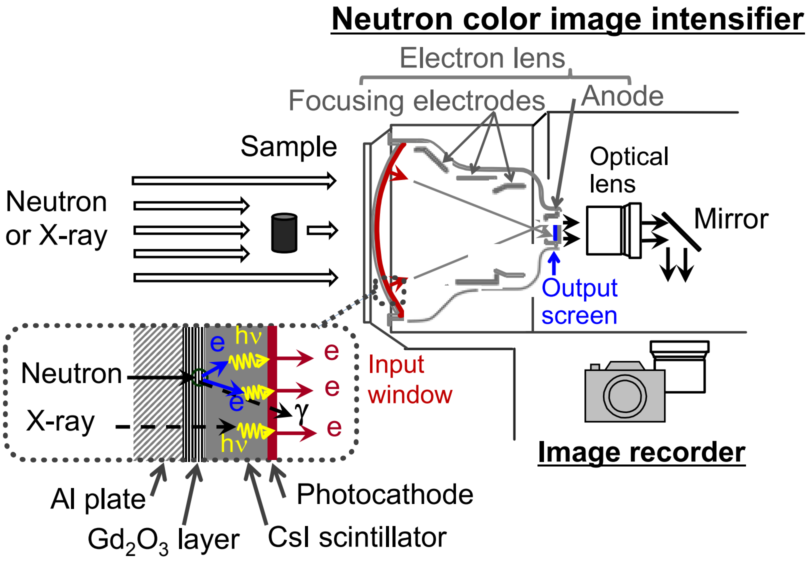

Figure 2: Vacuum-tube type neutron color image intensifier

4. Data processing procedure to obtain a transmission image

For an example of data processing procedure, neutron images of a cadmium test sample are shown in Fig. 3. Fig. 3(a) and (b) show the neutron images that were measured with and without the test sample, respectively. Additionally, the image for the dark current noise of camera sensor and the natural background radiation was measured without the neutron beam in order to determine the offset level (Fig. 3(c)). As shown in Fig. 3(d), the transmission image is obtained from three measured images by the following expression,

$$B_d(i) = (B_a(i)-B_c(i))/(B_b(i)-B_c(i)), \quad \cdots\cdots\cdots \quad (1)$$

where $B_a(i)$, $B_b(i)$, $B_c(i)$, and $B_d(i)$ are the brightness values at the *i* th pixel in Fig. 3(a), (b), (c), and (d), respectively. To preserve the data information, we treated the images as the CANON RAW (CR2) data format using the DCRAW reader [5] plugged in the ImageJ program. After the calculation using the equation (1), the transmission image is converted from CR2 to JPEG, and plotted with an adjustment of the maximum and minimum ranges of brightness value as shown in Fig. 3(d).

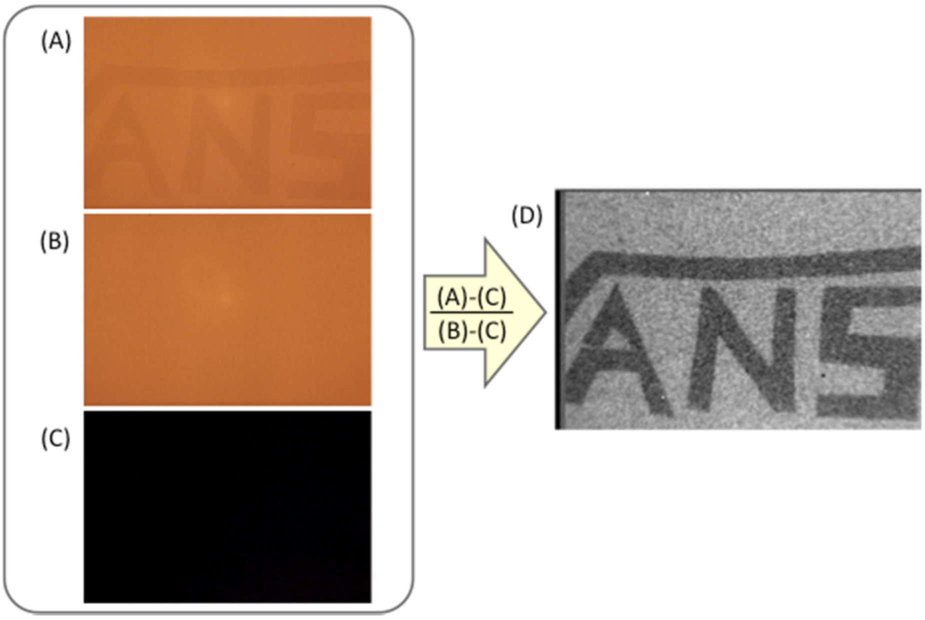

Figure 3: Measured and derived neutron images for the cadmium test sample

5. Results of the complementary imaging

Fig. 4(a) and (b) show the transmission images of the LED flashlight which were measured with the X-ray and neutron beams, respectively. The transmission images were obtained by using the equation (1) in the previous section. The portion of the flashlight was captured in the images. The structures such as the NiMH rechargeable cell, LED switching circuit, adapter, and light reflector (from the left-hand side) were observed on the inside of the housing, where the external appearance of the flashlight with the cell is shown in Fig. 4(d). These images were directly compared by calculating the ratio of the brightness value of X-ray image to the one of the neutron image at the same pixel. As plotted in Fig. 4(c), the outlines of cell, circuit, adapter, and reflector were enhanced while the outline of housing vanished on the resultant image. The results suggest that substances at the bright pixels are relatively radiolucent for X-ray and radiopaque for neutron. Because the neutron time-of-flight (TOF) method was not applied in this measurement, further information about the substances of sample would be obtained by applying the TOF method to the measurement with other image recorder such as a high-speed camera. In addition, the γ-flash component, which is contaminated in the neutron beam at the initial time of TOF [6], would be discriminated from the neutron image.

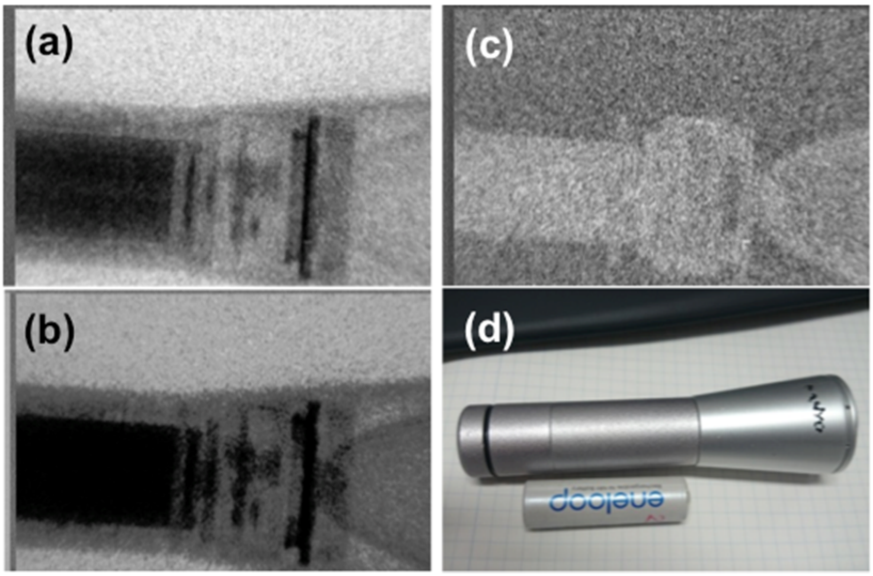

Figure 4: Transmission images of the LED flashlight measured with the X-ray (a) and neutron beam (b). Enhanced contrast image obtained from the dataset of X-ray and neutron transmission images (c). Photograph of the external appearance of the flashlight and size AA cell (d).

6. Conclusion

The neutron and X-ray imaging measurements were performed using the composite source system at the 45-MeV electron linear accelerator facility in Hokkaido University. The detector based on the NCII was applied to the both beams for dual-use purpose. The flashlight was used as the sample. In the transmission images, the structures were observed inside the housing of flashlight. The transmission images were directly compared at the same pixel. As the result, the enhanced contrast image obtained from the dataset of X-ray and neutron transmission images.

Acknowledgments

The research is supported under the Photon and Quantum Basic Research Coordinated Development Program by the Ministry of Education, Culture, Sports, Science, and Technology (MEXT), Japan.

References

[1] Sato T, Niita K, Matsuda N, Hashimoto S, Iwamoto Y, Noda S, Ogawa T, Iwase H, Nakashima H, Fukahori T, Okumura K, Kai T, Chiba S, Furuta T and Sihver L, Particle and Heavy Ion Transport Code System PHITS, Version 2.52. J. Nucl. Sci. Technol. 2013;50:913-923.

[2] Shibata K, Iwamoto O, Nakagawa T, Iwamoto N, Ichihara A, Kunieda S, Chiba S, Furutaka K, Otuka N, Ohsawa T, Murata T, Matsunobu H, Zukeran A, Kamada S, Katakura J. JENDL-4.0: a new library for nuclear science and engineering. J Nucl Sci Technol. 2011;48:1-30.

[3] Hara KY, Taira H, Sato H and Kamiyama T. 2014 Symposium on Nuclear Data. Proceedings of the 2014 Symposium on Nuclear Data; 2014 November 27-28; Sapporo, JAEA-Conf 2015-003, p.203(2015).

[4] Nittoh K, Konagai C, Yahagi M, Kiyanagi Y and Kamiyama T. Development of Neutron Color Image Intensifier for Pulsed Neutron Source. Physics Procedia 2015;69:177-184.

[5] Coffin D. DCRAW. Available from: http://www.cybercom.net/~dcoffin/dcraw/.

[6] Hara KY, Harada H, Toh Y and Hori J. γ-Flash suppression using a gated photomultiplier assembled with an $LaBr_3$(Ce) detector to measure fast neutron capture reactions. Nucl. Instr. Methods. 2013;A723:121-127.

37 Optimization of Experimental System Design for Benchmarking of Large Angle Scattering Reaction Cross Section at 14 MeV Using a Shadow Bar

Naoya Hayashi, Seiki Ohnishi, Fuminobu Sato, Isao Murata
Department of Sustainable Energy and Environmental Engineering, School of Engineering,
Osaka University, 2-1 Yamadaoka, Suita, Osaka 565-0871, Japan
E-mail:n.hayashi@qr.see.eng.osaka-u.ac.jp

Abstract

At 14 MeV, it is known that the absolute value of large angle scattering cross section is small. The contribution is thus thought to be neglected in the neutronics design of fusion reactor. However, in case that a neutron source can be regarded as a beam like a neutron streaming, large angle scattering cross sections might affect the nuclear design result largely. In fact, in fusion neutronics benchmark experiments using a neutron beam so far, there was a difference observed between experiment and simulation. Also it is known that there are differences in large angle scattering cross sections among nuclear data libraries. Then we have been carrying out preliminary benchmark experiments for verification of large angle scattering reaction cross sections of iron for a few years.

The purpose of the present study is to optimize the experimental system design to realize an accurate benchmarking of large angle scattering reaction cross sections. Finally, we reached the optimized experimental system which was supposed to perform more accurate benchmark experiments for large angle scattering reaction cross sections

1. Introduction

The reaction cross section of iron which is used as the main structural material is important in neutronics design of fusion reactor. However, because the large angle scattering reaction cross section is known to be small among reaction cross sections of iron. It was thought that the contribution in the result of transport calculation is small. On the other hand, it is reported that when the structure becomes as large as the fusion reactor, the activation or exposure dose in the deeper places by like neutron streaming could be affected by the effect of the large angle scattering reaction. As in the previous research, Ohnishi carried out fusion neutronics

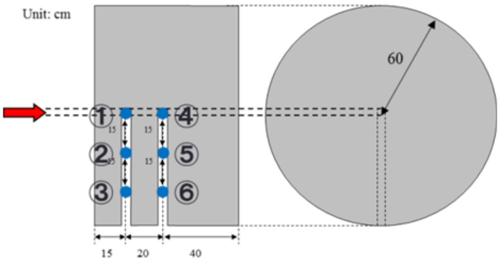

Fig. 1 The experimental system of fusion neutronics benchmark experiment

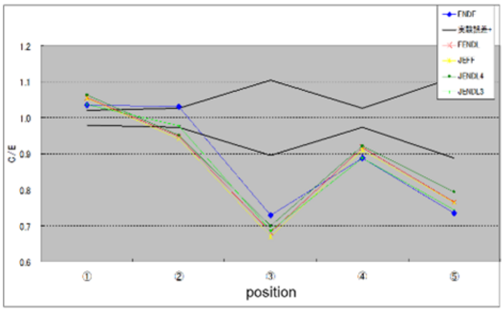

Fig. 2 The result of fusion neutronics benchmark experiment

benchmark experiments using a neutron beam and examined the effect of the large angle scattering reaction [1]. The experimental system is shown in Fig.1. Collimated beam neutrons were irradiated to the center of the assembly. In the assembly, six activation foils (niobium and indium) were arranged at positions shown in Fig.1 to confirm how neutrons are scattered by measuring the radioactivities of them. The C/E value of each activation foil is shown in Fig.2. The activation foil which was placed in a deep and off-center position, especially foil 3 and 5, shows a disagreement between calculation and experiment.

Neutron elastic scattering reaction cross sections are included in all nuclear data libraries. However, it is known that there are differences in large angle scattering cross section among them even in the case of iron as shown in Fig.3. Under these circumstances, it would be an important task to examine a hypothesis that the differences observed in the previous research by Ohnishi would really be due to the uncertainty of the large angle scattering cross section.

This aim of the present study is to design an optimized experimental system using a shadow bar to benchmark the large angle scattering cross section.

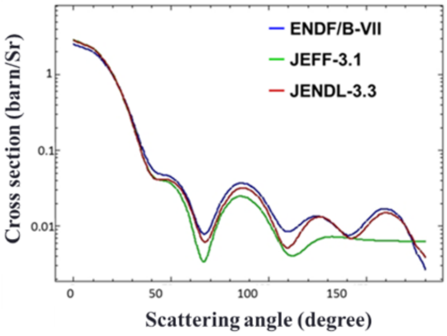

Fig. 3 Angle distribution of neutron elastic scattering of ^{56}Fe [2][3][4][5]

2. Experimental system design procedure

According to the discussion in Chap. 1, we designed the experimental system in order to extract the contribution of large angle scattering reaction especially for iron. In the simulation, MCNP-5 and JENDL-4.0 were used. The basic experimental arrangement is shown in Fig.4.

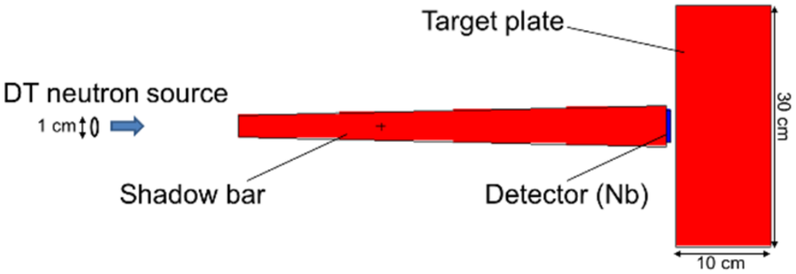

Fig. 4 Schematic experimental arrangement

In this experiment, a shadow bar plays an important role to suppress direct incidence of 14 MeV DT neutrons. The thickness of an iron target plate is set to be thin (as thin as 2 MFP) so that neutrons scattered to forward directions can mostly go through the target plate. The large angle scattered neutrons in the plate are incident to a niobium foil, which is placed just behind the shadow bar, in order to activate the foil. The induced radioactivity is measured by a Ge detector.

2.1 Detail of the experimental system

We assume the DT neutron source to be an isotopic disk neutron source (1 cm in diameter). This is fixed to simulate the specification of the intense 14 MeV neutron source facility, OKTAVIAN in Osaka University where we will carry out practical benchmark experiments. In this calculation, the beam intensity is 1.0×10^{10} (neutron/s) and the irradiation time is 6 hours.

The dimension of the iron target plate is 30 cm in height, 30 cm in width and 10 cm in thickness. By making the target plate thin, i.e., around 2 MFP, we can reduce the number of scattering reaction inside the target plate and make the contribution of the large angle scattering reaction relatively dominant.

The thickness of the niobium foil is 5 mm and the diameter is changed for the bottom diameter of the shadow bar. The reason why we chose niobium is that the energy threshold of ^{93}Nb(n,2n)^{92m}Nb reaction is as high as 9MeV and also the reaction cross section is enough high as 0.464 barn. Therefore, the niobium foil can be activated by the large angle scattered neutrons of around 13.5 MeV, however, it cannot react with neutrons moderated in the shadow bar.

The shadow bar material is iron because the macroscopic cross section at 14 MeV is large to attenuate the 14 MeV neutrons. The detail is described in the next section.

2.2 Shadow bar

In this study, we mainly optimize the shape of the shadow bar to extract the contribution of large angle scattering reaction more effectively. Here, we defined 4 parameters as shown in Fig.5.

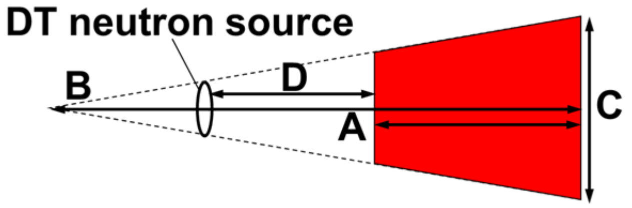

A: Thickness of the shadow bar

B: Height of the shadow bar cone

C: Bottom diameter of the shadow bar

D: Distance between the DT neutron source and the shadow bar

Fig. 5 Parameters of the shadow bar

Next, we calculate a ratio of radioactivity, R=Rn/Rf. Rn is a radioactivity induced by neutrons which enter the detector via the iron target. Rf is the one by neutrons which enter the detector after transmitting the shadow bar. Figure 6 shows the concept of Rn and Rf. This ratio R was used as an index of performance evaluation of this experimental system.

Fig. 6 The overview of Rn and Rf

Rn represents the contribution of large angle scattered neutrons. Therefore, if R becomes larger, it means more large angle scattered neutrons are contributed the induced radioactivity. In the experimental system design, we change the parameters which are shown in Fig.5 and examine the relation between R and radioactivity of the activation foil to optimize the experimental system.

3. Design Result

First, we examine the relation between the distance D, in Fig.5, and R. In this calculation, A=55 cm, B=80 cm and C=5cm are assumed. The relation between D and R is shown in Fig.7 and the relation between D and radioactivity (Rn and Rf) is shown in Fig.8.

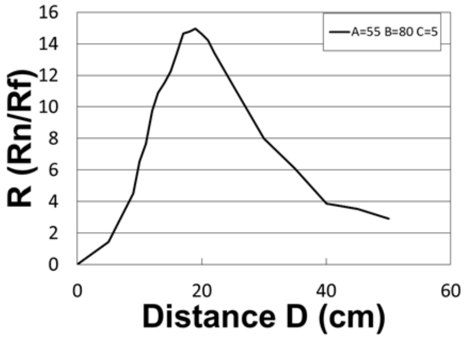

Fig. 7 Relation of D and R

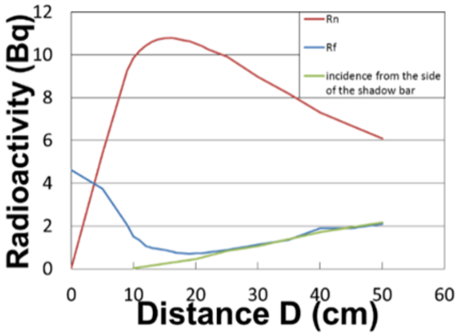

Fig. 8 Relation of D and radioactivity Rn and Rf

As shown in Fig.8, Rn becomes larger when the neutron source position leaves from the shadow bar, because the solid angle of the neutron source viewing the shadow bar decreases. However, when it goes too far, Rn becomes smaller, because the neutron flux incident to the target plate becomes smaller.

Then, if the neutron source position moves farther from the position shown in Fig. 9, neutrons begin to enter from the side surface of the shadow bar. Only the contribution is extracted and shown in the figure. The contribution is slowly increasing with increase of D. As a result, Rf increases similarly as in Fig. 8. Finally, for these reasons, R has a peak as shown in Fig.7. This is the general trend of this experimental system.

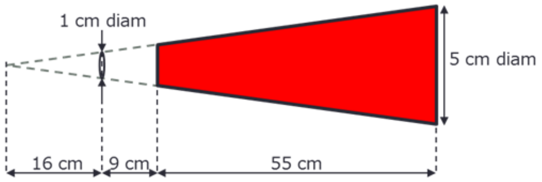

Fig. 9 Position of the neutron source just fitting to the shadow bar cone

Second, we optimize the thickness of the shadow bar (A in Fig.5). From Fig. 10, in which B=80 cm and C=5 cm are assumed, R shows the best result at A=50 cm for B=80 cm. By changing the thickness of the shadow bar cone (B in Fig.5) as shown in Fig.11, A=50 cm gives the largest R for various B values.

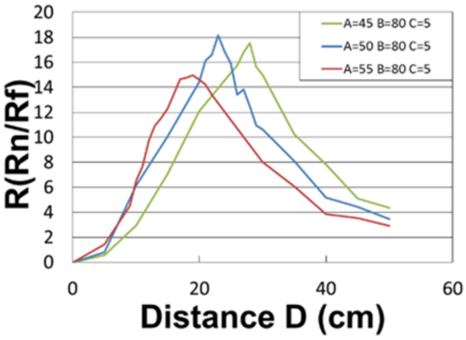

Fig. 10 Relation of D and Rn for A change

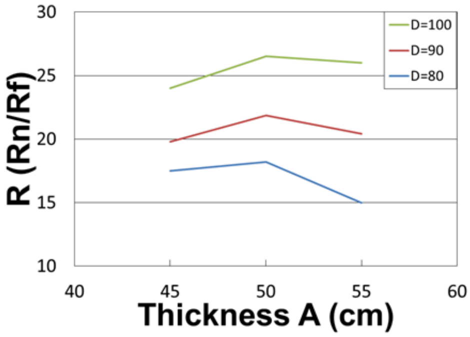

Fig. 11 Relation of A and R for B change

From this result, we chose 50 cm for the thickness A.

Third, we examined the height of the shadow bar cone (B in Fig.5). We calculated R by changing B for A=50 cm, C=5 cm. The results are summarized in Fig.12. We can find when B becomes longer, maximum R becomes larger, however, the radioactivity of the activation foil becomes smaller as shown in Fig.13. Accordingly, it is confirmed that there is a tradeoff relation between R and the radioactivity of the foil. In the experiment, we want to obtain a better value of R, but also want to keep enough radioactivity for accurate measurement by a detector.

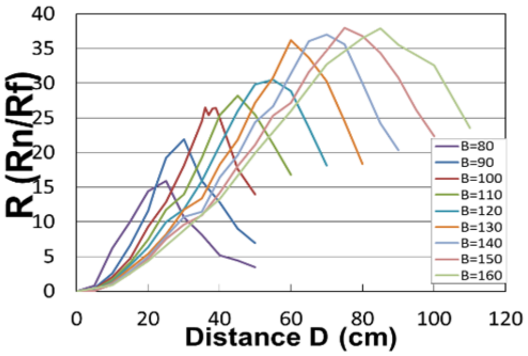

Fig. 12 Relation of D and R for B change.

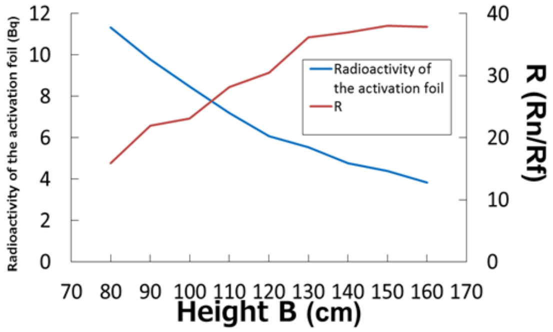

Fig. 13 Trend of R and the radioactivity of the activation foil for B.

Fourth, we optimized the bottom diameter of the shadow bar (C in Fig.5). In this calculation, A=50 cm is assumed. For B=100 cm, 120 cm, 140 cm, 160 cm, curves of R are plotted as a function of C in Fig.14.

From the result, when C is 2~4 cm, it shows higher values of R. However, when C is 2 cm, the radioactivity is not enough for realization of an accurate measurement because the amount of activation foil decreases with decrease of C. Then, we chose 3 cm for C.

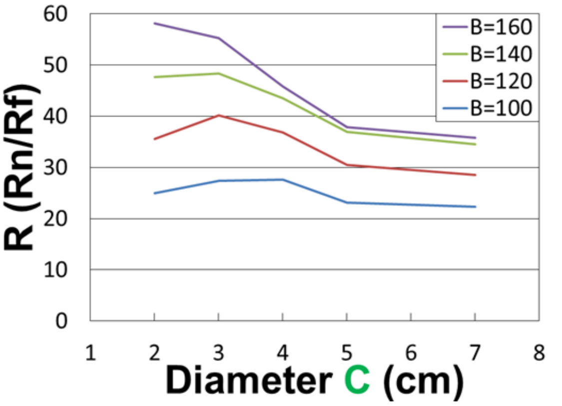

Fig. 14 Each peak of R change for B and C.

Finally, from these results, we finally determined B and D. For that, we set the criterion, R>50, because R=50 is enough high to realize an accurate benchmarking of reaction cross section. The final value of B is thus more than 150 cm. Then, for A=50 cm, B=150 cm and C=3 cm the largest radioactivity is found for D=60 cm as shown in Fig. 15, i.e., the shadow bar should be positioned at 60cm from the front surface of it. The radioactivity in that case is 2.29 Bq, which is an

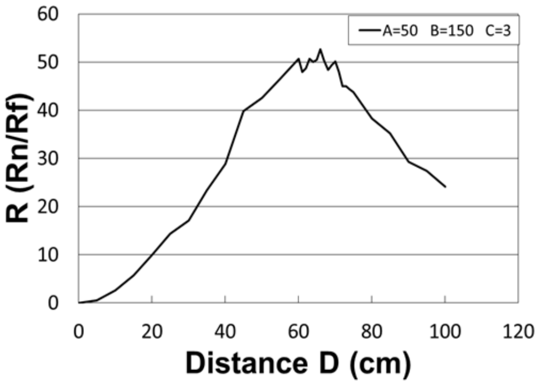

Fig. 15 Relation of R and D for A=50cm, B=150 cm, C=3cm.

enough large value to be measured in an acceptable statistical accuracy.

4. Conclusion

From the present study, we finally determined the optimized experimental system, in the case of A=50 cm, B=150 cm, C=3 cm, by which the radioactivity was estimated to be around 2.29 Bq with the intense 14 MeV neutron source facility OKTAVIAN of Osaka University. Hereafter we will prepare the shadow bar to carry out a benchmark experiment of iron first. Then, we will consider how the results of this experiment can contribute to the improvement of the accuracy of the evaluated nuclear data libraries.

References

[1] Seiki Ohnishi et al.: “New integral experiments for large angle scattering cross section data benchmarking with DT neutron beam at JAEA/FNS”, *Fusion Engineering and Design*, **87**, pp. 695-699 (2012).

[2] K. Shibata, T. Kawano, T. Nakagawa, O. Iwamoto, J. Katakura, T. Fukahori, S. Chiba, A. Hasegawa, T. Murata,H. Matsunobu, T. Ohsawa, Y. Nakajima, T. Yoshida, A. Zukeran, M. Kawai, M. Baba, M. Ishikawa, T. Asami, T. Watanabe, Y. Watanabe, M. Igashira, N. Yamamuro, H. Kitazawa, N. Yamano and H. Takano: “Japanese Evaluated Nuclear Data Library Version 3 Revision-3: JENDL-3.3,” J. Nucl. Sci. Technol. 39, 1125 (2002).

[3](Eds.) T. Nakagawa, H. Kawasaki and K. Shibata: "Curves and Tables of Neutron Cross Sections in JENDL-3.3 (Part I and II), “JAERI-Data/Code 2002-020, (2002).

(Ed.) K. Shibata: "Descriptive Data of JENDL-3.3 (Part I and II),” JAERI-Data/Code 2002-026, (2003).

[4] Arjan Koning et al.: “The JEFF-3.1 Nuclear Data Library” JEFF report 21, OECD (2006).

[5]M.B. Chadwick et al.: “ENDF/B-VII.0: Next Generation Evaluated Nuclear Data for Nuclear Science and Technology”, Nucl. Data Sheets, 102, pp.2931-3060 (2006).

38 Contribution from Gd capture gamma-rays in GAGG based SPECT for boron neutron capture therapy

Nobuhide Saraue*, Masanobu Manabe, Ryosuke Ohya, Fuminobu Sato, Isao Murata

Division of Sustainable Energy and Environmental Engineering,
Graduate School of Engineering, Osaka University,
Yamada-oka 2-1, Suita, Osaka 565-0871, Japan
*Email : nsaraue@qr.see.eng.osaka-u.ac.jp

GAGG based SPECT system for boron neutron capture therapy (BNCT), BNCT-SPECT, has been proposed to monitor the treatment effect of BNCT in real time. The characterization measurement of a GAGG scintillator was carried out to investigate whether to meet the design requirements for BNCT-SPECT and the contribution from Gd(n,γ) reaction was estimated numerically. As a result, the GAGG scintillator had enough performance for BNCT-SPECT and the contribution from Gd(n, γ) reaction was substantially smaller. In the next phase, we will start the optimum design for the BNCT-SPECT system.

1. Introduction

Recently, boron neutron capture therapy (BNCT) attracts as a new promising radiation therapy. It can destroy tumor cells using alpha particles and lithium nuclei emitted from ^{10}B(n,α) ^{7}Li reaction. This therapy has a specific advantage that tumor cells are only killed without damage of normal tissues compared with conventional radiation therapies. However, there are some problems left which should be solved for practical use. One of them is that it is difficult to know the local boron dose during irradiation. Thus, we have been developing a SPECT system for BNCT so-called BNCT-SPECT which can obtain a three-dimensional image of the treatment effect in real time. The principle is simple, i.e., to measure 478 keV gamma-rays promptly emitted from an excited state of the ^{7}Li nucleus generated by the ^{10}B(n,α) ^{7}Li reaction. However, it is difficult to selectively measure 478 keV gamma-rays because capture gamma-rays of 2.22 MeV produced by the ^{1}H(n, γ)^{2}H reaction and 511 keV annihilation gamma-rays become a critical background. For this reason, a CdTe detector was selected as an elemental measuring device, because it has a high detection efficiency and excellent energy resolution. So far we examined theoretically and experimentally for the BNCT-SPECT system since about 10 years ago by the authors' group [1~3]. As a result of the previous study, we confirmed that the CdTe detector has enough performance as the elemental measuring device for the BNCT-SPECT system. On the other hand, we found out some problems, i.e., the S/N ratio of the peak of 487 keV in the measured pulse height spectrum was not enough (less than unity) and the necessarily large CdTe crystal was very expensive to realize the BNCT-SPECT system [4].

In this study, we started to investigate scintillators as the elemental measuring device because recently very high performance scintillators have been developed. And, of course, it can suppress the cost compared to the CdTe crystal. In this paper, we selected a GAGG scintillator which would have feasibility to realize the BNCT-SPECT system. The GAGG scintillator has extremely superior performance, i.e, the detection efficiency due to its large density is high and the energy resolution is good enough as the elemental measuring device for the BNCT-SPECT system. However, the GAGG scintillator contains gadolinium. Seemingly we cannot ignore the contribution from Gd capture gamma-rays in the GAGG scintillator because the neutron capture cross-section of Gd is remarkably large at epithermal energy regions. Therefore, we estimated numerically the contribution with MCNP-5 and investigated feasibility of the BNCT-SPECT using the GAGG scintillator.

2. Principle of BNCT-SPECT

Fig. 1 shows the concept of the BNCT-SPECT system. $^{10}B(n,\alpha)\,^{7}Li$ reaction expressed by the following two nuclear reactions is utilized for BNCT.

$$
\begin{aligned}
{}^{10}B + n &\rightarrow \alpha + {}^{7}Li + Q' \quad (2.79\ \text{MeV})\ (6.1\%)\\
&\rightarrow \alpha + {}^{7}Li^{*} + Q \quad (2.31\ \text{MeV})\ (93.9\%)\\
&\qquad\quad \hookrightarrow {}^{7}Li + \gamma \quad (478\ \text{keV})
\end{aligned}
$$

94 % of ^{7}Li emitted from this reaction are in an excited state ($^{7}Li^{*}$). Then, 478 keV prompt gamma-rays are emitted simultaneously via transition from the first excited state to the ground state in half-life of 10^{-14} sec. The number of the prompt gamma-rays is proportional to the number of $^{10}B(n,\alpha)\,^{7}Li$ reaction. Therefore, if the prompt gamma-rays can be measured three-dimensionally, we can estimate the three-dimensional image of the treatment effect with the BNCT-SPECT system.

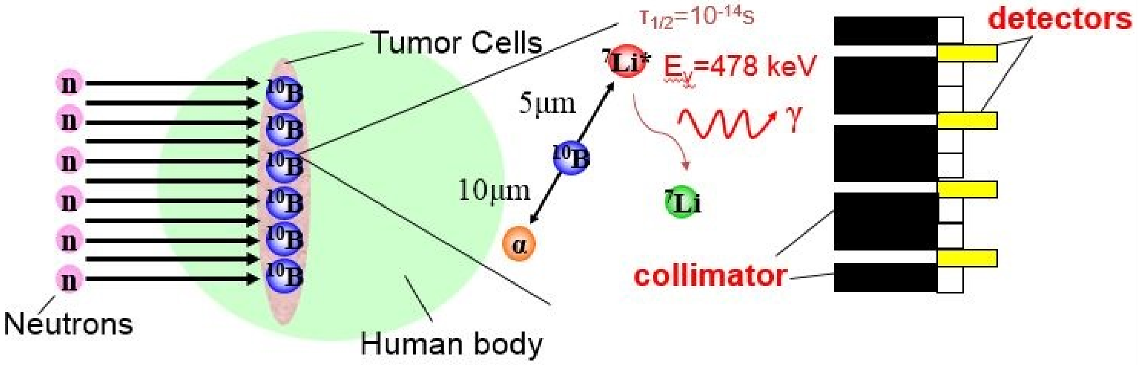

Fig. 1 Concept of the BNCT-SPECT system

3. Design requirements

The BNCT-SPECT system is required to discriminate the 478 keV prompt gamma-rays from other gamma-rays in a high background field. In addition, it is necessary to measure the image accurately. The design requirements are thus summarized as follows:

(1) The measuring time should be less than 60 minutes, because the irradiation time of BNCT is normally less than 60 minutes.

(2) The number of counts per a unit detector should be measured more than 1000 counts in order to suppress the statistical accuracy within several percent.

(3) The spatial resolution should be less than a few mm so that the image obtained can be utilized for medical purposes.

(4) The energy resolution, full width at half maximum (FWHM), should be less than 33 keV, so as to measure separately the 478 keV prompt gamma-rays and the 511 keV annihilation gamma-rays caused by high energy gamma-rays created in the neutron field.

It is necessary to downsize the detector to meet requirement (3). However, high detection efficiency for the 478 keV prompt gamma-rays is required to meet requirements (1) and (2). In addition, the detector is required to have a sufficiently high energy resolution to meet requirement (4). For this purpose, we started to investigate several scintillators, because recently very high performance scintillators have been developed.

Table 1 shows properties of various scintillators. A GAGG scintillator has feasibility to meet requirements (1) and (2) because of its large density and high light yield compared to other scintillators. In addition, the GAGG scintillator has a good energy resolution to meet requirement (4). Furthermore, feasibility to meet requirement (3) is expected since the GAGG scintillator has no deliquescency. Therefore, we finally selected the GAGG scintillator.

Table 1 Physical and scintillation properties

Scintillators	GAGG(Ce)	LuAG(Pr)	BGO	LSO(Ce)	NaI(Tl)	CsI(Tl)	$LaBr_3$(Ce)
Density (g/cm^3)	6.63	6.7	7.13	7.4	3.67	4.53	5.08
Light yield (photon/MeV)	60,000	22,000	8,000	26,000	45,000	56,000	75,000
Energy resolution (%@^{137}Cs−662keV)	5.2	4.2	12	9	5.6	5.7	2.6
Deliquescency	No	No	No	No	Yes	Yes	Yes
Melting point (℃)	1,850	1,970	1,050	2,050	651	621	783

4. Measurement with GAGG scintillator

In this chapter, we carried out measurement of the basic property of the GAGG scintillator to confirm whether the GAGG scintillator really meet the design requirements given in Chap. 3. Fig. 2 shows the schematic experimental setup. In this study, we selected a MPPC (Multi-Pixel Photon Counter) to compose a SPECT system. First, we measured the energy resolution of the GAGG scintillator (4 x 4 x 20 mm) with four standard gamma-ray sources (^{241}Am (59.54 keV) ^{133}Ba (356.01 keV) ^{22}Na (511.00 keV) ^{137}Cs (661.66 keV)). As a result, FWHMs of 478 keV and 511 keV were 35.1 keV and 36.5 keV, respectively. Separate measurement of 478 keV and 511 keV would be possible, although this value was slightly larger than the target value described in chapter 3. In addition, we expect that it would be able to surely carry out the separate measurement with an electric cooling type MPPC, because it is known that the light yield increases at a low temperature from the temperature characteristics of the GAGG scintillator. Next, we measured the intrinsic efficiency of the GAGG scintillator. For the intrinsic efficiency, we compared experimental and calculation values with MCNP5. As a result, a fairly good agreement was obtained, meaning that precise design calculations would be possible with MCNP5 for other dimensions of the GAGG crystal.

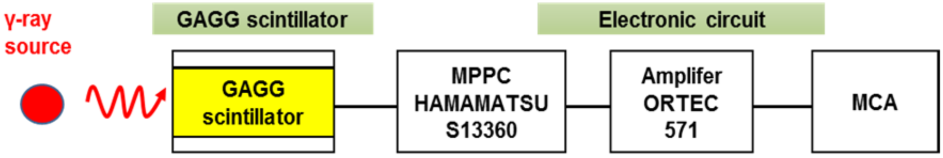

Fig. 2 Schematic experimental setup.

5. Numerical estimation of the contribution from Gd(n,γ) reaction

We have to examine influence from other possible nuclear reactions induced by epi-thermal neutrons, because the BNCT-SPECT system is positioned in an intense epi-thermal neutron field and Gd is contained in GAGG. Fig.3 shows neutron reaction cross sections of ^{155}Gd and ^{157}Gd. As shown in the figures, it is clearly not possible to ignore the contribution of gamma-rays emitted from Gd(n,γ) reactions. The thermal neutron capture cross sections of ^{155}Gd and ^{157}Gd are approximately 60000 barns and 250000 barns, respectively [5]. Therefore, we calculated the contribution to the measured pulse height spectrum for gamma-rays from Gd(n,γ) reactions with MCNP5 by using the previously proposed calculation model for the BNCT-SPECT system including a collimator, water phantom and even an irradiation room[4]. Fig. 4 shows the calculation model. A broad parallel beam (3 cmφ) of 10 keV neutrons was used as a neutron source. F4, F5 and F8 tallies were used to estimate the reaction rate, neutron flux and pulse height spectrum, respectively. The dimensions of the GAGG are assumed to be the same size the CdTe detector, i.e., 2 x 2.5 x 20 mm.

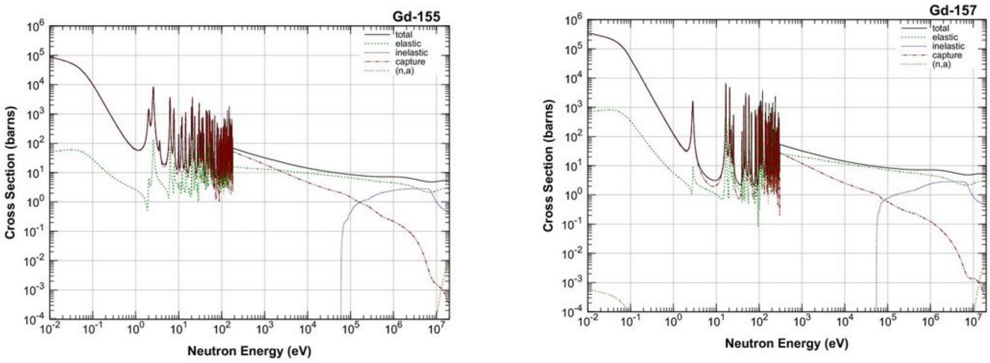

Fig.3. Cross-section of ^{155}Gd and ^{157}Gd

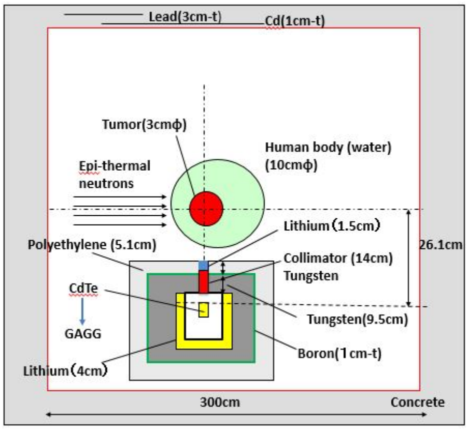

Fig. 4 Calculation model of the BNCT-SPECT system taking into account an irradiation

Figs. 5 and 6 show the calculation results. In Fig. 5, the pulse height spectrum for the gamma-ray energy of up to 2.4 MeV is shown. In Fig. 6, the spectrum around 478 keV of interest is enlarged. The black, blue and green lines are spectra of 478 keV gamma-rays emitted from ^{10}B(n,α) reaction, capture gamma-rays of ^{155}Gd in the detector and capture gamma-rays of ^{157}Gd in the detector, respectively. The red line is the total gamma-ray spectrum of the three components. As a result, the contribution from Gd(n,γ) reaction was confirmed to be sufficiently small compared to the 478 keV gamma-rays. The main reason is that the number of atoms of ^{155}Gd and ^{157}Gd in GAGG was small though the cross sections are extremely large.

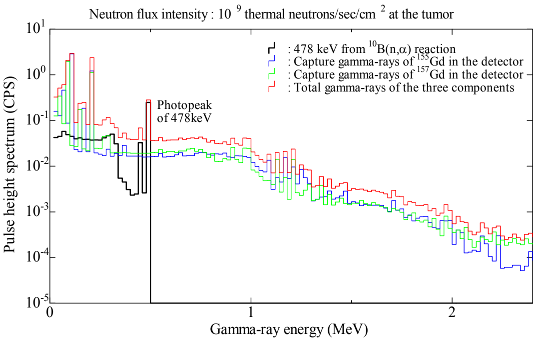

Fig. 5 Calculated PHS up to 2.4

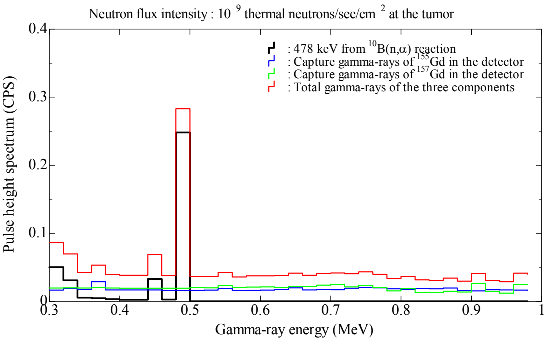

Fig.6 Calculated PHS around 478 keV

6. Conclusion

In this study, we confirmed the feasibility of the GAGG scintillator to be used as an elemental detector to realize the BNCT-SPECT system from the performance measurement results. Also, from numerical simulations with MCNP5 it was confirmed that the contribution of γ-rays emitted from Gd(n,γ) reaction was sufficiently small compared to the 478 keV gamma-rays.

From the series study so far, we will move to development phase of the GAGG based BNCT-SPECT system. In particular, we will first fix the optimum dimensions of the GAGG scintillator to meet the requirements. After confirming the possibility of separate measurement of the 478 keV prompt gamma-rays and the 511 keV annihilation gamma-rays experimentally, we will design the optimum collimator for the BNCT-SPECT system.

Reference

[1] T. Mukai, I. Murata, M. Ito and H. Miyamaru, “Development of CdTe detector for BNCT-SPECT,” Proc. Of the 2009 Annual Symposium on Nucl. Data, Nov. 26-27, 2009, RICOTTI, Tokai-mura, Ibaraki-ken, Japan, JAEA-Conf 2010-005, pp.75-80 (2010).

[2] I. Murata, T. Mukai, M. Ito, H. Miyamaru and S. Yoshida, “Feasibility study on BNCT-SPECT using a CdTe detector,” Progress in Nucl. Sci. Technol., 1, pp.267-270 (2011).

[3] I. Murata, S. Nakamura, M. Manabe, H. Miyamaru and I. Kato, “Characterization Measurement of A Thick CdTe Detector for BNCT-SPECT – Detection Efficiency and Energy Resolution –,” presented in 15th International Congress on Neutron Capture Therapy (ICNCT-15), Sept. 10-14, 2012, Tsukuba, Japan (2012).

[4] M. Manabe, S. Nakamura and I. Murata, “Study on Measuring Device Arrangement of Array-type CdTe Detector for BNCT-SPECT” presented in 7th Young Researcher’s Boron Neutron Capture Therapy (7YBNCT), September 22-26, 2013, Granada, Spain (2013).

[5] K. Shibata, O. Iwamoto, T. Nakagawa, N. Iwamoto, A. Ichihara, S. Kunieda, S. Chiba, K. Furutaka, N. Otuka, T. Ohsawa, T. Murata, H. Matsunobu, A. Zukeran, S. Kamada, and J. Katakura: "JENDL-4.0: A New Library for Nuclear Science and Engineering,"*J. Nucl. Sci. Technol.* 48(1), 1-30 (2011).

39

Development of An Epi-thermal Neutron Field for Fundamental Researches of BNCT with A DT Neutron Source

Y. Osawa, S. Imoto, F. Sato, I. Murata
Graduate School of Engineering, Osaka University, Yamadaoka 2-1, Suita, Osaka, Japan
Email:y-osawa@qr.see.eng.osaka-u.ac.jp

Abstract

Boron Neutron Capture Therapy (BNCT) is a radiation cancer therapy which can destroy selectively tumor cells, simultaneously suppressing influence against healthy cells. In Japan, Accelerator Based Neutron Sources (ABNS) are being developed for applying to BNCT. However, the spectrum of ABNS depends on kinds of accelerators. We thus should measure the neutron spectrum and flux intensity precisely and accurately for each ABNS. For this purpose, in the author's group, development of a low-energy neutron spectrometer is underway. In this study, we designed and constructed an epi-thermal neutron field using a DT neutron source, and carried out spectrum index and absolute flux intensity measurements with activation foils.

1 Introduction

Recently, Boron Neutron Capture Therapy (BNCT) is known to be a new promising cancer therapy. As shown in Fig. 2, ^{10}B is accumulated in cancer cells, and then thermal neutrons are irradiated. As a result, tumor cells can selectively be destroyed, simultaneously suppressing influence against healthy cells. Up to now, only nuclear reactors have been used as a neutron source for BNCT because of requiring a strong low-energy neutron source. Recently, in Japan, Accelerator Based Neutron Sources (ABNS) which can be constructed in medical facilities such as hospitals are being developed instead of nuclear reactors. However, in the case of ABNS based BNCT, patients should be positioned very close to the accelerator target because the source strength of ABNS is weak at present. This leads to a problem that the spectrum is distorted and becomes different from the standard field obtained in nuclear reactors. In addition, the spectrum depends on kinds of accelerators. Therefore we should measure the neutron spectrum and flux intensity precisely and accurately for each ABNS. In the author's group, a low-energy neutron spectrometer based on a ^{3}He position sensitive proportional counter was developed for measuring the epi-thermal neutron field of BNCT (Fig. 1) [1]. Verification of the spectrometer validity has been carried out by using an epi-thermal neutron field made with an AmBe neutron source [2]. However, there is a serious problem we face due to the weakness of the utilized AmBe source intensity, that is, the statistical accuracy was seriously deteriorated. As a result, it took a very long time to complete one measurement. The objectives of this study are thus to design and develop a new intense epi-thermal neutron field by using an ABNS, i.e., a DT neutron source, for fundamental researches of BNCT and to examine the characteristics of the produced neutron field experimentally.

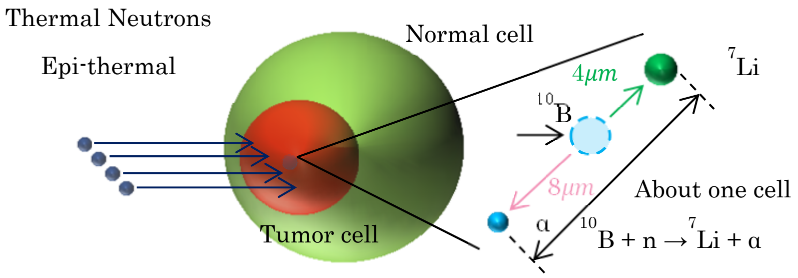

Fig. 2 Principle of BNCT

Fig. 1 ^{3}He position sensitive proportional counter

2 Design of Epi-thermal Neutron Column

In this study, design of an epi-thermal neutron column was carried out using Monte Carlo N-Particle Transport Code (MCNP-5) [3]. Differently from the previous design, the Intense 14 MeV Neutron Source Facility OKTAVIAN of Osaka University was used instead of AmBe as a strong neutron source [4]. In the OKTAVIAN Facility, a DT reaction is employed to produce 14 MeV neutrons and the neutron intensity reaches around 1.0×10^{9} n / sec in a pulse mode. The present epi-thermal column consists of moderator, reflector and shield. For moderating 14 MeV neutrons, we set an Aluminum Fluoride cylinder as the first moderator at the nearest side of the neutron source. The cylinder surrounding was filled with granular Teflon to supplement the function of the Aluminum Fluoride (Fig. 3 (Step 1)). Next, we set a reflector which consists of Graphite and Lead blocks surrounding the first moderators so that the neutron flux intensity could be increased over all the range of the neutron energy（Fig. 3 (Step 2)）. Up to Step 2, direct contributions of high energy neutrons around 14 MeV were remaining. We thus arranged an Iron shield in front of the moderator being in the downstream side. As a result of the installation of the iron shield, the contributions of around 14 MeV neutrons were suppressed to be much smaller than the previous steps（Fig. 3 (Step 3)）. Finally, we used Titanium plates as the second moderator to cut higher energy neutrons over 10 keV（Figure3(Step 4)）. Fig. 4 shows the designed epithermal neutron column based on Step 1 ~ Step 4. From Fig. 3, we can confirm that the obtained epi-thermal neutron field has a peak in the epi-thermal energy region and fast neutron contribution is well suppressed. In actual experiments, we can easily cut thermal neutrons below 0.5 eV by using cadmium if the thermal neutrons are not necessary in the experiments.

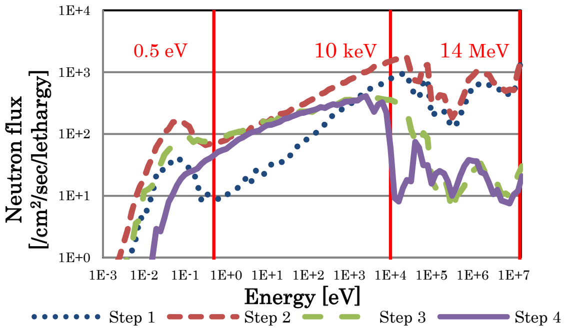

Fig. 3 Designed neutron spectrum

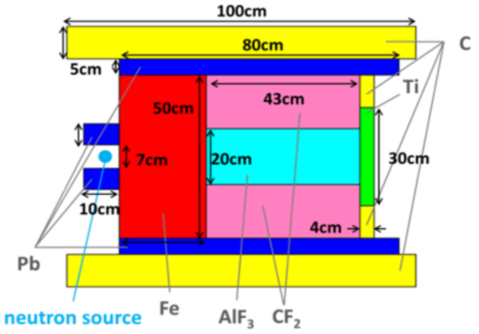

Fig. 4 Design of column

3 Experiment

3.1 Construction of epi-thermal column

We constructed the epi-thermal neutron column in a steel container for neutron slowing-down using materials shown in Table 1. Figure 5 is a picture showing inside of the epi-thermal neutron column in the middle step of construction. A cylinder of aluminum fluoride moderator was set inside an aluminum box, and then granular Teflon was poured in this box to fill up around the cylinder. Five Iron shield plates were set in front of the box and reflector blocks of graphite and lead were arranged so as to cover the moderators and shield entirely. Figures 5 ~ 8 show the finally constructed epi-thermal neutron column.

Table 1 Materials of the epi-thermal neutron column

Material	Shape	Size	Mass / Density
Aluminum Fluoride	Cylinder	ϕ20 cm × 42 cm	40.5 kg
Teflon	Granular		1.23 g/cm^3
Carbon	Block	10 cm × 10 cm × 100 cm	16.8 kg
Lead	Block	5 cm × 10 cm × 20 cm	11.4 kg
Iron	Plate	50 cm × 50 cm × 5 cm	98.4 kg
Titanium	Plate	10 cm × 10 cm × 3 cm	1.35 kg
Polyethylene	Block	5 cm × 10 cm × 20 cm	0.96 kg

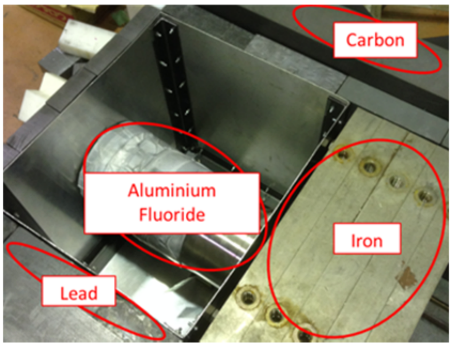

Fig. 5 Inside of epi-thermal neutron column.

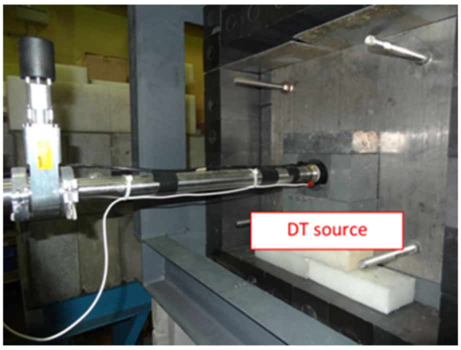

Fig. 6 Epi-thermal neutron column front view

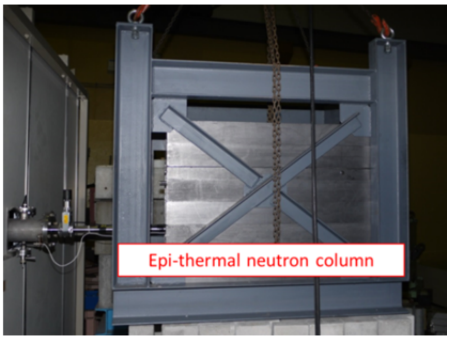

Fig. 8 Epi-thermal neutron column from back view.

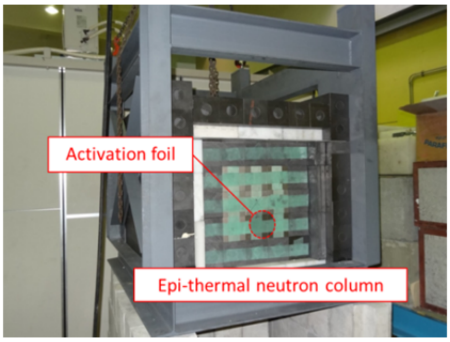

Fig. 7 Epi-thermal neutron column from side view.

3.2 Experimental procedure

For characterization of the constructed epi-thermal neutron column, we measured of neutron flux intensity and spectral index with activation foils as shown in Table 2. ^{197}Au(n,γ)^{198}Au reaction is sensitive to low energy neutrons. In this experiment, we used gold foils with and without a cadmium absorber and measured the reaction rates to confirm whether the epi-thermal neutron field was formed properly. Indium and aluminum foils were used for an evaluation of the amount of fast neutrons. The indium foil was covered with cadmium because ^{115}In (n,γ) ^{116m}In reaction has a large cross section with a resonance in the thermal energy region. ^{115}In(n,n')^{115m}In reaction and ^{27}Al(n,α)^{24}Na reaction are threshold reactions in the energy region of fast neutrons. Thus we can examine existence of fast neutrons. We conducted two experiments using the activation foils listed in Table2 as in the following procedure;

Experiment 1: Spectrum index measurement with activation foils (gold foils with and without cadmium, a indium foil with cadmium and an aluminum foil).

Experiment 2: Measurement of the epi-thermal neutron flux with gold foils at an off-set position.

Figure 9 shows a schematic vertical view of the experimental setup. In Experiment 1, we confirmed whether the epi-thermal neutron field was formed suppressing fast neutrons. In Experiment 2, we shifted the setting position of gold foils vertically from the neutron source height at 35 cm (off-set heights were 30 cm, 40 cm, 45 cm and 50 cm). We measured the flux intensity at the off-set positions so that we could examine uniformity of the irradiation field. In this measurement, the neutron energy was divided into three ranges, thermal neutrons (~0.5 eV), epi-thermal neutrons (0.5 eV~10 keV) and fast neutrons (10 keV). The irradiation time was five hours. Absolute neutron source intensity was determined using a niobium foil.

Table 2 Activation foils used.

Isotope	Nuclear Reaction	γ-ray energy [keV]	Half life	Threshold [MeV]
^{197}Au	^{197}Au(n,γ)^{198}Au	411.8	2.69 d	
^{115}In	^{115}In(n,n')^{115m}In	336.3	4.49 h	1.2
^{27}Al	^{27}Al(n,α)^{24}Na	1369	14.7 h	7.2

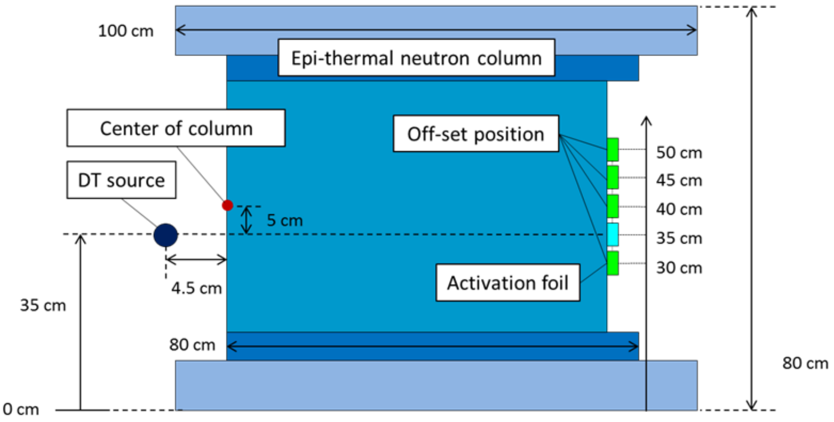

Fig. 9 Schematic vertical view of the experimental setup

4 Result and Discussion

The absolute DT neutron intensity was determined to be 1.78×10^8 n/s from a niobium foil in this experiment. After irradiation, we measured decay gamma rays of each activation foil with Ge detectors. The results are shown in Table 3 and Figure 10. The reaction rates measured by several kinds of activation foils are tabulated in Table 3. Figure 10 shows reaction rates of gold foils at off-set positions.

Experiment 1: From the results of Table 3, we confirmed that the epi-thermal neutron field was formed because the gold foil without cadmium was activated sufficiency. Thermal neutron contribution was observed from the results of gold foils with and without cadmium. However, in actual applications the thermal neutrons can easily be removed with a cadmium sheet put on the front surface of the assembly. From the C/E results of gold foils, there was about 20 % error observed. We expect that this discrepancy is due to scattered neutrons by a steel container, because the container has a complicated structure and really heavy. Next, as for the evaluation of fast neutrons, in the measurement we could not detect γ-rays from the aluminum foil. For the indium foil having a little lower threshold energy than aluminum, we successfully measured the activity although the statistical accuracy was very bad. Nevertheless, it was confirmed that the higher energy contribution was substantially suppressed. From the results above, we concluded that an excellent epi-thermal neutron field was successfully constructed simultaneously removing fast neutrons.

Experiment 2: Figure 10 shows reaction rates for three energy regions and measured results of gold foils. As a result, the measured reaction rate of gold agrees well with the calculation. It can also be found that the epi-thermal neutrons are dominant in the field. In addition, difference of the reaction rate between on-the-axis and off-set positions was not seen. It means that the neutron flux is uniform on the front surface of the assembly and it is possible to irradiate a larger sample with this epi-thermal neutron column.

Table 3 Comparison of experiment and calculation.

Activation foil	Reaction rate [/s/source_neutron] (experiment)	Reaction rate [/s/source_neutron] (calculation)	C/E
Gold	3.22E-6 ± 1.96 %	2.49E-6	0.773
Gold with Cadmium	2.23E-6 ± 2.38 %	2.62E-6	1.172
Indium	1.46E-6 ± 10.6 %	2.68E-9	0.018
Aluminum	Not detected	1.04E-10	

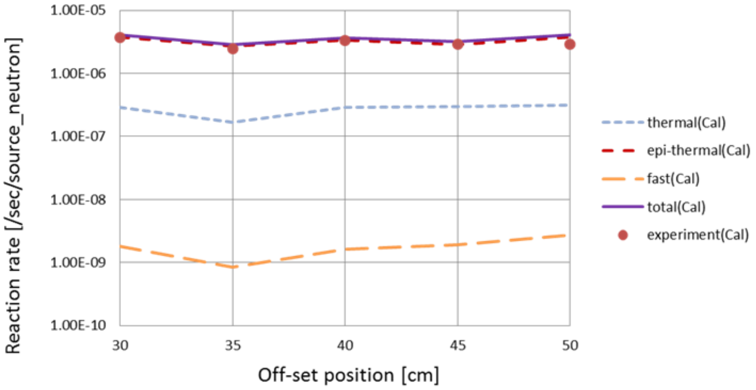

Fig. 10 Results at off-set positions

5 Conclusion and Future Work

In this study, we designed and constructed the epi-thermal neutron column and then we measured the neutron flux intensity and spectral index with activation foils. As a result, we confirmed the epi-thermal neutron column was successfully formed so as to supply a high epi-thermal neutron flux field simultaneously suppressing fast neutrons substantially. Through the present experiment, if the OKTAVIAN facility provides the spec value of 1.0×10^9 n/s, the present epi-thermal neutron column is expected to give a better epi-thermal flux value of over 1.0×10^4 n/s/cm^2 and would be available for fundamental researches of BNCT.

In the next step, we will verify the developed low-energy neutron spectrometer with the presently developed epi-thermal neutron column.

Reference

[1] I.Murata, H.Miyamaru, “Low-energy neutron spectrometer using position sensitive proportional counter —Feasibility study based on numerical analysis” Nuclear Instruments and methods in Physics Research A 589,445-454(2008).

[2] K.Tsubouchi, “Design calculation of epi-thermal neutron field with DT neutron source for low energy neutron spectrometer developed for BNCT”, Master’s thesis, Osaka University (2014) [in Japanese].

[3] X-5 Monte Carlo Team: MCNP-A General Monte Carlo N-Particle Transport Code(2003) N-particle transport code, version 5(2003).

[4] K.Sumita, A.Takahashi, T.Iida, J.Yamamto, S.Imoto, K,Matuda “Osaka University 14MeV Intense Neutron Source and its Utilizations for Fusion Studies (OKTAVIAN Program)” FUSION TECHNOLOGY 1982 Volume.1, 675-680

40 Development plan of real-time gamma-ray spectrum / dose measurement system for medical staff

Mina Kobayashi[1], Fuminobu Sato[1], Isao Murata[1]
[1]Division of Sustainable Energy and Environmental Engineering Graduate School of Engineering,
Osaka University, Yamada-oka 2-1, Suita, Osaka 565-0871
e-mail: mkobayashi@qr.see.eng.osaka-u.ac.jp

In the recent year, radiations have been used very well in the medical field, but the exposure dose of medical staffs is not focused on. The purpose of this study is to estimate a spectrometer which can show gamma-ray spectrum / dose simultaneously in real time for decreasing the exposure dose of the medical staffs and making them understand the risk of radiation very well. Then the spectrometer consists of a CsI scintillator MPPC. Experiments were conducted with a CsI crystal of 3 x 3 x 3 cm^3 and various standard gamma-ray sources. The results were compared with simulations by MCNP5 to verify the performance of the CsI scintillator. As a result, the performance of the CsI scintillator, i.e., detection efficiency and energy resolution, was better than NaI. It means the CsI scintillator can be utilized for the present detector system. In the next step, the estimated response function of the detector will be checked experimentally. After that, the unfolding process for deriving the energy spectrum in real time will be established with the Bayesian estimation method.

1. Introduction

Recently, medical applications of radiation have been widely spread, i.e., radiation therapy, production of radioactive drugs and so on. However, exposure of medical staffs is sometimes not focused on, because treatment of patients is the first priority. This situation can be observed not only in Osaka University Medical Hospital but also others. We, specialists of radiations, would thus think that we should try to decrease radiation exposure to them as low as possible. The purpose of this study is to develop a system which can measure the energy spectrum and dose of gamma-rays at the same time in the medical application spot.

In the past study, there were monitors which can indicate the pulse height spectrum and dose [1], but they cannot indicate the gamma-ray energy spectrum and dose at the same time. If these kinds of systems would be realized, the medical staffs in hospitals could be guided to aware the risk of radiation and finally the exposure dose to them could be suppressed substantially.

In the present paper, a development plan of the measuring system is described and ongoing preparation including a detector test with a selected scintillation crystal is detailed.

2. Measuring System

2.1 Design concept of the system

The essential conditions for designing a spectrometer are as follows.

(1) The spectrometer is small and light for practical use by medical staffs.

(2) The elemental measuring device has high detection efficiency and good energy resolution.

To meet these conditions, we chose a scintillator as a detection device of gamma-rays, because a semiconductor detector surely having a good energy resolution is normally large and heavy. In regard to the dynamic range, the upper energy of gamma-rays was set to 3MeV, because radioactive nuclides are the main source of gamma-rays after operating an accelerator for particle radiation therapy, or making radioisotope medicine. Of course, high energy gamma-rays are emitted by (n,γ) reaction in boron neutron capture therapy (BNCT) at the reactor. However, even in the case of BNCT the source will be considered to change to an accelerator based neutron source. From the above, the first goal of the energy range for designing the spectrometer in this study is up to 3MeV. And we used a Multi-Pixel Photon Counter (MPPC) as a photon counting device, because the MPPC is really smaller and lighter than a photomultiplier tube (PMT).

2.2 Selection of detection device

The scintillator we select in this study must have a similar performance to NaI because NaI is regarded as a convenient and the most popular detector for measuring gamma-rays among various scintillators. But NaI has deliquescency, so the measurement system tends to be large and heavy. Therefore, instead of NaI, CsI is used in this study, because CsI has almost the same performance as NaI. The following is other important reasons:

(1) CsI has a good energy resolution and detection efficiency almost equal to NaI.

(2) Large CsI crystals become available commercially.

(3) CsI can easily be shaped and a bare crystal can be used as a detector because of no deliquescency.

(4) The wave length of scintillation light from CsI fits the dynamic range of MPPC.

First of all, we prepared a CsI crystal of $3\times3\times3\text{cm}^3$ and measured the basic performance of CsI attached to the MPPC.

2.3 Derivation of energy spectrum by Bayesian estimation

The present measuring system utilizes a CsI detector to measure the pulse height spectrum of gamma-rays. After the pulse height spectrum is obtained, it is converted into the energy spectrum and furthermore from the energy spectrum the dose rate is estimated with the flux-dose conversion factor. The point in this study is the energy spectrum and dose can be evaluated at the same time by conducting conversion from the pulse height spectrum to the energy spectrum in real time. This is the goal of the present study.

For this purpose, we employ the Bayesian estimation process to convert from the measure pulse height spectrum to the energy spectrum continuously in real time. In our laboratory, the spectrum type Bayesian estimation has been used for years to estimate the energy spectrum, in which as the first step pulse height spectrum is measured and thereafter it is converted into the energy spectrum as the post process. In this study, this flow is continuously conducted by the sequential Bayesian estimation [2], the detail of which is described in the following.

The Bayes theorem is known as a conditional probability in mathematics. The feature is "by updating an initial thought regarding something with newly obtained objective information, we can obtain a new and more probable result than before". By the use of this process continuously, we think we can estimate the energy spectrum in real time.

Eq.1 shows the relation of the pulse height spectrum and energy spectrum.

$$\begin{pmatrix} y_1 \\ \vdots \\ y_i \\ \vdots \\ y_n \end{pmatrix} = \begin{pmatrix} R_{11} & R_{12} & \cdots & R_{1j} & \cdots & R_{1n} \\ \vdots & & & \vdots & & \vdots \\ R_{i1} & & & R_{ij} & & R_{in} \\ \vdots & & & \vdots & & \vdots \\ R_{n1} & \cdots & & R_{nj} & \cdots & R_{nm} \end{pmatrix} \cdot \begin{pmatrix} \varphi_1 \\ \vdots \\ \varphi_j \\ \vdots \\ \varphi_n \end{pmatrix} \tag{1}$$

In the equation (1), y_i is pulse height spectrum and it is called posterior probability in the Bayesian estimation. It means, when a spectrometer detects a signal at channel *i,* the signal would come from an event originated from energy E_j in the energy spectrum ψ. R_{ij} means a likelihood, which is defined as the response function of the detector for each energy, E_j, in radiation measurements, and ψ_j is the energy spectrum and it is called prior probability. This is the probability that the energy of an incident radiation goes into an energy division E_j when the radiation enters the detector. We can derive the energy spectrum from the measured pulse height spectrum and the estimated response function of the detector.

The basic expression of the Bayesian estimation, which is the conditional probability of *j* for *i*, is expressed by the following equation (2).

$$P(j/i)=\frac{R_{ij}\varphi_j}{\Sigma R_{ij}\,\varphi_j} \tag{2}$$

The denomination of the right side corresponds to y_i and the numerator means the relative probability of a detected signal to be assigned to ψ_j in Eq. (1). The first step of the sequential Bayesian estimation is to set an arbitrary initial spectrum to ψ and to derive y_i with equation, $y_i = \Sigma R_{ij}\psi_j,$ from Eq. (1). We calculate the probability of an event *j* of ψ from the measured even y_i with the response function *R* using Eq. (2), if a signal at *i* is detected. As a result, the ψ is adjusted by adding the contribution of the detected signal at *i*. Thereafter we derive a new y_i. By repeating this process many times, we can obtain the converged energy spectrum.

There is no precedent which showed the energy spectrum could be estimated accurately by the sequential Bayesian estimation. And generally, it is known that the convergence of the sequential Bayesian estimation is very slow. However we think even if the spectrum estimation is not converged, we can estimate the dose, because the dose being theoretically an integral quantity of the spectrum has to de converged faster. As for the energy spectrum, we will plan to obtain an approximate result.

3. Experiment

3.1 Experimental arrangement

We set up a proto-type measuring device with a CsI crystal and MPPC as shown in Fig.1. The pulse height spectra were measured with several standard gamma-ray sources (^{22}Na,^{60}Co,^{133}Ba,^{137}Cs and,^{241}Am) to check the energy resolution and peak efficiency. The CsI crystal and MPPC was in a box, and a standard gamma-ray source is place at 10cm from the CsI scintillator surface. Fig.2 shows a block diagram of the experimental arrangement.

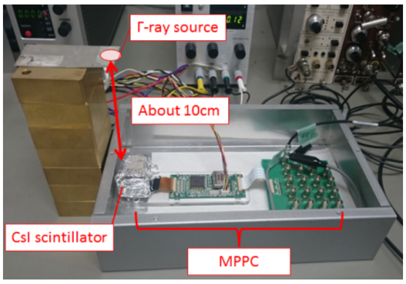

Figure 1. Photo of experimental set up

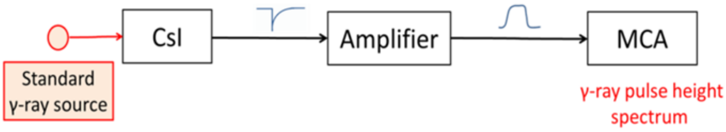

Figure 2. Block diagram of experimental arrangement

3.2 Experimental results and discussion

Fig.3 shows the measured pulse height spectra with the CsI detector. Gamma-ray energies of the used standard gamma-ray sources are listed in Table 1. Fig.4 shows the measured energy resolution, compared with that of NaI in order to confirm both are more-or-less the same [3]. Fig.5 shows the measured peak efficiency compared with calculation results by MCNP5 (Monte Carlo N-Particle Transport Code) [4] in order to confirm reproducibility of efficiency by calculations for upcoming design of the prototype detector. The C/E (C_{CsI}/E_{CsI}, C_{NaI}/E_{CsI}) is shown in Fig.6 to expand the difference between the result of CsI and NaI.

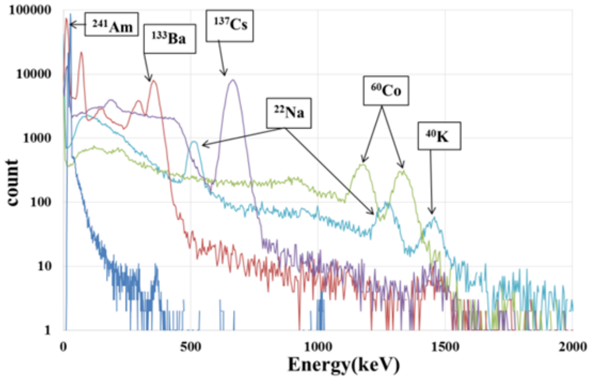

Figure 3. Measured gamma-ray pulse height spectra

Table 1. Standard gamma-ray sources

Source	Energy(keV)
^{22}Na	511 1274.537
^{60}Co	1173.228 1332.49
^{133}Ba	356.0134
^{137}Cs	661.657
^{241}Am	59.5409

In Fig.3 we can observe photopeaks of the used standard gamma-rays in Table 1 and in addition around 1500 keV there is a single peak in all the spectra. This is a background radiation of ^{40}K. We find the energy resolution of CsI is better than that of NaI from Fig.4. Regarding the peak efficiency of CsI, from Fig.5 we find that the agreement of measured and calculated values is excellent, and from Fig.6 we confirm from the C_{CsI}/E_{CsI}, MCNP5 can reproduce the experimental peak efficiency very well. It means that we can predict peak efficiencies for other scintillator sizes by MCNP5 in order to analyze and fix the final crystal size. And we notice C_{CsI}/E_{CsI} is larger than C_{NaI}/E_{CsI} except ^{241}Am. It means that the peak efficiency of CsI is higher than that of NaI. From the above, CsI can thus work as a spectrometer better than NaI. Therefore CsI is suitable for the present spectrometer. In the next step, we will fix the suitable size numerically by MCNP5 and estimate the detector response function and check the function experimentally.

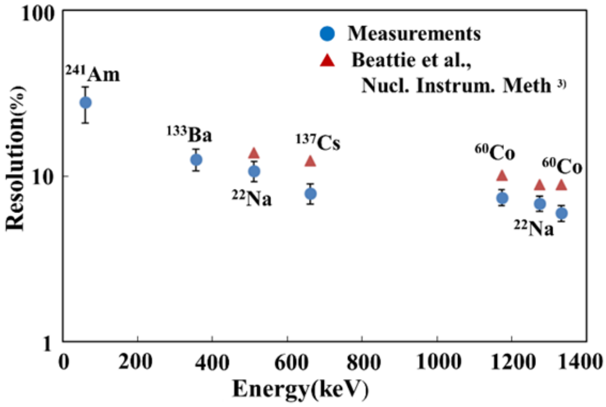

Figure 4. Measured energy resolution of CsI compared with the measured value of NaI [3].

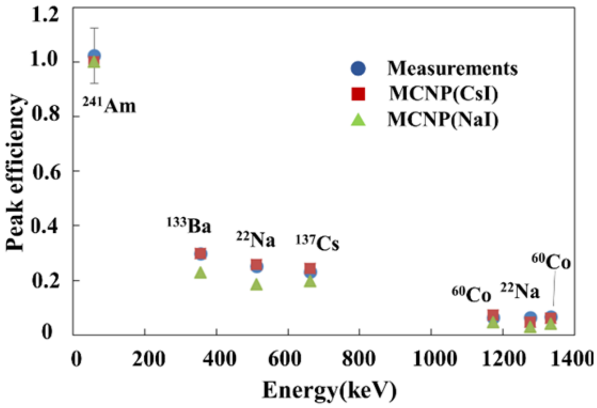

Figure 5. Measured peak efficiency of CsI compared with the simulation result of NaI and CsI by MCNP5.

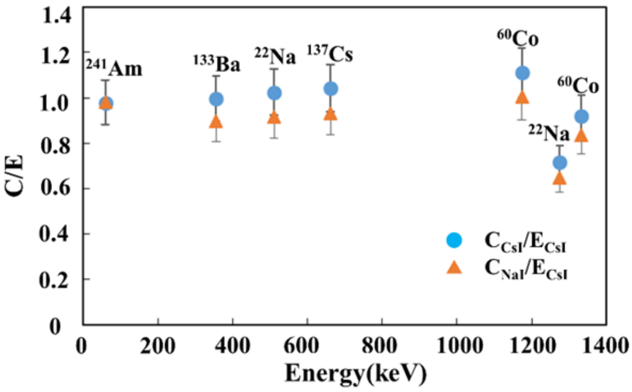

Figure 6. Ratio of calculation to experiment (C/E) for peak efficiency, C_{CsI}/E_{CsI}, C_{NaI}/E_{CsI}.

4. Conclusion

For the medical staffs in hospitals, numerical and experimental examination of a measurement system was carried out, which can show gamma-ray spectrum / dose simultaneously in real time. From the experimental results with a CsI scintillator of 3 x 3 x 3 cm^3 and MPPC, it was confirmed that the CsI scintillator could be utilized for the present detector system, because the performance of the CsI scintillator, i.e., detection efficiency and energy resolution, was found to be better than NaI. In the future, the response function will be evaluated and checked experimentally. Thereafter, the unfolding process for deriving the energy spectrum in real time will be established with the Bayesian estimation method followed by construction of the prototype system.

Acknowledgements

The authors would like to express their sincere gratitude to Mr. K. Imagawa of I.S.C.Lab. Co., Ltd for his supporting our experiment.

References

[1]Nakamori T, et al.: Development of a gamma-ray imager using a large area monolithic 4 x 4 MPPC array for a future PET scanner, *JINST 7 C01083*(2012).

[2]Iwasaki S: A new approach for unfolding problems based only on the Bayes' Theorem, *Proceedings of the 9th International Symposium on Reactor Dosimetry*, pp.245-252(1997).

[3]R.J.D.Beattie J.Byrne.: A Monte Carlo program for evaluating the response of a scintillation counter to monoenergetic gamma rays, *Nuclear Instrument and Method* **104,** pp.163-168(1972).

[4]X-5 Monte Carlo Team: MCNP – A General N-Particle Transport Code, Version 5, Los Alamos National Laboratory, *LA-UR-03-1987*(2003).

41 Investigation for Copper Nuclear Data based on New Integral Experiment on Copper with DT Neutron Source at JAEA/FNS

Saerom Kwon, Masayuki Ohta, Kentaro Ochiai, Satoshi Sato, Chikara Konno

Japan Atomic Energy Agency, Tokai-mura, Naka-gun, Ibaraki-ken, Japan

In order to examine the large underestimation for the measured data related to neutrons below a few keV in the copper integral experiment which had been carried out at JAEA/FNS 20 years ago, we performed a new integral experiment by using a copper assembly of 630 mm in diameter and 608 mm in thickness covered with lithium oxide blocks, which reduced background neutrons from concrete walls and so on, and presented it at the last Symposium on Nuclear Data. At that time it was confirmed that the large underestimation for the reaction rates sensitive to lower energy neutrons also remained in this experiment though the effect of background neutrons was reduced.

In this study we have investigated the copper data in the nuclear data libraries by using the follow methods: (a) replacement of the copper isotope data, (b) modification of the elastic scattering and capture cross section data. As a result it is found out that the underestimation tendency decreases by adequate modification of the elastic scattering and capture cross section data. In addition, the reaction rates sensitive to neutrons above a few MeV also have clear discrepancies among recent nuclear data libraries. We have figured out that the discrepancies occur by the inelastic scattering and (n, np) reaction cross section data of copper. The specific cross section data of copper should be reassessed.

This is a blank page.

42 New Benchmark Experiment on Lead with DT Neutron Source at JAEA/FNS

Saerom Kwon, Masayuki Ohta, Satoshi Sato, Kentaro Ochiai, Chikara Konno

Japan Atomic Energy Agency, Tokai-mura, Naka-gun, Ibaraki-ken, Japan

Lead is the most commonly discussed candidate material for a gamma ray shielding, a liquid type tritium breeder (LiPb) and a neutron multiplying in fusion reactor systems. Thus validation for lead nuclear data is one of essential issues to establish in advance. Although a benchmark experiment on lead with DT neutron source had been performed at JAEA/FNS [1], the measured data related to lower energy neutrons below a few keV had included background neutrons scattered in concrete walls in the experiment room. Hence, we designed and performed a new benchmark experiment with a lead assembly (55.7 * 55.7 * 60.7 cm, rectangular shaped) covered with Li_2O blocks which absorb the background neutrons at the same facility. In the center of the lead assembly, we measured reaction rates of the ^{93}Nb(n,2n)^{92m}Nb, ^{27}Al(n,α)^{24}Na, ^{115}In(n,n')^{115m}In, ^{197}Au(n,γ)^{198}Au and ^{186}W(n,γ)^{187}W with the activation foil method. We calculated using the Monte Carlo neutron transport code, MCNP5-1.40 and the latest nuclear data libraries, ENDF/B-VII.1, JEFF-3.2 and JENDL-4.0. As a response function, JENDL Dosimetry File 99 was used.

The calculated reaction rates related to neutrons above a few MeV were in good agreement with the measured ones within 10%. However, the calculated reaction and fission rates related to neutrons below a few keV underestimated the measured ones with the depth of the assembly. We investigated the nuclear data of lead in detail in order to find out reasons of the underestimation. We figured out that the nuclear data of ^{208}Pb in ENDF/B-VII.1 and in JEFF-3.2 were dominant factors for the discrepancy of the reaction rates related to neutrons above a few MeV and below a few keV, respectively. This study calls into question the lead data among the latest nuclear data libraries.

Reference

[1] K. Ochiai, et al., J. Korean Physical Society 59 (2011) 1953.

43 Some comments on KERMA factors and DPA cross-section data in ACE and MATXS files of JENDL-4.0

Chikara KONNO, Saerom KWON, Masayuki OHTA, and Satoshi SATO

Sector of Fusion Research and Development, Japan Atomic Energy Agency
Tokai-mura, Naka-gun, Ibaraki-ken 319-1195 Japan
e-mail : konno.chikara@jaea.go.jp

A lot of the KERMA factors and DPA cross-section data have some problems, which are not known well by users. Now we examine the KERMA factors and DPA cross-section data included in the official ACE and MATXS files of JENDL-4.0 with those of ENDF/B-VII.1 and JEFF-3.2. As a result, they are different from those of ENDF/B-VII.1 and JEFF-3.2 for a lot of nuclei, which is considered to be caused by the following new problems; 1) kinematics KERMA factors are not correct for nuclei without detailed secondary particle data (energy-angular distribution data), 2) huge gas production cross-section data cause huge KERMA factors and DPA cross-section data in low neutron energy, 3) it seems that NJOY does not adequately process gamma production data of the capture reaction in File 6 and produces incorrect kinematics KERMA factors and DPA cross-section data for nuclei with Files 12-15, MT3, due to some defects of NJOY. The ACE and MATXS files of JENDL-4.0 with these problems should be revised based on this study.

1. Introduction

KERMA (Kinetic Energy Release in MAterial) factors and damage (DPA) cross-section data which are used for calculating nuclear heating and damage are not included in nuclear data libraries but estimated from nuclear data libraries with the NJOY code [1] and stored to ACE and MATXS files [1] for nuclear analyses. ACE files include average heating numbers, which are KERMA factors divided by total cross-sections, and DPA cross-section data. MATXS files include energy-balance and kinematics KERMA factors and DPA cross-section data, which are extracted with the TRANSX [2] code. However a lot of the KERMA factors and DPA cross-section data have some problems [3], which are not known well by users. Now we examine the KERMA factors and DPA cross-section data included in the official ACE [4] and MATXS [5] files of JENDL-4.0 and the official ACE files of ENDF/B-VII.1 [6] and JEFF-3.2 [7].

2. Method

For 406 nuclei in JENDL-4.0, we extracted the KERMA factors and DPA cross-section data from the official ACE files of JENDL-4.0 and compared them with those from the official ACE files of ENDF/B-VII.1 and JEFF-3.2. The KERMA factors and DPA cross-section data in the official MATXS files of JENDL-4.0 were deduced with the TRANSX code and were compared with those in the official ACE files of JENDL-4.0. Note that the KERMA factors of a lot of nuclei in JENDL-4.0 with inconsistent energy-balance are already replaced with the kinematics KERMA factors with the kinematics method. We also extracted elastic scattering, capture, hydrogen production and helium production cross-section data from the ACE files in order to investigate reasons of differences of the KERMA factors and DPA cross-section data among the three nuclear data libraries. KERMA factors and DPA cross-section data were also calculated with the PHITS code (kinematic method) from reaction cross-section data in the ACE files in order to check if NJOY produced KERMA factors and DPA cross-section data adequately.

3. Results and discussion

A lot of the KERMA factors and DPA cross-section data are different among JENDL-4.0, ENDF/B-VII.1 and JEFF-3.2. It is considered that the differences are caused by the following problems, except for the energy-balance problem.

1) Kinematics KERMA factors are not correct for nuclear data libraries without detailed secondary particle data (energy-angular distribution data).
2) Gas production data determine several KERMA factors and DPA cross-section data in low neutron energy.
3) It seems that NJOY produces incorrect KERMA factors and DPA cross-section data due to the following problems.
    - NJOY does not adequately process gamma production data of the capture reaction in File 6 of the nuclear data libraries, though it does gamma production data of the capture reaction in Files 12-15 of the nuclear data libraries.
    - NJOY produces incorrect kinematics KERMA factors for nuclei with Files 12-15, MT3.

The details of the problems are described below.

3. 1 Problem on kinematics KERMA

The KERMA factors of a lot of nuclei in the JENDL-4.0 ACE files with inconsistent energy-balance are already replaced with the maximum KERMA factors with the kinematics method, but it is found out that the maximum KERMA factors with the kinematics method is not always correct for nuclei without detailed secondary particle data (energy-angular distribution data). Figure 1 shows the KERMA factors with the energy-balance and kinematics methods of ^{56}Fe in (a) ENDF/B-VII.1 and (b) JENDL-4.0, respectively, which are calculated with NJOY. The KERMA factor with the kinematics method is almost the same as that with the energy-balance method in the case of ^{56}Fe in ENDF/B-VII.1 because the ^{56}Fe data in ENDF/B-VII.1 have detailed secondary particle data. On the other hand, the ^{56}Fe data in JENDL-4.0 do not include detailed secondary particle data for the (n,2n), (n,n'p), (n,n'a) and (n,n'$_{\mathrm{cont}}$) reactions and so on, where NJOY adopts the one-particle recoil approximation. Probably this one-particle recoil approximation is not appropriate because the kinematics KERMA factor calculated with the PHITS [8] code is almost the same as the energy-balance KERMA factor as shown in Fig. 1 (b). The kinematics KERMA factors adopted in the JENDL-4.0 ACE files should be reassessed, for example ^{56}Fe, ^{58}Ni, etc.

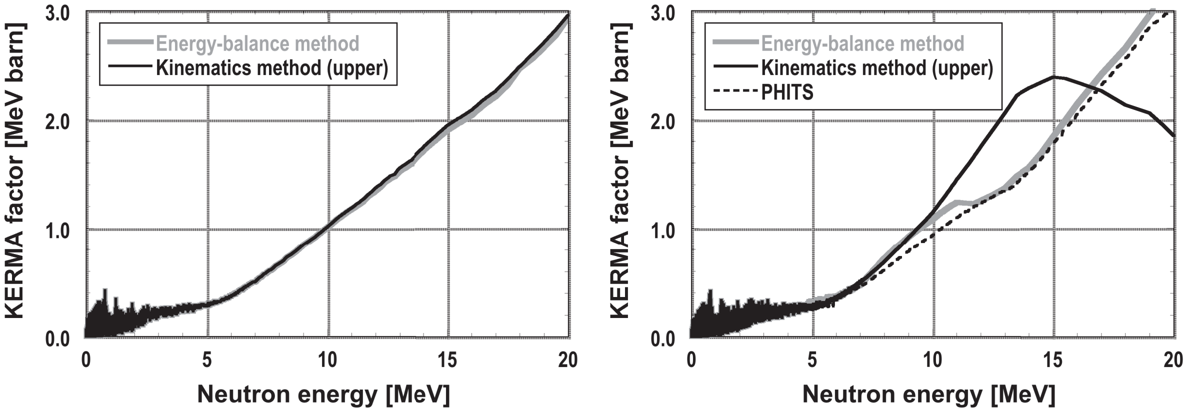

(a) ENDF/B-VII.1 (b) JENDL-4.0

Fig. 1 KERMA factors of ^{56}Fe.

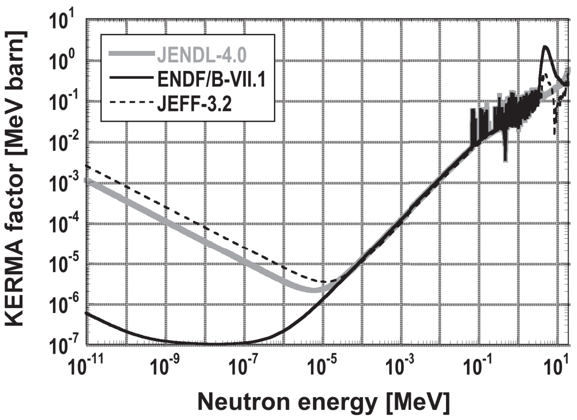

Fig. 2 KERMA factors of ^{208}Pb.

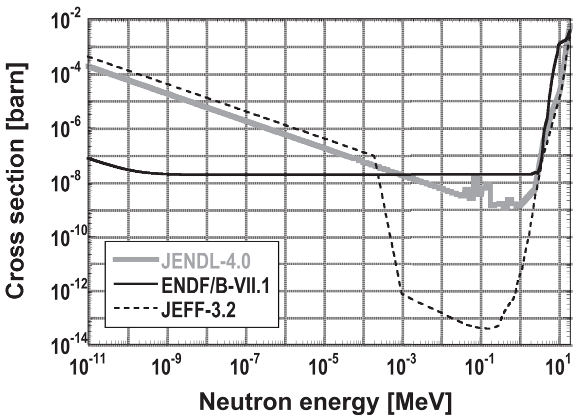

Fig. 3 Helium production cross-section data of ^{208}Pb.

3. 2 Problem on gas production cross-section data

Several KERMA factors and DPA cross-section data in JENDL-4.0 are drastically different from those in ENDF/B-VII.1 and JEFF-3.2 as shown in Fig. 2; ^{32}S, ^{33}S, ^{39}K, ^{40}K, ^{40}Ca, ^{152}Gd, ^{153}Gd, ^{161}Dy, ^{180}W, ^{183}W, ^{186}Os, ^{187}Os, ^{208}Pb, ^{209}Bi. This problem is due to drastically different gas production cross-section data except for ^{152}Gd as shown in Fig. 3. These gas production cross-section data should be reassessed and revised if necessary. Note that the reason for ^{152}Gd is a wrong Q value (0 eV) of the (n,α) reaction in ^{152}Gd of ENDF/B-VII.1 and JEFF-3.2.

3. 3 Problems on NJOY

Figure 4 (a) shows the KERMA factors of ^{55}Mn in JENDL-4.0, ENDF/B-VII.1 and JEFF-3.2. The KERMA factor of ^{55}Mn in JENDL-4.0 is by a factor of 2 or 3 larger than those in ENDF/B-VII.1 and JEFF-3.2 below a few hundred eV, though the capture cross-section data of ^{55}Mn in JENDL-4.0, ENDF/B-VII.1 and JEFF-3.2 are almost the same. From our detailed investigation, it is found out that the KERMA factors and DPA cross-section data of a lot of nuclei with gamma data of the capture reaction in File 6 (e.g. ^{55}Mn in ENDF/B-VII.1 and JEFF-3.2) are different from those with gamma data of the capture reaction in Files 12-15 (e.g. ^{55}Mn in JENDL-4.0). NJOY outputs the following message only in the former case.

```
“mf6, mt102 does not give recoil za=xxxx
    photon momentum recoil used.”
```

It seems that NJOY cannot process capture reaction data in File 6 adequately. As a trial, the gamma data of the capture reaction in File 6 of ^{55}Mn in ENDF/B-VII.1 are converted to those in Files 12-15 and are processed with NJOY. Figure 4 (b) shows the result, where the KERMA factor [ENDF/B-VII.1 (MF6→MF12-15) in Fig. 4 (b)] of the converted ^{55}Mn in ENDF/B-VII.1 agrees with that in JENDL-4.0 well. It is considered that the difference of the KERMA factors in low neutron energy is due to the difference of the gamma data format for the capture reaction and that NJOY cannot process capture reaction data in File 6 adequately. In this figure the kinematics KERMA factor [ENDF/B-VII.1 (PHITS) in Fig. 4 (b)] with PHITS is also plotted, which supports the NJOY problem. This problem occurs for a lot of nuclei with gamma data of the capture reaction in File 6 and in DPA cross-section data.

Figure 5 shows the KERMA factors of ^{35}Cl in JENDL-4.0 and JEFF-3.2. The KERMA factor in JENDL-4.0, which is a kinematics KERMA because the ^{37}Cl data in JENDL-4.0 have no secondary gamma data, is different from that in JEFF-3.2, which is an energy-balance KERMA. It seems that kinematics KERMA factors for nuclei without secondary gamma data are not correct because the kinematics KERMA factor of the secondary-gamma-data-deleted ^{37}Cl data in JEFF-3.2 [JEFF-3.2 (no 2nd. gamma) in Fig. 5] is the same as that in JENDL-4.0 as shown in Fig. 5. This problem also occurs for DPA cross-section data.

Dr. Shibata pointed out that it was difficult to keep energy-balance in Files 12-15, MT3, particularly for the capture reaction [9]. JENDL-4.0 stores gamma production data of the capture reaction for a lot of nuclei (e.g. ^{92}Mo) to Files 12-15, MT3. Figure 6 shows the DPA cross-section data of ^{92}Mo in JENDL-4.0 and ENDF/B-VII.1. The DPA cross-section data of ^{92}Mo in JENDL-4.0 are by a factor of 2 larger than those in ENDF/B-VII.1 (the gamma production data of the capture reaction for ^{92}Mo in ENDF/B-VII.1 are stored in Files 12-15, MT102). As a trial, the gamma production data blow 500 keV in Files 12-15, MT3 of ^{92}Mo in JENDL-4.0 are moved to Files 12-15, MT102 and are processed with NJOY. Figure 6 shows the result, where the DPA cross-section data [JENDL-4.0 (mf12-15, mt3→mf12-15, mt102) in Fig. 6] of the converted ^{92}Mo in JENDL-4.0 are almost the same as those in ENDF/B-VII.1. It seems that NJOY cannot process gamma production data in Files 12-15, MT3 adequately.

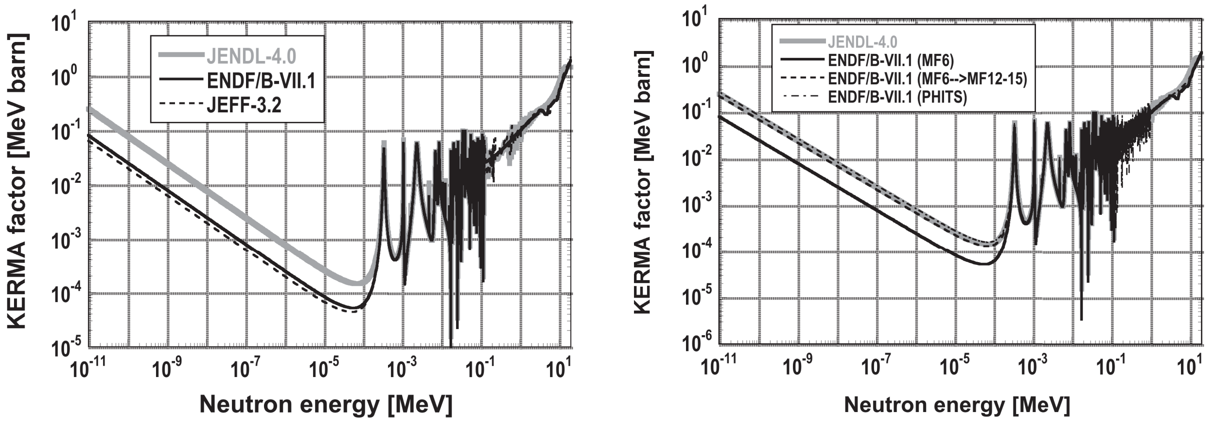

(a) Original nuclear data libraries (b) Reformatted nuclear data libraries

Fig. 4 KERMA factors of ^{55}Mn.

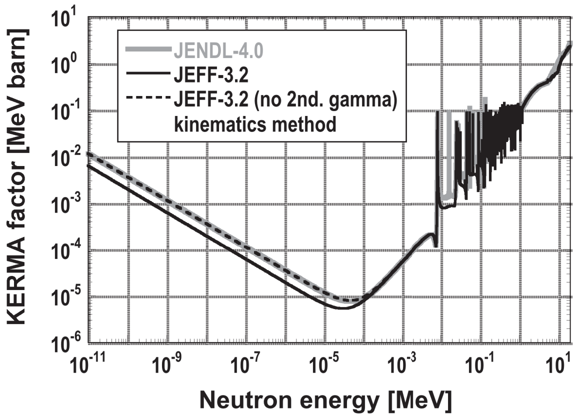

Fig. 5 KERMA factors of ^{35}Cl.

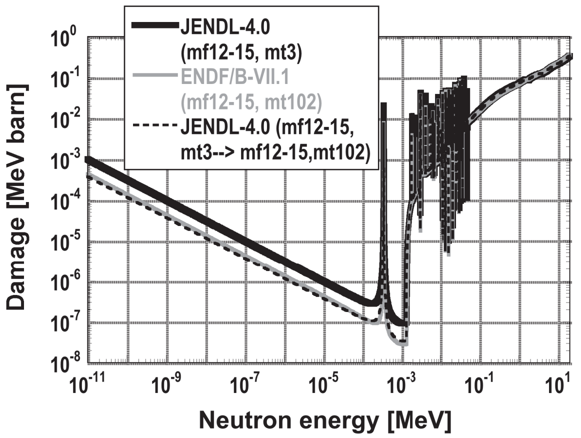

Fig. 6 DPA cross-section data of ^{92}Mo.

4. Conclusion

We compared KERMA factors and DPA cross-section data in the ACE files of JENDL-4.0 with those of ENDF/B-VII.1 and JEFF-3.2 in more detail. As a result, it was found out that the KERMA factors and DPA cross-section data had the following problems, except for the energy-balance problem.

1) Kinematics KERMA factors are not correct for nuclei without detailed secondary particle data (energy-angular distribution data).
2) Gas production data determine KERMA factors and DPA cross-section data in low neutron energy.
3) It seems that NJOY does not adequately process gamma production data of the capture reaction in File 6 and produces incorrect kinematics KERMA factors for nuclei with Files 12-15, MT3, due to some defects of NJOY.

ACE files with the problems should be revised based on this study. We also would like to request the JENDL evaluators to add detailed secondary particle data including gamma data suit to estimate KERMA factors and DPA cross-section data in the next JENDL.

References

[1] A.C. Kahler et al. : "The NJOY Nuclear Data Processing System, Version 2012," LA-UR-12-27079 (2012).
[2] R.E. MacFarlane : "TRANSX 2: a code for interfacing MATXS cross-section libraries to nuclear transport codes," LA-12312-MS (1993).
[3] C. Konno et al. : Nuclear Data Sheets, 118, 450 (2014).
[4] http://prodas.jaea.go.jp/?AceLibJ40
[5] http://rpg.jaea.go.jp/main/ja/db_matxslibj40/
[6] D.L. Conlin et al. : "Continuous energy neutron cross section data tables based upon ENDF/B-VII.1," LA-UR-13-20137 (2013).
[7] https://www.oecd-nea.org/dbforms/data/eva/evatapes/jeff_32/
[8] T. Sato, et al. : J. Nucl. Sci. Tecnol., 50, 913 (2013).
[9] K. Shibata : private communication (2012).

44 A Simple Method for Modification of Capture Reaction and Elastic Scattering Nuclear Data in Analyses of Nuclear Data Benchmark Experiments

Chikara KONNO, Saerom KWON, Masayuki OHTA, and Satoshi SATO

Sector of Fusion Research and Development, Japan Atomic Energy Agency
Tokai-mura, Naka-gun, Ibaraki-ken 319-1195 Japan
e-mail : konno.chikara@jaea.go.jp

In order to specify reasons of the discrepancy between the calculated and measured results in analyses of benchmark experiments, some parts of some isotope data in nuclear data files are often modified and the modifies nuclear data files are processed with the NJOY code and the new ACE or MATXS files are used. However it is not easy to modify capture and elastic scattering data below 1 MeV with resonance data. Thus we devised a simple method to use capture and elastic scattering cross section data generated from resonance data with the NJOY code. This method was applied to detailed analyses of copper and molybdenum benchmark experiments at JAEA/FNS and it was demonstrated that this method was very useful.

1. Introduction

We have carried out a lot of nuclear data benchmark experiments at the Fusion Neutronics Source facility in Japan Atomic Energy Agency [1, 2]. We often encounter discrepancies between calculated and measured ones in the analyses of the experiments. Then, in order to specify reasons of the discrepancy between the calculated and measured results, some parts of some isotope data in nuclear data files are modified and the modifies nuclear data files are processed with the NJOY code [3] and the new ACE or MATXS files are used in the analysis [4]. This method is simple but works well. Recently we have an increased need to modify capture and elastic scattering data below 1 MeV as shown in Fig. 1. This modification is not easy, because capture reaction and elastic scattering data below 1 MeV of a lot of nuclei include resonance data are hard to treat to users. Thus we devise a simple method in order to modify capture reaction and elastic scattering data below 1 MeV with resonance data easily.

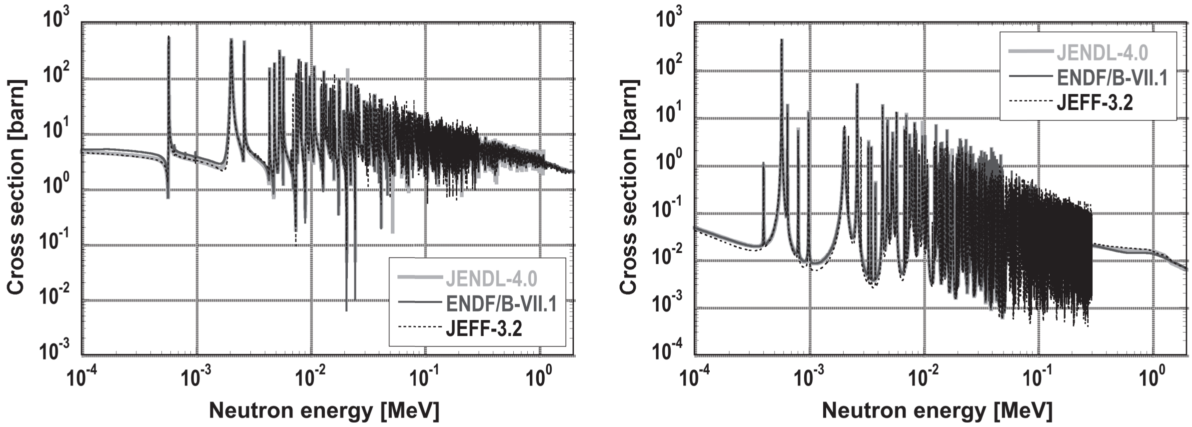

(a) Elastic scattering (b) Capture reaction

Fig. 1 Elastic scattering and capture reaction cross sections of ^{63}Cu.

2. Method

The method is the following,

1) A PENDF (Pointwise ENDF), where the cross section data of the capture reaction and elastic scattering are also pointwise above 10^{-5} eV, of 0 K is produced from the original nuclear data file (ORG) with the reconr module of NJOY.

2) The Files 2 (resonance parameters) and 3 (reaction cross sections) data of the capture reaction and elastic scattering in the original nuclear data file are replaced with those in the PENDF file and the LRP parameter [5] of the File 1 (general information) in the replaced original nuclear data file is changed to 0. It is confirmed that the ACE file produced from the replaced nuclear data file (MOD1) is the same as that from the original nuclear data file as shown in Fig. 2. Then the replaced nuclear data file can be also changed for the capture reaction and elastic scattering easily.

3) After necessary modification of the replaced nuclear data file as shown in Fig. 3, a new

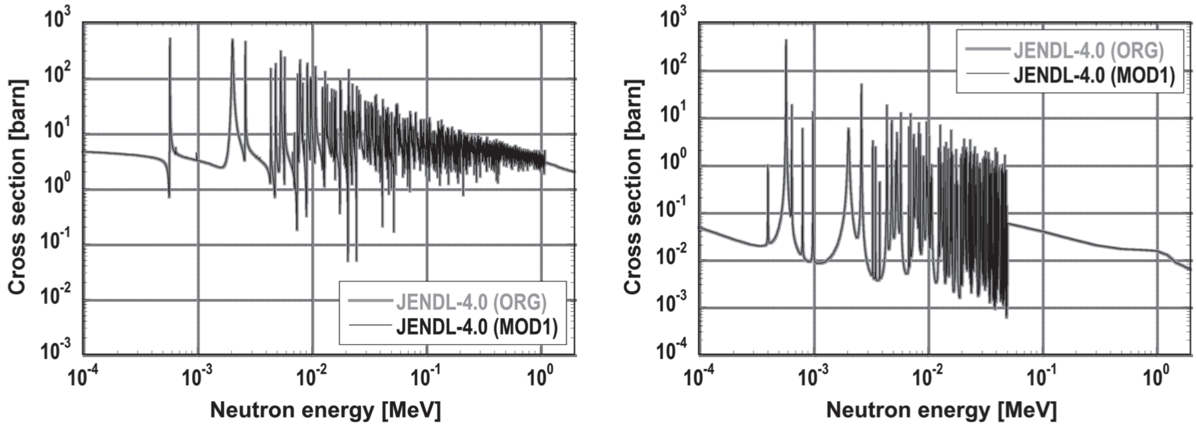

(a) Elastic scattering (b) Capture reaction

Fig. 2 Comparison between ORG and MOD1 for elastic scattering and capture reaction cross sections of ^{63}Cu.

ACE file is produced from the modified nuclear data file (MOD2) as the original one with NJOY and the ACE file is used for benchmark experiment analyses. Note that NJOY does not Doppler-broaden the elastic scattering and capture reaction cross section data above the lowest threshold energy of the threshold reactions. This problem appeared when the capture reaction cross section data was replaced with those of JEFF-3.2 [6] in ^{63}Cu of JENDL-4.0 [7]. The upper resonance energy of the capture reaction of ^{63}Cu in JEFF-3.2 is 300 keV, while the threshold energy of the (n,p) reaction of ^{63}Cu in JEND-4.0 is 100 keV. In this case NJOY did not Doppler-broaden the capture reaction cross section data above 100 keV in the case that the capture reaction cross section data was replaced with those of JEFF-3.2 in ^{63}Cu of JENDL-4.0. Thus we modified the threshold energy of the (n,p) reaction, e.g. from 100 keV to 300 keV or more.

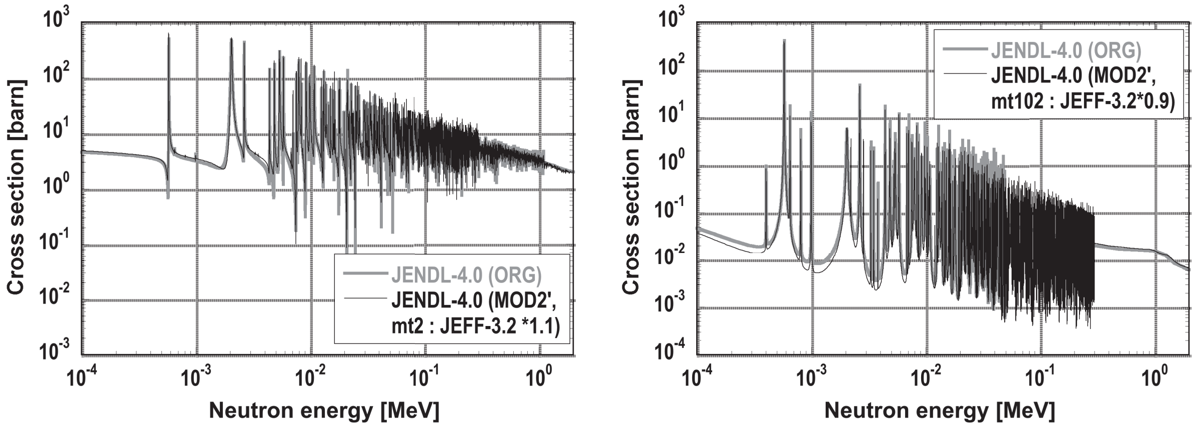

(a) Elastic scattering
(JEFF-3.2 multiplied by 1.1
between 100 eV to 300 keV)

(b) Capture reaction
(JEFF-3.2 multiplied by 0.9
between 100 eV to 300 keV)

Fig. 3 Examples of ORG and MOD2 (elastic scattering and capture reaction cross section data in JENDL-4.0 are replaced with those in JEFF-3.2 and elastic scattering cross section data are increased by 10 % and capture reaction cross section data are decreased by 10 %) for elastic scattering and capture reaction cross sections of ^{63}Cu.

This method has been adopted in the detailed analyses of the new copper and molybdenum benchmark experiments [8, 9]. It is confirmed that this method is very useful.

3. Conclusion

A simple method with PENDF data for cross section data of the capture reaction and elastic scattering is devised to easily modify capture reaction and elastic scattering data below 1 MeV for analyses of benchmark experiments. This method is applied to the recent benchmark experiments at JAEA/FNS. It is demonstrated that this method is very useful.

References

[1] F. Maekawa, C. Konno, Y. Kasugai, Y. Oyama and Y. Ikeda : “Data Collection of fusion neutronics benchmark experiment conducted at FNS/JAEA,” JAERI-Data/Code 98-021 (1998).

[2] Y. Oyama, S. Yamaguchi and H. Maekawa : “Experimental results of angular neutron flux spectra leaking from slabs of fusion reactor candidate materials, I,” JAERI-M 90-092 (1990).

[3] A.C. Kahler et al. : “The NJOY Nuclear Data Processing System, Version 2012,” LA-UR-12-27079 (2012).

[4] C. Konno, K. Ochiai, M. Wada, K. Kosuke and S. Sato : Fusion Engineering and Design, 84, 1095 (2009).

[5] M. Herman and A. Trkov : “ENDF-6 Formats Manual,” BNL-90365-2009 (2009).

[6] https://www.oecd-nea.org/dbforms/data/eva/evatapes/jeff_32/

[7] K. Shibata, O. Iwamoto, T. Nakagawa, N. Iwamoto, A. Ichihara, S. Kunieda, S. Chiba, K. Furutaka, N. Otuka, T. Ohsawa, T. Murata, H. Matsunobu, A. Zukeran, S. Kamada and J. Katakura : J. Nucl. Sci. Technol., 48, 1 (2011).

[8] S. Kwon, S. Sato, M. Ohta, K. Ochiai and C. Konno : Fusion Engineering and Design (in press), http://dx.doi.org/10.1016/j.fusengdes.2015.10.036.

[9] M. Ohta, S. Sato, S. Kwon, K. Ochiai and C. Konno : Fusion Engineering and Design (in press), http://dx.doi.org/10.1016/j.fusengdes.2015.11.001.

45 Validation of IRDFF in Neutron Field of Li_2O Assembly with DT Neutrons at JAEA/FNS

Satoshi Sato, Saerom Kwon, Masayuki Ohta, Chikara Konno

Japan Atomic Energy Agency, Tokai-mura, Naka-gun, Ibaraki-ken, Japan

In order to validate a new dosimetry cross section data library, International Reactor Dosimetry and Fusion File release 1.0 (IRDFF 1.0), we perform an integral experiment using the Li_2O assembly and the DT neutron source at JAEA/FNS in this study. We already performed an integral experiment using the graphite assembly and the DT neutron source at JAEA/FNS, and confirmed that most of the data in IRDFF were valid in the neutron field of the graphite assembly with DT neutrons. The neutron fields in the graphite and Li_2O assemblies are very different. The neutron field in the graphite assembly has the thermal neutron peak, and is almost flat in the neutron energy range between the thermal neutron and 10 MeV. On the other hand, there are few neutrons below 100 eV in the neutron fields of the Li_2O assembly. The reaction rates in the Li_2O assembly have little contributions from neutrons below 100 eV, we can validate IRDFF 1.0 for the neutron field of the energy from 100 eV to 15 MeV in the Li_2O assembly with DT neutrons in this study. We place a lot of activation foils (Al, Ti, V, CuMnNi, Fe, Co, Ni, Zn, Y, Mg, Zr, Mo, Nb, In, Tm, W and Au foils) at depths of 10.1 and 30.4 cm along the center axis of the Li_2O assembly with dimensions of 65.8 cm in height, 65.8 cm in width and 60.7 cm in thickness, and measure the dosimetry reaction rates of the reactions with half-lives longer than 40 minutes. We analyze the experiment by using MCNP5-1.40 with the nuclear data library ENDF/B-VII.1 and IRDFF-v.1.05. Most of the calculated results show very good agreements with the measured ones within 10 %, and we confirm that most of the data in IRDFF-v1.05 are valid in the neutron field of the Li_2O assembly with DT neutrons.

46 New Integral Experiment on Tungsten and Vanadium-alloy with DT Neutrons at JAEA/FNS

Satoshi Sato, Saerom Kwon, Masayuki Ohta, Chikara Konno

Japan Atomic Energy Agency, Tokai-mura, Naka-gun, Ibaraki-ken, Japan

In order to validate the nuclear data, integral experiments on tungsten and vanadium with the DT neutron source at JAEA/FNS were performed over 20 years ago. The calculated reaction rates of the ^{197}Au(n,γ)^{198}Au and ^{186}W(n,γ)^{187}W reactions, which are sensitive to low energy neutrons, at the depth of 40 cm in the tungsten mockup underestimated the measured ones by 20 – 30 % in the previous study, while that of the ^{93}Nb(n,2n)^{92m}Nb reaction at the depth of 40 cm overestimated the measured ones by 15 – 20 %. The calculated reaction rate of the ^{197}Au(n,γ)^{198}Au reaction in the vanadium mockup underestimated the measured one by 30 – 60 % in the previous study. Background neutrons scattered in the concrete wall of the experimental room are considered to cause these underestimations. In order to reduce background neutrons, we propose new experimental assemblies and perform new integral experiments on tungsten and vanadium-alloy (V-4Cr-4Ti) with the DT neutron source at JAEA/FNS in this study. A rectangular tungsten assembly of 35.5 cm in height, 35.5 cm in width and 50.7 cm in thickness is covered with Li_2O blocks of 5.1 cm in thickness for the front part, 15.2 cm in thickness for the side parts and 20.2 cm in thickness for the rear part to exclude background neutrons which might affect the measured data. A rectangular vanadium-alloy assembly of 13.6 cm in height, 15.2 cm in width and 15.2 cm in thickness is covered with Li_2O blocks of 10.2 cm in thickness for the front part, 25.3 cm in thickness for the side parts and 25.3 cm in thickness for the rear part. Using activation foils and micro fission chambers, we measure the reaction rates of the ^{93}Nb(n,2n)^{92m}Nb, ^{27}Al(n,α)^{24}Na, ^{115}In(n,n')^{115m}In, ^{197}Au(n,γ)^{198}Au, ^{186}W(n,γ)^{187}W, ^{235}U(n,f) and ^{238}U(n,f) reactions. We analyze the experiment by using MCNP5-1.40 with the recent nuclear data libraries, ENDF/B-VII.1, JEFF-3.2, JENDL-4.0 and FENDL-3.0. All the calculation results generally show good agreement with the measured ones in both tungsten and vanadium-alloy experiments. The calculation results of the ^{197}Au(n,γ)^{198}Au reaction by JENDL-4.0 show slightly better agreement with the measured ones compared with those by ENDF/B-VII.1 and JEFF-3.2 in the tungsten experiment. The calculation results of the ^{186}W(n,γ)^{187}W reaction by JEFF-3.2 show slight overestimation with the measured ones in the vanadium-alloy experiment. It is concluded that the nuclear data of tungsten and vanadium have no problem.

47 Analysis of Benchmark Experiment on Molybdenum at JAEA/FNS

Masayuki Ohta, Saerom Kwon, Kentaro Ochiai, Satoshi Sato, Chikara Konno

Japan Atomic Energy Agency, Tokai-mura, Naka-gun, Ibaraki-ken, Japan

A benchmark experiment with a Mo assembly of 253 × 253 × 354 mm^3 and the DT neutron source at JAEA/FNS was carried out to validate recent nuclear data of Mo and was presented at the last Symposium on Nuclear Data. As a result it was found out that the ratios of the calculated reaction rates to the experimental ones generally decreased with the increasing distance from the front surface of the assembly.

Here the reasons of the underestimation are investigated. We focus on the cross section data of ^{nat}Mo. The reaction cross sections of ^{nat}Mo are derived from the Mo isotope data in ENDF/B-VII.1, JEFF-3.2 and JENDL-4.0 by using the MIXR module in the NJOY99 code. The comparison between these evaluated data and the experimental data of ^{nat}Mo suggests that the (n,2n) cross section data in JEFF-3.2 seem to be more appropriate than those in JENDL-4.0 and ENDF/B-VII.1 and that the (n,γ) cross section data seem to be larger by about 30% in higher energy region. As a trial, we exchange the (n,2n) cross section data of all the Mo stable isotopes in JENDL-4.0 with those in JEFF-3.2, and multiply the (n,γ) cross section data above 100 eV of all the Mo stable isotopes except for ^{98}Mo in JENDL-4.0 by 0.7. We make temporary ACE files by using the NJOY99 code from the modified JENDL-4.0 files (JENDL-4.0.mod). The calculated results with the JENDL-4.0.mod show fairly good agreements with all the measured reaction rates and fission rates except for the reaction rate of the ^{115}In(n,n')^{115m}In reaction. The calculated result for the reaction rate of the ^{115}In(n,n')^{115m}In reaction with JENDL-4.0.mod is not so improved. It is concluded that the (n,2n) cross section data for the Mo stable isotopes in JEFF-3.2 are more appropriate than those in JENDL-4.0 and the (n,γ) cross section data of the Mo stable isotopes except for ^{98}Mo in JENDL-4.0 are larger.

This is a blank page.

国際単位系（SI）

表１．SI 基本単位

基本量	SI 基本単位	
	名称	記号
長さ	メートル	m
質量	キログラム	kg
時間	秒	s
電流	アンペア	A
熱力学温度	ケルビン	K
物質量	モル	mol
光度	カンデラ	cd

表２．基本単位を用いて表されるSI組立単位の例

組立量	SI 組立単位	
	名称	記号
面積	平方メートル	m^2
体積	立方メートル	m^3
速さ，速度	メートル毎秒	m/s
加速度	メートル毎秒毎秒	m/s^2
波数	毎メートル	m^{-1}
密度，質量密度	キログラム毎立方メートル	kg/m^3
面積密度	キログラム毎平方メートル	kg/m^2
比体積	立方メートル毎キログラム	m^3/kg
電流密度	アンペア毎平方メートル	A/m^2
磁界の強さ	アンペア毎メートル	A/m
量濃度(a)，濃度	モル毎立方メートル	mol/m^3
質量濃度	キログラム毎立方メートル	kg/m^3
輝度	カンデラ毎平方メートル	cd/m^2
屈折率(b)	（数字の）　1	1
比透磁率(b)	（数字の）　1	1

(a) 量濃度（amount concentration）は臨床化学の分野では物質濃度（substance concentration）ともよばれる。

(b) これらは無次元量あるいは次元１をもつ量であるが、そのことを表す単位記号である数字の１は通常は表記しない。

表３．固有の名称と記号で表されるSI組立単位

組立量	SI 組立単位			
	名称	記号	他のSI単位による表し方	SI基本単位による表し方
平面角	ラジアン(b)	rad	1 (b)	m/m
立体角	ステラジアン(b)	sr(c)	1 (b)	m^2/m^2
周波数	ヘルツ (d)	Hz		s^{-1}
力	ニュートン	N		$m\ kg\ s^{-2}$
圧力，応力	パスカル	Pa	N/m^2	$m^{-1}\ kg\ s^{-2}$
エネルギー，仕事，熱量	ジュール	J	N m	$m^2\ kg\ s^{-2}$
仕事率，工率，放射束	ワット	W	J/s	$m^2\ kg\ s^{-3}$
電荷，電気量	クーロン	C		s A
電位差（電圧），起電力	ボルト	V	W/A	$m^2\ kg\ s^{-3}\ A^{-1}$
静電容量	ファラド	F	C/V	$m^{-2}\ kg^{-1}\ s^4\ A^2$
電気抵抗	オーム	Ω	V/A	$m^2\ kg\ s^{-3}\ A^{-2}$
コンダクタンス	ジーメンス	S	A/V	$m^{-2}\ kg^{-1}\ s^3\ A^2$
磁束	ウエーバ	Wb	Vs	$m^2\ kg\ s^{-2}\ A^{-1}$
磁束密度	テスラ	T	Wb/m^2	$kg\ s^{-2}\ A^{-1}$
インダクタンス	ヘンリー	H	Wb/A	$m^2\ kg\ s^{-2}\ A^{-2}$
セルシウス温度	セルシウス度(e)	℃		K
光束	ルーメン	lm	cd sr(c)	cd
照度	ルクス	lx	lm/m^2	$m^{-2}\ cd$
放射性核種の放射能 (f)	ベクレル (d)	Bq		s^{-1}
吸収線量, 比エネルギー分与, カーマ	グレイ	Gy	J/kg	$m^2\ s^{-2}$
線量当量, 周辺線量当量, 方向性線量当量, 個人線量当量	シーベルト (g)	Sv	J/kg	$m^2\ s^{-2}$
酸素活性	カタール	kat		$s^{-1}\ mol$

(a)SI接頭語は固有の名称と記号を持つ組立単位と組み合わせても使用できる。しかし接頭語を付した単位はもはやコヒーレントではない。

(b)ラジアンとステラジアンは数字の１に対する単位の特別な名称で、量についての情報をつたえるために使われる。実際には、使用する時には記号rad及びsrが用いられるが、習慣として組立単位としての記号である数字の１は明示されない。

(c)測光学ではステラジアンという名称と記号srを単位の表し方の中に、そのまま維持している。

(d)ヘルツは周期現象についてのみ、ベクレルは放射性核種の統計的過程についてのみ使用される。

(e)セルシウス度はケルビンの特別な名称で、セルシウス温度を表すために使用される。セルシウス度とケルビンの単位の大きさは同一である。したがって、温度差や温度間隔を表す数値はどちらの単位で表しても同じである。

(f)放射性核種の放射能（activity referred to a radionuclide）は、しばしば誤った用語で”radioactivity”と記される。

(g)単位シーベルト（PV,2002,70,205）についてはCIPM勧告2（CI-2002）を参照。

表４．単位の中に固有の名称と記号を含むSI組立単位の例

組立量	SI 組立単位		
	名称	記号	SI 基本単位による表し方
粘度	パスカル秒	Pa s	$m^{-1}\ kg\ s^{-1}$
力のモーメント	ニュートンメートル	N m	$m^2\ kg\ s^{-2}$
表面張力	ニュートン毎メートル	N/m	$kg\ s^{-2}$
角速度	ラジアン毎秒	rad/s	$m\ m^{-1}\ s^{-1}=s^{-1}$
角加速度	ラジアン毎秒毎秒	rad/s^2	$m\ m^{-1}\ s^{-2}=s^{-2}$
熱流密度，放射照度	ワット毎平方メートル	W/m^2	$kg\ s^{-3}$
熱容量，エントロピー	ジュール毎ケルビン	J/K	$m^2\ kg\ s^{-2}\ K^{-1}$
比熱容量，比エントロピー	ジュール毎キログラム毎ケルビン	J/(kg K)	$m^2\ s^{-2}\ K^{-1}$
比エネルギー	ジュール毎キログラム	J/kg	$m^2\ s^{-2}$
熱伝導率	ワット毎メートル毎ケルビン	W/(m K)	$m\ kg\ s^{-3}\ K^{-1}$
体積エネルギー	ジュール毎立方メートル	J/m^3	$m^{-1}\ kg\ s^{-2}$
電界の強さ	ボルト毎メートル	V/m	$m\ kg\ s^{-3}\ A^{-1}$
電荷密度	クーロン毎立方メートル	C/m^3	$m^{-3}\ s\ A$
表面電荷	クーロン毎平方メートル	C/m^2	$m^{-2}\ s\ A$
電束密度，電気変位	クーロン毎平方メートル	C/m^2	$m^{-2}\ s\ A$
誘電率	ファラド毎メートル	F/m	$m^{-3}\ kg^{-1}\ s^4\ A^2$
透磁率	ヘンリー毎メートル	H/m	$m\ kg\ s^{-2}\ A^{-2}$
モルエネルギー	ジュール毎モル	J/mol	$m^2\ kg\ s^{-2}\ mol^{-1}$
モルエントロピー, モル熱容量	ジュール毎モル毎ケルビン	J/(mol K)	$m^2\ kg\ s^{-2}\ K^{-1}\ mol^{-1}$
照射線量（Ｘ線及びγ線）	クーロン毎キログラム	C/kg	$kg^{-1}\ s\ A$
吸収線量率	グレイ毎秒	Gy/s	$m^2\ s^{-3}$
放射強度	ワット毎ステラジアン	W/sr	$m^4\ m^{-2}\ kg\ s^{-3}=m^2\ kg\ s^{-3}$
放射輝度	ワット毎平方メートル毎ステラジアン	$W/(m^2\ sr)$	$m^2\ m^{-2}\ kg\ s^{-3}=kg\ s^{-3}$
酵素活性濃度	カタール毎立方メートル	kat/m^3	$m^{-3}\ s^{-1}\ mol$

表５．SI 接頭語

乗数	名称	記号	乗数	名称	記号
10^{24}	ヨタ	Y	10^{-1}	デシ	d
10^{21}	ゼタ	Z	10^{-2}	センチ	c
10^{18}	エクサ	E	10^{-3}	ミリ	m
10^{15}	ペタ	P	10^{-6}	マイクロ	μ
10^{12}	テラ	T	10^{-9}	ナノ	n
10^{9}	ギガ	G	10^{-12}	ピコ	p
10^{6}	メガ	M	10^{-15}	フェムト	f
10^{3}	キロ	k	10^{-18}	アト	a
10^{2}	ヘクト	h	10^{-21}	ゼプト	z
10^{1}	デカ	da	10^{-24}	ヨクト	y

表６．SIに属さないが、SIと併用される単位

名称	記号	SI 単位による値
分	min	1 min=60 s
時	h	1 h =60 min=3600 s
日	d	1 d=24 h=86 400 s
度	°	$1° = (\pi/180)$ rad
分	’	$1' = (1/60)° = (\pi/10\ 800)$ rad
秒	”	$1'' = (1/60)' = (\pi/648\ 000)$ rad
ヘクタール	ha	$1\ ha=1\ hm^2=10^4 m^2$
リットル	L，l	$1\ L=1\ l=1\ dm^3=10^3 cm^3=10^{-3} m^3$
トン	t	$1\ t=10^3\ kg$

表７．SIに属さないが、SIと併用される単位で、SI単位で表される数値が実験的に得られるもの

名称	記号	SI 単位で表される数値
電子ボルト	eV	$1\ eV=1.602\ 176\ 53(14)\times10^{-19} J$
ダルトン	Da	$1\ Da=1.660\ 538\ 86(28)\times10^{-27} kg$
統一原子質量単位	u	1 u=1 Da
天文単位	ua	$1\ ua=1.495\ 978\ 706\ 91(6)\times10^{11} m$

表８．SIに属さないが、SIと併用されるその他の単位

名称	記号	SI 単位で表される数値
バール	bar	$1\ bar=0.1 MPa=100\ kPa=10^5 Pa$
水銀柱ミリメートル	mmHg	$1\ mmHg \approx 133.322 Pa$
オングストローム	Å	$1\ Å=0.1 nm=100 pm=10^{-10} m$
海里	M	1 M=1852m
バーン	b	$1\ b=100 fm^2=(10^{-12} cm)^2=10^{-28} m^2$
ノット	kn	1 kn=(1852/3600)m/s
ネーパ	Np	SI単位との数値的な関係は、対数量の定義に依存。
ベル	B	
デシベル	dB	

表９．固有の名称をもつCGS組立単位

名称	記号	SI 単位で表される数値
エルグ	erg	$1\ erg=10^{-7}\ J$
ダイン	dyn	$1\ dyn=10^{-5} N$
ポアズ	P	$1\ P=1\ dyn\ s\ cm^{-2}=0.1 Pa\ s$
ストークス	St	$1\ St=1 cm^2\ s^{-1}=10^{-4} m^2\ s^{-1}$
スチルブ	sb	$1\ sb=1 cd\ cm^{-2}=10^4 cd\ m^{-2}$
フォト	ph	$1\ ph=1 cd\ sr\ cm^{-2}=10^4 lx$
ガル	Gal	$1\ Gal=1 cm\ s^{-2}=10^{-2} ms^{-2}$
マクスウエル	Mx	$1\ Mx = 1G\ cm^2=10^{-8} Wb$
ガウス	G	$1\ G=1 Mx\ cm^{-2}=10^{-4} T$
エルステッド (a)	Oe	$1\ Oe \triangleq (10^3/4\pi) A\ m^{-1}$

(a) ３元系のCGS単位系とSIでは直接比較できないため、等号「 ≙ 」は対応関係を示すものである。

表10．SIに属さないその他の単位の例

名称	記号	SI 単位で表される数値
キュリー	Ci	$1\ Ci=3.7\times10^{10} Bq$
レントゲン	R	$1\ R = 2.58\times10^{-4} C/kg$
ラド	rad	$1\ rad=1 cGy=10^{-2} Gy$
レム	rem	$1\ rem=1\ cSv=10^{-2} Sv$
ガンマ	γ	$1\ \gamma=1\ nT=10^{-9} T$
フェルミ		1 フェルミ$=1\ fm=10^{-15} m$
メートル系カラット		1 メートル系カラット$= 0.2\ g = 2\times10^{-4} kg$
トル	Torr	1 Torr = (101 325/760) Pa
標準大気圧	atm	1 atm = 101 325 Pa
カロリー	cal	1 cal=4.1858J（「15℃」カロリー），4.1868J（「IT」カロリー），4.184J（「熱化学」カロリー）
ミクロン	μ	$1\ \mu=1 \mu m=10^{-6} m$

（第8版，2006年）